

UNIVERSITÄT  
BAYREUTH

Bayreuther Graduiertenschule für Mathematik und Naturwissenschaften  
Fotophysik synthetischer und biologischer multichromophorer Systeme

---

# Charge and excitation-energy transfer in time-dependent density functional theory

---

## **Genehmigte Abhandlung**

zur Erlangung des akademischen Grades eines Doktors der  
Naturwissenschaften (Dr. rer. nat.) im Promotionsprogramm  
Fotophysik synthetischer und biologischer multichromophorer Systeme  
der Bayreuther Graduiertenschule für Mathematik und  
Naturwissenschaften

von

**Dirk Hofmann-Mees**

geb. Hofmann

aus

Coburg

Erstgutachter: Prof. Dr. Stephan Kümmel  
Zweitgutachter: Prof. Dr. V. Martin Axt

Tag der Einreichung: 06. September 2012  
Tag des Kolloquiums: 19. Dezember 2012



# Abstract

Learning about and understanding the mechanisms and pathways of charge and excitation-energy transfer of natural molecular complexes is a promising approach for the tailored design of new artificial energy-converting materials. Therefore, next to extensive experimental investigations, a theoretical method that is able to reliably describe and predict these phenomena from first principles is of practical relevance. In principle, density functional theory (DFT) and time-dependent density functional theory (TDDFT) appear as natural choices to study the relevant sizable molecules on a first-principles scale at bearable computational cost. However, the application of standard local and semilocal density functional approximations suffers from well-known deficiencies, in particular, as far as the simulation of charge-transfer phenomena is concerned. The present thesis approaches charge and excitation-energy transfer with the objective of improving the predictive power and extending the range of applicability of (TD)DFT.

The deficiencies of standard density functional approximations have been related to self-interaction. Hence, one major aspect of this work is the extension of the self-interaction correction in Kohn-Sham DFT that is based on the generalized optimized effective potential to TDDFT using a real-time propagation approach. The multiplicative Kohn-Sham potential allows for a transparent analysis of the exchange-correlation potential during time evolution. It reveals frequency-dependent field-counteracting behavior and step structures that appear in dynamic charge-transfer situations. The latter are important for the proper description of charge transfer. Self-interaction correction allows to access many cases that are difficult for standard TDDFT ranging from chain-like systems over excitonic excitations in semiconductor nanoclusters to short- and long-range charge-transfer excitations. At the same time, it does not spoil the reasonable accuracy that already (semi)local functionals exhibit for local excitations. Moreover, the TDDFT perspective on self-interaction correction sheds new light also on the ground-state formalism. Complex degrees of freedom in the energy-minimizing transformation of the generalized optimized effective potential approach yield smoother orbital densities that appear more reasonable when inserted into approximate functionals in the self-interaction correction formalism. This work provides new insight into the use of different functional approximations. Last but not least, the influence of spin-symmetry breaking and step structures of the potential on the preference to transfer integer units of the elementary electric charge between largely separated donor and acceptor moieties is illustrated when static external electric fields are applied. This work has been reported in three publications and one submitted manuscript.

In the field of excitation-energy transfer, recent discoveries of quantum coherence effects shed new light on the mechanisms behind energy-transfer rates. The latter are affected by a number of different properties of the isolated molecules, but involve also effects due to the

environment of the system. This thesis addresses excitation-energy transfer phenomena from two perspectives. First, I use real-time propagation TDDFT to investigate the intermolecular coupling strength and the coupling mechanism between single fragments of supermolecular setups. These investigations base on standard closed quantum system TDDFT and exploit the coherent oscillation of excitation energy between separated molecules after the initial excitation process. Second, I use open quantum system ideas in the framework of TDDFT to study the influence of the system's environment on the energy-transfer time scales and pathways in a circular arrangement of molecules using an effective energy-dissipation mechanism. The first part of these results is published. The second part is presented in this thesis and includes work in progress.

# Kurzfassung

Ein viel versprechender Ansatz, um künstliche Materialien für Zwecke der Energieumwandlung zu entwickeln, besteht darin, neues Wissen über die Mechanismen und Übertragungswege von Ladung und Anregungsenergie in Molekülkomplexen, die in der Natur vorkommen, zu erwerben. Dafür werden neben umfangreichen experimentellen Untersuchungen auch Methoden benötigt, mit denen man solche Phänomene zuverlässig theoretisch beschreiben und vorhersagen kann. Prinzipiell bieten sich die Dichtefunktionaltheorie (DFT) und die zeitabhängige Dichtefunktionaltheorie an, um Systeme der relevanten Größe mit tragbarem numerischem Aufwand ausgehend von physikalischen Grundprinzipien zu untersuchen. Allerdings wurden in Anwendungen der DFT mit lokalen und semilokalen Dichtefunktional-Näherungen Probleme aufgezeigt, die insbesondere in Simulationen von Ladungstransferphänomenen kritisch sind. Daher untersucht die vorliegende Dissertation Ladungs- und Energietransferphänomene mit dem Ziel, die Vorhersagen der (zeitabhängigen) DFT zu verbessern und deren Anwendungsbereich zu erweitern.

Die Probleme, die sich aufzeigen, wenn man herkömmliche Dichtefunktional-Näherungen verwendet, wurden mit der sogenannten Selbstwechselwirkung in Verbindung gebracht. Deshalb ist die Erweiterung der Methode zur Selbstwechselwirkungskorrektur, die im Rahmen der Kohn-Sham-DFT auf dem Verfahren der verallgemeinerten optimierten effektiven Potentiale beruht, auf den Bereich der zeitabhängigen DFT einer der zentralen Aspekte dieser Arbeit. Die Erweiterung beruht auf einem Echtzeitpropagationsverfahren und verwendet ein multiplikatives Kohn-Sham-Potential, mit dem man auf transparente Art und Weise den Zeitverlauf des Austausch-Korrelationspotentials untersuchen kann. In der vorliegenden Arbeit wird aufgezeigt, dass dieses Potential frequenzabhängiges Gegenfeldverhalten aufweist und sich Stufenstrukturen in Ladungstransfersimulationen aufbauen. Diese Strukturen sind für eine zuverlässige Beschreibung von Ladungstransferphänomenen wichtig. Darüber hinaus ermöglicht das Selbstwechselwirkungskorrekturverfahren die Untersuchung vieler Systeme, die für herkömmliche zeitabhängige DFT als notorisch schwierig gelten, ohne dabei die Genauigkeit zu verlieren, die bereits (semi)lokale Funktionale bei der Beschreibung lokaler Anregungen aufweisen. Unter diesen Systemen befinden sich kettenförmige Moleküle, Halbleiter-Nanocluster, deren Anregungen als exzitonisch gelten, sowie kurz- und langreichweitige Ladungstransferanregungen. Weiterhin liefern die Erkenntnisse aus den Untersuchungen der zeitabhängigen DFT neue Einblicke in den Grundzustandsformalismus. Die Verwendung von komplexwertigen Freiheitsgraden zur Bestimmung der energieminimierenden Transformationen im Verfahren der verallgemeinerten optimierten effektiven Potentiale führt zu glatteren Orbitaldichten. Diese Orbitaldichten scheinen besser geeignet zu sein, um sie im Rahmen des Selbstwechselwirkungskorrekturverfahrens in genäherte Funktionale einzusetzen. In dieser Arbeit diskutiere ich neue Einsichten in die Verwendung unterschiedlicher Näherungen der

Funktionale. Weiterhin erläutere ich den Einfluss von Spinsymmetriebrechung und Stufenstrukturen im Potential darauf, ob beim Ladungstransfer durch externe elektrische Felder zwischen zwei weit entfernten Donor- und Akzeptormolekülen der Ladungstransfer ganzzahliger Vielfacher der Elementarladung bevorzugt wird oder nicht. Die gefundenen Resultate sind in drei Publikationen veröffentlicht und ein weiteres Manuskript wurde bereits eingereicht.

Im Forschungsgebiet des Anregungsenergietransfers haben aktuelle Erkenntnisse zur Rolle sogenannter Quantenkohärenzen neue Einblicke in die Mechanismen des Energietransfers geliefert. Die relevanten Energietransferraten werden von vielen verschiedenen Eigenschaften der Moleküle und durch Effekte der Umgebung des Systems beeinflusst. In dieser Arbeit untersuche ich den Anregungsenergietransfer aus zwei Richtungen. Einerseits verwende ich Echtzeitpropagation im Rahmen der zeitabhängigen DFT, um die Kopplungsstärke und den Kopplungsmechanismus zwischen zwei einzelnen Molekülen zu untersuchen. Dieser Studie liegt eine Herangehensweise zugrunde, die ein geschlossenes Quantensystem benutzt und in deren Rahmen man kohärente Oszillationen der Anregungsenergie zwischen den Molekülen beobachten kann. Andererseits nutze ich einen Ansatz, offene Quantensysteme in Kombination mit dem Formalismus der zeitabhängigen DFT zu verwenden, um den Einfluss der Umgebung des Systems auf die Zeitskala und die Wege des Anregungsenergietransfers zu untersuchen. Ich habe dazu einen heuristischen Dissipationsmechanismus entwickelt und wende diesen auf eine ringförmige Anordnung von Molekülen an. Der erste Teil dieser Ergebnisse ist bereits veröffentlicht, während der zweite Teil Untersuchungen enthält, die in dieser Arbeit erstmals präsentiert werden.

# Contents

<b>Abstract</b>	<b>III</b>
<b>Kurzfassung</b>	<b>V</b>
<b>Contents</b>	<b>VII</b>
<b>1 Motivation</b>	<b>1</b>
<b>2 Density functional theory and time-dependent density functional theory</b>	<b>3</b>
2.1 Density functional theory . . . . .	4
2.1.1 Basics of density functional theory . . . . .	4
2.1.2 Kohn-Sham density functional theory . . . . .	4
2.2 Time-dependent density functional theory . . . . .	6
2.2.1 An introduction to time-dependent density functional theory . . . . .	6
2.2.2 TDDFT linear response formalism . . . . .	7
2.2.3 Real-time propagation TDDFT . . . . .	8
2.3 The transition density analysis tool . . . . .	9
2.4 Exact properties and features of the exchange-correlation potential . . . . .	10
2.5 Exchange-correlation functionals . . . . .	12
2.5.1 Approximations for the exchange-correlation energy functional . . . . .	12
2.5.2 Exchange-correlation functionals in TDDFT . . . . .	14
2.6 Numerical realization . . . . .	15
<b>3 Self-interaction correction</b>	<b>17</b>
3.1 The self-interaction problem . . . . .	17
3.2 Self-interaction correction . . . . .	18
3.3 The optimized effective potential and its generalization . . . . .	19
3.3.1 The optimized effective potential method . . . . .	19
3.3.2 Generalization of the OEP to unitarily variant functionals . . . . .	20
3.4 Unitary optimization with different types of orbitals . . . . .	21
3.5 Generalized self-interaction correction in DFT . . . . .	22
3.6 Generalization of SIC in TDDFT . . . . .	24
3.7 Performance of generalized SIC in TDDFT . . . . .	26

<b>4</b>	<b>Charge transfer and charge-transfer excitation energies</b>	<b>29</b>
4.1	The charge-transfer problem of DFT and TDDFT and some solution ideas . . .	29
4.2	Self-interaction correction and charge transfer . . . . .	31
4.2.1	The integer preference of electron jumps . . . . .	31
4.2.2	The performance of GSIC on charge-transfer excitation energies . . . .	35
<b>5</b>	<b>Excitation-energy transfer</b>	<b>37</b>
5.1	Intermolecular coupling and real-time TDDFT . . . . .	37
5.2	Open quantum systems in the density functional context . . . . .	39
5.2.1	The Stochastic Schrödinger equation . . . . .	40
5.2.2	Stochastic Schrödinger equation and Kohn-Sham density functional theory . . . . .	41
5.2.3	A single-particle approach in practice . . . . .	43
5.3	Pathways and time constants of excitation-energy transfer . . . . .	44
5.3.1	The excitation-energy transfer model system . . . . .	44
5.3.2	Practical simulation approach . . . . .	46
5.3.3	Resonant excitation spread and decay time constants . . . . .	48
5.3.4	Influence of energetic off-resonance . . . . .	49
5.3.5	Influence of the intrasystem coupling . . . . .	50
5.4	Summary and Outlook . . . . .	51
	<b>Appendix</b>	<b>55</b>
<b>A</b>	<b>Polarizability and static charge-transfer properties</b>	<b>55</b>
A.1	Polarizability and field-counteracting potentials in self-interaction free density functional theory . . . . .	55
A.2	Polarizability of polyacetylene chains . . . . .	59
A.3	Static charge transfer in a transparent model system . . . . .	60
<b>B</b>	<b>Multigrid Poisson solver</b>	<b>63</b>
B.1	Multigrid and defect correction . . . . .	64
B.1.1	The multigrid idea . . . . .	64
B.1.2	An introduction to defect correction . . . . .	66
B.2	Features of the PARSEC code in the multigrid context . . . . .	67
B.3	The multigrid implementation in PARSEC . . . . .	69
B.4	Assessment of the multigrid solver . . . . .	71
<b>C</b>	<b>Algorithms for the unitary optimization</b>	<b>75</b>
C.1	Algorithmic principles . . . . .	75
C.1.1	Fois loops based on the Pederson criterion . . . . .	75
C.1.2	Energy gradient based algorithm . . . . .	77
C.1.3	Energy gradient and line-search optimization . . . . .	78
C.2	The unitary optimization algorithms in PARSEC . . . . .	80
C.2.1	Initialization of the optimization steps . . . . .	80
C.2.2	The PARSEC implementation . . . . .	82

<b>D Förster-type potentials and stochastic time-dependent density functional theory</b>	<b>85</b>
D.1 Förster-type potentials and grid partitioning . . . . .	85
D.1.1 The Förster-type potential expansion in Donor-Acceptor systems . . .	85
D.1.2 Using Förster-type potentials in supermolecular systems . . . . .	87
D.1.3 Partition-selective excitation and observation . . . . .	88
D.2 Unraveling the coupling strength with TDDFT . . . . .	88
D.3 Stochastic time-dependent density functional theory . . . . .	90
D.3.1 An attempt towards a theoretical justification of stochastic time-dependent density functional theory with specific bath operators . . . . .	90
D.3.2 Bath operators in the single-particle KS framework and related features	95
D.3.3 PARSEC features and input parameters . . . . .	97
<b>E PARSEC miscellaneous</b>	<b>99</b>
E.1 General comments on the PARSEC input . . . . .	99
E.2 Determining the midpoint Hamiltonian during propagation via extrapolation	99
E.3 On the fly Fourier transformation of the time-dependent density . . . . .	101
E.4 Propagation miscellaneous . . . . .	101
E.5 Adaptation of the diagonalization tolerance during the ground-state procedure	102
E.6 Ground-state miscellaneous . . . . .	103
<b>Acknowledgment</b>	<b>105</b>
<b>List of publications and manuscripts</b>	<b>107</b>
<b>List of abbreviations, functionals, and methods</b>	<b>109</b>
<b>Bibliography</b>	<b>113</b>
<b>Erklärung</b>	<b>133</b>
<b>Publication 1</b>	<b>135</b>
<b>Publication 2</b>	<b>147</b>
<b>Publication 3</b>	<b>155</b>
<b>Publication 4</b>	<b>169</b>
<b>Manuscript 1</b>	<b>189</b>



# Chapter 1

## Motivation

*For actually, in spite of the variety of topics involved, the whole enterprise is intended to convey one idea only – one small comment on a large and important question. In order not to lose our way, it may be useful to outline the plan very briefly in advance.*

Erwin Schrödinger  
What is life? (1944)

Today's energy demands are a driving force for the investigation of new energy converting materials, concepts, and devices. In particular, because of world-wide attempts to reduce pollution originating from conventional power plants and political decisions against nuclear power generation via nuclear fission, renewable and sustainable energy recovery is a growing field in industry and academia. In this context, development of methodologies for solar energy harvesting is inspired by the tremendous efficiency of energy recovery in biological systems. In recent years, researchers all over the world returned to the original building blocks of natural light harvesting (LH) systems, and materials and chromophores out of the toolbox of organic and macromolecular chemistry are experiencing a boom.

A detailed understanding of the mechanisms and pathways of energy recovery in natural molecular LH complexes is a promising starting point for the tailored design of new artificial energy-converting materials. Future development in the field of molecular electronic devices will require a close cooperation of synthetic chemistry, material and device characterization, and application design. On all stages of this development also theoretical investigations are needed to support elementary understanding and decision making. In particular, for a target-oriented design of high efficiency LH materials, it is important to understand the mechanisms of charge transfer (CT) and excitation-energy transfer (EET) of many single transfer steps. In multichromophoric supermolecules such as LH systems, the rates of these mechanisms are affected by a number of different properties and phenomena. In particular, they involve the interaction between many unique system components and the interplay with the system's environment.

A theoretical method that is supposed to provide insight into the physics of technologically relevant organic materials, therefore, needs to fulfill a couple of criteria: (i) handle the relevant system size even beyond single multichromophoric molecules, (ii) guarantee reliability of its results, and (iii) provide predictive power beyond standard test systems. In principle, (time-dependent) density functional theory (TD)DFT appears as a natural choice to study sizable molecules on a first-principles scale at bearable computational cost.

However, the validity of (TD)DFT results strongly depends on the underlying approximations for exchange-correlation (xc) effects. Application of standard local and semilocal density functionals suffers from well-known deficiencies: incorrect dissociation limits [ZY98], wrong asymptotic behavior of the potential [PZ81], and overestimation of electrical response properties [vGSG<sup>+</sup>99]. Problems are reported in semiconductor nanoclusters [ORR02, OCL97, RL98, RL00, VOC02, VOC06], where standard TDDFT functionals tend to underestimate low-lying optical excitations [MCR01]. Moreover, dynamical properties like transport characteristics [TFSB05] are overestimated and one observes an incorrect representation of CT states [DWHG03, Toz03]. Therefore, to guarantee the reliability and predictive power of (TD)DFT, there is serious need for the improvement of xc functionals.

During this thesis, I focused on the elementary processes of CT and EET, and the theoretical description of such processes in the framework of (TD)DFT. In particular, I investigated self-interaction correction (SIC) ideas based on Kohn-Sham (KS) theory and their application in and extension to real-time propagation TDDFT as one promising approach to deal with the CT problem. I found that SIC implemented via the generalized optimized effective potential (GOEP) [KKM08] and approximations to the GOEP yields polarizabilities, excitation energies, and CT properties in good agreement with reference calculations. In the field of EET, I developed a tool that uses standard TDDFT real-time propagation to compute the coupling strength between chromophores in a supermolecular environment. Further investigations, required an extension of the standard formulation of closed quantum system TDDFT to open quantum systems that allows for the inclusion of decoherence and dissipation effects. I investigated such a scheme in the framework of stochastic TDDFT and demonstrated its applicability to EET in circularly arranged model systems in the spirit of natural LH systems. This work includes four publications referred to as Pub1 - Pub4 and one submitted manuscript referred to as Man1 that are assembled at the back of this thesis.

This cumulative dissertation is organized as follows. Chapter 2 provides an elementary introduction to DFT and TDDFT including all concepts that are important for this thesis. I introduce the self-interaction problem, self-interaction correction ideas, and their implementation in KS DFT and TDDFT in Chap. 3. In Chap. 4, I discuss the CT problem and demonstrate how explicit SIC helps with CT investigations. Finally, I present the investigations on EET and the coupling mechanism in Chap. 5 that comprises unpublished results and work in progress concerning open quantum system treatment ideas in the TDDFT framework. Supplementary results and findings are gathered in Appendix A. Many of the results required enormous numerical effort that could only be accomplished by performance enhancement and the implementation of new algorithms to the PARSEC program package. Therefore, the other chapters B to E of the appendix give an overview, in parts detailed explanations, and more insight into the implementations and the practical usage of the new functionalities. They are supposed to serve as an overview and guide for future PARSEC users.

## Chapter 2

# Density functional theory and time-dependent density functional theory

*The large and important and very much discussed question is:  
How can the events in space and time which take place within the  
spatial boundary of a living organism be accounted for by physics and  
chemistry?*

Erwin Schrödinger  
What is life? (1944)

Density functional theory and time-dependent density functional theory are the methodological basis of this dissertation. They are both in principle exact formulations of many-particle quantum theory, at the same time providing means to study sizable systems at comparably low computational cost. The numerical advantages of (TD)DFT rest upon its single-particle representation of many-particle quantum systems using the Kohn-Sham scheme. Yet, reliability of (TD)DFT results strongly depends on the approximations that are used for many-particle exchange-correlation effects in this single-particle representation. I give a short review of the basics of DFT in Sec. 2.1. However, the main focus of this work is on TDDFT. Its basic concepts are introduced in Sec. 2.2. There, I also discuss the two most important routes to obtain excitation energies: the TDDFT *linear response formalism* that is well-known as the *Casida approach* and TDDFT based on *real-time propagation* of the KS system. In Sec. 2.3, I explain the idea of using *transition densities* to investigate the origin of excitation peaks in the absorption spectra computed with TDDFT methods. I complement this basic introduction with Sec. 2.4 on fundamental features of the KS scheme and the xc potential that are vital background for understanding some of the aspects of this work. In Sec. 2.5, I introduce important xc functional approximations. Finally, details about the numerical realization of this work are provided in Sec. 2.6. Throughout this thesis, I use the Born-Oppenheimer approximation and consider the electronic structure problem only.

For a more detailed discussion of DFT, I recommend the books of Dreizler and Gross [DG90] and of Fiolhais *et al.* [NFM03], as well as the review article of Capelle [Cap02]. Recent overviews of TDDFT are provided in the two books of Marques *et al.* [MUN<sup>+</sup>06] and [MMN<sup>+</sup>12], and in the following review articles [GDP96, MG04, EBF07, CHR12].

## 2.1 Density functional theory

### 2.1.1 Basics of density functional theory

Density functional theory in its original formulation is a method to compute ground-state (GS) properties of a many-particle system without the need to solve Schrödinger's equation. Instead, DFT uses the GS density  $n(\mathbf{r})$  as its basic variable, thus avoiding to compute the fully interacting many-particle wave function. This choice of the basic variable amounts to a drastic reduction of the number of degrees of freedom from  $3N$  coordinates of the Schrödinger wave function to three coordinates in the density representation. Therefore, while it is impossible to store the fully interacting wave function of sizable systems, DFT calculations can in principle be performed with up to hundreds or even thousands of atoms.

The mathematical equivalence of these formulations of quantum mechanics was settled by Pierre Hohenberg and Walter Kohn [HK64] in 1964. Today, the basis of DFT is well-known as the two *Hohenberg-Kohn (HK) theorems*.

**First HK theorem:** Given a particle-particle interaction  $W(\mathbf{r}, \mathbf{r}')$ , there exists a one-to-one correspondence between the electron density  $n(\mathbf{r})$ , the many-particle wave-function  $\Psi$ , and the local external potential  $v_{\text{ext}}(\mathbf{r})$ . Thus, the GS Hamiltonian  $H$ , the GS wave function  $\Psi_0$ , and all observables of the system are unique functionals of the GS density.

**Second HK theorem:** The GS energy  $E_0 = E[n_0]$  follows from a variational principle. It can be computed from the variational equation

$$\frac{\delta E[n]}{\delta n(\mathbf{r})} = 0 \quad (2.1)$$

taking the functional derivative of the energy density functional  $E[n]$  with respect to the density. The energy functional splits into the HK functional and contributions  $V[n]$  of the external potential  $v(\mathbf{r})$ , i.e.,  $E[n] = F_{\text{HK}} + V[n]$ . The universal HK functional subsumes the kinetic and the electron-electron interaction energy  $T[n]$  and  $W[n]$ .

Although the HK theorems provide the theoretical framework for a density representation of quantum mechanics, they do not give any explicit form of the exact HK functional. In light of the complexity of solving Schrödinger's equation, finding  $F_{\text{HK}}$  can even be considered intractably difficult [SV09]. Therefore, practical DFT calculations need to rely on reasonable approximations for  $F_{\text{HK}}$ .

### 2.1.2 Kohn-Sham density functional theory

The final breakthrough of DFT came with a single-particle representation of the many-particle system, the so-called *Kohn-Sham scheme* [KS65]. In the Kohn-Sham (KS) approach, the many-particle problem is mapped onto an auxiliary system of non-interacting particles that is supposed to give the same density as the true interacting system. Many-particle effects are covered by an effective local potential. To this end, the KS partitioning of the total energy gives a good starting point for developing approximations for  $F_{\text{HK}}$  and the related potential contributions. With regard to discussions in the following chapters, I use the notation of spin DFT [vBH72] with additional spin index  $\sigma$ . Atomic units are used throughout. In this formulation, the total energy of the electronic problem with Coulomb interaction reads

$$E[n_{\uparrow}, n_{\downarrow}] = F_{\text{HK}}[n_{\uparrow}, n_{\downarrow}] + V[n] = T_{\text{S}}[\{\varphi_{i\sigma}[n_{\sigma}]\}] + E_{\text{H}}[n] + E_{\text{xc}}[n_{\uparrow}, n_{\downarrow}] + V[n]. \quad (2.2)$$

$T_S[\{\varphi_{i\sigma}[n_\sigma]\}]$  is the kinetic energy functional of the  $N = N_\uparrow + N_\downarrow$  non-interaction electrons that are represented by the auxiliary orbitals  $\{\varphi_{i\sigma}\}$ , i.e.,

$$T_S[\{\varphi_{i\sigma}[n_\sigma]\}] = -\frac{1}{2} \sum_{\sigma=\uparrow,\downarrow} \sum_{i=1}^{N_\sigma} \int \varphi_{i\sigma}^*[n_\sigma](\mathbf{r}) \nabla^2 \varphi_{i\sigma}[n_\sigma](\mathbf{r}) d^3r, \quad (2.3)$$

and  $E_H[n]$  is the classical Hartree interaction

$$E_H[n] = \frac{1}{2} \int \int \frac{n(\mathbf{r})n(\mathbf{r}')}{|\mathbf{r} - \mathbf{r}'|} d^3r d^3r'. \quad (2.4)$$

The exchange-correlation (xc) energy functional  $E_{xc}[n_\uparrow, n_\downarrow]$  includes all many-particle effects that are not covered by the other functionals. Thus, it is related to  $F_{HK}[n_\uparrow, n_\downarrow]$ ,

$$E_{xc}[n_\uparrow, n_\downarrow] = F_{HK}[n_\uparrow, n_\downarrow] - T_S[\{\varphi_{i\sigma}[n_\sigma]\}] - E_H[n]. \quad (2.5)$$

The xc energy functional is the great unknown of DFT and needs to be approximated (see Sec. 2.5.1). The success of DFT depends on the quality of these approximations. Last but not least,  $V[n]$  considers external fields, e.g., the field of the atomic nuclei. In the following, any coupling of  $V[n]$  to the spin degrees of freedom is disregarded.

Based on the KS energy partitioning, the variational principle of the HK theorems leads to a set of single-particle Schrödinger equations, the so-called KS equations

$$\underbrace{\left[ -\frac{\nabla^2}{2} + v_{KS,\sigma}[n_\uparrow, n_\downarrow](\mathbf{r}) \right]}_{h_{KS,\sigma}(\mathbf{r})} \varphi_{i\sigma}(\mathbf{r}) = \epsilon_{i\sigma} \varphi_{i\sigma}(\mathbf{r}). \quad (2.6)$$

Here, I introduced the KS Hamiltonian  $h_{KS,\sigma}(\mathbf{r})$  that acts on the KS orbitals  $\{\varphi_{i\sigma}\}$ . The local multiplicative KS potential  $v_{KS,\sigma}[n_\uparrow, n_\downarrow](\mathbf{r})$  reads

$$v_{KS,\sigma}[n_\uparrow, n_\downarrow](\mathbf{r}) = v_H[n](\mathbf{r}) + v_{xc,\sigma}[n_\uparrow, n_\downarrow](\mathbf{r}) + v_{ext}(\mathbf{r}). \quad (2.7)$$

The single contributions are calculated as functional derivatives of the corresponding energy functionals with respect to the density, thus  $v_H[n](\mathbf{r}) = \int \frac{n(\mathbf{r}')}{|\mathbf{r} - \mathbf{r}'|} d^3r'$  and the xc potential reads

$$v_{xc,\sigma}[n_\uparrow, n_\downarrow](\mathbf{r}) = \frac{\delta E_{xc}[n_\uparrow, n_\downarrow]}{\delta n_\sigma(\mathbf{r})}. \quad (2.8)$$

Finally, the density of the KS system can be computed from the KS orbitals according to

$$n(\mathbf{r}) = \sum_{\sigma=\uparrow,\downarrow} n_\sigma(\mathbf{r}) = \sum_{\sigma=\uparrow,\downarrow} \sum_{i=1}^{N_\sigma} |\varphi_{i\sigma}(\mathbf{r})|^2. \quad (2.9)$$

In the basic KS DFT rationale,  $n(\mathbf{r})$  is the central quantity of physical significance, whereas the KS orbitals are auxiliary functions that do not necessarily carry physical meaning. Further insight into the properties of the KS system and the xc potential are provided in Sec. 2.4. In practical KS calculations,  $v_{KS,\sigma}$  is unknown at the beginning. Hence, the KS equations need to be solved self-consistently starting from some initial guess and iteratively updating the KS potential and diagonalizing the KS Hamiltonian.

## 2.2 Time-dependent density functional theory

### 2.2.1 An introduction to time-dependent density functional theory

Although the HK theorems lay the foundation for a density representation of the fully interacting many-particle system, they do not establish a direct relation between the GS density and truly dynamic or excited-state properties. The investigation of such properties using density functionals is based on time-dependent density functional theory. In TDDFT, the *Runge-Gross theorem* [RG84] is the complement of the HK theorems of GS DFT. Given an initial state and particle-particle interaction, it establishes a one-to-one correspondence between the time-dependent (TD) density  $n(\mathbf{r}, t)$  and the TD external potential  $v_{\text{ext}}(\mathbf{r}, t)$  up to a purely TD function  $c(t)$ . With  $v_{\text{ext}}(\mathbf{r}, t)$  and the initial state  $\Psi(t_0)$ , also the TD wave-function is determined uniquely up to a TD phase via solution of the TD Schrödinger equation. As expectation values of any operator are not sensitive to the phase of the wave function, in principle, each observable is a functional of  $n(\mathbf{r}, t)$  and the initial state. The Runge-Gross proof has been refined by van Leeuwen [vL99] who covers the *non-interacting  $v$ -representability question* of TD densities by a construction procedure of the external potential of the alternative reference system [vL99, MUN<sup>+</sup>06]. Moreover, the *initial-state dependence* of the density representation has been discussed in Refs. [MB01] and [MBW02].

To derive a calculation scheme for dynamic properties, Runge and Gross [RG84] suggested a variational principle that rests upon an action functional. However, Refs. [vL98] and [vL01] demonstrate that TDDFT based on the Runge-Gross action leads to contradictions in the symmetry and causality requirements of one of the most important ingredients of TDDFT *linear response theory*, namely the xc kernel

$$f_{\text{xc}}(\mathbf{r}, t; \mathbf{r}', t') = \frac{\delta^2 \mathcal{A}_{\text{xc}}}{\delta n(\mathbf{r}, t) \delta n(\mathbf{r}', t')}, \quad (2.10)$$

where  $\mathcal{A}_{\text{xc}}$  is the xc part of the Runge-Gross action [RG84]. Van Leeuwen [vL98, vL01] solved this problem by introducing a new action functional that is based on the time contour method due to Keldysh (for more details, see Refs. [vL98, vL01, MUN<sup>+</sup>06, Mun07]). The thus obtained variational principle yields a set of *time-dependent Kohn-Sham equations*

$$i \frac{\partial}{\partial t} \varphi_{j\sigma}(\mathbf{r}, t) = h_{\text{KS},\sigma}(\mathbf{r}, t) \varphi_{j\sigma}(\mathbf{r}, t), \quad (2.11)$$

where the TD KS Hamiltonian reads

$$h_{\text{KS},\sigma}(\mathbf{r}, t) = -\frac{\nabla^2}{2} + v_{\text{H}}(\mathbf{r}, t) + v_{\text{xc},\sigma}(\mathbf{r}, t) + v_{\text{ext}}(\mathbf{r}, t). \quad (2.12)$$

The TD xc potential  $v_{\text{xc},\sigma}(\mathbf{r}, t)$  follows from the functional derivative

$$v_{\text{xc},\sigma}(\mathbf{r}, t) = \left. \frac{\delta \mathcal{A}_{\text{xc}}}{\delta n(\mathbf{r}, \tau)} \right|_{n=n_{\sigma}(\mathbf{r}, t)} \quad (2.13)$$

of the xc part of the new action functional with respect to the density  $n(\mathbf{r}, \tau)$  where the time variable  $\tau$  is the Keldysh pseudo time, but the functional derivative is taken at the physical TD density  $n(\mathbf{r}, t)$  [vL98, vL01]. By the basic theorems of TDDFT,  $v_{\text{xc},\sigma}(\mathbf{r}, t)$  is a functional

of the TD density and its entire history, the initial interacting wave function, and the initial state of the KS system. Finally, based on xc approximations, the TD density follows from the  $N_\sigma$  occupied orbitals per spin channel of the TD KS system according to

$$n(\mathbf{r}, t) = \sum_{\sigma=\uparrow, \downarrow} \sum_{j=1}^{N_\sigma} |\varphi_{j\sigma}(\mathbf{r}, t)|^2. \quad (2.14)$$

Practical calculations of TDDFT rely either on the *linear response formalism* or on *real-time propagation* of the KS system. Both approaches are introduced in the following.

### 2.2.2 TDDFT linear response formalism

Today, most TDDFT excitation energy investigations are based on the linear response formalism. The linear response of the GS density to small perturbations  $\delta v_{\text{ext}}(\mathbf{r}', t')$  of the external potential reads

$$\delta n(\mathbf{r}, t) = \int \int \chi[n_{\text{GS}}](\mathbf{r}, \mathbf{r}', t - t') \delta v_{\text{ext}}(\mathbf{r}', t') d^3r' dt', \quad (2.15)$$

where  $\chi[n_{\text{GS}}](\mathbf{r}, \mathbf{r}', t - t')$  is the linear response function of the interacting system. For the sake of clarity, I use a spin-independent notation here and in the next section. Based on the fundamental theorems of TDDFT, the density response may be expressed in terms of the linear response of the KS system due to changes of the KS potential [PGG96]. Hence, a relation between  $\chi[n_{\text{GS}}](\mathbf{r}, \mathbf{r}', t - t')$  and the linear response function of the KS system  $\chi_{\text{KS}}$  exists [PGG96, MUN<sup>+</sup>06]. In frequency space, the interacting linear response function is

$$\begin{aligned} \chi(\mathbf{r}, \mathbf{r}', \omega) &= \chi_{\text{KS}}(\mathbf{r}, \mathbf{r}', \omega) \\ &+ \int \int \chi_{\text{KS}}(\mathbf{r}, \mathbf{r}_1, \omega) \left\{ \frac{1}{|r_1 - r_2|} + f_{\text{xc}}(\mathbf{r}_1, \mathbf{r}_2, \omega) \right\} \chi(\mathbf{r}_2, \mathbf{r}', \omega) d^3r_1 d^3r_2, \end{aligned} \quad (2.16)$$

where  $\chi_{\text{KS}}(\mathbf{r}, \mathbf{r}', \omega)$  is the frequency-dependent linear response of the KS system reading

$$\chi_{\text{KS}}(\mathbf{r}, \mathbf{r}', \omega) = 2 \lim_{\eta \rightarrow 0^+} \sum_{i,a} \left\{ \frac{\xi_{ia}(\mathbf{r}) \xi_{ia}^*(\mathbf{r}')}{\omega - \omega_{ia} + i\eta} - \frac{\xi_{ia}^*(\mathbf{r}) \xi_{ia}(\mathbf{r}')}{\omega + \omega_{ia} + i\eta} \right\}. \quad (2.17)$$

It depends on the eigenvalue differences  $\omega_{ia} = \varepsilon_a - \varepsilon_i$  between all possible combinations of occupied KS orbitals  $i$  and unoccupied KS orbitals  $a$  and on the orbital products  $\xi_{ia}(\mathbf{r}) = \varphi_i^*(\mathbf{r}) \varphi_a(\mathbf{r})$  of the corresponding GS KS orbitals [MUN<sup>+</sup>06]. It has poles at frequencies  $\omega_{ia}$ . The KS response contribution to Eq. (2.16) includes only those effects that are encoded in the single-particle GS KS system, whereas the Hartree-exchange-correlation (Hxc) kernel

$$f_{\text{Hxc}}(\mathbf{r}, \mathbf{r}', \omega) = \frac{1}{|r - r'|} + f_{\text{xc}}(\mathbf{r}, \mathbf{r}', \omega) \quad (2.18)$$

needs to cover all many-particle effects beyond that.

Finding the excitation energies of the interacting systems in linear response amounts to finding the poles of  $\chi(\mathbf{r}, \mathbf{r}', \omega)$ . Casida [Cas95, Cas96] developed a matrix-equation formulation for practical implementations of this strategy. In this approach, solution of the eigenvalue problem [Cas96, MUN<sup>+</sup>06]

$$\sum_{i', a'} R_{ia, i' a'} F_{i' a'} = \Omega^2 F_{ia}, \quad (2.19)$$

where

$$R_{ia,i'a'} = \omega_{ia}^2 \delta_{ii'} \delta_{aa'} + 4\sqrt{\omega_{ia}\omega_{i'a'}} K_{ia,i'a'} \quad (2.20)$$

and

$$K_{ia,i'a'}(\omega) = \int \int \xi_{ia}^*(\mathbf{r}) f_{\text{Hxc}}(\mathbf{r}, \mathbf{r}', \omega) \xi_{i'a'}(\mathbf{r}') d^3r d^3r', \quad (2.21)$$

yields the excitation energies  $\Omega$  of the interacting system. The corresponding oscillator strength is encoded in the eigenvectors [Cas96]. This procedure is well-known as the “*Casida approach*” of linear response TDDFT. It is most frequently used in today’s TDDFT based applications and implemented in most quantum chemistry codes.

An approximate approach to finding  $\Omega$  from TDDFT linear response provides means for more insight into the influence of the individual contributions of Eq. (2.16), i.e., contributions from the GS KS system and Hartree-exchange-correlation effects. It is based on the single-pole approximation [PGG96]: Assuming that the true excitation  $\tilde{\Omega}$  is dominated by one transition from a single occupied orbital  $j$  to a single unoccupied orbital  $b$ , all other contributions to the total response can be neglected. Thus, one obtains [PGG96, AGB03]

$$\tilde{\Omega} \approx \omega_{jb} + 2 \text{Re}\{K_{jb,jb}(\omega_{jb})\}. \quad (2.22)$$

Equation (2.22) is used in Sec. 4.1 to explain the CT problem of TDDFT.

### 2.2.3 Real-time propagation TDDFT

In this thesis, I mainly used the real-time (RT) propagation approach to TDDFT which does not require explicit linear response theory, but is directly based on the TD KS equations of Sec. 2.2.1. The central idea of this method is to compute the time evolution of the density from RT propagation of the TD KS system

$$\varphi_j(\mathbf{r}, t) = U(t, t_0)\varphi_j(\mathbf{r}, t_0) = \mathcal{T} \exp \left[ -i \int_{t_0}^t h_{\text{KS}}(\mathbf{r}, t') dt' \right] \varphi_j(\mathbf{r}, t) \quad (2.23)$$

via application of the propagator  $U(t, t_0)$ . All other observables need to be obtained from  $n(\mathbf{r}, t)$ . This is a crucial point because in some situations it is difficult to extract information that is easily available in the Casida approach from the time evolution of the density, e.g., see Chap. 4. In such cases, new investigation ideas need to be developed as for instance the *transition density analysis tool* of Sec. 2.3. Yet, some important observables are explicit functionals of the density, in particular the TD dipole moment

$$\mathbf{d}(t) = \int \mathbf{r}n(\mathbf{r}, t) d^3r. \quad (2.24)$$

Excitation energies emerge as peaks in the spectrum of the TD density after some initial excitation [ZS80, CRS97]. Most importantly, optical excitations that are sensitive to the dipole moment cause peaks at frequencies  $\omega$  in the Fourier transformation  $\mathbf{d}(\omega)$  of the TD dipole moment that correspond to optical excitation energies. To compute the latter, the system is typically excited by an initial moment boost and the resulting TD dipole moment is used as basic observable [YB96, YB99a, YB99b, MCBR03, CAO<sup>+</sup>06, MK07, Mun07, Mun09]. Here, the boost is applied initially by multiplying  $\exp(i\frac{\mathbf{r}\cdot\mathbf{p}_{\text{boost}}}{\hbar})$  to the GS KS orbitals. This introduces an excitation energy  $E_{\text{excit}}$  via the momentum  $|\mathbf{p}_{\text{boost}}| = \sqrt{2mE_{\text{excit}}/N}$ . The

Fourier transformation of the dipole signal after such a momentum boost can be related to the *dynamical polarizability* and the *dipole strength function* [ZS80, YB96, CRS97, CAO<sup>+</sup>06], where peak positions correspond to excitation energies and peak heights are related to the oscillator strength of the transitions. As long as one is interested only in the position of excitation peaks, the dipole power spectrum [CRS97, Mun07, Mun09]

$$D(\omega) = \sum_{j=1}^3 |d_j(\omega)|^2 \quad (2.25)$$

gives a reliable and relatively clean signal in the frequency domain. Other applications involve excitations via TD external fields, e.g., laser fields. Such external perturbations may be included in terms of explicitly TD external potentials that act during propagation. More insight into external laser fields, possible laser pulse shapes, and applications are given in Refs. [Mun07] and [Mun09].

The RT propagation approach comes along with some advantages in comparison to the explicit linear response formulation. First, the xc kernel does not need to be computed, as RT propagation is based on the potential only. The determination of  $f_{\text{xc}}$  may be complicated, in particular, in case of xc approximations where already the determination of  $v_{\text{xc}}$  is difficult. Second, RT propagation shows a more advantageous scaling [YB99b]. However, for many applications, this scaling argument holds only for really large particle numbers, because multipliers that are modifying the scaling behavior are typically notably larger in case of the RT approach. Third, RT propagation is not limited to the linear response regime. Thus, it can be applied to non-perturbative and non-linear phenomena, as for instance excitation by strong laser fields. Finally, the RT propagation method is applicable to general TD situations and, therefore, illuminates the RT evolution of explicitly TD observables.

## 2.3 The transition density analysis tool

At first glance, RT propagation does not seem to provide more information about the nature of excitations than their energetic position and the corresponding oscillator strength. From this alone, it appears difficult to make clear statements about the performance of different functional approximations by just comparing the computed absorption spectra. For a trustworthy assessment of excitation energy results, it is important to know the nature of the excitation peaks, i.e., to understand the character of the underlying transitions. The Casida approach [Cas95, Cas96] allows this in a natural way as it decomposes excitations into transitions from occupied to unoccupied orbitals with a certain weighting factor. In this way, one can, e.g., distinguish between local and CT excitations. In principle this information is also available from RT propagation, but extracting the information from the TD orbitals is tedious. Therefore, I suggested an analysis tool for the RT signal that is based on the *transition density* and allows to explore the nature of excitations. The transition density is directly related to the TD density, thus well defined in the framework of TDDFT [KAR01, BCOR04, TK09].

The transition density  $\rho_\omega(\mathbf{r})$  corresponding to an excitation at frequency  $\omega$  is proportional to the negative of the imaginary part of the Fourier transformation  $\delta n(\mathbf{r}, \omega)$  of the TD density fluctuations  $\delta n(\mathbf{r}, t) = n(\mathbf{r}, t) - n(\mathbf{r}, 0)$  according to [BCOR04, TK09]

$$\rho_\omega(\mathbf{r}) \propto -\text{Im}\{\delta n(\mathbf{r}, \omega)\}. \quad (2.26)$$

In PARSEC, I implemented a step by step Fourier transformation during time propagation to calculate  $\rho_\omega(\mathbf{r})$  for preset frequencies (see Appendix E.3 for details). The obtained transition densities are a unique fingerprint of the excitation and can be used to distinguish between excitations of different character. “Visual inspection” of transition densities helps to assign excitations peaks of spectra computed by different methods or functional approximations. Examples of how transition density fingerprints are used to identify transitions of known character in spectra from different functionals are given in Pub2 and Pub4.

More insight into the nature of transitions is available if the contributions of occupied to unoccupied orbital transitions are known. In this case, the transition density can be written as a weighted sum of occupied and unoccupied orbital products [BCOR04]

$$\rho_\omega(\mathbf{r}) \propto \sum_i^{\text{occup.}} \sum_j^{\text{unoccup.}} a_{ij}^\omega \varphi_i(\mathbf{r}) \varphi_j^*(\mathbf{r}) \quad (2.27)$$

with weighting factors  $a_{ij}^\omega$ . Transition densities from RT propagation are compared to transition densities from GS orbital products in Pub2 and Pub4 to identify CT transitions and the corresponding excitation energies in two important model systems that exhibit different CT character. Moreover, in an attempt to set the “visual inspection” idea on a more objective footing, I suggested two quantitative comparison criteria that are explained in Pub4.

## 2.4 Exact properties and features of the exchange-correlation potential

The work presented in this thesis is deeply rooted in the KS framework of DFT. The KS scheme provides some theoretical and technical advantages: it fulfills exact conditions as, e.g., Janak’s ionization-potential theorem [Jan78], exact KS eigenvalues are good approximations to relaxed vertical ionization potentials [CGB02, Kör09], using local potentials has numerical advantages, and the local multiplicative potential allows for a transparent analysis of the response behavior and interpretability of orbitals and eigenvalues [DKK<sup>+</sup>11]. Taking exact properties of the KS system and its xc contribution into account, is an established route for improving xc functional approximations. Therefore, concluding the overview of DFT and TDDFT basics, I comment on the *derivative discontinuity* and its manifestation in the xc potential and name some other important features and exact properties of the KS approach.

One property of the DFT description of xc effects that is important for this work is related to the behavior of the total energy of a quantum system when its total electron number passes integer values. This situation was studied by Perdew *et al.* [PPLB82] based on a statistical mixture of  $N$ - and  $(N+1)$ - electron systems to realized fractionally occupied systems with total electron number  $N + \omega$ , where  $0 \leq \omega \leq 1$ . The important finding of Ref. [PPLB82] is that the GS energy  $E_{N+\omega}$  of fractionally occupied systems varies linearly with the fractional occupation  $\omega$  between the energies of the  $N$ - and  $(N+1)$ - electron system as

$$E_{N+\omega} = (1 - \omega)E_N + \omega E_{N+1}. \quad (2.28)$$

This straight-line behavior of the total energy between integer electron numbers implies discontinuous changes of its slope with respect to the fractional particle number  $Z$  when it

passes integers  $N$ . Thus, also the *chemical potential*  $\mu(Z) = \partial E_Z / \partial Z$  jumps discontinuously

$$\mu(Z) = \begin{cases} -IP(N) = E_N - E_{N-1}, & N-1 < Z < N \\ -EA(N) = E_{N+1} - E_N, & N < Z < N+1 \end{cases} \quad (2.29)$$

when  $Z$  passes integer occupations  $N$  [PPLB82].  $IP$  and  $EA$  are the ionization potential and the electron affinity of the  $N$ -electron system. The discontinuity at the integer electron number  $N$  is given by  $\Delta = IP(N) - EA(N)$ . This difference is called the *fundamental gap*. In KS DFT,  $\Delta$  may be separated into two contributions

$$\Delta = \Delta_{\text{KS}} + \Delta_{\text{xc}}, \quad (2.30)$$

the *KS gap*  $\Delta_{\text{KS}}$  and the *derivative discontinuity* of the xc potential  $\Delta_{\text{xc}}$  [PL83]. The KS gap is the difference  $\varepsilon_{\text{LUMO}}^{\text{exact KS}} - \varepsilon_{\text{HOMO}}^{\text{exact KS}}$  of the HOMO (highest occupied molecular orbital) and the LUMO (lowest unoccupied molecular orbital) eigenvalue of the yet unknown exact  $N$ -electron KS system.  $\Delta_{\text{xc}}$  quantifies the integer jump of the xc potential when in an open system framework with non-integer particle numbers the electron number passes integer values [PPLB82, PL83, SS83, Per90, DG90]. Hence, it is defined as

$$\Delta_{\text{xc}} = v_{\text{xc}}^+(\mathbf{r}) - v_{\text{xc}}^-(\mathbf{r}) = (IP(N) - EA(N)) - (\varepsilon_{\text{HOMO}}^{\text{exact KS}} - \varepsilon_{\text{LUMO}}^{\text{exact KS}}), \quad (2.31)$$

where the potentials  $v_{\text{xc}}^+(\mathbf{r})$  and  $v_{\text{xc}}^-(\mathbf{r})$  correspond to the limiting cases when the fractional electron occupation approaches  $N$  from above or from below according to

$$v_{\text{xc}}^+(\mathbf{r}) = \lim_{\omega \rightarrow 0} \left. \frac{\delta E_{\text{xc}}}{\delta n(\mathbf{r})} \right|_{N+\omega}, \quad (2.32)$$

$$v_{\text{xc}}^-(\mathbf{r}) = \lim_{\omega \rightarrow 0} \left. \frac{\delta E_{\text{xc}}}{\delta n(\mathbf{r})} \right|_{N-\omega}. \quad (2.33)$$

The discontinuous behavior of the GS energy reflects the strong tendency of true electronic systems to reject fractional occupation [Per90]. Perdew [Per90] related the derivative discontinuity to the *principle of integer preference*: In a system composed of separate subsystems, nature always prefers to locate integer charges on each object. Although this concept was introduced in an ensemble formulation of quantum systems with fractional occupations, it also manifests in the xc potential of systems with integer electron numbers in terms of *step-like structures* [SP08, GGS09].

The dissociation process of diatomic molecules is one such situation where step-like structures are important to support integer number of electrons on fragments of the system [PPLB82, Per90, RPC<sup>+</sup>06, KAK09, TMM09, Kör09, MKK11]: When two different atoms A and B with different electronegativity dissociate, a step emerges in the exact xc potential in between the two atoms as they move apart. It is needed to align the eigenvalues corresponding to the HOMO of A and B in the infinitely separated case via relative shifts of the A and B potential wells in order to avoid fractional charge transfer during the dissociation process [KAK09]. A second kind of step-like structure was observed in  $v_{\text{xc}}$  at the boundaries of the shells of the atomic shell structure [KLI92, GvLB94, vLGB95]. Step structures appear also during TD processes [LK05, MK05], as for instance at the boundary of an emerging potential plateau during ionization due to strong external fields [LK05].

A different manifestation of step-like structures and the derivative discontinuity is the *field-counteracting behavior* of  $v_{xc}$  when external fields are applied. A field-counteracting trend of the xc potential has been identified to be decisive for the description of static response properties such as polarizabilities [vGSG<sup>+</sup>99, GvGSB00, KKP04, KMK08, KAK09]. More insight into the static field-counteracting behavior is given in Appendix A.1.

The derivative discontinuity, step-like structures, and field-counteracting behavior are particularly important also for Coulomb blockade effects [CBKR07, KSK<sup>+</sup>10] and charge-transfer investigations [TFSB05, Mai05, HG12]. In Chap. 4, the latter topic is discussed in greater detail in static and dynamic situations.

Exact properties of the GS functional [MMN<sup>+</sup>12] beside the derivative discontinuity include scaling relations and signs of the energy contributions, the xc virial theorem, freedom from self-interaction in one-electron systems [PZ81] (see Chap. 3 for more details), properties of the xc hole, zero-force and torque theorem of the xc potential, and the asymptotic behavior of the potential. In TDDFT, during time propagation fundamental conservation laws should be respected. In particular, the total energy should remain constant when no external perturbation acts. The torque and zero-force theorems [Vig95, GDP96] also apply in TDDFT. The latter states that the xc potential cannot exert a net force on the system as

$$\int n(\mathbf{r}, t) \nabla v_{xc}(\mathbf{r}, t) d^3r = 0. \quad (2.34)$$

More exact constraints on density functionals and their relevance in TDDFT are discussed in Refs. [HPB99, MUN<sup>+</sup>06, MMN<sup>+</sup>12].

## 2.5 Exchange-correlation functionals

### 2.5.1 Approximations for the exchange-correlation energy functional

The practical usability and reliability of DFT and TDDFT strongly depends on the quality of the used xc density functionals. This aspect has not been settled so far. I give an introduction into the most important and for this thesis most relevant approximations to  $E_{xc}$  in the following.

**Local and semilocal functionals:** The earliest and still one of the most wide-spread approximations is the *local density approximation* (LDA) [HK64] and its extension to spin-dependent cases, the *local spin-density approximation* (LSDA) [vBH72]. The rationale behind LDA is to use the functionals of the exchange and correlation energies ( $\epsilon_x^{\text{hom}}(n^{\text{hom}})$  and  $\epsilon_c^{\text{hom}}(n^{\text{hom}})$ ) of the homogeneous electron gas and replace the homogeneous electron density  $n^{\text{hom}}$  by the local density  $n(\mathbf{r})$  according to

$$\epsilon_{xc}^{\text{hom}}[n(\mathbf{r})] = \left[ \epsilon_x^{\text{hom}}(n_0) + \epsilon_c^{\text{hom}}(n_0) \right]_{n_0=n(\mathbf{r})}. \quad (2.35)$$

The exchange part of the homogeneous electron gas xc energy has an analytical expression. The correlation contribution is only known from highly accurate quantum Monte-Carlo simulations [CA80] and needs to be parametrized for application in DFT, e.g., the parametrization of Perdew and Wang [PW92]. The LDA xc energy reads

$$E_{xc}^{\text{LDA}}[n] = \int \epsilon_{xc}^{\text{hom}}(n(\mathbf{r})) n(\mathbf{r}) d^3r. \quad (2.36)$$

*Semilocal functionals* are the first class of beyond-LDA functionals. Historically, the first step beyond purely local functionals was to include also gradients of the density into the xc functional. However, consistent improvements were obtained only when the so-called *generalized gradient approximations* (GGAs) [LM83, PY86, Per86] were introduced. One of the most popular GGAs, the non-empirical GGA of Perdew, Burke, and Ernzerhof (PBE) [PBE96], is based on exact constraints, e.g., to the xc hole. Other functionals use free parameters and fit those to data sets from reference calculations or experimental findings. For instance, the semiempirical BLYP functional combines Becke88 exchange [Bec88] with the correlation functional of Lee, Yang, and Parr (LYP) [LYP88]. A second class of semilocal functionals are the so-called *meta-GGAs* that may include also higher-order derivatives of the density, the kinetic energy density, and gradients of the latter. Note that meta-GGAs may already fall into the next class of functionals, the so-called *orbital functionals*, because they may include explicit orbital dependence although they are semilocal in nature.

**Orbital functionals:** *Orbital-dependent functionals* comprise explicit dependence of the orbitals of the KS system beyond semilocal contributions [KK08]. They are still implicit density functionals because the orbitals themselves are implicit functionals of the density. Prominent representatives of this class of functionals are the self-interaction correction (SIC) of Perdew and Zunger [PZ81] and the exact exchange (EXX) functional

$$E_x[\{\varphi_{j\tau}\}] = -\frac{1}{2} \sum_{\sigma=\uparrow,\downarrow} \sum_{i,j=1}^{N_\sigma} \int \int \frac{\varphi_{i\sigma}^*(\mathbf{r})\varphi_{j\sigma}^*(\mathbf{r}')\varphi_{j\sigma}(\mathbf{r})\varphi_{i\sigma}(\mathbf{r}')}{|\mathbf{r}-\mathbf{r}'|} d^3r d^3r', \quad (2.37)$$

the Fock exchange integral known from Hartree-Fock (HF) theory computed with KS orbitals. The latter includes exact exchange only and finding a compatible correlation functional is known to be difficult. In the SIC approach, exchange and correlation are based on the underlying xc functional approximation on top of which the self-interaction correction is performed (see Pub3 and Chap. 3 for a discussion and more details).

The price one has to pay when using orbital functionals are difficulties when computing the xc potential via the functional derivative of  $E_{xc}$  with respect to the density, because one does not know the explicit density dependence of the orbitals. A solution to this problem, the optimized effective potential (OEP) method [SH53, TS76, GKG97, KK08], yields a multiplicative xc potential in the KS sense. This method is introduced in the context of SIC in Chap. 3. As an alternative to the OEP, one may leave the grounds of KS theory and rely on the generalized KS (GKS) approach [SGV<sup>+</sup>96]. In the GKS scheme, the constraint of strictly non-interacting reference systems is relaxed and interacting reference systems that use a single Slater determinant are allowed. The potential in the GKS approach is no longer a local but an orbital-specific one. Typically, functionals implemented via the GKS method involve at least a fraction of EXX, thus most GKS potentials include a fraction of the nonlocal Fock potential [KK10]. Details about the GKS approach and differences to the theoretical framework of the KS scheme are discussed in Refs. [SGV<sup>+</sup>96, KK10, BLS10].

**Hybrid functionals:** In the *hybrid functional* idea, basically a fraction of the EXX functional is mixed with some semilocal (sl) density functional. For instance, a one-parameter hybrid can be written as

$$E_{xc}^{\text{hyb}} = aE_x + (1-a)E_x^{\text{sl}} + E_c^{\text{sl}} \quad (2.38)$$

with the mixing parameter  $a$ . In this case, one mixes the semilocal exchange  $E_x^{\text{sl}}$  with exact exchange and takes the full correlation  $E_c^{\text{sl}}$  of the semilocal functional. Typically, the

mixing parameter of such hybrid functionals is chosen empirically, for instance by fitting the functional to a test set of atomic and molecular properties. Probably the most prominent hybrid functional is B3LYP [Bec93, SDCF94], a three-parameter hybrid functional based on a weighted mixture of LDA exchange and correlation, LYP correlation, Becke88 exchange, and EXX. The three parameters are obtained empirically from fitting to a set of atomic properties. Other approaches emphasize the density dependence of such mixing parameters and suggest approaches to compute mixing parameters from the density alone [MVO<sup>+</sup>11].

Recently, the *range-separated hybrid functional* idea became increasingly popular. It rests upon a range-separation scheme [Sav95] of the electron-electron interaction into a short-range and a long-range part. In those two parts, the electron-electron interaction is treated with different functional approximations. Each of those approximations is supposed to play a specific role: Typically semilocal functionals are used in the short-range part, whereas EXX is supposed to dominate the long-range contribution. The transition between short and long range is determined by a partitioning scheme and a range-separation parameter  $\gamma$  [Sav95, VS06, LB07, BLS10, KSSB11]. The inverse of this parameter  $1/\gamma$  can be interpreted to be a characteristic length scale that distinguishes between short and long range. The choice of  $\gamma$  is the key element of the performance of such range-separation ideas. First approaches of this kind were based on empirical range-separation parameters [YTH04, VS06, LB07, CHG07], but only recently parameter tuning to some additional theoretical constraints [SKB09a, SKB09b, BLS10, KSSB11] has been employed. *Tuned range-separated hybrid functionals*, as long as the underlying xc functionals are non-empirical, do not rely on empirical input data.

Hybrid functionals involve an explicit dependence on the orbitals. Thus, the difficulties with orbital functionals already discussed in the previous section apply again. Usually, hybrid functionals are implemented via the GKS scheme [SGV<sup>+</sup>96, KSSB11]. An implementation within the KS framework of DFT can be performed based on the OEP method.

### 2.5.2 Exchange-correlation functionals in TDDFT

The xc action functional and the corresponding TD xc potential in TDDFT are very complex quantities, presumably even more complex than their static counterparts. Yet, the validity of results from TDDFT calculations strongly depends on the quality of the description of xc effects. Therefore, although the action functional formalism provides a solid starting point for developing functional approximations, finding reliable TD xc potentials for practical calculations can be tedious, in particular, for difficult applications like charge transfer.

Today, most applications of TDDFT rely on the so-called *adiabatic approximation* [GDP96, EBF07]. The rationale behind this approach is that in cases where the external potential varies slowly enough in time, the time evolution of the system loses its dependence on the past, and can be well described by the instantaneous density. Thus, the adiabatic approximation amounts to using well-known functionals and the corresponding potentials from GS DFT as TD xc potentials according to

$$v_{\text{xc},\sigma}^{\text{adia}}[n](\mathbf{r}, t) = v_{\text{xc},\sigma}[n_t](\mathbf{r}) = \frac{\delta E_{\text{xc}}[n_t]}{\delta n_{t,\sigma}(\mathbf{r})}, \quad (2.39)$$

where the time variable  $t$  is considered as a parameter of the density  $n_t$ . For linear response calculations the adiabatic approximations may also be applied to the xc kernel. The adiabatic xc kernel is completely local in time, thus transforming it into Fourier space yields a frequency-independent xc kernel [MUN<sup>+</sup>06].

In principle, the adiabatic approximation introduced so far may be applied to every GS xc approximation. Many applications of TDDFT rely on the adiabatic local density approximation (ALDA, TDLDA), which is the simplest extension of GS DFT to the TD case. Surprisingly, ALDA works quite well far beyond its obvious range of validity, namely slowly varying densities both in space and in time [MUN<sup>+</sup>06]. Other applications use GGAs, hybrid functionals, or orbital functionals as introduced in Sec. 2.5.1. In any case, one should be careful in choosing the right functional for each application depending on the system and observable one is interested in.

Care should be taken when using the term “adiabatic” and considering its implications on the history dependence of such approaches. Explicit density functionals implemented via Eq. (2.39) neglect all memory dependence of the system evolution of times  $t' \leq t$ . When it comes to explicitly orbital-dependent functionals, however, the TD KS orbitals in general depend on the entire history of the density  $n(\mathbf{r}, t')$  for  $t' \leq t$ , thus recover in a natural way part of the memory dependence that is not in the TD density [GDP96, MBW02, MMN<sup>+</sup>12]. In this case, the “adiabatic approximation” should better be termed *orbital-adiabatic approximation* in contrast to *density-adiabatic approximation*.

## 2.6 Numerical realization

Most DFT and RT TDDFT investigations presented throughout this thesis are based on the Bayreuth version [MK07, Mun07, Mun09] of the PARSEC program package [KMT<sup>+</sup>06]. PARSEC is a real-space electronic-structure code that uses norm-conserving pseudopotentials of Troullier-Martins [TM91] type and a high-order finite difference schemes for numerically representing the Laplacian operator [CTS94, KMT<sup>+</sup>06]. The GS version is designed for solving the KS equations by numerical diagonalization of the KS Hamiltonian. The Bayreuth version includes solution of the OEP equation [KK08, Kör09] via the construction scheme of Refs. [KP03a, KP03b] and approximations to the OEP, as for instance the Krieger-Li-Iafrate (KLI) approximation [KLI92] and the Slater approximation [Sla51].

The practical realization of the RT propagation idea is based on stepwise numerical propagation with time steps  $\Delta t$  using the propagator  $U(t + \Delta t, t)$  [CAO<sup>+</sup>06, Mun07, Mun09]. The PARSEC real-time TDDFT implementation uses a Taylor series up to fourth order to numerically expand  $U(t + \Delta t, t)$  combined with the exponential midpoint rule [MK07, Mun07, Mun09]. In this scheme, the potential needs to be determined twice per time step. Other propagation techniques are explained in Ref. [CMR04]. To avoid spurious reflection of density that moves to the boundary of the numerical grid, RT PARSEC offers absorbing boundaries [RSA<sup>+</sup>06, Mun07, Mun09]. Last but not least, the Bayreuth version of TD PARSEC [MK07, Mun07] includes RT propagation of orbital functionals implemented via the time-dependent KLI approximation.

For the feasibility of most RT calculations presented in this thesis, numerical optimization of the original PARSEC version and the implementation of new algorithms were needed to reach acceptable computation times. One of the most time-consuming steps during time propagation is the evaluation of the Hartree potential via solution of Poisson’s equation. Numerical efficiency of the Poisson solver is especially important when orbital functionals as, e.g., the EXX or the SIC are used. Therefore, I implemented a multigrid solver as an alternative to the existing conjugate gradient solver. Details about the numerical realiza-

tion are described in Appendix B. Further code optimizations are compiled in Appendix E. It includes an extrapolation scheme to avoid explicit determination of the potential for the midpoint Hamiltonian, some evaluation tools and extra features for the propagation, an adaptation scheme of the diagonalization accuracy to reduce diagonalization times during the GS self-consistency iterations, and some additional features for GS PARSEC. All implementations that are directly related to the PARSEC functionalities used in this thesis are described in the following chapters and the related appendices.

## Chapter 3

# Self-interaction correction

*Another feature which at least induced a semblance of popularity was the lecturer's intention to make clear the fundamental idea, ...*

Erwin Schrödinger  
What is life? (1944)

Density functional theory and time-dependent density functional theory have gained popularity because of their success in predicting and explaining properties of many different kinds of systems and their applicability to sizable systems at bearable computational cost. However, standard density functionals may suffer from well-known deficiencies: incorrect dissociation limits [ZY98], wrong asymptotic behavior of the potential [PZ81], overestimation of electrical response properties [vGSG<sup>+</sup>99] and transport characteristics [TFB05], incorrect representation of charge-transfer (CT) states [DWHG03, Toz03], and problems with excitonic effects in confined systems [RL98, MCR01, ORR02, VOC06]. Deficiencies of this kind have been attributed to the *self-interaction error* (SIE) of standard, explicitly density dependent functionals. The *self-interaction correction* (SIC) is a promising approach for curing these deficiencies of DFT and TDDFT.

I provide insight into the *self-interaction problem* of DFT and correction ideas in Secs. 3.1 and 3.2. The SIC of Perdew and Zunger (PZ) is an explicitly orbital-dependent density functional. In KS DFT, it requires implementation via the *optimized effective potential* (OEP) or *generalized OEP* (GOEP) method introduced in Sec. 3.3. The unitary variance of PZ SIC is taken into account in the GOEP by additional unitary transformations (see Sec. 3.4). The impact of these transformations on the performance of SIC is discussed in Sec. 3.5. Finally, I present in Sec. 3.6 one of the main results of this thesis: the *TDDFT extension of GOEP SIC*. An overview of the performance of this method on a wide range of test systems is given in Sec. 3.7 and Chap. 4.

### 3.1 The self-interaction problem

The self-interaction problem of DFT lies at the heart of the energy partitioning of KS theory. In the KS scheme, the Hartree energy represents the classical part of the Coulomb interaction, thus the xc energy needs to cover everything beyond the Hartree contribution. The self-interaction problem of this energy partitioning manifests most clearly in a single-electron (se) system, where the electron is described by the single-particle wave function

$\varphi^{\text{se}}(\mathbf{r})$  with density  $n^{\text{se}}(\mathbf{r}) = |\varphi^{\text{se}}(\mathbf{r})|^2$ . In this case, the Hartree energy does not vanish, but includes the Coulomb interaction of the single electron with itself. In the exact KS approach, this spurious self-interaction needs to be covered by the xc energy [PZ81], thus the sum of Hartree and xc energy contributions should vanish according to

$$E_{\text{H}}[n^{\text{se}}] + E_{\text{xc}}[n^{\text{se}}, 0] = 0. \quad (3.1)$$

As a matter of fact, however, most xc density functional approximations  $E_{\text{xc}}^{\text{app}}$  do not cover this single-electron SIE, i.e., typically  $E_{\text{H}}[n^{\text{se}}] + E_{\text{xc}}^{\text{app}}[n^{\text{se}}, 0] \neq 0$ .

The self-interaction error is well defined in the single-electron case, yet more difficult in a many-particle context. The PZ attempt towards defining *many-electron self-interaction* is based on an extension of the single-electron criterion of Eq. (3.1) [PZ81]. In this approach, the occupied orbitals from a DFT single particle approach are interpreted to represent the  $N_{\sigma}$  electrons of the system. Then, a functional is declared to be self-interaction free, when

$$\sum_{\sigma=\uparrow,\downarrow} \sum_{j=1}^{N_{\sigma}} [E_{\text{H}}[n_{j\sigma}] + E_{\text{xc}}^{\text{app}}[n_{j\sigma}, 0]] = 0, \quad (3.2)$$

where the orbital densities  $n_{j\sigma}(\mathbf{r}) = |\varphi_{j\sigma}(\mathbf{r})|^2$ . The ambiguity of this definition has led to alternative definitions of self-interaction in many-electron systems [RPC<sup>+</sup>06, MSCY06, KKM08]. One prominent criterion for the freedom of many-electron self-interaction is the straight line behavior of the total energy with respect to non-integer particle numbers [RPC<sup>+</sup>06, MSCY06, KKM08] that is introduced in Sec. 2.4. Perdew [Per90] related the SIE to the derivative discontinuity concept. The dependence of the total energy from standard density functionals on fractional electron numbers was investigated by Refs. [MSCY06, VSP07] with the conclusion: None of the investigated standard xc density functionals strictly fulfills the straight-line criterion.

## 3.2 Self-interaction correction

The PZ definition of a functional's freeness from self-interaction leads to the PZ self-interaction correction scheme. The idea of the correction is to identify the energy related to the interaction of every KS particle with itself and subtract this spurious energy contribution from the xc energy of some xc approximation  $E_{\text{xc}}^{\text{app}}[n_{\uparrow}, n_{\downarrow}]$  according to

$$E_{\text{xc}}^{\text{SIC}}[n_{\uparrow}, n_{\downarrow}] = E_{\text{xc}}^{\text{app}}[n_{\uparrow}, n_{\downarrow}] - \sum_{\sigma=\uparrow,\downarrow} \sum_{j=1}^{N_{\sigma}} [E_{\text{H}}[n_{j\sigma}] + E_{\text{xc}}^{\text{app}}[n_{j\sigma}, 0]]. \quad (3.3)$$

However, the SIC idea of Eq. (3.3) raises some questions. First, the SIC approach is applicable to in principle all available xc functional approximations. Some of them have been advocated [PZ81] and some of them have been reported to be doubtful [VSP<sup>+</sup>06]. On top of which approximate  $E_{\text{xc}}^{\text{app}}[n_{\uparrow}, n_{\downarrow}]$  should SIC be performed then? Second, in Eq. (3.3), orbital densities are inserted into GS xc functionals that are designed for GS densities. Is it justified to insert orbital densities into GS functionals? Third, related to the last question one might ask: Is the choice of orbital densities a unique one? And if the answer is no, do different choices of the orbital densities influence the performance of SIC?

These questions are addressed in Pub3 and Pub4, and the obtained insight is summarized throughout this chapter. For the following discussions it is important to state that the PZ SIC energy is not invariant under unitary transformations among the occupied orbitals: As long as the density remains the same, constructing different orbital sets via unitary transformation  $U_{ij}^\sigma$  of the occupied orbitals is allowed. Thus, one may obtain new orbital densities that yield different SICs. Suggestions to solve this “unitary variance problem” are based on two orbital sets [PHL84, PHL85, PL88, GND00, PAZ01, KKM08, MDRS08, MDRS09a] that take different roles [KP03c]: The canonical orbital set  $\{\varphi_{j\sigma}(\mathbf{r})\}$  of  $N_\sigma$  occupied orbitals solves the single particle equations and a second orbital set  $\{\tilde{\varphi}_{j\sigma}(\mathbf{r})\}$  is used to set up the SIC xc energy (3.3) uniquely. The orbital sets are connected by  $U_{ij}^\sigma$  according to

$$\tilde{\varphi}_{i\sigma}(\mathbf{r}) = \sum_{j=1}^{N_\sigma} U_{ij}^\sigma \varphi_{j\sigma}(\mathbf{r}). \quad (3.4)$$

I use the term generalized SIC (GSIC) to refer to such approaches.

Finally, the SIC energy functional directly depends on the orbitals and, therefore, is only an implicit functional of the density. The OEP method provides means for handling such explicit, orbital-dependent functionals in the KS framework. To deal with the unitary variance of SIC, one needs to use the GOEP formalism [KKM08], where the freedom of unitary transformations in the space of occupied orbitals is taken into account in the derivation of the OEP equation. This is what I introduce in the next section.

### 3.3 The optimized effective potential and its generalization

#### 3.3.1 The optimized effective potential method

The OEP scheme is a method to compute the local, multiplicative xc potential from explicitly orbital-dependent functionals. Using the chain rule when computing the potential  $v_{\text{xc},\sigma}(\mathbf{r}) = \frac{\delta E_{\text{xc}}[\{\varphi_{j\tau}\}]}{\delta n_\sigma(\mathbf{r})}$  via the functional derivative of the xc energy with respect to the density, one obtains the *optimized effective potential integral equation* [KK08, Kör09] for  $v_{\text{xc},\sigma}^{\text{OEP}}$ . A solution scheme to the OEP equation in real space based on the so-called orbital shifts was introduced in Refs. [KP03a, KP03b] and its implementation to the PARSEC program package is described in Ref. [Kör09]. Solving the OEP equation is feasible, but can be a tedious task. Therefore, most practical applications rely on approximations to the OEP.

The most widely used approximation to the OEP is the *Krieger-Li-Iafrate* (KLI) approximation [KLI92]. Originally, it was derived from an approximation to the denominator of the Greens function of the KS system, one of the ingredients of the OEP integral equation. Later investigations of this approximation clarified that it can be interpreted as a mean-field approximation to the OEP equation [GKKG00, KK08]. The KLI potential equation

$$v_{\text{xc},\sigma}^{\text{KLI}}(\mathbf{r}) = v_{\text{xc},\sigma}^{\text{SLA}}(\mathbf{r}) + \frac{1}{2n_\sigma(\mathbf{r})} \sum_{j=1}^{N_\sigma} n_{j\sigma}(\mathbf{r}) [(\bar{v}_{\text{xc},j\sigma}^{\text{KLI}} - \bar{u}_{\text{xc},j\sigma}) + \text{c.c.}] \quad (3.5)$$

has an analytic solution [KK08]. Here, the orbital-specific potentials  $u_{\text{xc},j\sigma}(\mathbf{r})$  are

$$u_{\text{xc},j\sigma}(\mathbf{r}) = \frac{1}{\varphi_{j\sigma}^*(\mathbf{r})} \frac{\delta E_{\text{xc}}[\{\varphi_{k\tau}\}]}{\delta \varphi_{j\sigma}(\mathbf{r})} \quad (3.6)$$

and the orbital-density averaged potentials are given by

$$\bar{v}_{xc,j\sigma}^{\text{KLI}} = \int \varphi_{j\sigma}^*(\mathbf{r}) v_{xc,\sigma}^{\text{KLI}}(\mathbf{r}) \varphi_{j\sigma}(\mathbf{r}) d^3r \quad (3.7)$$

and

$$\bar{u}_{xc,j\sigma} = \int \varphi_{j\sigma}^*(\mathbf{r}) u_{xc,j\sigma}(\mathbf{r}) \varphi_{j\sigma}(\mathbf{r}) d^3r. \quad (3.8)$$

The first term of Eq. (3.5) is the so-called Slater (SLA) [Sla51] contribution

$$v_{xc,\sigma}^{\text{SLA}}(\mathbf{r}) = \frac{1}{2n_\sigma(\mathbf{r})} \sum_{j=1}^{N_\sigma} n_{j\sigma}(\mathbf{r}) [u_{xc,j\sigma}(\mathbf{r}) + u_{xc,j\sigma}^*(\mathbf{r})], \quad (3.9)$$

whereas the second term is the response potential with the characteristic  $(\bar{v}_{xc,j\sigma}^{\text{KLI}} - \bar{u}_{xc,j\sigma})$  contribution. For a unique designation of implementation methods in combination with functionals, I use the notation “method-functional”, e.g., KLI-SIC denotes SIC implemented via the KLI approximation.

The KLI approximation to the full OEP equation is realized on the level of the OEP potential and not directly on the level of xc energy expressions. An energy functional corresponding to the KLI potential does not exist. Moreover, the KLI expression itself is not invariant with respect to unitary transformations of the canonical KS orbitals [SG01]: In case of the EXX functional, the Slater contribution is invariant, but the KLI response potential may change due to unitary transformations of the occupied orbitals that are relevant in subspaces of degenerate orbitals when degeneracies occur. A solution to the unitary variance of the KLI-EXX potential is available via a modification of the KLI approximation [SG01, GB01, GGB02, Jou07, KK08]. The new potential approximation is known as the *localized Hartree-Fock* [SG01] or *common energy denominator approximation* [GB01] (LHF-CEDA). It includes also non-diagonal contributions in terms of occupied orbital products  $\varphi_{i\sigma} \varphi_{j\sigma}^*$  and their complex conjugate to the response part of Eq. (3.5). However, in case of the SIC functional the unitary variance problem of the KLI potential is even more involved than in KLI-EXX as it appears already on the level of the Slater potential. Moreover, as the LHF-CEDA approximation is tailored to the EXX functional, it is not clear from the start that it can readily be applied to other orbital-functional approximations. In particular application to the SIC appears difficult as the SIC functional involves orbital combinations that are very different to the EXX orbital structure, e.g., the EXX functional is unitarily invariant whereas the SIC functional is not.

### 3.3.2 Generalization of the OEP to unitarily variant functionals

To take the freedom of unitary transformations of unitarily variant orbital functionals into account in the OEP method one has to add an additional step in the derivation of the OEP potential when executing the functional chain rule. This leads to the *GOEP integral equation* (for details, see Refs. [KKM08, Kör09]). For the sake of clarity, I focus only on the case of the PZ SIC energy functional from now on. If not stated explicitly, SIC of the L(S)DA functional is performed throughout. In the GOEP integral equation, the potentials  $u_{xc,j\sigma}(\mathbf{r})$  of the standard OEP equation are replaced by the *generalized orbital-specific potentials*

$$u_{xc,j\sigma}^{\text{G}}(\mathbf{r}) = \frac{1}{\varphi_{j\sigma}^*(\mathbf{r})} \sum_{i=1}^{N_\sigma} U_{ij\sigma} \tilde{\varphi}_{i\sigma}^*(\mathbf{r}) \tilde{v}_{i\sigma}^{\text{SIC}}(\mathbf{r}), \quad (3.10)$$

where

$$\tilde{v}_{i\sigma}^{\text{SIC}}(\mathbf{r}) = \frac{\delta E_{\text{xc}}^{\text{SIC}}[\{\tilde{n}_{k\tau}\}]}{\delta \tilde{n}_{i\sigma}(\mathbf{r})}. \quad (3.11)$$

Ref. [KKM08] shows that solutions of the GOEP equation can be obtained with well-known methods invented for the standard OEP case. Yet, for numerical reasons often the *generalized KLI* (GKLI) approximation is used [KKM08]. For converting the standard KLI to the GKLI potential,  $u_{\text{xc},j\sigma}(\mathbf{r})$  in Eqs. (3.5) to (3.9) needs to be replaced by the generalized  $u_{\text{xc},j\sigma}^{\text{G}}(\mathbf{r})$  [KKM08, Kör09]. The formal separation of the KLI potential into Slater and response part applies also in the GKLI case. Thus, the *generalized Slater* (GSLA) corresponds to Eq. (3.9), where  $u_{\text{xc},j\sigma}(\mathbf{r})$  is replaced by  $u_{\text{xc},j\sigma}^{\text{G}}(\mathbf{r})$ .

With the GKLI approximation at hand, I investigated its behavior when the KS orbitals change unitarily as already discussed in the context of KLI in Sec. 3.3.1. The GKLI approach heals part of the KLI problem:  $v_{\text{xc},\sigma}^{\text{GSLA}}(\mathbf{r})$  is invariant under unitary transformations among occupied KS orbitals as long as the optimized orbitals  $\{\tilde{\varphi}_{i\sigma}(\mathbf{r})\}$  that are inserted into Eqs. (3.10) and (3.11) are the same. However, the response contribution remains variant also in the GKLI case. This finding explains part of the convergence problem of O<sub>2</sub> in Pub3. Moreover, close examination of the splitting into Slater and response contributions reveals differences between these two contributions in the KLI and in the GKLI approximation in terms of their response behavior to external electric fields. It appears that GSLA covers part of the response that is not covered by the standard SLA approximation. More details about this observation are discussed in Appendix A.1.

### 3.4 Unitary optimization with different types of orbitals

The unitary variance of the SIC energy functional appears to be a weakness of the SIC approach, but can be turned into a strength in GSIC as the degrees of freedom of  $U_{ij\sigma}$  provide means to include additional constraints into the energy functional. Exploiting this feature, many promising improvements have been obtained in GS DFT [PHL84, PHL85, PL88, KKM08, DKK<sup>+</sup>11]. However, some important aspects have not been discussed before. In particular, the use of complex numbers for the optimized orbitals and the unitary transformation appears natural from a TDDFT perspective, but has not been investigated in GS GSIC using the GOEP framework so far. Therefore, to conclude the GSIC scheme, I address the question of how the unitary transformation of Eq. (3.4) that enters the GOEP formalism can be defined. This short introduction is needed as a background for the overview of the performance of GSIC in Sec. 3.5. As it is closely related to Pub3, a more detailed discussion can be found there.

**Energy-minimizing transformation:** The idea of using *energy-minimizing transformations* is based on a suggestion of Pederson, Heaton, and Lin [PHL84, PHL85, PL88] that is applied in KS DFT [KKM08, MDRS09b]. The unitary transformation of GS DFT is used to support the variational energy-minimization procedure of Hohenberg and Kohn: The orbitals  $\{\tilde{\varphi}_{i\sigma}\}$  and the transformation  $U_{ij\sigma}$  are chosen such that the total energy is minimized via unitary optimization of the SIC energy contribution exploiting its freedom of unitary transformations. This Pederson *et al.* criterion leads to a set of equations [PHL84]

$$\langle \tilde{\varphi}_{i\sigma} | \tilde{v}_{i\sigma}^{\text{SIC}}(\mathbf{r}) - \tilde{v}_{j\sigma}^{\text{SIC}}(\mathbf{r}) | \tilde{\varphi}_{j\sigma} \rangle = 0 \quad \forall i, j \text{ occupied}. \quad (3.12)$$

(see Pub3 for more details). However, starting from real canonical KS orbitals, there are still two possible choices of the orbitals  $\{\tilde{\varphi}_{i\sigma}\}$  and the transformation  $U_{ij\sigma}$ : They can be chosen either both real-valued or both complex-valued. Each choice correspond to one definition of the unitary transformation:  $U_{ij\sigma}$  is defined according to Eq. (3.12) with numbers either restricted to be real or free to be complex. These options influence the shape of the resulting orbital densities  $\tilde{n}_{i\sigma} = |\tilde{\varphi}_{i\sigma}|^2$  and, therefore, may exhibit different performances of the SIC. This influence is discussed in detail in Pub3 and summarized in Sec. 3.5. I denote energy-minimizing GSIC based on the GOEP, GKLI, and GSLA methods by GOEP-SIC, GKLI-SIC, and GSLA-SIC. If not stated explicitly, complex-valued energy minimization is used throughout this thesis.

**Spatially localizing transformation:** A second definition of the unitary transformation is based on the observation that typically localized or *Foster-Boys* (FOBO) orbitals [Boy60, FB60, ER63, PM89] are good approximations to real energy-minimizing orbitals [KKM08]. This finding is rationalized in Ref. [Kör11] and supported by Pub3. Performing the FOBO unitary optimization is numerically less expensive, thus serves as a reasonable alternative to energy-minimizing transformations. The FOBO transformation can also be performed with complex-valued orbitals. Yet, the FOBO criterion is not sensitive to the degrees of freedom provided by complex numbers. I denote GSIC with FOBO localization based on the GKLI potential by FOBO-SIC.

The optimization procedure of the energy-minimization and spatial localization criteria is one of the most time-consuming steps in GSIC calculations. Therefore, to guarantee reasonable numerical performance, I implemented new algorithms that are based on energy gradients (see Appendix C). Best performance can now be obtained in PARSEC with an algorithm that uses conjugate gradients, step-size optimization, and that takes the unitary constraint of  $U_{ij\sigma}$  into account explicitly. This algorithm was adapted and implemented to PARSEC in collaboration with Peter and Simon Klüpfel. More details are explained in Pub3 and Appendix C.1.3. The extension of existing algorithms in PARSEC (see Ref. [Kör09]) to complex-valued  $\{\tilde{\varphi}_{i\sigma}\}$  and  $U_{ij\sigma}$  is presented in Appendix C.1. In Appendix C.2, I compiled an overview of PARSEC features and user-input options related to GSIC.

### 3.5 Generalized self-interaction correction in DFT

Many of the features of GOEP and its GKLI approximation were already investigated in the work of Thomas Körzdörfer [KKM08, Kör09]. Both approaches yield GS energies and spin densities in close agreement [KKM08]. The relation between GKLI and GOEP is illustrated further by the results in Appendix A. Yet, using complex degrees of freedom in the unitary transformation yields a new perspective on the GS GOEP-SIC approach. The influence of complex-valued unitary transformations and optimized orbitals is the content of Pub3. In the context of Pub4, I performed supplementary investigations on the response behavior of chain-like systems depending on different approximations to the GOEP and different choices of  $U_{ij\sigma}$ . These findings are presented in detail in Appendix A.1. Here, I give a summary of the SIC and GSIC results of this thesis.

Investigations of total energies and bond lengths of a representative set of dimers and small molecules in Pub3 show that the choice of the unitary transformation has notable influence on the outcome of GKLI-based calculations, while standard KLI-SIC results may

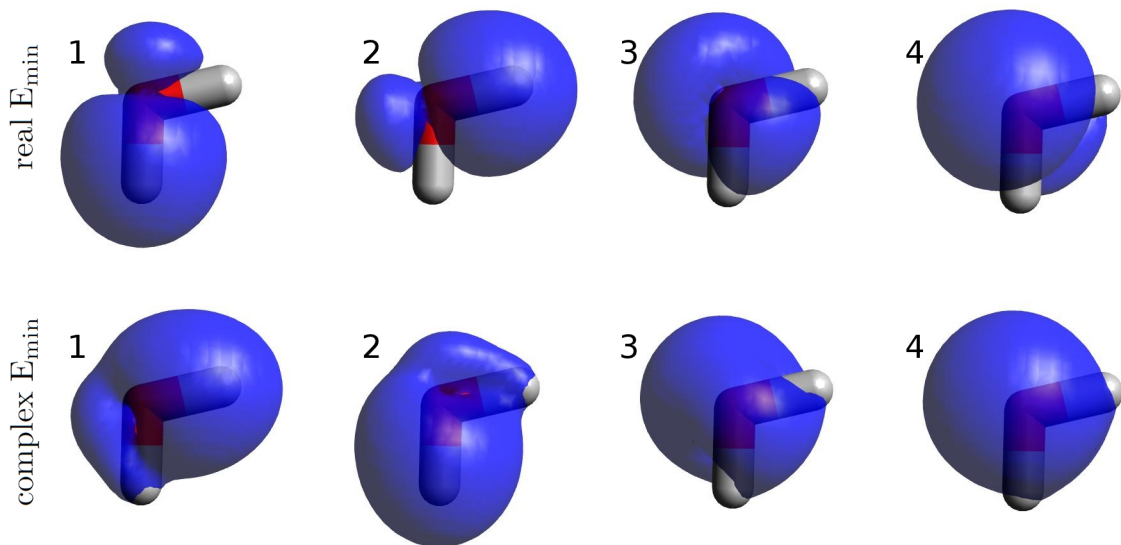


Figure 3.1: Orbital densities of the energy-minimizing orbitals of  $\text{H}_2\text{O}$  computed self-consistently with GKLI-SIC using real-valued energy minimization (upper part) and complex-valued energy minimization (lower part). The numbering of the optimized orbital densities is arbitrary as their order does not carry physical meaning. One clearly observes for the example of  $\text{H}_2\text{O}$  that the orbital densities of real-valued energy-minimizing orbitals form nodal planes, whereas nodal planes are avoided in the complex-valued case.

be compromised by deficiencies of the KLI potential (see Sec. 3.3.1). Total GSIC energies decrease with increasing the degrees of freedom of the unitary transformation from real-valued to complex-valued numbers. The influence on the bond length differs for single-bond and multiple-bond systems. In case of single-bond systems, increasing the degrees of freedom leads to increasing bond-length underestimation. For double- and triple-bond systems, GKLI-SIC with a complex-valued energy-minimizing transformation improves upon the known SIC bond-length underestimation [GU97, VSP<sup>+</sup>06]. Total energies and bond lengths computed with FOBO-SIC are close to real-valued energy-minimizing GKLI-SIC.

The difference between real and complex energy minimizing orbitals is related to the formation of nodal planes of the orbital densities  $\tilde{n}_{i\sigma}(\mathbf{r})$ . The optimized orbitals  $\{\tilde{\varphi}_{i\sigma}\}$  need to be orthogonal like the canonical KS orbitals. Real-valued orbitals preserve this orthogonality via formation of nodal planes that are passed on to the orbital densities. However, using complex degrees of freedom, nodal planes of the orbital densities can be avoided while preserving orthogonality of the optimized orbitals. This finding is illustrated with the orbital densities of  $\text{H}_2\text{O}$  in Fig. 3.1 and with CO in Pub3. Thus,  $\tilde{n}_{i\sigma}(\mathbf{r})$  without nodal planes are smoother and, therefore, closer to GS densities. Such orbital densities are important in the context of the question whether it is allowed to insert orbital densities into GS xc energy functionals: Hope is high that smooth orbital densities of the complex-valued case are closer to the realm where (semi)local functionals are appropriate. The reduced appearance of nodal planes in complex-valued  $\tilde{n}_{i\sigma}(\mathbf{r})$  also serves as an explanation why the SIC of PBE is more sensitive to changes from real to complex numbers than the SIC of

LSDA (see Pub3). The PBE functional is more sensitive to large changes of the density due to its dependence on density gradients. Therefore, allowing or avoiding nodal planes where large density gradients occur makes a more pronounced difference for PBE than for LSDA.

More insight into the performance of different (G)OEP approximations is provided from the results of Appendix A.1 and Appendix A.2, where energy minimization in GKLI-SIC is always performed with complex-valued orbitals. The response of hydrogen chains to static electric fields shows that SLA-SIC and KLI-SIC may exhibit a distorted response behavior. This finding can be understood from the unitary invariance of both the SIC energy expression and the KLI potential approximation. Instead, the GKLI-SIC potential is a reasonably good approximation to full GOEP-SIC and exhibits the field-counteracting behavior of the xc potential that is important for a proper description of polarizabilities (see Sec. 2.4). GSLA-SIC gives polarizabilities close to GKLI-SIC for short chains, but the polarizability deviations to GKLI-SIC increase with increasing chain length. This finding is in line with the observation that GSLA-SIC does not show a clear field-counteracting response behavior. In case of hydrogen chains, FOBO-SIC polarizabilities are close to GKLI-SIC, but slightly worse. The situation reverses in polyacetylene chains, where FOBO-SIC polarizabilities are slightly closer to reference calculations than GKLI-SIC. The comparison between hydrogen and polyacetylene chains indicates that localization effects play different roles in different kinds of systems. Only detailed investigations show if orbital localization or full energy minimization gives results closer to reference calculations and to experimental findings.

### 3.6 Generalization of SIC in TDDFT

One of the main aspects of this work is the extension of GSIC from GS DFT to TDDFT covered by Pub2 and Pub4. The motivation for this extension was based on the promising features of GKLI-SIC in DFT, see for instance Refs. [KKM08, KKM09, Kör09, DKK<sup>+</sup>11] and Sec. 3.5. The GKLI-SIC performance is good news for application in TDDFT for two reasons. First, the time-dependent OEP (TDOEP) is known to be very demanding to solve [MK06, WU08]. Therefore, most applications of orbital functionals in TDDFT rely on a TD extension of the KLI approximation [UGG95, MK06]. Second, however, the *time-dependent KLI* (TDKLI) approximation suffers from its own problems beyond the deficiencies known for GS KLI: RT propagation of the TDKLI potential shows stability issues and zero-force theorem violation [MKvLR07, MDRS09b, MDRS11]. Therefore, starting with GSIC in TDDFT, hope was high that the additional degrees of freedom provided by the unitary transformation together with the SIC functional could be exploited to support propagation stability. Then, the promising features of SIC could help in TDDFT to study questions that were considered too difficult for local and semilocal density functionals.

The extension of SIC to TDDFT by Tong and Chu [TC98b, TC98a] uses the PZ SIC energy functional in an orbital-adiabatic sense (see Sec. 2.5.2) together with the TDKLI approximation. TD SIC with GKLI is based on a similar rationale, i.e., the orbitals and the unitary transformation are used at every instant of time to keep the system on a stable energy path during propagation. The GSIC extension to TDDFT results from three steps. First, the generalized orbital-specific potentials are transferred to the TD case, thus reading

$$u_{xc,j\sigma}^G(\mathbf{r}, t) = \frac{1}{\varphi_{j\sigma}^*(\mathbf{r}, t)} \sum_i^{N_\sigma} U_{ij}^\sigma(t) \tilde{\varphi}_{i\sigma}^*(\mathbf{r}, t) \tilde{v}_{i\sigma}^{\text{SIC}}(\mathbf{r}, t), \quad (3.13)$$

where

$$\tilde{v}_{i\sigma}^{\text{SIC}}(\mathbf{r}, t) = \frac{\delta E_{\text{xc}}^{\text{SIC}}[\{\tilde{n}_{k\tau}\}]}{\delta \tilde{n}_{i\sigma}(\mathbf{r}, t)}. \quad (3.14)$$

Second, the standard orbital-specific potentials  $u_{\text{xc},j\sigma}(\mathbf{r}, t)$  need to be replaced by the generalized ones in the TDKLI potential [TC98b, TC98a, MK06]

$$v_{\text{xc},\sigma}^{\text{TDKLI}}(\mathbf{r}, t) + f_{\sigma}(\mathbf{r}, t) = v_{\text{xc},\sigma}^{\text{TDSLAs}}(\mathbf{r}, t) + \frac{1}{2n_{\sigma}(\mathbf{r}, t)} \sum_{j=1}^{N_{\sigma}} n_{j\sigma}(\mathbf{r}, t) [(\bar{v}_{\text{xc},j\sigma}^{\text{TDKLI}}(t) - \bar{u}_{\text{xc},j\sigma}(t)) + \text{c.c.}], \quad (3.15)$$

where

$$f_{\sigma}(\mathbf{r}, t) = -\frac{\text{i}}{4n_{\sigma}(\mathbf{r}, t)} \sum_{j=1}^{N_{\sigma}} \nabla^2 n_{j\sigma}(\mathbf{r}, t) \int_{-\infty}^t (\bar{u}_{\text{xc},j\sigma}(t') - \bar{u}_{\text{xc},j\sigma}^*(t')) dt' \quad (3.16)$$

is the so-called memory term and the TD Slater (TDSLAs) contribution reads

$$v_{\text{xc},\sigma}^{\text{TDSLAs}}(\mathbf{r}, t) = \frac{1}{2n_{\sigma}(\mathbf{r}, t)} \sum_{j=1}^{N_{\sigma}} n_{j\sigma}(\mathbf{r}, t) (u_{\text{xc},j\sigma}(\mathbf{r}, t) + u_{\text{xc},j\sigma}^*(\mathbf{r}, t)). \quad (3.17)$$

Orbital-averaged potentials are computed in analogy to Eqs. (3.7) and (3.8) of the ground state. Third, in the TD case, the unitary transformation is a TD function that connects the TD KS orbitals and a second optimized orbital set according to

$$\tilde{\varphi}_{i\sigma}(\mathbf{r}, t) = \sum_{j=1}^{N_{\sigma}} U_{ij}^{\sigma}(t) \varphi_{j\sigma}(\mathbf{r}, t). \quad (3.18)$$

Thus, a suitable choice of  $U_{ij}^{\sigma}(t)$  concludes the *time-dependent GKLI* (TDGKLI) approximation of the SIC functional and establishes *time-dependent GSIC* (TDGSIC). Replacing  $u_{\text{xc},j\sigma}$  by  $u_{\text{xc},j\sigma}^{\text{G}}$  in Eq. (3.17) yields the *time-dependent GSLAs* (TDGSLAs) approximation.

Although this extension appears straight forward at first glance, there are a lot of hidden difficulties and obstacles. The first issue concerns the choice of  $U_{ij}^{\sigma}(t)$  that is discussed comprehensively in Pub4. The central idea is to apply the energy-minimization and the spatial localization criteria known from GS DFT (see Sec. 3.4) at every instant of time. This proceeding is in line with the orbital-adiabatic use of the SIC energy functional. I use the shortcut TDGKLI-SIC for complex-valued energy minimization and TDFOBO-SIC for spatial localization together with the TDGKLI approximation. Yet, optimizing either of the GS criteria for many ten thousands of time steps during time propagation renders application of TDGSIC impractical for sizable systems. When propagating the GSIC ground state without external perturbation, I realized that part of the TD transformation could also be performed analytically. This idea enabled the breakthrough of TDGSIC. In such a setup,  $U_{ij}^{\sigma}(t)$  evolves from  $U_{ij}^{\sigma}(t - \Delta t)$  of the previous time step with the KS eigenvalues  $\varepsilon_j$ , i.e.,

$$U_{ij}^{\sigma}(t) = e^{\text{i}\varepsilon_j \Delta t} U_{ij}^{\sigma}(t - \Delta t). \quad (3.19)$$

This time propagation of the unitary transformation can be used as an initial guess for subsequent unitary optimization at every instant of time or as an approximation to the

TD transformation. More details are explained in Pub4. All TDGSIC propagations are performed with complex TD orbitals and transformations. They are started from a ground state with complex-valued  $U_{ij}^\sigma$  optimization because, otherwise, when starting from real-valued optimized orbitals and transformations the additional degrees of freedom of the complex-valued TD transformation may instantaneously change the ground state even without external perturbation.

Finally, the choice of the unitary transformation is important for the explicit memory dependence of the GKLI approximation via its generalized  $f_\sigma(\mathbf{r}, t)$  ( $f_\sigma^G(\mathbf{r}, t)$ ) contribution. While  $f_\sigma(\mathbf{r}, t)$  vanishes in TDKLI-SIC [UGG95, GDP96, TC98a, TC98b, MK06], it is not clear from the start that  $f_\sigma^G(\mathbf{r}, t)$  vanishes in TDGKLI-SIC. Pub4 demonstrates that the contribution of the TDGKLI memory term depends on the criterion for  $U_{ij}^\sigma(t)$ . When energy minimization is used in the ground state and during time propagation, the memory term does not contribute to TDGKLI. For all other cases, the memory dependence via  $f_\sigma^G(\mathbf{r}, t)$  remains unclear. Explicit choices for  $f_\sigma^G(\mathbf{r}, t)$  are explained in Pub4. Note that no matter how  $f_\sigma^G(\mathbf{r}, t)$  contributes to the TDGKLI memory, propagation of SIC with TDGKLI includes an implicit dependence on the history of the density  $n(\mathbf{r}, t')$  for  $t' \leq t$  via the KS orbitals in a natural way [GDP96, MBW02, MMN<sup>+</sup>12].

### 3.7 Performance of generalized SIC in TDDFT

First investigations of TDGSIC [Hof08] focused on the propagation stability question of Na<sub>5</sub>, a notoriously problematic system for RT propagation. Here, the propagation instability manifests in zero-force theorem violation and notable drifts of the total energy from its GS value although no external field acts [MKvLR07, Mun07]. Reference [Hof08] indicates that propagation stability can be increased by increasing the numerical accuracy of the unitary optimization. However, using the initial guess of Eq. (3.19) puts this finding into a new perspective. The appendix of Pub4 demonstrates that TDGSIC schemes show much better stability than propagation with TDKLI-SIC even for the difficult case of Na<sub>5</sub>. For most applications, reasonably stable propagation of TDGSIC can be performed in a time window that is long enough for computing the dipole spectrum. However, as a warning, one should be aware that instability problems may occur and always check for stability issues. Based on this reassuring finding, TDGSIC is ready for applications to dynamic situations and investigations of excitation features. I summarize the results on the performance of TDGSIC in the following.

Hydrogen chains are a transparent model system to study the response behavior of the potential for different approximations to  $v_{xc}(\mathbf{r}, t)$ . For slowly varying external perturbations, one expects the TD xc potential to perform similar to GS xc potentials, i.e., that it counteracts the external field (see Sec. 2.4). Pub4 demonstrates that the TD response to such an external potential parallels the response behavior known from GS xc potentials:  $v_{xc}(\mathbf{r}, t)$  of TDLDA follows the external field, whereas TDGKLI-SIC exhibits a field-counteracting behavior. At higher frequencies of the external perturbation, TDGKLI-SIC develops complicated features that can not be assigned to a simple frequency-dependent response behavior. Similar studies of different approximations to TDGKLI-SIC are also presented in Pub4. Interestingly, TDFOBO-SIC exhibits a response behavior very similar to TDGKLI-SIC. While a clear assignment of the energy-minimizing GSLA-SIC response was difficult in the GS case,

TDGSLA-SIC unambiguously follows the external field even at elevated frequencies of the external perturbation. Moreover, using only Eq. (3.19) for the unitary transformation spoils the field-counteracting behavior of the xc potential already at low frequencies of the external field. Thus, the results of Pub4 show that the response term of the (G)KLI approximation and optimizing the unitary transformation at every instant of time are important for a proper field-counteracting response behavior.

The TD response behavior studies are complemented in Pub4 by investigations of hydrogen chain excitations energies. Whereas TDKLI-SIC results suffer from propagation instability and do not improve upon TDLDA, TDGSIC notably shifts the lowest excitation energies to higher values. TDGKLI-SIC excitation energies are in close agreement to B3LYP but deviate from approximate coupled-cluster singles-and-doubles model excitation energies by at least 0.9 eV. In conclusion, TDGKLI-SIC and its TDFOBO-SIC approximation show promising performance on hydrogen chains. Yet, already static polarizabilities of hydrogen chains exhibit large deviations between OEP and GOEP [KK11] (for more background, see Appendix A.1) and a comparison between TDOEP and TDGOEP is not available. Because of the peculiar nature of hydrogen chains [vFdBvL<sup>+</sup>02], the performance of TDGSIC also needs to be assessed for real molecules.

Application to metal clusters in Pub4 shows that TDGSIC does not spoil the good accuracy that already TDLDA reaches. However, TDGSIC improves in cases where (semi)local functionals exhibit systematic failures: In hydrogenated silicon clusters, quantum confinement and excitonic effects are known to play an important role [OCL97, RL98, RL00, ORR02, VOC02, VOC06]. Here, low-lying optical excitations are underestimated by standard functionals and TDKLI-SIC [MCR01], in particular for the very small clusters. Pub2 and Pub4 demonstrate that TDGSIC notably improves and yields excitation energies in good agreement with results from the GW Bethe-Salpeter equation approach. Lowest excitation energies of oligo-acetylenes in Pub4 also improve upon TDLDA and reveal differences between the different possible choices of the unitary transformation during time propagation. Last but not least, TDGSIC also gives promising results for static and dynamic CT situations as well as CT excitation energies. This is the topic of the next chapter.



## Chapter 4

# Charge transfer and charge-transfer excitation energies

*The obvious inability of present-day physics and chemistry to account for such events is no reason at all for doubting that they can be accounted for by those sciences.*

Erwin Schrödinger  
What is life? (1944)

A trustworthy description and theoretical prediction of charge transfer is one of the well-known and longstanding problems of (time-dependent) density functional theory [DWHG03, Toz03, Mai05, TFSB05, KBE06, TS07, KBY07, TS08, EVV09, LBBS12]. Typically, energies of electronic excitations that exhibit CT character are underestimated when calculated with (semi)local xc functionals [DWHG03, Toz03, Mai05]. Transport properties as, e.g., conductance and  $I$ - $V$  characteristics of molecular electronic devices may be severely in error [TFSB05, KBE06, TS07, KBY07, TS08, LBBS12] when calculated from the Landauer-Büttiker approach [Lan57, Büt86] based on non-equilibrium Green's function theory in combination with DFT using standard xc functionals. Recently, also RT propagation has been used to study CT scenarios [KSA<sup>+</sup>05, CEVV06], but the reliability of results is limited by the quality of xc functional approximations. I provide more insight into the CT problem of (TD)DFT in Sec. 4.1 and complement this discussion by some solution ideas. The CT failure is commonly related to the self-interaction error of (semi)local xc functionals [TFSB05, TS07, KBY07, TS08] and the lack of a derivative discontinuity in such approaches [TFSB05, KBE06, TS07, TS08, LBBS12]. Therefore, self-interaction correction is a promising approach for improving the (TD)DFT description of CT phenomena. I discuss in Sec. 4.2 how generalized KS SIC introduced in Chap. 3 performs in static and dynamic CT situations and how it improves the description of CT excitation energies.

### 4.1 The charge-transfer problem of DFT and TDDFT and some solution ideas

The discussion of the CT problem of TDDFT in the literature [DWHG03, Toz03, DHG04, GB04, Mai05, TFSB05, MT06, ZSK<sup>+</sup>09, Aut09, IHG10, FRM11, HG12] reveals the many facets of this intriguing issue. Among the many different perspectives to approach the CT

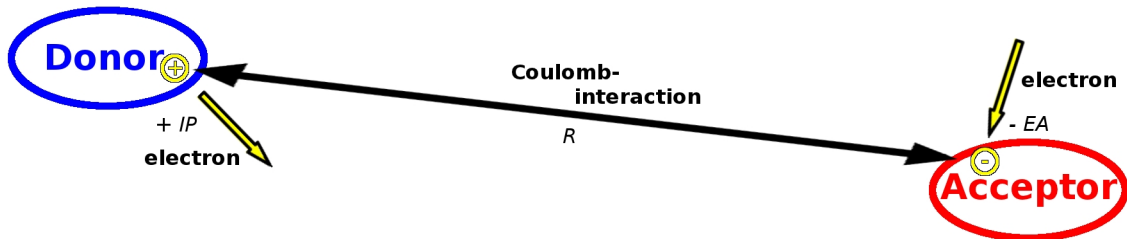


Figure 4.1: Model CT situation between a donor (D) and an acceptor (A) separated by the large distance  $R$ . See the main text.

problem, in the following, I present one that is based on the long-range CT between a donor (D) and an acceptor (A) subunit separated by the large distance  $R$  (for an illustration, see Fig. 4.1). The excitation energy that is needed to transfer one integer unit of the elementary electric charge  $e$  from D to A is given by Mulliken's rule [Mul50, SKB09a, SKB09b]

$$\Omega^M = IP^D - EA^A - \frac{1}{R}. \quad (4.1)$$

The ionization potential  $IP^D$  of D is the energy that needs to be paid when removing one electron from D, and the electron affinity  $EA^A$  of A is the energy one gains when adding one electron to A. The third term amounts to the energy gain due to the Coulomb interaction between the additional negative charge on A and the positive charge of D. The excitation energy needed for a very long-range charge transfer ( $R \rightarrow \infty$ ) equals the difference  $IP^D - EA^A$  between the ionization potential of D and the electron affinity of A.

The important question now is how TDDFT behaves [DWHG03, Toz03, DHG04]. For a transparent illustration, I use the TDDFT linear response approach in single-pole approximation (see Sec. 2.2.2). One assumes that in the case of a well separated D and A, the eigenvalues and orbitals of the entire system correspond to the eigenvalues and orbitals of the isolated D and A, and the charge transfer is dominated by the transition from the HOMO (H) located on D to the LUMO (L) located on A. With these assumptions, the excitation energy reads

$$\Omega = \omega_{KS} + 2 \int \int \varphi_H^D(\mathbf{r}) \varphi_L^A(\mathbf{r}) f_{Hxc}(\mathbf{r}, \mathbf{r}', \omega_{KS}) \varphi_H^D(\mathbf{r}') \varphi_L^A(\mathbf{r}') d^3r d^3r', \quad (4.2)$$

where  $\omega_{KS} = \varepsilon_L^A - \varepsilon_H^D$  abbreviates the eigenvalue difference. The overlap of KS orbitals localized on D and orbitals localized on A decreases exponentially with the distance  $R$ , thus the orbital products of the last term of Eq. (4.2) vanish when  $R \rightarrow \infty$ . This term contributes to the CT excitation energy only when the kernel diverges to compensate for the vanishing overlap [GB04]. Note that by definition the exact xc kernel exhibits all features that are required to yield correct CT excitation energies. However, adiabatic, (semi)local xc approximations do not show singular behavior of the xc kernel. Resulting CT excitation energies are dominated by  $\omega_{KS}$ , which is typically not a good approximation to the fundamental gap  $\Delta = IP^D - EA^A$ , and do not exhibit the  $1/R$  behavior.

This deficiency of standard, explicitly density-dependent functionals has been analyzed from different perspectives. Strong frequency dependence of the xc kernel and a proper

inclusion of the particle number discontinuity have been identified to be important for the reliable description of charge transfer [Toz03, Mai05, TFSB05, MT06, HG12]. Moreover, the CT problem has frequently been related to the self-interaction error of many density functional approximations [TFSB05, TS07, KBY07, TS08].

Recent approaches to improve upon the CT failure of (semi)local functionals include orbital and hybrid functionals. Exact exchange that does not suffer from the SIE yields the correct  $1/R$  dependence [DWHG03, IHG10] due to the non-local contribution of the Fock exchange functional, but misses correlation effects. Standard hybrid functionals include only a fraction of EXX and, therefore, only partially correct for the CT problem. Yet, range-separated hybrid functionals where EXX dominates the long range have been shown to predict CT excitations reliably [YTH04, CHG07, LB07, SKB09b, KSBK11].

Beside the just presented approaches, I demonstrate in the following section that KS (TD)GSIC improves the (TD)DFT description of CT situations. The findings of Chap. 3 already reveal first indications for this improvement: GSIC exhibits a field-counteracting response behavior to static external electric fields and improves static polarizabilities of chain-like systems (see Chap. 3.5 and Appendix A). The field-counteracting behavior is related to the derivative discontinuity and manifests also in step-like structures of the potential (see Sec. 2.4 for an introduction). Such kind of discontinuous structures of the potential lead to singular features in the xc kernel that may compensate for the vanishing orbital overlap. In energy-minimizing TDGKLI-SIC, the field-counteracting behavior carries over to the response at low-frequency TD external perturbations and exhibits notable frequency dependence when external fields with higher frequencies are applied (see Sec. 3.7). Last but not least, the SIC functional is non-local and its xc potential shows the proper  $1/r$  asymptotic decay [PZ81, GKKG00].

## 4.2 Self-interaction correction and charge transfer

### 4.2.1 The integer preference of electron jumps

In this section, I demonstrate how (TD)GSIC describes the static and dynamic charge transfer between two well separated D and A moieties. To this end, I chose a transparent model system [KBY07] of two hydrogen chains as depicted in the left part of Fig. 4.2. The chains are separated by a distance of 8 Å which is large enough for the overlap of the electronic structure of the two chains to almost vanish, but which is at the same time short enough to allow charge transfer driven by external fields from one chain (D) to the other (A). Therefore, one expects charge transfer to proceed in jumps of integer units of  $e$  from D to A when external fields with sufficient field strength are applied. Man1 investigates this system in static and dynamic situations at different external field strengths and reveals the peculiar features of the (TD)GSIC xc potential that support integer preference of the electron jumps. Here, I summarize and complement the findings of Man1. Beyond that, I present in Appendix A.3 one additional observation of the total energy of the CT system with respect to the external electric field strength. I start with GS DFT investigations before I turn to the dynamic scenario.

The first important result of Man1 is that GSIC exhibits – in contrast to (semi)local and standard hybrid functionals – *integer particle preference* during the charge transfer from D to A when static external fields are applied. This finding is illustrated in the right part of

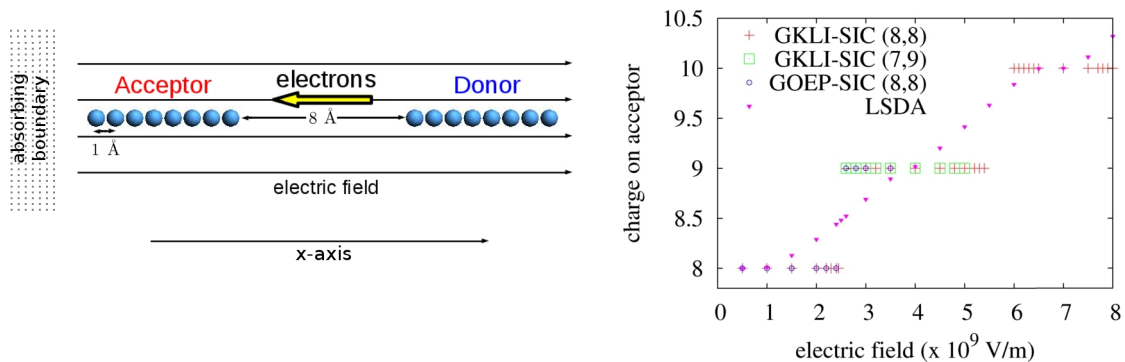


Figure 4.2: Left: Charge-transfer model system [KBY07] of two identical hydrogen chains ( $H_8$  with an H distance of 1 Å) separated by a distance of 8 Å. An electric field transfers charge from the right (donor, D) to the left (acceptor, A) hydrogen chain. The absorbing boundary is used only during time propagation. Right: Integrated charge of the A chain depending on the field strength of the external electric field computed with GKLI-SIC, GOEP-SIC, and LSDA. The charge is computed by integration over the left half space of the real-space grid. The numbers in brackets indicate the number of electrons per spin channel between the first and the second electron jump using the notation “(spin up, spin down)”. Note that convergence problems of GKLI-SIC (7,9) occurred in between  $5.1 \times 10^9$  V/m and  $5.4 \times 10^9$  V/m where I was able to converge solely the GKLI-SIC (8,8).

Fig. 4.2. The first electron jump of GSIC can be computed to within  $0.1 \times 10^9$  V/m accuracy. However, in case of the second jump I faced convergence difficulties due to degeneracies at the Fermi level and, therefore, an uncertainty of  $0.3 \times 10^9$  V/m remains. As already stated in Man1, the integer preference behavior of GKLI-SIC is in good agreement with full complex energy-minimizing GOEP-SIC. I support this finding by GOEP-SIC calculations presented in the right part of Fig. 4.2 for external electric fields with field strengths from 0.0 V/m to  $3.5 \times 10^9$  V/m: The integrated charges on the acceptor chain and total energies in GOEP-SIC are almost identical with the GKLI-SIC results. However, OEP-SIC calculations suffered from serious convergence difficulties that prohibited a reliable computation of the integrated charge on the A chain. In full OEP-SIC, the KS orbitals fulfill two roles at the same time [KKM08]: They attempt to optimize both the kinetic and the SIC energy, thus need to decide between being delocalized or localized. It is likely that the underlying compromise impedes OEP-SIC convergence.

Second, the local, multiplicative xc potential allows to transparently analyze the  $v_{xc}$  features that support the integer preference behavior. Man1 demonstrates that step structures in the GKLI-SIC xc potential rise in between the two hydrogen chains before electron jumps occur. At the same time, the potential well of the A chains is shifted upwards. Thus, the potential barrier for an electron jump increases and the step structure works against fractional charge transfer. When the electron jumps, the xc potential changes discontinuously: The potential wells shift relative to each other and a *reverse step structure* appears that keeps the just transferred electron on the A chain. With further increasing the external field strength, first, the reverse step feature decreases before another cycle of emerging xc poten-

	first electron jump						second electron jump							
	process	↓D	↓A	↑D	↑A	↓	↑	process	↓D	↓A	↑D	↑A	↓	↑
(S)		4	4	4	4	8	8							
(1)	↑D → ↑A	4	4	3	5	8	8	↓D → ↓A	3	5	3	5	8	8
(2)	↓D → ↓A	3	5	4	4	8	8	↑D → ↑A	3	5	3	5	8	8
(3)	↑D → ↓A	4	5	3	4	9	7	↓D → ↑A	3	5	3	5	8	8
(4)	↓D → ↑A	3	4	4	5	7	9	↑D → ↓A	3	5	3	5	8	8

Table 4.1: The left part of the table shows four realizations (indicated in the first two columns) of the first electron jump from D to A starting from the configuration in the first row labeled by (S). It explicitly highlights the spin of the electrons, thus lists the number of electrons per spin up (↑) or down (↓) on the D and A moieties in the central columns. When external fields are present, this assignment of electrons in terms of KS orbitals to D, A, and spin-channels is unique as the KS orbitals are localized on either side of the real-space grid. In the last two columns of the left part, I summed up the number of electrons per spin channel after the electron transfer. The right part of the table indicates the consecutive second electron jump starting from the corresponding configuration after the first jump. All paths end with the same distribution of electrons over spin channels and D and A sides.

tial structures before and after the second electron jump starts. These step and reverse step features are one more example of the relation between the derivative discontinuity, integer particle preference, and structures of the xc potential.

The third important aspect of Man1 is the role of *spin-symmetry breaking* for a reliable description of the CT situation. The true physical charge transfer of one electron should be an equally weighted superposition of a spin-up and a spin-down electron jump. Yet, performing GKLI-SIC calculations and starting from a ground state with eight electrons per spin channel – a symmetric distribution of electrons over spin channels – one observes that spin symmetry breaks as the first electron transfers only in one of the spin channels. Investigating these calculations in detail, one finds that the GKLI-SIC KS ground state exhibits a *weak aufbau principle violation* after the first electron transfer: The HOMO of one spin channel is higher in energy than the LUMO of the other spin channel. Thus, the electron occupation points to a situation with an unequal distribution of electrons over spin channels. Fixing the occupation numbers of the KS system to investigate this alternative configuration yields a KS ground state with an aufbau principle violation that points back to the previous configuration. Taking into account that the just discussed cases may be realized also with the opposite spin assignment, four realizations of the first electron transfer appear. They are outlined in Table 4.1 together with the consecutive second electron jump.

One observes that in realizations (1) and (2) eight electrons are in each of the spin channels, whereas in realizations (3) and (4) two more electrons are in one of the spin channels after the first electron transfer. Although the last two realizations appear unphysical because the applied electric field can hardly induce a spin-flip, they are all relevant for the GKLI-SIC realization of a one-electron charge transfer: All realizations are degenerate in terms of the total energy, the field strengths where the electron jumps occur, and the number of electrons on D and on A (see Fig. 4.2 on the right). Here, only realizations (1) and (3) are discussed because realizations (1) and (2) as well as (3) and (4) are equivalent in terms of the relevant

effects. The aufbau principle violation together with the degeneracy of all four realizations reflect that transferring an electron of either spin channel is equally probable in the true physical CT situation. Thus, breaking the spin symmetry in GSIC is an “easy way” to model the physics that may otherwise be too difficult for approximate density functionals.

Differences between realizations (1) and (3) appear in the details of how the xc potential builds up the reverse step and newly appearing step structures after the first and before the second electron transfer (see Man1). In realization (1), the reverse step appears only in the up-spin potential, decreases with increasing external field strength, and a step builds up in the down-spin potential. Instead, in realization (3) the reverse step after the first electron jump and the step counteracting the second electron jump emerge in both spin channels. Details about the step and reverse step structures are explained in Man1. After the second electron jump the symmetric distribution of electrons into spin channels is recovered.

Last but not least, I turn to the truly TD investigations of Man1. There, the external field strength of  $8.0 \times 10^9$  V/m is chosen to be strong enough that according to the GS investigations two electrons may be transferred from the D to the A chain during time evolution. Moreover, charge may be accelerated to the boundary of the grid, thus the system may ionize. I use an absorbing boundary on the A end of the grid to remove this density and prevent it from being spuriously reflected back to the system (see Fig. 4.2).<sup>1</sup> Man1 reveals that in time-dependent LSDA (TDLSDA) the potential barrier between the two chains decreases and a notable fraction of charge is transferred from D to A. Instead, a *time-dependent step* that works against spurious fractional charge transfer builds up in the TDGKLI-SIC xc potential as a function of time. Similar features are also important for the ionization of the system. In TDLSDA, fractions of the density start to arrive at the absorbing boundary already after 2 fs. In GKLI-SIC, step structures appear also at the outer boundaries of the system and counteract ionization.

Man1 investigates only the early stage of the time evolution of the CT system for several conceptual and technical reasons. First, the absorbing boundary removes density from the system when ionization occurs. However, the unitary optimization scheme of GKLI-SIC so far is defined only for integer occupations [Kör09] and it is not clear how the unitary transformation needs to be implemented in other cases. Moreover, there is no charge-injection mechanism that could feed density from the opposite side of the grid to compensate for the absorbed density. Second, I estimated the propagation time until the first electron transfer occurs in TDGKLI-SIC from the TDLSDA time evolution. In the present setup, after 100 fs not more charge than a quarter of one unit of  $e$  has been transferred in TDLSDA. Already this time scale is tedious for TDGKLI-SIC propagation and I expect the first electron to jump not before 200 fs. Third, I expect spin-symmetry breaking to be important also during the time propagation to realize the transfer of the first integer unit of  $e$ . For the role of spin-symmetry breaking in TDDFT, see also Refs. [FRM11, DL11]. It remains to be investigated if and how this may succeed with TDGKLI-SIC.

Yet, already the short time evolution discussed in Man1 reveals the TD step structures that are important for reliable CT simulations. This together with the integer preference and occurring step structures of the model system in static CT situations raise hope that (TD)GSIC is a valid functional for investigations of electron transport in more complex and more realistic CT scenarios.

---

<sup>1</sup>Calculations were performed on an ellipsoidal grid with semi-principal axes of 50 bohr along the  $x$ -axis and 28 bohr perpendicular to the  $x$ -axis. The absorbing-boundary layer was 2.5 bohr thick.

### 4.2.2 The performance of GSIC on charge-transfer excitation energies

Having discussed static and explicitly TD simulations of charge transfer in Sec. 4.2.1, I finally turn to another important field of CT investigations, namely to CT excitation energies that are part of the linear response absorption spectra. In the literature, assessments of the performance of xc approximations on CT excitation energies are mostly carried out with transparent test systems in the long-range CT limit with almost vanishing orbital overlap of Sec. 4.1 using the Casida approach [DWHG03, GB04, IHG10]. In this case, the decomposition of the underlying transition into occupied to unoccupied orbital products can be used to identify CT excitation energies. The latter in turn allow for a straight forward investigation of the  $1/R$  dependence and comparison to excitation energies obtained from higher level wave-function theory reference calculations. Very long-range CT excited states carry only an almost vanishing oscillator strength because of the exponentially decaying overlap between the D and A moieties. Therefore, although they are still visible in the Casida-type linear response formalism, detecting very long-range CT excitation energies from the RT dipole signal is impracticable as the latter relies on non-vanishing transition dipole moments.

Alternative CT test systems are provided by the study of Peach *et al.* in Ref. [PBHT08]. It includes CT excited states that were classified as being of short-range and of long-range CT type. For the investigations of the performance of TDGKLI-SIC on CT excitation energies, I chose two systems: 4-(N,N-dimethylamino)benzotrile (DMABN) [JFTL02, PBHT08] and a dipeptide molecule [SAF98, TAH<sup>+</sup>99, PBHT08, RLG10]. In DMABN, a local excitation is seen experimentally at 4.25 eV and an excitation that has been classified as being of short-range CT character [JFTL02] at 4.56 eV. The dipeptide is a hallmark CT test system that exhibits a long-range CT excitation from one peptide unit to the other [RLG10] at 7.18 eV in the complete active space perturbation theory of second order (CASPT2) reference [SAF98]. Whereas in case of DMABN local and semilocal functionals yield a reasonable description of both the energetic position and the character of the lowest CT excitations, (semi)local functionals as well as standard hybrid functionals fail badly in case of the dipeptide [PBHT08].

Pub2 and Pub4 demonstrate that TDGKLI-SIC improves the situation. To clearly relate excitation energies computed via different functionals and methods (RT propagation, Casida approach, and others), and to identify CT excitation energies uniquely, I developed the transition density analysis idea that is outlined in Sec. 2.3. Based on this identification tool, one observes that TDGKLI-SIC correctly shifts the lowest TDLDA excitation energies of DMABN by about 0.2 eV to 4.1 eV (local) and 4.4 eV (short-range CT). Thus, it improves local and short-range CT excitations towards experimental results without spoiling the reasonable accuracy that already (semi)local functionals have. In the dipeptide, the TDLDA CT excitation energy underestimation is more severe: The CASPT2 CT excitation at 7.18 eV appears at 5.2 eV in TDLDA. Again TDGKLI-SIC improves and the lowest CT excitation energy of the dipeptide appears at 7.2 eV. This demonstrates the power of TDGKLI-SIC to correctly describe long-range CT excitations in the framework of KS TDDFT. Note that in contrast to the findings of the previous section, the improvements of excitation energies are obtained without breaking the spin symmetry. This observation emphasizes the importance of the spatial structure and frequency dependence of the xc potential in TDGKLI-SIC for a reliable description of CT phenomena.



## Chapter 5

# Excitation-energy transfer

*On grounds upon which we cannot enter here, we have to assume that a small system can by its very nature possess only certain discrete amounts of energy, called its peculiar energy levels. The transition from one state to another is a rather mysterious event, which is usually called a 'quantum jump'.*

Erwin Schrödinger  
What is life? (1944)

Electronic *excitation-energy transfer* (EET) after light absorption is one of the key processes in the natural light harvesting (LH) event and a prerequisite for charge generation in the LH reaction center [Küh95, CF09]. The efficiency of the entire light harvesting process is determined by the rates of charge transfer and EET of many single transfer steps contributing to the entire mechanism. These rates are affected by a number of different properties and phenomena: the electronic structure of the single chromophores, the electronic coupling between different system components, the geometry and arrangement of all constituents, the energetic and position (dis)order, and the interplay with the environment. TDDFT naturally lends itself to be used for investigations of the *intermolecular coupling strength* and has been applied [HFHGHG01, Hsu03, Neu07, Neu08, MLCGM08, FKH<sup>+</sup>08, CMLM<sup>+</sup>09, SFK09] using the Casida approach. In Sec. 5.1, I present a real-time TDDFT approach for investigating the *intermolecular coupling strength* and *coupling mechanism*. Real-time approaches are a good starting point for including decoherence and relaxation processes that are needed for studying EET. However, to investigate the RT dynamics of a system in contact with a dissipative bath, one needs to go beyond the standard TDDFT scheme and apply *open quantum system ideas*. Here, I use an approach that is based on the *stochastic TD KS equation* [DVD07, DDV08, ADV09, ADV11, MMN<sup>+</sup>12]. I give a short introduction to this method in Sec. 5.2 and present how it can be exploited to investigate EET in circularly arranged supermolecular setups in Sec. 5.3.

### 5.1 Intermolecular coupling and real-time TDDFT

The Förster model is probably the most prominent method to interpret experimental data of EET [För46, För48, För65, New91, Spe96, HDRS98, Sch03, SPB<sup>+</sup>06, MNMB07, BWLT07, KN12]. However, when using this model for the interpretation of actual data one should

always check its validity as, e.g., the applicability of Förster theory depends on the underlying coupling mechanism between the donor and the acceptor moiety. Förster theory relies on a dipole-dipole interaction between the transition dipole moments on D and A. Based on a formulation in the weak coupling limit, the Förster EET rate exhibits a characteristic  $1/R^6$  dependence. Therefore, when applying Förster theory for instance as a spectroscopic ruler on the nanoscale [Str78], it should be clarified if the assumptions on which Förster theory is based are fulfilled.

The first investigations of the coupling strength and coupling mechanism [Hof08] between a donor and an acceptor molecule focused on the distance dependence of the coupling strength in an attempt to distinguish between Förster- and non-Förster-type coupling in a resonant situation of two equal molecules. This work is published in Pub1. It demonstrates in a test system of two sodium dimers and a more realistic system of two benzaldehyde molecules at which distance the Förster-type coupling approximations breaks down. To this end, a multipole expansion is performed explicitly in the Hartree contribution of the KS potential along two routes, namely starting from the Hartree energy and starting directly on the level of the Hartree potential. This expansion is truncated after the dipole-dipole coupling term. Pub1 argues that the expansion route starting from the Hartree potential yields a potential with a more natural behavior and, therefore, uses this potential during time propagation. I explain the potential expansion idea in greater detail together with its implementation to the PARSEC code in Appendix D.1. From a comparison between two real-time evolutions of the coupled system of two molecules, one with the full Hartree potential and one with the Hartree potential in multipole expansion and truncated after the dipole-dipole term, one can distinguish between Förster- and non-Förster-type coupling in both example systems.

Second, Pub1 suggests a scheme to directly compute the intermolecular coupling strength from the real-time propagation of two interacting molecules. This investigation is based on the Davydov splitting and extracts the coupling-matrix element between the initial and the final state of EET from the dipole moment time evolution using a resonant two-level model. It clearly reveals in the sodium dimer test case that the coupling is of dipole-dipole type for distances above 25 bohr, whereas clear deviations from the dipole-dipole character can be observed for distances below 20 bohr.

However, to also investigate the influence of the energetic alignment of two neighboring molecules on the coupling strength one needs to go beyond the resonant coupling case. The illustration in the following is based on the well-approved  $\text{Na}_2$  model system of Pub1.<sup>1</sup> For excitations oriented along the bond axis,  $\text{Na}_2$  is almost a single level system as there is one prominent excitation at 2.1 eV and a second excitation at 4.1 eV with notably smaller oscillator strength.  $\text{Na}_2$  exhibits strong dipolar character and the electronic structure can be modified easily by bond-length variation starting from the experimental bond length of 5.78 bohr. The relation between bond-length variation and energetic detuning is depicted in the left part of Fig. 5.1. Due to variations of the bond length on the order of 1 bohr, excitation-energy shifts of about 0.25 eV can be induced.

In an off-resonant coupling situation between two isolated excited molecules where two excitation energies are close and all others far off, a two-level picture [Neu08] similar to Pub1 can be applied to determine the coupling-matrix element. In analogy to the resonant case,

---

<sup>1</sup>All calculations in this chapter are based on the LDA functional. I used real-space grids with a grid spacing of 0.7 bohr, an LDA pseudopotential with a core cut-off radius of  $r_c(\text{Na}) = 3.09$  bohr, and propagation time steps of 0.003 fs for closed quantum system and 0.001 fs for open quantum system investigations.

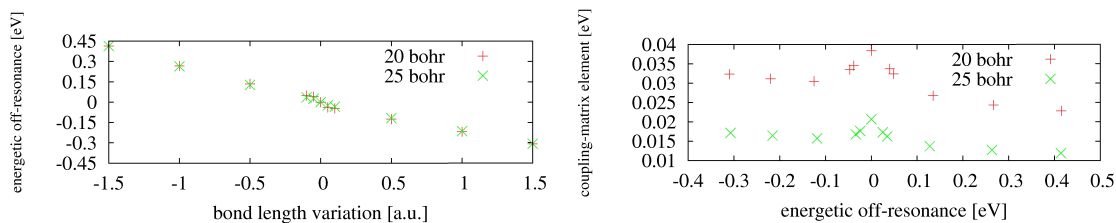


Figure 5.1: Left panel: Excitation-energy variation of one sodium dimer depending on variations of the bond length. I computed this property from a supersystem calculation as explained in Appendix D.2 using 20 bohr and 25 bohr dimer distances. Right panel: Coupling-matrix element calculated in a system of two  $\text{Na}_2$  depending on the energetic off-resonance (shift of the excitation energy from its value at the GS geometry) of one of the dimers.

the coupling strength can be extracted from a suitable observation of the dipole moments of each subsystem (for details, see Appendix D.2). The results of the coupling-matrix element as a function of the energetic off-resonance of the excitation energy of one of the dimers are shown in the right part of Fig. 5.1. One observes a general trend of the coupling-matrix element to decrease with increasing excitation energy within the data range investigated here. A clear resonance peak of the coupling strength appears at the resonant coupling situation. It is by about a factor of 1.4 larger than the coupling in off-resonant situations. In summary, RT propagation TDDFT provides a tool not only to distinguish between Förster- and non-Förster-type coupling but also to compute the coupling-matrix element in resonant and off-resonant coupling situations based on two-level models.

## 5.2 Open quantum systems in the density functional context

So-far, I have been discussing RT TDDFT methods to approach electronic excitations and the coupling between separated fragments of supermolecular setups. This closed quantum system TDDFT formulation describes the coherent system evolution, but does not include decoherence and dissipation effects. Therefore, to study the role of coherent energy transfer and the environment of the system for EET pathways and time scales in the context of LH systems, one needs to go beyond the closed quantum system formulation. Usually, such studies are based on the density-matrix formalism and master equations where the models of Haken and Stobl, the model of Redfield, polaron modifications, or related theories are employed [JJS02, YF02, JCRE08, IF09, RMAG09, KNOC11, Sil11]. The latter approaches typically use input such as coupling parameters and excitation energies from the experiment or from electronic-structure theory. Here, I introduce an alternative to master equations that addresses the EET problem directly from the electronic-structure theory perspective. It rests upon RT TDDFT and uses the stochastic TD KS equation [DVD07, DDV08, ADV09, ADV11, MMN<sup>+</sup>12]. The rationale behind this approach is to use the strength of (TD)DFT in describing static and dynamic properties of the electronic structure, while the interaction with the system’s environment is treated effectively via the open quantum system scheme. The approach opens a path for investigating the influence of electronic-structure properties on EET. I start with an introduction to the *stochastic Schrödinger equation* (SSE) and outline recent research about using SSEs in KS TDDFT.

### 5.2.1 The Stochastic Schrödinger equation

The stochastic Schrödinger equation is an alternative formalism to quantum master equations that is able to deal with quantum systems in contact with an external bath [DCM92, GN99, BP06, vK07, Wei08, MMN<sup>+</sup>12]. It exhibits some advantages in the TDDFT context as I outline at the end of this section. In contrast to quantum master equation approaches, the SSE does not work on the level of density matrices but uses a statistical ensemble of state vectors to unravel the open quantum system dynamics directly on the level of wave functions. To this end, the so-called Feshbach projection-operator method can be employed to separate the system and bath degrees of freedom of a combined Hamiltonian of system and environment [DCM92, GN99]. Such approaches start from a total Hamiltonian for system and bath where the system degrees of freedom are coupled to a bosonic environment

$$H = H_S \otimes I_B + I_S \otimes H_B + \lambda H_{SB}. \quad (5.1)$$

$I_S$  and  $I_B$  denote identities in the system (S) and bath (B) Hilbert spaces. Here, the system includes all dynamics and observables of the core system, e.g., of one molecular complex. The bath and system-bath coupling describe the environment as for example surrounding molecules and its interactions with the core system part. The system of interest is described by the many-particle Hamiltonian

$$H_S = \sum_{i=1}^N \left[ \frac{[\mathbf{p}_i + \mathbf{A}_{\text{ext}}(\mathbf{r}_i, t)]^2}{2} + v_{\text{ext}}(\mathbf{r}_i, t) \right] + \sum_{i<j}^N W(\mathbf{r}_i - \mathbf{r}_j) \quad (5.2)$$

of the electronic degrees of freedom, where  $\mathbf{p}$  is the momentum operator,  $\mathbf{A}_{\text{ext}}$  an external vector potential,  $v_{\text{ext}}$  a scalar external potential, and  $W$  describes the particle-particle interaction. Spin indices are omitted here and in the following. The environment, given by  $H_B$ , induces a fluctuating force that drives the system due to the interaction between the system and the bath

$$H_{SB} = \sum_{\alpha} S_{\alpha} \otimes B_{\alpha}. \quad (5.3)$$

The latter is expressed by many-particle operators  $S_{\alpha}$  and  $B_{\alpha}$  in the most general case, where  $S_{\alpha}$  operates on the system degrees,  $B_{\alpha}$  on the bath degrees of freedom, and  $\alpha$  denotes different possible system-bath coupling mechanisms. The bath may have a complex structure and not all of its microscopic details are relevant for the system dynamics. The driving force that is induced by the bath may, therefore, be subsumed by a stochastic noise that can usually be characterized by mean values and correlation functions [GN99].  $\lambda$  determines the strength of the system-bath coupling and serves as an expansion parameter.

The derivation of the SSE in the so-called Born-Markov limit involves some approximations [DCM92, GN99, ADV11, MMN<sup>+</sup>12]: The Born approximation assumes that a perturbative expansion up to second order in the coupling parameter  $\lambda$  is sufficiently accurate. The description of the environment in terms of the bath relies on the fact that the bath degrees of freedom form a dense energy spectrum and remain in thermal equilibrium. The Markov approximation amounts to assuming that the bath thermalization time scales are much shorter than relevant system time scales. Thus, the bath does not retain memory of the system-bath interaction at previous times. Moreover, the derivation invokes that there are no initial correlations between system and bath and the phases of the bath degrees of

freedom can be described by a random-phase approximation. Finally, one arrives at the SSE in the Born-Markov limit [DCM92, GN99, ADV11, MMN<sup>+</sup>12]

$$i\partial_t\Psi_S(t) = H_S(t)\Psi_S(t) - \frac{i}{2}\sum_{\alpha} S_{\alpha}^{\dagger}S_{\alpha}\Psi_S(t) + \sum_{\alpha} l_{\alpha}(t)S_{\alpha}\Psi_S(t), \quad (5.4)$$

where  $l_{\alpha}(t)$  are stochastic processes with vanishing ensemble average and  $\delta$ -time-correlation

$$\overline{l_{\alpha}(t)} = 0, \quad \overline{l_{\alpha}(t)l_{\beta}(t')} = 0, \quad \overline{l_{\alpha}^{*}(t)l_{\beta}(t')} = \delta_{\alpha\beta}\delta(t-t'). \quad (5.5)$$

The bar denotes the statistical average over an ensemble of stochastic processes. For the sake of convenience, the coupling strength parameter  $\lambda$  has been absorbed in the bath operator  $S_{\alpha}$ . The first term of the SSE (5.4) determines the usual unitary system evolution under the action of the Hamiltonian  $H_S$ . Although the SSE employs the system Hilbert space only, the coupling to the bath is still included by the second term that describes dissipation effects due to the system-bath interaction. Finally, the third term introduces fluctuations in the time evolution: Although the dissipative term causes the probability density to decay in time, the norm of the state vector  $\Psi(t)$  averaged over a statistical ensemble of realizations is conserved up to fourth order in the system-bath coupling parameter  $\lambda$ . For the sake of a clear notation, in the following I use only a single bath operator  $S$  and, therefore, omit indices at the bath operator. A single bath operator is sufficient for the investigations of Sec. 5.3 as well.

As a result of the stochastic nature of Eq. (5.4) the system wave function can not be simulated by a single evolution of the SSE but needs to be represented by a statistical ensemble of wave functions  $\{\Psi_s(t)\}$ . Starting from a pure initial state, the time evolution of expectation values

$$\langle O_S \rangle = \overline{\langle \Psi(t) | O_S | \Psi(t) \rangle} \quad (5.6)$$

of physical observables  $O_S$  can be calculated from the statistical average over all ensemble members  $\{\Psi_s(t)\}$ . Yet, it is important to note that a reliable computation of smooth observables requires a large enough set of stochastic realizations.

Finally, I address one of the noteworthy differences of the SSE and Redfield and similar master-equation-type approaches. In the latter, positivity of the statistical operator may not be guaranteed in cases of stochastic Hamiltonians, TD Hamiltonians, or TD bath operators [FO05, DDV08, DDV09]. The SSE yields normalized ensemble-averaged wave functions with a positive weight for arbitrary TD operators, thus positivity is guaranteed in any case. This aspect is particularly important if one intends to use KS Hamiltonians and DFT approximations that depend on internal degrees of freedom of the system for each ensemble member separately, as this renders the Hamiltonian stochastic [DVD07, DDV08, DDV09]. Hence, the SSE is a solid starting point for a DFT theory of open quantum systems.

### 5.2.2 Stochastic Schrödinger equation and Kohn-Sham density functional theory

In this section, I begin with an introduction to the open quantum system SSE approach in the framework of TD current density functional theory (TDCDFT) of Refs. [DVD07, DDV08]. In contrast to standard TD(C)DFT, the open quantum system scheme uses ensemble-averaged quantities. Therefore, one introduces the ensemble-averaged particle density

$$\overline{n(\mathbf{r}, t)} = \langle \overline{n(\mathbf{r})} \rangle, \quad (5.7)$$

where the density operator is defined as

$$n(\mathbf{r}) = \sum_{i=1}^N \delta(\mathbf{r} - \mathbf{r}_i), \quad (5.8)$$

and the ensemble-averaged current density

$$\overline{\mathbf{j}(\mathbf{r}, t)} = \overline{\langle \mathbf{j}(\mathbf{r}, t) \rangle}, \quad (5.9)$$

where the current operator reads

$$\mathbf{j}(\mathbf{r}, t) = \frac{1}{2} \sum_{i=1}^N \{ \delta(\mathbf{r} - \mathbf{r}_i), \mathbf{p}_i + \mathbf{A}_{\text{ext}}(\mathbf{r}_i, t) \} \quad (5.10)$$

and  $\{.,.\}$  denotes the anticommutator bracket. The theorem of stochastic TDCDFT of Refs. [DVD07, DDV08] states that under reasonable physical conditions for a given and fixed bath operator  $S$ , many-particle interaction  $W$ , and initial state  $\Psi(t_0 = 0)$  a one-to-one correspondence between the external vector potential  $\mathbf{A}_{\text{ext}}(\mathbf{r}, t)$  and the ensemble-averaged current density  $\overline{\mathbf{j}(\mathbf{r}, t)}$  exists. The theorem paves the way for a non-interacting KS scheme of open quantum system TDCDFT as it guarantees the existence of a KS system that yields the same current density as the true interacting system. The KS Hamiltonian reads

$$H_{\text{KS}}(\{\mathbf{r}_k\}, t) = \sum_{i=1}^N \left[ \frac{[\mathbf{p}_i + \mathbf{A}_{\text{ext}}(\mathbf{r}_i, t) + \mathbf{A}_{\text{xc}}(\mathbf{r}_i, t)]^2}{2} + v_{\text{ext}}(\mathbf{r}_i, t) + v_{\text{H}}(\mathbf{r}_i, t) \right] \quad (5.11)$$

with the xc vector potential  $\mathbf{A}_{\text{xc}}(\mathbf{r}, t)$  and the Hartree potential  $v_{\text{H}}(\mathbf{r}, t)$ . The KS Slater determinant  $\Phi_{\text{KS}}(t)$  evolves according to the open system KS equation [DVD07]

$$i\partial_t \Phi_{\text{KS}}(t) = H_{\text{KS}} \Phi_{\text{KS}}(t) - \frac{i}{2} S^\dagger S \Phi_{\text{KS}}(t) + l(t) S \Phi_{\text{KS}}(t). \quad (5.12)$$

The xc vector potential in the open quantum system approach may in general depend on  $\overline{\mathbf{j}(\mathbf{r}, t)}$ , the initial states  $\Psi(t_0)$  and  $\Phi_{\text{KS}}(t_0)$ , and the bath operator  $S$ . For practical calculations, however, one needs to rely on existing approximations for the xc vector potential as the true  $\mathbf{A}_{\text{xc}}(\mathbf{r}, t)$ , especially in open quantum systems, is not known [DVD07].

The proof of the stochastic TDCDFT theorem is based on the reasoning of well-known proofs of TDDFT [RG84, vL99] and TDCDFT [Vig04] and discussed in detail in Refs. [DVD07, DDV08, ADV11]. Therefore, I do not reiterate the entire proof, but focus on some crucial aspects and comments. First, a notable difference between the closed and the open quantum system approach is that the usual continuity equation between the density and the current density does not hold in the open quantum system case. Due to the coupling to the external bath, additional terms appear in the equation of motion of ensemble-averaged expectation values [Fre90, DDV08]. The continuity equation of the ensemble-averaged density and current density reads

$$\partial_t \overline{n(\mathbf{r}, t)} = -\nabla \cdot \overline{\mathbf{j}(\mathbf{r}, t)} + \mathcal{F}_{\text{B}}(\mathbf{r}, t), \quad (5.13)$$

where the density modulation that is induced by the bath is described by

$$\mathcal{F}_{\text{B}}(\mathbf{r}, t) = \frac{1}{2} \overline{2S^\dagger n S - S^\dagger S n - n S^\dagger S}. \quad (5.14)$$

The proof of the above stated one-to-one correspondence requires implicitly that  $\mathcal{F}_B(\mathbf{r}, t)$  is a functional of  $\overline{n(\mathbf{r}, t)}$  and  $\overline{\mathbf{j}(\mathbf{r}, t)}$  alone and that Eq. (5.13) can be solved uniquely to determine  $\overline{n(\mathbf{r}, t)}$  [DDV08, DDV09, ADV11]. However, although there is a unique relation between the density and the current density, the proof guarantees only the one-to-one correspondence between  $\overline{\mathbf{j}(\mathbf{r}, t)}$  and the vector potential. Therefore, the ensemble-averaged density of the true and the non-interacting system are not necessarily equal.

Second, the effect of the scalar potential  $v_{\text{ext}}(\mathbf{r}, t)$  is not discussed explicitly in Refs. [DVD07, DDV08] as it can be eliminated by a gauge transformation at all times [Vig04]. In the context of a non-interacting representation of an interacting many-particle system the use of scalar potentials is accompanied by difficulties: Even if a given current density is  $v$ -representable in an interacting many-particle system, the current density is not necessarily  $v$ -representable in the non-interacting representation of the same system [DV05].

One important application of open quantum system schemes are quantum transport problems where one is interested in the spatial distribution of the current density to investigate charge flow. Yet, the investigation in the following approaches EET processes where no charge transfer occurs. Such investigations can be based on the density and its moments alone without explicit need for the current density. From a practical point of view, the number of available approximations for  $\mathbf{A}_{\text{xc}}(\mathbf{r}, t)$  is limited, whereas there are plenty of choices for approximations for the (TD)DFT xc potential. Also for numerical reasons a density-based approach is preferable. For applications that are based on the time evolution of the density it is of great interest to find an open quantum system approach in the framework of TDDFT.

Extensions of TDDFT to open quantum systems were already performed by Burke *et al.* [BCG05] and Yuen-Zhou *et al.* [YZTRRAG10] based on density matrices and master equations. Both strategies aim at the representation of the density of the interacting open quantum system by an auxiliary system with a different particle-particle interaction. To prove the validity of such approaches, one needs to find the corresponding external potential of the auxiliary KS system that produces the same density under given conditions. The proofs of Refs. [BCG05] and [YZTRRAG10] are based on the reasoning of Refs. [RG84, vL99, Vig04] and rely on assumptions about the action of the bath operator. Yet, to the best of my understanding, details about the consequences of these assumptions, in particular with regard to practical calculations and choices of the bath operator, are open questions in the field, and the use of approximate KS Hamiltonians in master equations is debated. Moreover, a conclusive extension of the proof of stochastic TDCDFT that abandons the ensemble-averaged current density and establishes an open quantum system TDDFT scheme based on the ensemble-averaged density alone is not available yet.

### 5.2.3 A single-particle approach in practice

Practical applications of stochastic TDDFT so far rely on approximate realizations of the stochastic formalism in KS TDDFT. In the approach of Refs. [ADV09, ADV11], a heuristic bath operator [PDV08] is used that applies to single TD KS orbitals and allows for a single-particle KS approach to the open quantum system problem. In collaboration with Massimiliano Di Ventra and Heiko Appel, I applied a stochastic TDDFT scheme according to this rationale. The following investigations are based on the stochastic single-particle KS equations

$$i\partial_t\varphi_i(\mathbf{r}, t) = h_{\text{KS}}(\mathbf{r}, t)\varphi_i(\mathbf{r}, t) - \frac{i}{2}s_i^\dagger s_i\varphi_i(\mathbf{r}, t) + l(t)s_i\varphi_i(\mathbf{r}, t), \quad (5.15)$$

the usual non-interacting single-particle KS Hamiltonian of Eq. (2.12), and specific single-particle bath operators  $s_i$  [ADV09, ADV11]. In the following, xc effects are approximated by the LDA. The heuristic bath operator of the investigations presented below is introduced and motivated in Sec. 5.3.2. Beyond that, I also investigated the theoretical justification of this approach. More background about these investigations is presented in Appendix D.3.1.

The open quantum system simulations were carried out using the quantum-jump algorithm [DCM92, GPZ92, BP95, BP06] that has been introduced in the context of open quantum system KS equations in Ref. [ADV11]. The algorithm is implemented in a customized version of the PARSEC program package. Details on the bath operator implementation are gathered in Appendix D.3.2. The quantum-jump algorithm relies on a piecewise deterministic evolution of the norm-preserving single-particle equations

$$i\partial_t\varphi_i(\mathbf{r},t) = h_{\text{KS}}(\mathbf{r},t)\varphi_i(\mathbf{r},t) - \frac{i}{2}s_i^\dagger s_i\varphi_i(\mathbf{r},t) + \frac{i}{2}|s_i\varphi_i(\mathbf{r},t)|^2\varphi_i(\mathbf{r},t) \quad (5.16)$$

that are interrupted by quantum jumps. These jumps occur in the entire system and represent the non-deterministic action of the bath. The points of time where such a jump occurs are determined by a random process according to a waiting-time distribution. However, as in general this waiting-time distribution is not known beforehand, it needs to be determined alongside the actual propagation of Eq. (5.16) (for details, see Ref. [ADV11]): The waiting-time distribution can be determined from the decay of the norm

$$\eta(t) = \frac{1}{N} \sum_{i=1}^N \int |\varphi_i^{\text{aux}}(\mathbf{r},t)|^2 d^3r \quad (5.17)$$

of an auxiliary system of  $N$  particles in contact with the single-particle bath operators  $s_i$  starting from the same ground state and boost excitation as the original system and evolving according to

$$i\partial_t\varphi_i^{\text{aux}}(\mathbf{r},t) = h_{\text{KS}}(\mathbf{r},t)\varphi_i^{\text{aux}}(\mathbf{r},t) - \frac{i}{2}s_i^\dagger s_i\varphi_i^{\text{aux}}(\mathbf{r},t). \quad (5.18)$$

In this system, norm conservation is not build in explicitly. One obtains single waiting times that represent quantum-jump times by drawing random numbers in the interval  $[0,1]$  and choosing the time  $T$  when  $\eta(T)$  drops below this number. The waiting-time distribution follows from many samples of such single quantum-jump times. Each of these processes yields one KS orbital set  $\{\varphi_{i,s}(t)\}$  that is one member of the statistical ensemble of KS orbital sets. Physical observables are calculated from the statistical average over all ensemble members.

## 5.3 Pathways and time constants of excitation-energy transfer

### 5.3.1 The excitation-energy transfer model system

In the following, I use the stochastic open quantum system formalism introduced in the previous section with a heuristic bath operator for practical applications in the area of EET with the objective of studying EET in a supermolecular arrangement of molecules: I study a model system of circularly arranged molecules that is designed in analogy to circular LH complexes of the antenna system of LH organisms (see Fig. 5.2). The aim is to investigate the influence of electronic-structure properties on EET time scales and pathways in such

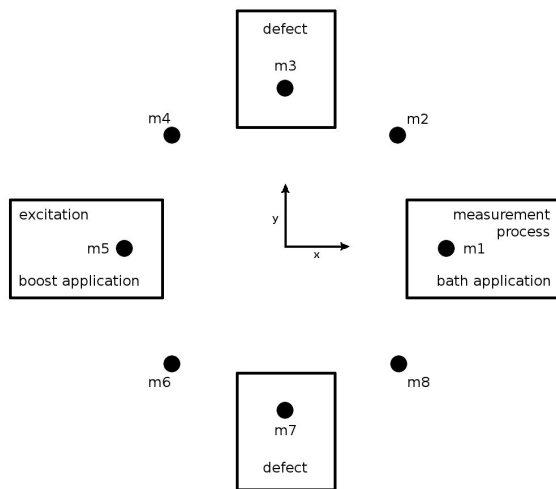


Figure 5.2: Circular arrangement of eight molecules  $m_1, m_2, \dots, m_8$  with equal intermolecular distance. In principle, the molecules may be chosen arbitrarily, but for the sake of clarity, I use  $\text{Na}_2$  as a model system. The excitation of the entire ring setup is performed via boost application at molecule  $m_5$ . I measure the excitation spread in this arrangement by application of a dissipative bath operator that serves as a measurement process at molecule  $m_1$ . For a transparent investigation of the influence of the intermolecular coupling and the energetic alignment of the molecules on energy-transfer pathways, I introduce defects in the molecules  $m_3$  and  $m_7$ . All other molecules are fixed according to their GS geometry.

supermolecules, especially the influence of the coupling and the energetic alignment. With this in mind, the physical picture behind these calculations is the following: One molecule of the complex gets excited via light absorption. Then, the excitation travels in the system due to the electronic interaction between the molecules. As a result the excitation spreads over the entire complex and I intend to measure the time scale of this excitation spread.

In a circular arrangement of molecules, there are at least three time scales relevant for the signal observed on the ring: the time scale related to the energy of the excited states, the time scale due to intermolecular coupling (here, more time scales are involved if the system is partly or in total off-resonant), and the time scale due to dissipative bath action. The latter process is needed to break the coherent evolution of the system (see Sec. 5.3.3 for an illustration). To allow for the investigation of the influence of electronic-structure properties on the excitation-energy spread, its time scale needs to be chosen such that it does not interfere with the EET time scale that is determined by the coupling mechanism and coupling strength. In this sense, the bath mechanism that I introduce in the next section plays the role of a measurement process.

In the basic model setup consisting of eight molecules as indicated in Fig. 5.2, all molecules in the circular arrangement and all intermolecular distances are equal. The actual study uses the  $\text{Na}_2$  model system, but the considerations in the following are not restricted to dimers and can be applied to more general systems. All sodium dimers are aligned along the  $z$ -axis and placed according to the setup of Fig. 5.2. Their centers of mass are in the  $x$ - $y$ -plane. Initially, starting from the ground state of the setup I introduce an excitation at one of the molecules. To be explicit in the assignment, I chose molecule  $m_5$ . I simulate the excitation due to light absorption by a momentum boost oriented along the  $z$ -axis. In the  $\text{Na}_2$  case, this dominantly amounts to an excitation at 2.1 eV. In practical calculations, the boost is applied only in one section of the real-space grid, so that only molecule  $m_5$  gets excited (see Appendix D.1.3 for details about the implementation). Defects in terms of variations of the electronic structure can be introduced easily by  $\text{Na}_2$  bond-length variation. To

guarantee unambiguousness and transparency of the investigations in the following sections, I modify only molecules m3 and m7, and fix all other system components. The relevant coupling parameters of Na<sub>2</sub> are discussed in detail in Sec. 5.1.

### 5.3.2 Practical simulation approach

The bath operator is supposed to act as an effective measurement process that allows to measure the time an initial excitation travels within the ring system. In the setup of Fig. 5.2, it operates on molecule m1 on the opposite side of the initial excitation to measure the time scale the excitation needs to travel halfway through the ring. The measurement process is supposed to model deexcitation, thus remove the entire excitation energy out of the system when the initial excitation has reached molecule m1. In contrast to true molecules where the excitation moves due to relaxation to lower lying energy levels, here the measurement processes immediately brings the supermolecule back to its ground state. The bath operator needs to model an incoherent mechanism without back transfer from the bath to the system. I assume that the bath is sensitive to dipolar excitation and couples to the dipole moment of molecule m1. For these reasons, the bath operator has the following structure

$$s_i = \sqrt{\gamma} \frac{|\mathbf{d}_1(t) - \mathbf{d}_1(t_0)|}{D} |\varphi_i(t_0)\rangle \langle \varphi_i(t)| \quad (5.19)$$

with three specific contributions. The first factor  $\sqrt{\gamma}$  is a free parameter that includes the effective decay rate  $\gamma$ . The second factor is sensitive to local changes of the dipole moment  $|\mathbf{d}_1(t) - \mathbf{d}_1(t_0)|$  of molecule m1. Here, the index denotes molecule m1 and indicates that the dipole moment is calculated only in the section of the grid that corresponds to m1. This factor ensures that the bath couples only to dipolar excitations and it renders the bath operator sensitive to the dipolar excitation that has reached molecule m1.  $D$  denotes a normalization factor of the dipole moment variations and needs to be chosen reasonably as discussed below. The third factor is a projector that takes the TD KS orbitals and projects the latter back onto their corresponding GS orbital. Details about the implementation of this bath operator and examples of alternative heuristic bath operators are assembled in Appendix D.3.2.

Having chosen one specific definition for the bath operator, I first assess its functionality, i.e., I adjust the normalization factor  $D$  and investigate its performance on a single Na<sub>2</sub>. The aim of this investigation is to find  $D$  such that the functionality of the scaling factors  $\sqrt{\gamma}$  and  $(|\mathbf{d}_1(t) - \mathbf{d}_1(t_0)|)/D$  in front of the projector is clearly split into two contributions:  $D$  needs to be determined such that the decay time  $\tau$  of the relaxation process is determined only by the decay rate  $\gamma$ , thus  $\tau = 1/\gamma$ . The dipole dependent scaling factor is intended to guarantee for the coupling to the dipole moment of molecule m1 and should not interfere with the role of  $\gamma$ . Therefore, the normalization factor needs to be adapted to the dipole oscillations of the isolated model molecule m1, i.e., of one isolated Na<sub>2</sub>.

In the procedure for the determination of  $D$ , I calculated 100 fs of the dipole moment time evolution of a single Na<sub>2</sub> in a closed quantum system after an initial momentum boost that was applied along the bond axis of the dimer. Here, only the dipole moment along this axis gets excited by the boost and the investigation can be restricted to this dipole moment component. There are various different options to determine the normalization based on the existing dipole moment data:  $D$  may be chosen to be the first maximum, the average over

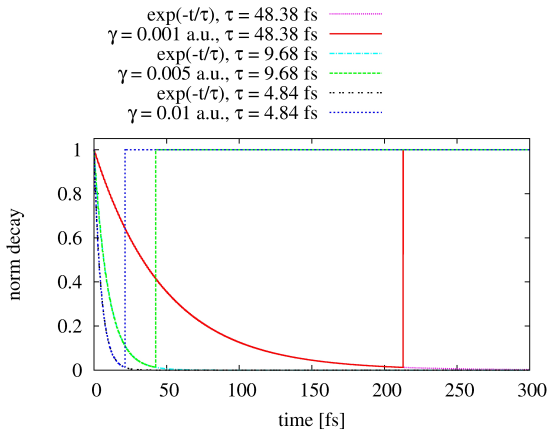


Figure 5.3: Norm decay  $\eta(t)$  (see Eq. (5.17)) of a single model molecule. The damping is performed with different decay-time constants  $\tau$  after an initial boost excitation with 0.001 eV excitation energy. The norm decay always follows an exponential function  $\exp(-t/\tau)$  with the preset time  $\tau$ . Here, quantum jumps were performed as the norm dropped below 0.014 %. They manifest in vertical lines where the norm jumps back to one and stays for the rest of the time evolution as application of the bath operator does not change the ground state.

all maxima, the absolute average, and the absolute square average of the dipole moment. I found by numerical tests that only normalization according to the average of the absolute square of the dipole moment gives an exponential decay with time constant  $\tau$  that I aimed at by setting the decay rate. This observation is robust with regard to different decay-time constants as Fig. 5.3 shows. All computed decay times are in accordance with the preset decay rate.

Another influencing factor on the determination of  $D$  is the energy that one introduces to the system by the boost excitation. I interpret the excitation procedure as a single absorption process of one energy portion. The dissipation of such an energy portion due to the measurement process should be independent of the boost strength as long as the boost strength corresponds to a single excitation process. Therefore, in the single excitation case, the normalization factor needs to be adapted to the boost strength. I guarantee for the boost strength adaptation by always determining  $D$  from a closed quantum system calculation with the same initial boost excitation as in the open quantum system calculation that I aim at. In the following, a boost with 0.001 eV excitation energy is used consistently. The thus obtained normalization factor yields a decay time that is independent of the boost strength.

The excitation process could likewise be performed by application of an external laser field. In this case, an instantaneous excitation could be simulated by a short pulse and the determination of the normalization factor should then be performed using the dipole signal after the pulse excitation.

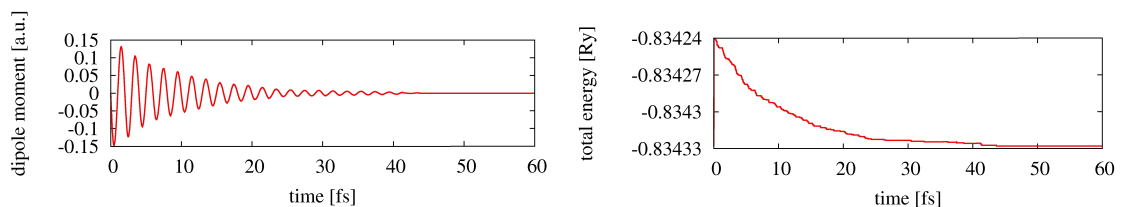


Figure 5.4: Left, ensemble-averaged dipole moment ( $z$ -component) and, right, total energy of a single molecule in contact with a dissipative bath that induces a decay time of 10 fs. Both figures are calculated from an ensemble of 200 members.

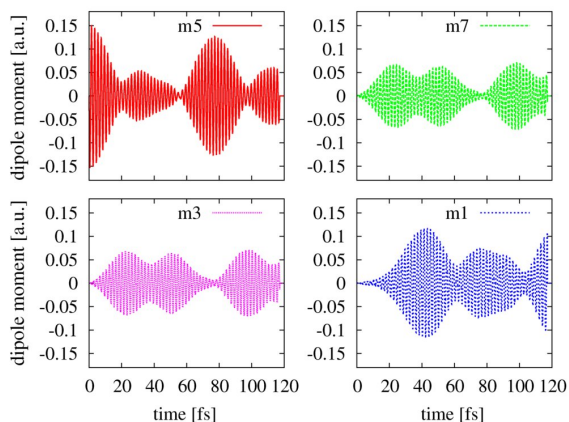


Figure 5.5: Time evolution of the dipole moment ( $z$ -component) of four molecules of a circular setup of eight equal sodium dimers according to Fig. 5.2. The intermolecular distance is 20 bohr. Here, an initial boost excitation was applied at  $t = 0$  in the subsystem m5 and no dissipative mechanism acts within the entire system. The oscillation pattern emerges due to interference of the dipolar excitation that is traveling in the ring system along both directions.

Having discussed the norm decay in detail, I finally provide some insight into how the bath operator works by investigating some relevant observables. The exponential decay of the norm translates into an exponential decay of the total energy and the envelope of the dipole moment oscillation (see Fig. 5.4). Thus, the bath operator fulfills all desired criteria and is ready for application in more complex molecular systems.

### 5.3.3 Resonant excitation spread and decay time constants

As a first step towards the investigation of EET in circular supermolecules, I study the perfectly resonant coupling situation where all molecules are the same. I use the setup of Fig. 5.2 with an intermolecular distance of 20 bohr and perform the boost excitation at molecule m5 as explained in Sec. 5.3.1. I start with the fully coherent case without system-bath coupling. The time evolution of the dipole moment of four molecules of this ring configuration is depicted in Fig. 5.5. One observes a fast oscillation of the dipole moment that corresponds to the lowest excitation energy of the model system at 2.1 eV while the envelope follows an interference pattern: At different points of time the largest dipole moment amplitude can be observed at different subsystems. This interference pattern emerges as the dipolar excitation travels in the ring system along both directions. It is governed by the intermolecular coupling strength, i.e., the time an excitation needs to be transferred between neighboring molecules. In the model system at a separation of 20 bohr, the coupling strength is 0.038 eV (see Pub1). Thus, if two of those model molecules were isolated, one would observe a resonance oscillation with a cycle duration of 107.8 fs where the maximum amplitude of the dipole oscillation can be observed on one of the two neighbors after each quarter of one period. In the circular setup, however, every molecule has neighbors on both sides, thus providing a pathway for excitation-energy spread.

I now add the bath mechanism of Sec. 5.3.2 acting on molecule m1. To measure the EET time, the bath needs to break the interference of the so-far fully coherent energy spread, thus it needs to operate on a comparably short time scale. Here, it acts with a decay time of 5 fs. This choice is motivated further in the following. I depict in Fig. 5.6 the time evolution of the dipole moment of four molecules like in Fig. 5.5. Due to the bath mechanism, one further time scale comes into play and one observes clearly how the oscillation of the dipole moment decays in all subsystems of the ring due to the dissipative process. The coupling to the bath breaks the coherent evolution and causes relaxation of the system back to its ground state.

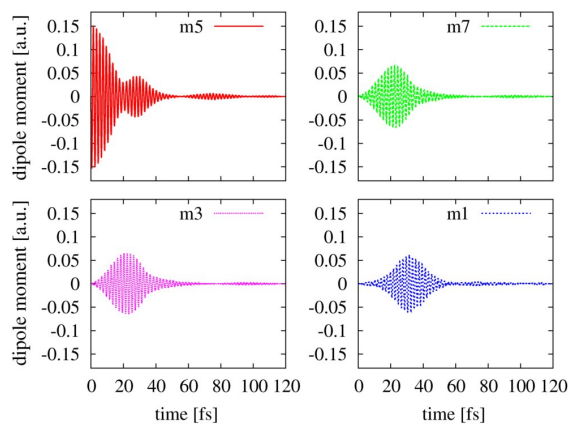


Figure 5.6: Ensemble-averaged dipole moment ( $z$ -component) time evolution of four molecules of the same circular setup as in Fig. 5.5. After an initial boost excitation at molecule  $m5$ , the excitation travels in the ring and decays due to a dissipative bath that is acting with a decay time of 5 fs on molecule  $m1$ .

To be able to measure the traveling time of an excitation in the circular setup, the decay time needs to be chosen short enough to sample the initial stage of the coherent EET before the interference pattern starts to build up. In the example of Fig. 5.6 the decay time of 5 fs fulfills this criterion: The dipole oscillation at molecule  $m1$  reaches only one maximum and subsequently decays to the ground state, thus no noticeable interference emerges.

I measure the time that the excitation needs to travel from molecule  $m5$  to molecule  $m1$  in terms of the lifetime of the excitation on the ring before relaxation occurs. To this end, I monitor the decay of the norm  $\eta(T)$  of the auxiliary system and take the quantum-jump times  $T$  when  $\eta(T)$  drops below preset thresholds. For the present setup and bath operator, a single simulation of the auxiliary system with a late quantum jump is sufficient because for each of the ensemble members the time evolution consists of two unique parts: a deterministic time evolution until the quantum jump occurs and a trivial time evolution after the system has jumped back to the ground state (for more details, see Appendix D.3.2). However, due to the interference along the excitation spread, monitoring just a single threshold of this norm decay may be dominated by interference effects, thus its meaningfulness may be compromised. Therefore, I considered the norm decay down to three different thresholds: 0.100, 0.050, and 0.012. The quantum-jump times  $T$  for the perfectly resonant situation are listed in Table 5.1. They serve as a good starting point for investigating the influence of electronic-structure properties on the time an excitation needs to spread in the circular arrangement of sodium dimers with an intermolecular distance of 20 bohr.

### 5.3.4 Influence of energetic off-resonance

Having examined the resonant excitation-energy spread, I now assess the influence of energetic off-resonance on the EET time scales by introducing defects in the ring setup. Such defects can be inserted via bond-length variations and/or removing one of the molecules. I compare in Table 5.1 the quantum-jump times  $T$  to the fully resonant situation of the previous section. I found that small changes of the bond length of -0.1 bohr in molecule  $m3$  or in both molecules  $m3$  and  $m7$  result only in a minor increase of the time scale set by the resonant case. Larger increases of the quantum-jump time  $T$  can be observed in cases where in one of the molecules the bond length is changed by -0.5 bohr. Note, that already in this data set the influence of interference effects on the quantum-jump times can be observed: While the times corresponding to the decay down to  $\eta = 0.100$  and  $\eta = 0.012$

m3	m7	$\eta = 0.100$	$\eta = 0.050$	$\eta = 0.012$
0.0 bohr	0.0 bohr	52 fs	75 fs	117 fs
-0.1 bohr	0.0 bohr	56 fs	110 fs	121 fs
-0.5 bohr	0.0 bohr	84 fs	97 fs	143 fs
-0.1 bohr	-0.1 bohr	57 fs	112 fs	123 fs
-0.1 bohr	-0.5 bohr	85 fs	97 fs	157 fs
-0.5 bohr	-0.5 bohr	166 fs	181 fs	211 fs
removed	0.0 bohr	80 fs	89 fs	125 fs
removed	-0.1 bohr	99 fs	125 fs	147 fs
removed	-0.5 bohr	205 fs	227 fs	265 fs

Table 5.1: Quantum-jump times  $T$  where the norm  $\eta(T)$  of the decaying auxiliary system drops below 0.100, 0.050, and 0.012. The calculations are performed in a circular setup of model molecules (see Fig. 5.2) with an intermolecular distance of 20 bohr. I modified the electronic structure by systematically introducing defects in the molecules m3 and m7 in terms of bond-length variation and/or removing one of the molecules. These modifications are indicated in the first two columns of the table. A bond-length reduction of 0.1 bohr (0.5 bohr) of one Na<sub>2</sub> amounts to an energetic detuning of the excitation energy of 0.049 eV (0.135 eV) and a reduction of the coupling-matrix element of 0.006 eV (0.012 eV).

give a clear picture, quantum-jump times at  $\eta = 0.050$  may exhibit a different behavior. Yet, one observes a clear rise of the transfer time as soon as the more severe defect of -0.5 bohr bond-length variation is introduced in both pathways between the initially excited molecule and the molecule where the measurement process works: All quantum-jump times increase by about a factor of two.

As an alternative defect, I investigated a setup where molecule m3 is removed from the ring. In this case, the coupling between molecules m2 and m4 is smaller by about a factor of one-eighth than the previous coupling strength between m3 and its neighbors because of the almost dipolar coupling in this distance regime. In this situation, as long as all other molecules are perfectly resonant, the quantum-jump times increase by about the same amount as they did due to less severe defects in molecule m3. Yet, introducing further defects in molecules m7, the energy-transfer process slows down notably as one observes the longest quantum-jump times in case of removed molecule m3 and bond-length variation of -0.5 bohr in molecule m7.

In conclusion, I found that in cases of resonance or close to resonance the EET time scale is not affected much by variations of the coupling strength and interference effects play a role for quantum-jump times corresponding to specific setups. However, as soon as sizable defects occur in both pathways of EET, the time scales determined by the measurement process notably increase. As a result EET is substantially hindered.

### 5.3.5 Influence of the intrasystem coupling

In the final investigation of this section, I examined the influence of the intermolecular electronic coupling mechanism on the quantum-jump time, especially the difference between full electronic coupling and the dipole-dipole coupling of Förster theory. In order to observe noticeable differences between Förster-type and full coupling, I chose an intermolec-

coupling	m3	$\eta = 0.100$	$\eta = 0.050$	$\eta = 0.012$
full	0.0 bohr	95 fs	116 fs	163 fs
Förster	0.0 bohr	86 fs	104 fs	152 fs
full	-0.1 bohr	99 fs	140 fs	182 fs
Förster	-0.1 bohr	94 fs	108 fs	154 fs
full	-0.5 bohr	109 fs	140 fs	209 fs
Förster	-0.5 bohr	89 fs	115 fs	185 fs

Table 5.2: Investigation of the quantum-jump times  $T$  in analogy to Table 5.1. Here, the molecules are arranged at a distance of 12 bohr. Thus, notable differences of the coupling strength exist between the cases of full electronic coupling and Förster-type dipole-dipole coupling. Moreover, defects in terms of bond-length variations are introduced in molecule m3 as indicated in the second column.

ular distance regime where such differences occur. For the  $\text{Na}_2$  model system, Pub1 has demonstrated that significant deviations from the dipole-dipole coupling can be observed for distances below 20 bohr where the dipole-dipole coupling approximation overestimates the true coupling strength. Therefore, I switched to a circular setup of 12 bohr distance between the molecules to guarantee for a clear analysis of the influence of the coupling behavior. I decided to keep the dissipation time constant of 5 fs of the previous calculations although for 12 bohr intermolecular distance the coupling-matrix element of 0.105 eV is notably larger than in the previous case (see Pub1). The results are compiled in Table 5.2.

One observes that Förster-type coupling overestimates the quantum-jump times of the measurement process in comparison to the true electronic coupling, thus it overestimates EET in the present setup. This finding parallels the fact that also the coupling-matrix element is overestimated by the dipole-dipole coupling (see Pub1). This result is consistently confirmed also in situations where defects are introduced in the circular arrangement. Finally, I note that the quantum-jump times observed for an intermolecular distance of 12 bohr are smaller than the numbers for 20 bohr, although in the latter case the coupling is notably weaker. This is a result of interference effects that are more pronounced in cases of stronger coupling. Therefore, it is difficult to compare absolute time scales unless the dissipation time constant of the measurement process is chosen short enough to prevent a build-up of interference due to excitation-energy spread along different available pathways.

## 5.4 Summary and Outlook

In summary, TDDFT in combination with the open quantum system framework is an attractive tool for studying excitation-energy transfer phenomena. Here, the heuristic bath operator that I introduced and implemented using a system of stochastic single-particle KS equations served as a measurement process for investigating the excitation-energy spread in a circular arrangement of molecules in the spirit of LH complexes. I demonstrated that indeed the dissipative mechanism breaks the interference pattern of coherent EET that is inherent to standard closed quantum system TDDFT and removes excitation energy from the system. The time scale of this relaxation is determined by the intermolecular coupling and the dissipation time constant. In this context, the strength of TDDFT is to yield a

comparably reliable description of the electronic structure of the entire complex and its subsystems on the level of available xc functional approximations. This together with the open quantum system framework provides a tool for studying the influence of electronic structure properties and intermolecular coupling mechanisms on EET processes. The results that are presented above demonstrate that small deviations of the electronic structure, for example via bond-length variation, cause only minor changes of the time scale monitored by the measurement process. Only when all EET pathways of the circular setup suffer from sizable defects, the EET time drops notably. Similarly, variations of the coupling mechanism, as for example via Förster-type dipole-dipole coupling, change the EET times in line with the changes of the coupling strength.

In future work, this and related open quantum system schemes in the TD(C)DFT framework should be assessed both from a theoretical and a practical perspective. On the conceptual side, there are still a number of open questions concerning open quantum system TD(C)DFT. First, a conclusive proof of the validity of the stochastic TDDFT framework using single-particle KS equations that applies to a broad range of bath mechanisms remains a topic for future investigations. Second, assumptions of the existing proofs on the range of bath operators need to be examined and the validity and range of applicability of approximate schemes needs to be assessed. Third, actual simulations using stochastic TDDFT rely on standard xc approximations although in the open quantum system framework the xc (vector) potential may in general also depend on the choice of the bath operator in addition to the dependencies that it already exhibits in standard TD(C)DFT. Therefore, the assessment of the range of applicability of standard functional approximations should be complemented by research towards functional approximations that are tailored to the open quantum system context. On the application side, simulations of more realistic systems using the existing and newly developed schemes should be performed to demonstrate the practical value of the open quantum system TDDFT scheme. In particular, the presented framework may be a powerful tool for unraveling the role of electronic structure properties and true quantum mechanical effects in LH systems beyond the description with standard rate equations.

# Appendix



## Appendix A

# Polarizability and static charge-transfer properties

The first appendix of this thesis includes a compilation of yet unpublished results and findings supplementing the previous work. I start in Sec. A.1 with results on model hydrogen chains and investigate differences that occur in longitudinal polarizabilities when SIC is performed via different methods. Such observations can be explained and understood if one analyzes the shape of the xc potential when external fields are applied. Analysis of the contributions to the xc potentials in approximations of the (G)OEP reveals differences in the way the KLI and SLA approximations on the one hand, and the generalized methods GKLI and GSLA on the other hand treat the so-called response part of the xc potential. Therefore, this transparent system allows to address the question about the quality of the (G)KLI and (G)SLA approximations compared to the full (G)OEP. In Sec. A.2, I perform a similar polarizability investigation with a realistic test system, the polyacetylene chains, complementing the results of Pub4. The compilation of additional results and findings closes in Sec. A.3 with an observation made in the CT model system of Man1, namely a discontinuous variation of the total energy in GSIC where the LSDA total energy varies continuously. Throughout this appendix, complex-valued energy minimizing transformations are used. For the notation in the figures and tables, I use only the shortcuts of implementation methods because they are all applied to the SIC functional. For instance, instead of “KLI-SIC” I write just “KLI”.

### A.1 Polarizability and field-counteracting potentials in self-interaction free density functional theory

For a transparent and conclusive investigation of the influence of xc potential approximations on polarizabilities and the shape of the xc potential [CMVA95, vGSG<sup>+</sup>99, GvGSB00, MSWY03, KKP04, KK06, PSB08, RPC<sup>+</sup>08, KMK08, AKK08, CK09, KK11], I chose hydrogen chains as a model system that allows for a clear-cut analysis. Here, the hydrogen chains are set up from H atoms with alternating H-distances of 2 bohr and 3 bohr.<sup>1</sup>

I provide in Table A.1 longitudinal polarizabilities of a set of hydrogen chains along the chain’s backbone calculated from the change of the dipole moment when an external field

---

<sup>1</sup>I used a hydrogen LDA pseudopotential with core cut-off radius  $r_c(\text{H}) = 1.39$  bohr. The grid spacing was 0.25 bohr.

	LDA	KLI	GKLI	GOEP	SLA	GSLA	FOBO	CC	MP4
H <sub>4</sub>	38	20	34	33	20	36	34	29	29
H <sub>6</sub>	73	62	64	62	65	68	65	51	52
H <sub>8</sub>	116	99	99	93	103	107	100	74	76
H <sub>10</sub>	165	152	136	132	174	150	138	99	101
H <sub>12</sub>	217	196	175	170	243	196	178	124	127

Table A.1: Polarizability in atomic units of H chains with alternating H-distance of 2 bohr and 3 bohr. In the first part of the table, I show LDA and (G)SIC results where the methods behind the latter are ordered according to increasing sophistication. In the second part of the table, I compiled results from the Slater approximation and calculations based on Foster-Boys orbitals. The final part shows reference values: CCSD(T) (CC) polarizabilities are obtained from Ref. [CK09] and MP4 results from Ref. [PSB08].<sup>2</sup>

is applied [KKP04, KK06]. I compare these results to Coupled-Cluster (singles, doubles, and perturbative triples, CCSD(T)) and Møller-Plesset perturbation theory of fourth order (MP4) reference values. These benchmarks are very close in the case of hydrogen chains, thus provide a solid basis for comparison. At first sight, one clearly observes the well-known polarizability overestimation of LDA. However, in the hydrogen chains presented here, full OEP-SIC is known to perform well and yield polarizabilities close to the CCSD(T) benchmark [KKM08, KMK08, KK11] (not shown here). This remarkable performance disappears if one uses the KLI or SLA approximation and SLA-SIC is even worse than LDA in the long-chain case. Part of the OEP-SIC performance however can be recovered by the GSIC approaches [KKM08, KK11]. Yet, in the hydrogen chains, GOEP-SIC is not as close to CCSD(T) results as full OEP-SIC [KK11]. The calculations show beyond the results of Ref. [KK11] that GKLI-SIC polarizabilities are comparably close to GOEP-SIC, while GSLA-SIC results although being notably better than bare SLA-SIC are further of. FOBO localization gives polarizabilities close to complex energy-minimizing GKLI-SIC that are at the maximum 1.8 % larger, as far as the data presented here is concerned. Moreover, if one computes the polarizabilities per H<sub>2</sub> repeat unit, the deviation between GOEP-SIC, GKLI-SIC, and FOBO-SIC remains almost the same, whereas the distance to GSLA-SIC polarizabilities increases with increasing chain length.

So-far, it is obvious that GSIC calculations in general improve upon LDA, but GSLA-SIC is not perfectly in line with the findings of GOEP-SIC, GKLI-SIC, and FOBO-SIC. Analysis of the shape of the xc potential and its behavior when an external field is applied gives more insight into the performance of the different SIC approximations. Here, the findings are exemplified with the H<sub>8</sub> chain. To this end, I investigated the change of the xc potential when an external field  $F$  of field strength 0.005 Ry/bohr is applied to the ground-state  $v_{xc}$  along the chain's backbone in  $x$ -direction. The GOEP, that gives results closest to the CCSD(T) polarizabilities, shows a pronounced field-counteracting behavior (see Fig. A.1 (a)), that is decisive for a proper description of the response [vGSG<sup>+</sup>99, GvGSB00, KKP04, KMK08]. LDA however misses the field-counteracting trend completely. An interesting observation can be made in the KLI-SIC and SLA-SIC response to the external field in Fig. A.1 (b). Both potentials do not follow the response pattern observed in GOEP-SIC but show a rather

<sup>2</sup>Benoît Champagne kindly provided a list of hydrogen chain CCSD(T) and MP4 polarizabilities.

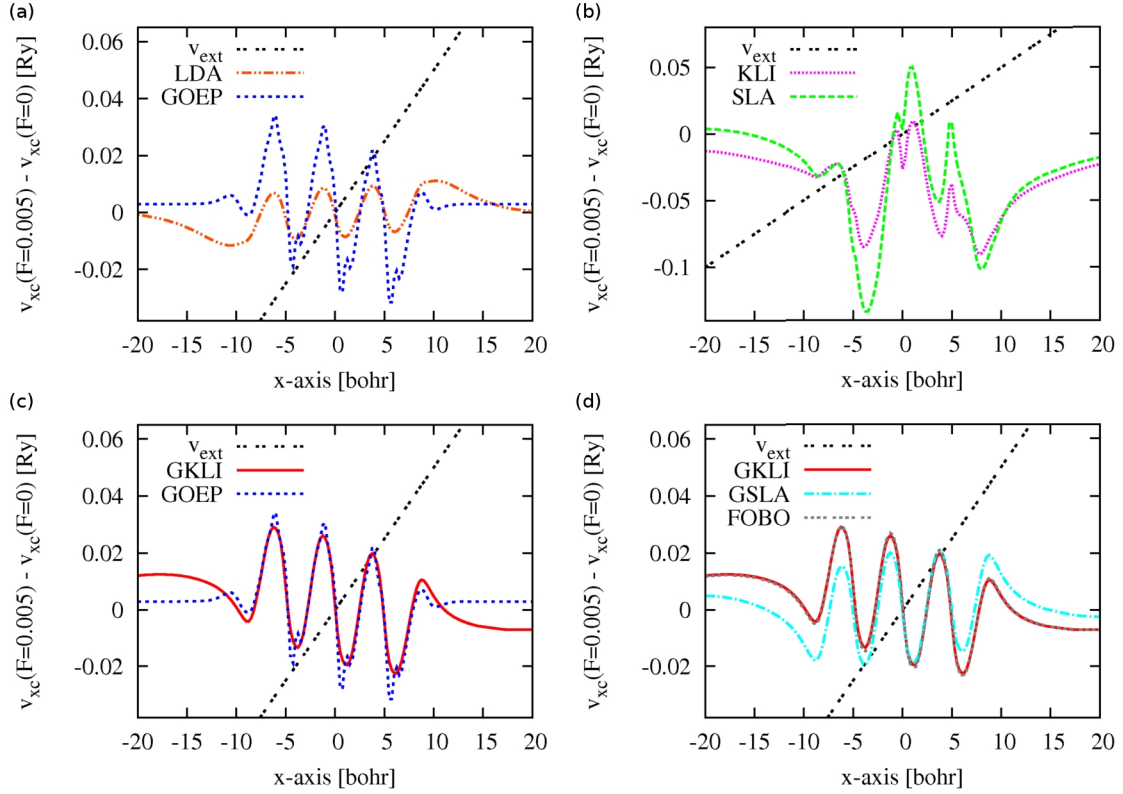


Figure A.1: Each of the panels shows the change of the xc potential  $v_{xc}(F) - v_{xc}(0)$  when an external field with field strength  $F = 0.005$  Ry/bohr is applied compared to the ground state with  $F = 0$  Ry/bohr. I depict LDA and GOEP-SIC in part (a), KLI-SIC and SLA-SIC in part (b), GKLI-SIC and GOEP-SIC in part (c), and GKLI-SIC, GSIA-SIC, and FOBO-SIC in part (d). The external potential is given throughout. FOBO-SIC and GKLI-SIC are almost identical in part (d). Note that the calculations were performed spin-dependently, but I show only one of the spin channels of the xc potential as both spin channels are identical in  $H_8$ .

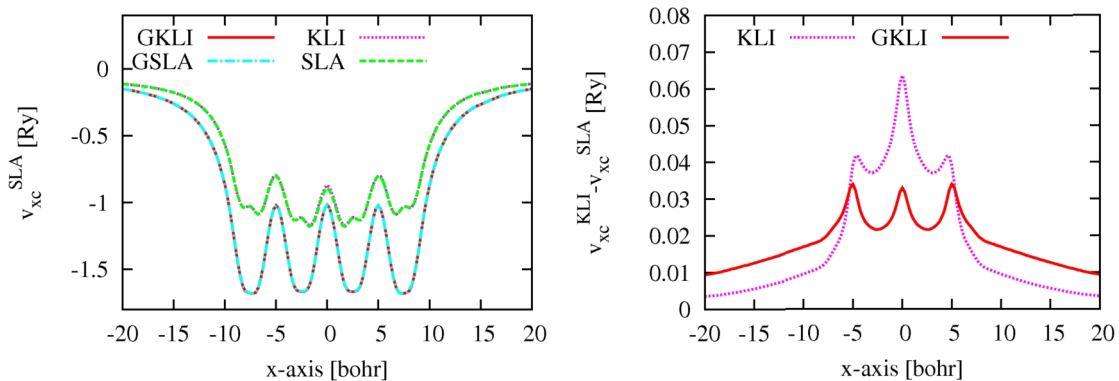


Figure A.2: Left panel: Slater contribution to the xc potential of GS  $H_8$  without external field in self-consistent KLI-SIC, SLA-SIC, GCLI-SIC, and GSIA-SIC calculations. The Slater contribution is almost the same in the cases of KLI-SIC and SLA-SIC as well as in the cases of GCLI-SIC and GSIA-SIC. Right panel: Corresponding response contributions  $v_{xc}^{KLI}(x) - v_{xc}^{SLA}(x)$  to the KLI-SIC and GCLI-SIC potential. The shape of the response potential differs notably between the standard and the generalized KLI approximation.

distorted response structure. Here, a clear statement about the field-counteracting behavior is difficult. I understand this finding as a consequence of the SIC functional suffering from unitary variance problems and the KLI-SIC and SLA-SIC potentials neither being functional derivatives nor being unitary invariant themselves (for more details, see the discussion and references in Pub3 and Sec. 3.3.1).

The field-counteracting behavior however is recovered in the GCLI-SIC approach. Fig. A.1 (c) clearly shows that the GCLI-SIC potential models the GOEP-SIC behavior reasonably in the central region but is less favorable in the near asymptotics. Such differences obviously cause the deviations of the polarizabilities observed in Table A.1. As far as the xc potential response is concerned, FOBO localization is a good approximation to the energy-minimizing GCLI-SIC and exhibits only small deviations from the GCLI-SIC behavior (see Fig. A.1 (d)). However, the interpretation of the GSIA-SIC response is not obvious: If one draws a line through the peaks of the GSIA-SIC response coming from the negative side, one finds for the first three peaks a slope in accordance with the external potential followed by a field-counteracting behavior at the end of the chain. Note that the field-counteracting contribution of the standard KLI potential is typically attributed to the so-called response part of  $v_{xc}$ , i.e., the difference between full KLI and its SLA contribution.

However, this assignment does not hold in the same way in the GSIC approaches as the total GSIA-SIC response exhibits a field-counteracting behavior in parts. Therefore, I isolated the Slater contribution to the KLI-SIC and GCLI-SIC potentials and investigated occurring differences as depicted in the left panel of Fig. A.2. In both cases, the self-consistent Slater only potential resembles the Slater contribution of the self-consistent (G)KLI potential, but misses the (G)KLI response term. Yet, one observes that the distribution between Slater and response contribution to the (G)KLI potential notably changes if one goes from the standard KLI to an energy-minimizing GCLI potential. This reshuffling of the Slater

contribution also affects the response part, as can be observed in the right panel of Fig. A.2. The response contribution of the KLI potential, which is an approximation to the standard OEP, is known to be important for orbital functionals in general. However, in the case of GSIC using GKLI it does not play an as pronounced role.

I conclude that approximations of the standard OEP may exhibit a distorted response if applied to the SIC functional. Therefore, I strongly recommend the use of generalized approaches that explicitly take the possible unitary freedom of orbital functionals as for instance of the SIC functional into account, particularly when it comes to approximations of the (G)OEP. In this context, the GKLI-SIC potential is a reasonable approximation to the GOEP-SIC in ground-state DFT and exhibits a proper field-counteracting behavior. GSLA-SIC notably improves upon SLA-SIC, but does not show a clear field-counteracting contribution and, therefore, yields polarizabilities further off.

Finally, note that although hydrogen chains are a transparent test system that allow for a clear-cut analysis of the behavior of the xc potential, they are artificial systems and of peculiar nature. Already in earlier works, it has been observed, e.g., that current DFT taking ultranonlocal xc effects into account leads to large polarizability improvements for real conjugated polymers, whereas in hydrogen chain models the improvements are small [vFdBvL<sup>+</sup>02]. Hence, care needs to be taken when drawing conclusions from absolute numbers calculated in such test systems. The performance in realistic molecules needs to be investigated independently. Therefore, in the following section I turn to real polyacetylene chains to further investigate the dependence of the polarizability on functional approximations and implementation methods.

## A.2 Polarizability of polyacetylene chains

The polyacetylene chains are an interesting real test system because they are almost as transparent as hydrogen chains, easy to modify in terms of the chain length, and reveal differences between different (G)SIC methods. Pub4 demonstrates that excitation energies of polyacetylene chains differ notably between different approximations to the TDGOEP, in particular TDFOBO-SIC calculations yield excitation energies that are closer to the reference values than energy-minimizing TDGKLI-SIC.

Here, I complement the data on excitation energies with results of polyacetylene polarizabilities and test if the observations made on the polarizabilities of hydrogen chains also hold in case of polyacetylene. To this end, I give the static polarizability of a selection of polyacetylene chains calculated with different functionals in Table A.2. The data confirms the general finding that LDA overestimates polyacetylene polarizabilities. SIC calculations based on standard KLI and SLA do not cure this overestimation: Standard KLI-SIC even surpasses LDA results and SLA-SIC is similar to LDA or slightly better. Thus, if at all, both methods are not able to improve much upon LDA at the end of the day. This finding parallels the excitation-energy results. It is reflected in an erroneous reduction of the lowest excitation energy in TDKLI-SIC. However, all GSIC schemes reduce the polarizability overestimation, thus cure part of the problem: Except for the shortest chain, C<sub>4</sub>H<sub>6</sub>, GKLI-SIC gives polarizabilities close to B3LYP. GSLA-SIC is close to GKLI-SIC results but tends to give slightly lower, thus better polarizabilities. FOBO localization gives the lowest polarizabilities of all approximate SIC schemes addressed so far. Here, the Foster-

	LDA	KLI	GKLI	GOEP	SLA	GSLA	FOBO	B3LYP	HF	MP2
C <sub>4</sub> H <sub>6</sub>	76	77	68	62	77	68	67	84	75	64
C <sub>6</sub> H <sub>8</sub>	173	175	160	140	171	158	154	164	142	112
C <sub>8</sub> H <sub>10</sub>	294	297	273	222	283	277	262	274	229	187
C <sub>10</sub> H <sub>12</sub>	457	466	426	322	445	435	406	413	332	267

Table A.2: Axial polarizability in atomic units of several polyacetylene chains calculated with different functionals. As a reference, I give MP2 results taken from Ref. [TTdM<sup>+</sup>95], HF taken from Ref. [KTRH95], and B3LYP polarizabilities that were calculated with TURBOMOLE.<sup>3</sup>

Boys criterion guarantees for spatial localization that is not necessarily equal to the complex energy-minimizing transformation.

Full GOEP-SIC calculations are notably better than GKLI-SIC and FOBO-SIC polarizabilities: For the longer polyacetylene chains, GOEP-SIC seems to improve by about half the distance between LDA and MP2 results. Interestingly, the GOEP-SIC polarizabilities presented here are close to, but slightly better than HF ones. Yet, there is still a noticeable gap to the MP2 reference. Therefore, I conclude that although GSIC approaches and especially the full GOEP-SIC improve upon LDA, the results do not coincide with polarizabilities from wave-function perturbation theory.

The observations made on the basis of the polarizability data are in line with the trend of the excitation energies where TDFOBO-SIC provides the highest values in best agreement to reference calculations and the experiment. Hence, in case of polyacetylene chains the trend of the lowest excitation energies can be related to the behavior of the static polarizability. Therefore, for systems that are similar to polyacetylene the polarizability could possibly be used as an indicator for the performance of excitation-energy evaluations, where TDGKLI-SIC and TDFOBO-SIC give improved results, but the deviation from reference values is still 0.3 eV at the maximum. Following the polarizability trend one may expect even better excitation energies from full TDGOEP-SIC, as for GOEP-SIC a significant reduction of the polarizability can be observed. I finally conclude that the (TD)GSIC scheme yields notable improvement of the LDA description of polyacetylene chains, where among the approaches available here FOBO localization gives the best numbers for excitation energies and GOEP-SIC exhibits the overall most promising polarizability results.

### A.3 Static charge transfer in a transparent model system

Finally, I complement the findings on the CT model of Man1 and Sec. 4.2.1 by one additional observation on the total energy of this system when static external fields are applied. If one plots as in Fig. A.3 the total energy of the model system versus the field strength of the external field, one observes almost straight line segments of the total energy that are interrupted by discontinuous changes of the slope. Slight deviations from these straight lines can be observed in the intermediate segment. Note that GOEP-SIC calculations for field strengths up to  $3.5 \times 10^9$  V/m are in almost perfect agreement with the GKLI-SIC findings. The field strengths where the slope changes discontinuously equal the field strengths where

<sup>3</sup>The B3LYP polarizabilities were kindly provided by Andreas Karolewski.

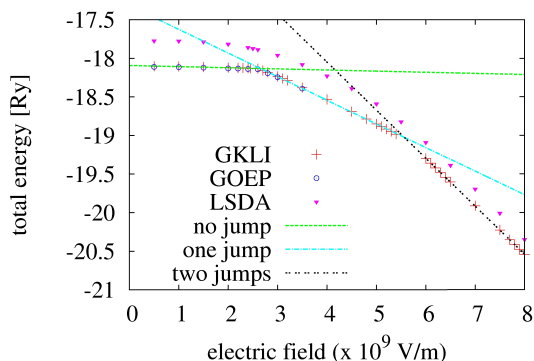


Figure A.3: Dependence of the total energy of the CT model system of the left part of Fig. 4.2 on the strength of the external field. I present the results computed with LSDA, GKLI-SIC, and GOEP-SIC. For this illustration, I subsumed the degenerate realizations of GKLI-SIC (see Sec. 4.2.1). As a guide for the eye, I fitted straight lines with a least-squares linear regression to the three segments of the GKLI-SIC data points from  $0.0 \text{ V/m}$  to  $2.5 \times 10^{-9} \text{ V/m}$ , from  $2.5 \times 10^{-9} \text{ V/m}$  to  $5.5 \times 10^{-9} \text{ V/m}$ , and from  $6.0 \times 10^{-9} \text{ V/m}$  to  $8.0 \times 10^{-9} \text{ V/m}$ . These segments correspond to the situation where no electron is transferred, one electron has jumped from the donor to the acceptor chain, and two electrons are transferred.

the electrons jump from the donor to the acceptor chain according to Man1 and the right part of Fig. 4.2. Thus, the discontinuous changes of the slope of the total energy can be attributed to these electron jumps. At the corresponding field strengths, the density reshuffles notably so that the field acts on very different density distributions before and after the electrons transfer. In Fig. A.3, this manifests in the different slopes of the total energy with respect to the electric field strength. Details of the latter dependence remain to be investigated.

At first sight, the straight line segments of the total energy of Fig. A.3 appear reminiscent of the straight line behavior of the total energy with fractional changes of the electron number that Perdew *et al.* reported in Ref. [PPLB82] (for an overview, see Sec. 2.4). Yet, the picture that emerges here is a different one as the calculations do not involve fractional charges of the entire system and Fig. A.3 shows the total energy versus the field strength in contrast to fractional charges that are depicted in Ref. [PPLB82]: Although some values of the external field strength can be related to specific integer occupations of D and A in GKLI-SIC calculations, none of the intermediate points corresponds to any fractional occupation of the two hydrogen chains. Still, the abrupt changes of the slope at the field strengths where electrons jump are a manifestation of the integer electron transfer behavior.

In principle, a relation between the external field strength and the (fractional) charge of the D or of the A chain may be set up in the case of LSDA using the fractional occupations of the single moieties in the LSDA data of the right part of Fig. 4.2. Yet, this picture does not coincide with the fractional occupation picture of the entire system of Perdew *et al.* [PPLB82] despite the striking analogy, because here the single moieties are not isolated and interactions between D and A need to be taken into account. In Fig. A.3, the LSDA functional exhibits a continuous concave shape of the total energy with respect to the external field strength. This finding reflects the fractional electron transfer behavior of LSDA where no abrupt density reshuffling occurs.



## Appendix B

# Multigrid Poisson solver

The solution of Poisson's problem is one of the key features of the PARSEC code as it is exploited to determine the Hartree potential instead of computing the Hartree potential integral directly [KMT<sup>+</sup>06]. The standard method to solve Poisson's equation in PARSEC is the conjugate gradient (CG) method [Saa03]. In a standard (semi)local density functional PARSEC run, the solution of Poisson's equation is not of central limiting character to the overall performance of the code as it is required only once per GS self-consistency iteration and once per time step if one assumes that one needs to perform a single potential evaluation per time step. Yet, for orbital-dependent functionals as for example SIC, EXX, and especially energy-minimizing GSIC, the efficiency of the Poisson solver is crucial for the overall performance. For instance, in SIC the Poisson solver needs to be called  $N + 1$  times both per self-consistency iteration and per time step, where  $N$  is the number of orbitals involved.

The situation is even more complicated in energy-minimizing GSIC calculations. Here, the Poisson solver is needed at least  $N$  times in each step that needs to be taken during the iterative unitary optimization of the unitary transformation in a GS calculation (see Appendix C). Most Poisson calls, however, are performed during TDGSIC time propagation. For instance, propagation of the 28 occupied orbitals of the DMABN molecule of Sec. 4.2.2 for 40 fs requires  $5 \times 10^4$  time steps, where in the example per time step and orbital on average 4.2 Poisson calls are performed. In total this makes about  $6 \times 10^6$  Poisson calls using the most efficient propagation scheme and algorithms available in PARSEC at current terms. This example clearly demonstrates that the solution of Poisson's equation is a performance limiting factor if one uses orbital functionals in PARSEC. For the feasibility of many calculations presented in this thesis, I addressed this performance bottleneck and implemented a new method based on multigrid (MG) and defect correction ideas to the solution of Poisson's equation in the PARSEC program package.

In this appendix, I give an elementary introduction to the basic MG and defect correction concepts and explain the implementation of the MG solver in the PARSEC code. The new algorithm turns out to be much more efficient than the CG Poisson solver. Moreover, the parallelization of the MG Poisson solver is adjusted to the requirements of SIC and EXX calculations, where orbital density dependent Poisson problems can be performed in parallel. For a more detailed introduction to the MG method, I recommend the book of Trottenberg, Oosterlee, and Schüller [TOS01], the book of Hackbusch [Hac85], and the introduction of MG methods in the Numerical Recipes [PTVF92]. Parts of the presentation in the following are based on these books.

## B.1 Multigrid and defect correction

### B.1.1 The multigrid idea

Typically, one uses the MG method for solving second-order partial differential equations. Here, for a clear-cut presentation in the PARSEC context, I focus on Poisson's equation in three dimensions

$$\nabla^2 v(\mathbf{r}) = -4\pi n(\mathbf{r}) = f(\mathbf{r}), \quad (\text{B.1})$$

where  $v(\mathbf{r})$  is the Hartree potential and  $n(\mathbf{r})$  the density. I abbreviate the inhomogeneity on the right hand side of Eq. (B.1) by  $f(\mathbf{r})$ . For a numerical solution, the Laplacian operator as well as the functions  $v(\mathbf{r})$  and  $f(\mathbf{r})$  are discretized on a grid. The discretized equation reads

$$\mathcal{L}_h v_h = f_h, \quad (\text{B.2})$$

where the discretized functions carry the index  $h$  corresponding to the grid spacing  $h$  and  $\mathcal{L}_h$  denotes the discretized version of the Laplacian operator. If one introduces  $\tilde{v}_h$  to be an approximate solution of Eq. (B.2), the error to obtain  $v_h$  is

$$u_h = v_h - \tilde{v}_h. \quad (\text{B.3})$$

The residual between the approximate result of  $\mathcal{L}_h \tilde{v}_h$  and the true result of  $\mathcal{L}_h v_h$  reads

$$r_h = \mathcal{L}_h \tilde{v}_h - f_h. \quad (\text{B.4})$$

Based on these definitions, Poisson's equation can be written in terms of  $r_h$  and  $u_h$  as

$$\mathcal{L}_h u_h = -r_h. \quad (\text{B.5})$$

One naturally arrives at an iterative procedure for new potentials

$$\tilde{v}_h^{(n+1)} = \tilde{v}_h^{(n)} + u_h^{(n)} \quad (\text{B.6})$$

that can be obtained from previous potentials  $\tilde{v}_h^{(n)}$  and solutions  $u_h^{(n)}$  of Eq. (B.5), where  $r_h$  is computed at each step  $n$  of the iteration according to Eq. (B.4).

The MG method is used to solve the central Eq. (B.5) of the previous iterative scheme. Understanding the main idea of the MG method is related to two basic principles [TOS01]: the smoothing principle and the coarse grid principle. I illustrate both principles using the expansion

$$u_h(x, y, z) = \sum_{k=1}^{N_x-1} \sum_{l=1}^{N_y-1} \sum_{m=1}^{N_z-1} a_{klm} \sin\left(\frac{k\pi}{N_x h} x\right) \sin\left(\frac{l\pi}{N_y h} y\right) \sin\left(\frac{m\pi}{N_z h} z\right) \quad (\text{B.7})$$

of the error [TOS01], where  $N_x$ ,  $N_y$ , and  $N_z$  are the number of grid points in  $x$ ,  $y$ , and  $z$  direction, respectively, and  $u_h(x, y, z)$  vanishes at the boundaries of the grid. The highest frequency components (large  $k$ ,  $l$ , or  $m$ ) contributing to this series are given by the grid spacing  $h$ : Only functions that vary on a length scale that is larger than the grid spacing can be represented after discretization. The maximum extension of the grid determines the lowest frequency components ( $k$ ,  $l$ , and  $m$  are small) of the Fourier series. Classical iterative

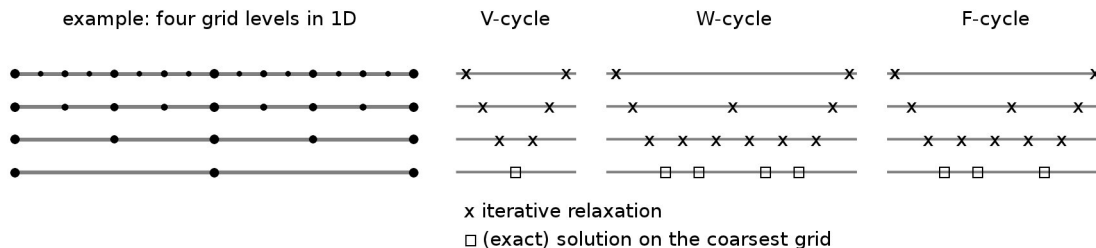


Figure B.1: The left panel illustrates the MG grid-level management with a one-dimensional example and four grid levels. At each coarser grid level the grid spacing doubles in comparison to the previous finer grid level. The grid points are depicted by full circles  $\bullet$ . Circles with smaller size are used only on finer grid levels. The right panels show the cycle succession of the three most prominent MG cycling schemes, the V-, W-, and F-cycle. On the very coarsest grid level an exact solution should be computed, whereas on the finer grid levels a couple of iterations of the iterative relaxation method are performed.

relaxation methods, for example Jacobi or Gauss-Seidel relaxation, efficiently solve high frequency components of Eq. (B.5). Therefore, application of these techniques amounts to a strong smoothing of the error of any approximation (smoothing principle) [TOS01]. Yet, determining lower frequency components is a tedious task using classical relaxation methods. This is where the coarse grid principle comes into play [TOS01]. For an explanation, consider two grids: a coarse and a fine one. The highest frequency components that can be sampled on the coarse grid are smaller than the highest frequency components that can be sampled on the fine one. Therefore, only functions that are smooth on the fine grid can be approximated reliably on the coarse grid. If one is sure that the functions that are involved in Poisson’s problem are smooth on the fine grid, the problem can be transferred to the coarse grid where finding solutions is more efficient.

The main idea of the multigrid method is to exploit those two principles for a fast solution of Eq. (B.5): High frequency components of the error are relaxed on fine grids and lower frequency components are solved on successively coarser grids. Moreover, this idea can equally be applied starting on the coarse grid side and proceeding to finer grids. Typically, one arranges the grid levels such that the grid spacing always changes by a factor of two. This type of grid management is illustrated with a one-dimensional example in the left part of Fig. B.1. In this scheme, only a few relaxation steps are needed per grid level. Subsequently, the solution is transferred either to a coarser grid by a so-called restriction operation or to a finer grid by prolongation. On this new grid level further relaxations are performed. As the classical relaxation methods can be conducted efficiently especially on the coarser grid levels, the solution of Eq. (B.5) can be obtained with comparably low numerical effort. For instance, the CG method is reported to need numerical operations on the order of  $N^{3/2} \log \varepsilon$  to solve the two-dimensional Poisson problem, while the iterative MG method yields a solution after about  $N \log \varepsilon$  operations [TOS01]. Here,  $N$  denotes the number of unknowns and  $\log \varepsilon$  reflects the fact that the numerical accuracy and, therefore, the stop criterion are assumed to be in the range of the discretization accuracy.

Based on the central MG idea, different cycling schemes have emerged to conduct a MG

cycle. In the following, I introduce the most prominent ones, the so-called V-, W-, and F-cycles [TOS01] as illustrated in the right part of Fig. B.1. All cycling schemes have in common that on the coarsest grid level a high quality solution of Poisson's equation needs to be obtained. In Fig. B.1, this aspect is depicted by the symbol  $\square$ . On all other grid levels a small number of standard relaxations are performed. The most basic cycling scheme is the V-cycle. Here, one goes from the finest grid successively down to the coarsest grid and straight back. In the W-cycling scheme, when going from grid level to grid level one always performs one additional V-cycle compared to the V-cycling scheme (see Fig. B.1). This amounts to a higher number of coarse grid solutions in the W- than in the V-cycle. One further alternative is the so-called F-cycle. Here, during the back transfer from coarse to fine grids, one consecutively goes  $n$  steps up and down starting with  $n = 1$  and increases  $n$  after each round until the finest grid level is reached. The numerical effort related to a full cycle differs [TOS01] for each cycling scheme, as every time a different number of steps and operations are involved. Yet, the different methods provide means to adapt the MG method to the special requirements of particular problems as one is able to tune the number of relaxations before and after transferring the error between grid levels.

### B.1.2 An introduction to defect correction

The numerical load involved in a classical relaxation step strongly depends on the number of neighboring points that are used to compute the Laplacian operator on the grid. One strategy of the PARSEC code to gain numerical efficiency is to treat the Laplacian operator of the kinetic energy with a higher-order expansion [KMT<sup>+</sup>06] as this allows for larger grid spacings. Therefore, also the solution of Poisson's equation needs to be performed by a high-order scheme. Yet, the high numerical performance of MG solvers is obtained by low order discretization using only immediate neighbors in the Laplacian operator as well as the fine to coarse grid restriction and the coarse to fine grid interpolation operations. A solution to this conflict is the so-called defect correction [Ste78, Hac81, Sch84, Hac85, TOS01].

Using defect correction one does not solve Poisson's equation

$$\hat{\mathcal{L}}_h v_h = f_h, \quad (\text{B.8})$$

with a higher-order discretization  $\hat{\mathcal{L}}_h$  of the Laplacian operator. Instead, the central idea is to determine the defect

$$d_h = f_h - \hat{\mathcal{L}}_h v_h + \mathcal{L}_h v_h \quad (\text{B.9})$$

related to different discretizations and solve Poisson's equation for this defect

$$\mathcal{L}_h v_h = d_h \quad (\text{B.10})$$

with a lower order Laplacian discretization  $\mathcal{L}_h$  by the MG method. The defect correction idea can be combined with the MG cycling schemes. In this case one needs to perform the following steps:

- (i) start from an initial guess  $\tilde{v}_h^{(0)}$ , set  $k = 1$
- (ii) compute one MG cycle with lower order discretization to obtain  $\tilde{v}_h^{(1)}$
- (iii) determine the defect  $d_h^{(k)}$  to the higher-order discretization using the actual approximate solution  $\tilde{v}_h^{(k)}$  in Eq. (B.9)

- (iv) solve  $\mathcal{L}_h \tilde{v}_h^{(k+1)} = d_h^{(k)}$  with one MG cycle to obtain  $\tilde{v}_h^{(k+1)}$
- (v) set  $k := k + 1$ , iterate steps (iii) to (v) until convergence of  $\tilde{v}_h$

Alternatively, defect correction does not have to be performed on the finest grid level only. Defect correction may also be included in the multigrid cycle, thus be performed on coarser grid levels. For instance, one may perform defect correction when reaching a higher grid level during the back transfer from the coarsest to the finest grid in the F-cycle and may conduct additional F-cycles from this grid level before going to the next higher level [TOS01].

## B.2 Features of the PARSEC code in the multigrid context

When implementing a MG Poisson solver into the PARSEC code, there are some peculiarities of the code that need to be considered. First, the PARSEC grid is shifted from the origin by one half of the grid spacing so that all grid points are symmetrically arranged with respect to the axis and planes of the coordinate system but no grid point is in the origin. This grid arrangement is in conflict with the coarsest possible MG grid level of only three grid points per dimension where two grid points are at the boundary and one grid point is at the origin. In MG implementations one likes to go down in the coarse grid hierarchy to this coarsest possible grid level as the solution there is trivially determined from the boundary condition. Therefore, I had to change the grid arrangement so that in case of MG PARSEC runs, the grid is no longer shifted with respect to the origin. The difference in the grid arrangement of CG and MG based calculations should not make any difference for general systems with arbitrary nuclei positions as long as the results are converged with respect to the grid spacing. Yet, the grid arrangement may affect special case, e.g., single atoms at the origin where the density is particularly high at the center of the grid. In such situations caution should be exercised with respect to the choice of the Poisson solver and results should be checked carefully.

Second, calculations in PARSEC are not performed on a cube or a cuboid but the grid has a spherical or an elliptical shape [KMT<sup>+</sup>06]. Such a shape is difficult in the context of MGs as in case of MG one likes to hold on to the grid points at the boundary and perform equidistant grid coarsening by factors of two. Therefore, the PARSEC MG implementation relies on a superordinate grid of cubic or cuboidal shape that contains all grid points of the original PARSEC grid plus some additional grid points that fill the gap between the PARSEC and the extended grid. With this grid extension, an additional immediate conflict emerges: On the one hand, one likes to go down in the coarse grid hierarchy to very coarse grids, at best down to a grid with only three points per dimension. On the other hand, if the PARSEC grid does not fit perfectly into this grid hierarchy, one may need to add a significant number of extra grid points on the finest grid level to guarantee that all PARSEC grid points are included in the superordinate grid. This conflict is of special significance in case of elliptical PARSEC grids. Here, the grid extension may differ notably for different directions of the coordinate system and, therefore, cubic superordinate grids may amount to a tremendous number of extra points.

To cope with the underlying conflict of interest, I tried to find a reasonable tradeoff between as small as possible cubic or cuboidal superordinate grids and grid hierarchies with coarsest grid levels that contain a minimum of grid points. The tradeoff is guided by practical experience with the PARSEC code. As the spherical PARSEC grid is just a special case of

the more general elliptical shape, I explain the case of elliptical PARSEC and cuboidal superordinate grids. In the following, small letters  $n$  indicate grid levels and capital letters  $N$  denote numbers of grid points on a specific grid level.

The first step is to determine the maximum number  $n^{\max}$  of possible grid levels. To this end, I start on the coarsest level with three grid points and build up a grid hierarchy until the number of grid points of the highest level exceeds the number of grid points  $N^{\min}$  along the coordinate axis with the smallest grid extension. The number of grid points per level going from a coarser to a finer grid can be computed by the recursion formula  $N^{\text{fine}} = 2N^{\text{coarse}} - 1$ , where  $N^{\text{coarse}} = 3$  at grid level  $n = 1$ . Thus,  $n^{\max}$  is the index of the first grid level where  $N^{\text{fine}}$  is greater than  $N^{\min}$ .

In the second step, I start with the number of grid points  $N^{\max}$  of the largest grid extension and go down the grid levels with the recursion formula  $N^{\text{coarse}} = \text{int}(N^{\text{fine}}/2) + 1$  until one of the following stop criteria is fulfilled: If the number of coarse grid points  $N^{\text{coarse}}$  reaches one of the numbers 6, 7, 10, 11, 14, or 15, the recursion stops and the number of grid levels  $l$  equals the number of recursion steps plus one. Otherwise, after the maximum of  $n^{\max} - 1$  steps the number of grid levels  $l$  is set to  $n^{\max}$ . The numbers of the first option are determined by the following rationale: The number of grid points in the grid hierarchy starting from three grid points are (3, 5, 9, 17, ...) as one can observe in Fig. B.1 on the left and starting from seven grid points one obtains (7, 13, 25, ...). If one goes from one of the numbers 6, 7, 10, 11, 14, or 15 down to the next odd number that is part of one of these hierarchies, one pays the prize of a significant number of additional grid points outside the PARSEC grid. To avoid the resulting memory requirements I stop at the listed numbers. Having determined the number of grid levels, the grid hierarchy is built for each direction of the coordinate system ( $i = x, y, z$ ) by the following steps:

- (i) iterate  $N_i^{\text{coarse}} = \text{int}(N_i^{\text{fine}}/2) + 1$  with  $l - 1$  steps starting from  $N_i^{\max}$
- (ii) if the resulting  $N_i^{\text{coarse}}$  is an even number, set  $N_i^{\text{coarse}} := N_i^{\text{coarse}} - 1$
- (iii) build the grid hierarchy with  $l$  levels on top of  $N_i^{\text{coarse}}$  using  $N_i^{\text{fine}} = 2N_i^{\text{coarse}} - 1$

Finally, note that one obtains the spherical case by setting  $N_i^{\max} = N^{\max}$  and performing the last three steps of the above procedure.

In many cases of the just presented grid hierarchy setup, PARSEC does not reach the coarsest grid level with three grid points only, thus the coarsest grid solution cannot be obtained trivially. I guarantee sufficient quality of the coarse grid solution by performing a great number of relaxation steps on the coarsest grid level. These iterations involve a notably reduced number of grid points and are comparably cheap. The specific number of relaxation steps is adapted to the largest number  $N_i$  and based on numerical tests.

For this thesis, I performed PARSEC calculations on confined systems where all orbitals and the density vanish outside a limited domain [BSK<sup>+</sup>03]. Yet, the Coulomb potential is of long-range nature and, therefore, the Hartree potential typically does not vanish within the bounds of the numerical grid. Hence, I finally comment on the setup of the boundary condition of the Poisson problem solver. In standard PARSEC calculations, the boundary is sufficiently far off so that the potential on the boundary is dominated by the multipole components of the density. The boundary condition is set up by calculating the potential in terms of the multipole expansion of the density [BSK<sup>+</sup>03, KMT<sup>+</sup>06]. For the CG solver, the potential is computed on the spherical or elliptical boundary of the standard PARSEC grid

[BSK<sup>+</sup>03]. In case of the MG solver, the boundary condition is set up by the same multipole expansion evaluated on the surface of the cube or the cuboid of the MG superordinate grid. Thus, different boundary conditions are used for the CG and the MG solver. However, if the size of the grid is chosen carefully enough, the influence of the boundary condition vanishes and no differences between CG and MG occur.

### B.3 The multigrid implementation in PARSEC

Having introduced the ideas of MG and defect correction and having discussed PARSEC peculiarities related to the implementation of the MG solver, I finally summarize the characteristics and functionalities of the MG solver that I implemented in PARSEC and introduce the input parameters related to the Poisson solver. These parameters are listed in Table B.1. Additional general remarks concerning the PARSEC input, especially its input data types, are compiled in Sec. E.1. The Poisson solver choice can be made with the input parameter *poissonsolver*. The PARSEC MG Poisson solver uses defect correction to adopt to the higher-order finite difference requirement of the PARSEC code. To this end, the low order finite difference solution of Eq. (B.10) takes only next neighbors into account. The order of the Laplacian of the higher-order discretization is determined by the input parameter *MG\_Laplace*. The cycling scheme of the MG can be selected with *MG\_Cycle\_mode*. All restriction operations during the MG cycles are performed by full-weighting restriction and I use standard trilinear interpolation for all prolongation operations [TOS01]. The relaxation method can be selected by the input parameter *MG\_Relaxation\_mode*. Both implemented methods are based on the well-known Gauss-Seidel relaxation [TOS01, Hac85, PTVF92]. Note that some more options are coded in the final PARSEC version of this thesis, but they are not addressable by the input.

The assessment of the convergence of the solution of Poisson's equation is adapted from Ref. [PTVF92]. The termination of the solver iterations is determined by a convergence criterion

$$\|r_h\| \leq \varepsilon, \quad (\text{B.11})$$

where the norm of the residual is required to be smaller than some given convergence parameter  $\varepsilon$ . The Numerical Recipes [PTVF92] suggest an estimate of this error in terms of the relative truncation error

$$\tau_h = \mathcal{L}_H(\mathcal{R}v_h) - \mathcal{R}\mathcal{L}_h(v_h), \quad (\text{B.12})$$

where  $\mathcal{R}$  denotes a restriction operation and the capital  $H$  indicates quantities and operations on a grid that is coarser by one level. It can be interpreted as a correction to the right hand side of Eq. (B.2) that makes the solution of Poisson's equation on the coarse grid

$$\mathcal{L}_H v_H = f_H + \tau_h, \quad (\text{B.13})$$

equal the fine grid solution as long as the solution is sufficiently smooth [PTVF92]. An approximate relative truncation error  $\tilde{\tau}_h$  follows from using the approximate solution  $\tilde{v}_h$  in Eq. (B.12). It gives an estimate of the convergence parameter [PTVF92] according to

$$\varepsilon = \alpha \|\tilde{\tau}_h\|, \quad \alpha \approx \frac{1}{3}. \quad (\text{B.14})$$

parameter name	type	options	explanation
<i>poissonsolver</i>	<i>int</i>	0 (D)	CG solver
		1	MG solver (obtained from the Kronik group)
		2	MG solver
		10	CG solver with grid shift as in MG
<i>MG_Convergence</i>	<i>dp</i>	1.0 (D)	scaling parameter for accuracy
<i>MG_Relaxation_mode</i>	<i>int</i>	1 (D)	standard red-black Gauss-Seidel relaxation
		2	red-black Gauss-Seidel with overrelaxation
<i>MG_Cycle_mode</i>	<i>int</i>	1 (D)	V-cycle
		2	F-cycle
		3	V-cycle, defect correction on all grid levels
		4	F-cycle, defect correction on all grid levels
		5	two F-cycles, then V-cycles
<i>MG_Laplace</i>	<i>int</i>	1-4 (D)	Laplacian order in defect correction

Table B.1: PARSEC input parameters and input values related to the Poisson solver. Each parameter is described in brief in the last column. The shortcut “*int*” denotes integer and the shortcut “*dp*” double precision data types. Default values are labeled by (D). All parameters with names that begin with “*MG*” are available only in case of *poissonsolver* “2” which is the MG solver introduced in this appendix.

I employ this estimate in PARSEC together with two definitions of the norm: (i) the square root of the integral over the square of  $\tilde{\tau}_h$  and (ii) the maximum value of  $|\tilde{\tau}_h|$ . This proceeding yields two different convergence parameters. To be on the save side, I scale both parameters by a factor of one half. Moreover, an additional scaling factor of this estimate can be applied by the input parameter *MG\_Convergence* that is multiplied to the estimate of  $\varepsilon$ . These convergence parameters are calculated on the fly based on the finest grid and the first grid coarser than the finest grid during the first call of the MG Poisson solver. In all further calls, convergence of the approximate solution  $\tilde{v}_h$  is tested every time the finest grid level is reached.

Last but not least, the MG Poisson solver is embedded into the parallel PARSEC environment. Therefore, let me finally comment on parallelization of MG methods in general and the PARSEC implementation in particular. Different methods and ideas for a MG parallelization are available in the literature [Bra81, MT96, Jun97, HJ97, Mit97, FJ00, ŠT03, DHL03, HKMR05, KSRS08]. Such parallelization strategies address the parallelization over the grid of a single Poisson solver call and involve grid partitioning and domain decomposition techniques. In these cases communication operations need to be performed during relaxation and interpolation on all grid levels of the coarse grid hierarchy when grid points that are treated by different processors are involved. Moreover, one has to find an appropriate distribution of grid points over processors in the parallel environment for all grid levels. This is an especially difficult task on the coarse grid levels where the number of grid points may be on the order of the processors that are involved. Therefore, to obtain a reasonable parallel speed-up, one needs to carefully design the management of grid levels and parallel distribution of numerical load.

Yet, with respect to the special requirements of PARSEC where solutions of Poisson’s

equation need to be performed for the orbital densities of all  $N$  occupied orbitals, a different parallelization strategy with parallelization over the orbitals lends itself to be used. I parallelized the  $N$  Poisson solver calls in PARSEC such that the Hartree potential of one orbital density is computed only by one processor. The advantage is that such a single Poisson solver call does not require any parallel communication, thus the sequential MG solver can be used. However, as the parallelization in all other PARSEC routines is implemented via grid partitioning, the new strategy requires an initial redistribution of orbital densities and a final redistribution of the corresponding orbital-specific Hartree potentials from grid partitioning to orbital parallelization and back. This redistribution is conducted by collective message passing interface (MPI) routines. It is designed such that if possible each processor performs the same number of Poisson calls. Yet, if an equal distribution of the numerical load is not possible, some processors are idle while the other processors work on their orbital-specific Poisson problems. Thus, in this parallelization strategy the number of processors should be adapted to the number of occupied orbitals: Dividing  $N$  by the number of processors should yield a number that equals or is slightly smaller than an integer. To use the sequential Poisson solver for computing the Hartree potential of the total density in a parallel environment, the following steps are performed:

- (i) the density is distributed to all processors
- (ii) each processor performs the same MG solver call with the total density as input and the Hartree potential on the entire grid as output
- (iii) each processor takes the appropriate part of the Hartree potential according to the grid partitioning from its own entire-grid solution to save communication overhead

## B.4 Assessment of the multigrid solver

Having implemented the MG solver as described before, I finally assessed the performance of the solver in terms of accuracy of the solution and of computation time. For a reasonable comparison to the CG method it was crucial to use a PARSEC grid that is identical in both Poisson solver cases. Therefore, I introduced a new Poisson solver method “*poissonsolver = 10*” that is a CG solver with the PARSEC grid shifted as in the MG case (CG shifted).

Using this new solver setup, I first compared the sequential solver version in terms of accuracy of the eigenvalues, Hartree energy, and dipole moment as well as the computation time for a test set of molecules representative for the systems investigated in the Kümmel group: Eigenvalue deviations were typically smaller than  $1 \times 10^{-3}$  %, Hartree energy deviations smaller than  $5 \times 10^{-4}$  %, and dipole moment deviations smaller than  $1 \times 10^{-5}$  atomic units. These deviations, if notable at all, are smaller than the accuracy that may be expected from density functionals, thus confirm the accuracy of the MG implementation. Yet, a detailed presentation of the test set goes beyond the scope of this appendix. Therefore, I just outline a single example that gives a flavor of the performance of the MG implementation.

I chose the small silicon cluster  $\text{Si}_4$  as a transparent test system (see Table B.2 for details of the system and the PARSEC setup). It is an ideal test case for parallelization as all eight occupied orbitals of  $\text{Si}_4$  can be distributed over the CPUs of an octo-core processor. The results of a KLI-SIC ground-state run are listed in Table B.3. First, one observes that CG shifted and MG give almost identical total energies and eigenvalues. Yet, deviations on the

test system	PARSEC input	MG grid setup
Si <sub>4</sub>	<i>Boundary_Sphere_Radius</i> : 18.0d0	number of grid
	<i>Grid_Spacing</i> : 0.4d0	points per
coordinates of the nuclei [bohr]:	<i>Expansion_Order</i> : 10	dimension:
0.000001, 2.246272, 0.000000	<i>States_Num</i> : 10	- sphere size: 93
3.739822, 0.000372, -0.000069	<i>Spin_Polarization</i> : .false.	- fine grid: 97
0.000001, -2.244924, 0.000001	<i>Convergence_Criterion</i> : 1.0d-05	- coarse grid: 7
-3.739817, 0.000373, 0.000052	<i>Diag_Tolerance</i> : 1.0d-07	
	<i>Eigensolver</i> : diagla	number of grid
occupied KS orbitals: 8	<i>Mixing_Method</i> : Anderson	levels: 5
	<i>Mixing_Param</i> : 0.3d0	
grid points (CG setup): 382,336	<i>Memory_Param</i> : 3	
grid points (MG setup): 38,915		

Table B.2: Si<sub>4</sub> test system for assessing the performance of the MG solver. I assembled important parameters of Si<sub>4</sub> and the grid setup in the left column, relevant PARSEC input parameters in the central column, and an overview over the number of grid points and different grid levels of the MG in the right column.

order of  $1 \times 10^{-3}$  % occur if one compares CG calculations with grid shifts relative to each other. Such deviations are solely related to the numerical representation on the grid and can be reduced by decreasing the grid spacing. I performed similar tests on a coarser PARSEC grid with a spacing of 0.6 bohr instead of 0.4 bohr and found notably larger deviations of that kind. However, deviations between CG shifted and MG were by almost three orders of magnitude smaller. Second, one finds in sequential runs that Hartree computation times are by about a factor of five and KLI computation times are by about a factor of six faster in MG than in CG cases. This is a clear indicator for the remarkable speed-up of the MG solver. Although in the parallel case the speed-up for single Hartree calls is only about a factor of 1.5, KLI xc potential evaluations are almost a factor of ten faster when using the MG than using the CG. This manifest also in a notable improvement of the total computation time.

I assessed also the performance of GSIC calculations with energy minimization using the

	$E_{\text{tot}}$ [Ry]    HOMO [Ry]		sequential			parallel		
			$T_{\text{H}}$ [s]	$T_{\text{KLI}}$ [s]	$T_{\text{tot}}$ [s]	$T_{\text{H}}$ [s]	$T_{\text{KLI}}$ [s]	$T_{\text{tot}}$ [s]
CG <sup>sh</sup>	-30.66069	-0.53198	7.91	47.88	2,275.35	2.14	13.19	503.15
CG	-30.66176	-0.53236	7.71	47.66	2,061.81	2.44	14.82	518.44
MG	-30.66068	-0.53198	1.51	7.61	1,745.35	1.47	1.32	374.64

Table B.3: Performance assessment of the sequential and parallel MG solver in a standard SIC KS self-consistent ground-state calculation using Si<sub>4</sub> as a test system (see Table B.2). The parallel environment uses eight CPUs on the same core. All PARSEC runs listed here required 11 iterations. Moreover, I compiled the average CPU times needed for the Hartree solver ( $T_{\text{H}}$ ), the KLI potential procedure ( $T_{\text{KLI}}$ ), and the total CPU time for the self-consistency iteration ( $T_{\text{tot}}$ ). The solution obtained with the CG solver where the grid is shifted as in the MG case (CG<sup>sh</sup>) serves as a reference.

gradient line-search optimization algorithm (see Sec. C.1.3). While eigenvalues and total energies are in reasonable agreement, the MG solver gains notable speed-up of the total self-consistency procedure. In the sequential PARSEC test, the MG procedure requires 21 self-consistency iterations and 212 optimization loops instead of 17 and 198 using the CG solver, but obtains convergence by about a factor of four faster ( $T_{\text{tot}}^{\text{MG}} = 5,743.6$  s instead of  $T_{\text{tot}}^{\text{CG shifted}} = 24,180.8$  s). In the parallel case, speed-up is even better as with a total time of 1,126.5 s the MG version is by about a factor of 5.6 faster than the CG run ( $T_{\text{tot}}^{\text{CG shifted}} = 6,259.8$  s).

Finally, I stress that although already in GS calculations the gain of computation time is remarkable, even better performance enhancement in terms of total computation time may be expected during time propagation. Therefore, I propagated  $\text{Si}_4$  for 1.0 fs with an electronic time step of 0.001 fs using the ‘‘Taylor’’ propagation algorithm [CMR04, MKHM06, Mun07, Mun09] and compared the total CPU times needed by the different methods. The sequential propagation based on the MG solver required 22,860 s CPU time in comparison to 117,044 s based on the CG shifted solver. Thus, in this case the MG version of the sequential code is by a factor of 5.1 faster than the CG version. Even better performance enhancement can be observed in the parallel version: The propagation takes 40,098 s using the CG shifted solver, whereas the MG version requires only 7,300 s for the first fs. This amounts to a speed-up with a factor of 5.5 of the entire propagation part of the PARSEC code due to the MG Poisson solver implementation.



## Appendix C

# Algorithms for the unitary optimization

The determination of the unitary transformation is the most time critical step in GSIC calculations. The unitary optimization in PARSEC is based on iterative algorithms where the time need manifests in two ways: first, the number of steps that are needed to obtain convergence of the iteration and, second, the numerical load per iteration step. In case of energy-minimizing unitary transformations, orbital-specific Hartree and xc potentials need to be computed per orbital in each step of the iteration. Therefore, a reasonable performance of the algorithm requires an efficient solution of Poisson's problem that is behind the computation of Hartree potentials. This aspect is discussed in Appendix B. Furthermore, optimization can be obtained by reducing the number of iteration steps required to achieve convergence. To this end, I implemented different algorithms in PARSEC that accomplish unitary optimization along different ideas. Moreover, to conduct unitary optimization with complex-valued optimized orbitals, algorithms that were available for real-valued orbitals needed to be customized for the complex case. In the following discussion, I focus on the more general complex-valued case. Based on the resulting equations, one obtains the algorithms for real-valued orbital optimization by neglecting all the complex conjugation signs.

### C.1 Algorithmic principles

#### C.1.1 Fois loops based on the Pederson criterion

The first algorithm discussed in this section is based on an idea of Fois, Penman, and Madden [FPM93]. It uses the Pederson criterion (3.12) and starts from an initial set of optimized orbitals  $\{\tilde{\varphi}_{j\sigma}^{(0)}\}$ . In each step ( $k$ ) of the iterative procedure a new unitary transformation

$$U_{ij\sigma}^{(k+1)} = \sum_{n=1}^{N_\sigma} S_{in\sigma}^{(k)} U_{nj\sigma}^{(k)} \quad (\text{C.1})$$

and thus a new set of optimized orbitals

$$\tilde{\varphi}_{i\sigma}^{(k+1)}(\mathbf{r}) = \sum_{j=1}^{N_\sigma} S_{ij\sigma}^{(k)} \tilde{\varphi}_{j\sigma}^{(k)}(\mathbf{r}) \quad (\text{C.2})$$

can be obtained by unitary rotations with the matrix  $S_\sigma^{(k)}$ . This transformation is assumed to perform only small changes. Thus, it varies only slightly from the unit matrix according to

$$S_{ij\sigma}^{\text{no}} = \delta_{ij} + \tau_{ij\sigma}, \quad (\text{C.3})$$

where  $\tau_{ij\sigma}$  are complex numbers  $|\tau_{ij\sigma}| \ll 1$  and  $\tau_{ij\sigma} = -\tau_{ji\sigma}^*$ . As in this approximation the transformation  $S_{ij\sigma}^{\text{no}}$  is not strictly unitary, Thomas Körzdörfer [Kör09] suggested to explicitly take care of the loss of unitarity by means of Löwdin's method of symmetric orthogonalization [Löw50, May02]: Using the Löwdin matrix

$$C_{ij\sigma} = \langle \tilde{\varphi}_{i\sigma}^{\text{no}} | \tilde{\varphi}_{j\sigma}^{\text{no}} \rangle^{-1/2} \quad (\text{C.4})$$

computed from the nonorthogonal orbitals

$$\tilde{\varphi}_{i\sigma}^{\text{no}} = \sum_j^{N_\sigma} S_{ij\sigma}^{\text{no}} \tilde{\varphi}_{j\sigma}^{(k)} \quad (\text{C.5})$$

one obtains a new orthogonal orbital set

$$\tilde{\varphi}_{i\sigma} = \sum_{j,m}^{N_\sigma} C_{im\sigma} S_{mj\sigma}^{\text{no}} \tilde{\varphi}_{j\sigma}^{(k)}. \quad (\text{C.6})$$

Inserting this new orbital set into Pederson's symmetry condition yields

$$\sum_{k,m=1}^{N_\sigma} C_{jm\sigma}^* S_{mk\sigma}^{\text{no}*} \sum_{l,n=1}^{N_\sigma} C_{in\sigma} S_{nl\sigma}^{\text{no}} \underbrace{\langle \tilde{\varphi}_{k\sigma}^{(k)} | \tilde{v}_{j\sigma}^{\text{SIC}} - \tilde{v}_{i\sigma}^{\text{SIC}} | \tilde{\varphi}_{l\sigma}^{(k)} \rangle}_{=:\langle k|j-i|l \rangle} = 0, \quad (\text{C.7})$$

where I introduced a shortcut for the bracket notation. The Löwdin matrix (C.4) can be approximated [GU97, Kör09] by

$$C_{ij\sigma} \approx \delta_{ij} - \frac{1}{2} (\langle \tilde{\varphi}_{i\sigma}^{\text{no}} | \tilde{\varphi}_{j\sigma}^{\text{no}} \rangle - \delta_{ij}) = \delta_{ij} + \frac{1}{2} \left( \sum_m^{N_\sigma} \tau_{im\sigma}^* \tau_{mj\sigma} \right) \quad (\text{C.8})$$

and expressed in terms of  $\tau_{ij\sigma}$  via Eqs. (C.5) and (C.3). Thus one readily computes

$$\sum_{n=1}^{N_\sigma} C_{in\sigma} S_{nl\sigma}^{\text{no}} = \delta_{il} + \tau_{il\sigma} + \underbrace{\frac{1}{2} \sum_{p=1}^{N_\sigma} \tau_{ip\sigma}^* \tau_{pj\sigma} + \frac{1}{2} \sum_{p,j=1}^{N_\sigma} \tau_{ip\sigma}^* \tau_{pq\sigma}^* \tau_{ql\sigma}}_{=:\omega_{il\sigma}}. \quad (\text{C.9})$$

Following the derivation of Fois *et al.* [FPM93] and Körzdörfer [Kör09] this result needs to be introduced into Eq. (C.7) and one obtains the final expression after a little algebra

$$\begin{aligned} \tau_{ij\sigma} &= \frac{1}{2} \langle j|j-i|i \rangle + \frac{1}{2} \sum_{l=1}^{N_\sigma} [\omega_{il\sigma} \langle j|j-i|l \rangle + \delta_{jl} \tau_{il\sigma}] \\ &+ \frac{1}{2} \sum_{k=1}^{N_\sigma} [\omega_{jk\sigma}^* \langle k|j-i|i \rangle - \delta_{ik} \tau_{jk\sigma}^*] + \frac{1}{2} \sum_{k,l=1}^{N_\sigma} \omega_{jk\sigma}^* \omega_{il\sigma} \langle k|j-i|l \rangle. \end{aligned} \quad (\text{C.10})$$

A final orthogonalization of the transformation of Eq. (C.3) using  $\tau_{ij\sigma}$  of Eq. (C.10) yields the unitary transformation  $S_{ij\sigma}^{(k)}$ . Thus, one obtains the new orbital set and transformation for the iteration procedure from Eqs. (C.1) and (C.2). The algorithmic implementation of this method is identical to the one described by Körzdörfer [Kör09]. Here, convergence is determined by the Pederson criterion. It is reached when the absolute value of the largest matrix element of the matrix of Eq. (3.12) is smaller than a given threshold which is typically less than  $10^{-5}$  Ry. Numerical tests of this method revealed that a notable number of iterations is required to obtain convergence of the Pederson criterion below a reasonable threshold. Yet, an optimization of this method in terms of larger steps is difficult. Therefore, I conclude that designing optimization algorithms based on the Pederson criterion of Eq. (3.12) is legitimate, but algorithms that base directly on the energy expression may be more efficient. I discuss such kind of algorithms in the following sections.

### C.1.2 Energy gradient based algorithm

The second algorithm presented in this appendix uses an energy gradient suggested by Messud *et al.* [MDRS09a]. It is based on the fact that the SIC energy varies with respect to unitary transformations of the occupied KS orbitals

$$\tilde{\varphi}_{i\sigma}(\mathbf{r}) = \sum_{j=1}^{N_\sigma} U_{ij\sigma} \varphi_{j\sigma}(\mathbf{r}). \quad (\text{C.11})$$

For computing the gradient of Messud *et al.* [MDRS09a], one needs to take the Lagrangian multiplier matrix into account that appears when minimizing the SIC energy with respect to the orbitals and guarantees orthogonality of the latter. This matrix does not appear in KS DFT. Therefore, the analogue KS energy gradient of the total energy  $E_{\text{tot}}^{\text{SIC}}$  in the GSIC formalism reads

$$D_{ij\sigma} = \partial_{U_{ij\sigma}^*} E_{\text{tot}}^{\text{SIC}} = -\langle \varphi_{j\sigma} | \tilde{v}_{i\sigma}^{\text{SIC}} | \tilde{\varphi}_{i\sigma} \rangle. \quad (\text{C.12})$$

It determines the direction in which the unitary transformation  $U_{ij\sigma}$  needs to be changed to find the total energy minimum starting from a fixed set of occupied KS orbitals. The gradient scaled by the gradient step size  $\eta$  can be used to find a new transformation

$$U_{ij\sigma}^{\text{no}} = U_{ij\sigma}^{(k)} - \eta D_{ij\sigma}^{(k)} \quad (\text{C.13})$$

at each step ( $k$ ) of a resulting iterative procedure starting from a previous transformation and optimized orbital set. As this transformation is nonorthogonal, the new transformation  $U_{ij\sigma}^{(k+1)}$  of the next iteration needs to be determined by orthogonalization of  $U_{ij\sigma}^{\text{no}}$ . In PARSEC, this a posteriori orthogonalization can be performed either by Gram-Schmidt or by symmetric Löwdin orthogonalization.

In gradient algorithms, the gradient step size is a natural starting point for performance enhancement. However, as application of the gradient is always followed by an orthogonalization to guarantee for unitarity of the transformation, the original search direction given by the gradient gets lost to some extent. Moreover, the gradient step size not only scales the application of the gradient, it also has a significant influence on the outcome of the a posteriori orthogonalization. This renders the optimization of the step size difficult. Therefore, in the PARSEC implementation of the energy-gradient algorithm, I introduced an adaptation

of the gradient step size depending on how the gradient performs during previous steps of the iteration: During the iteration, I monitor if application of the gradient improves the convergence criterion towards the preset convergence threshold or not. If the convergence parameter improves during three succeeding cycles, the gradient step size is multiplied by a factor of two until it reaches a preset maximum value. In this scheme, the initial gradient step size is 100 and the maximum value can be determined by the PARSEC input. On the contrary, in each cycle where the convergence parameter deteriorates, the gradient step size is divided by a factor of two and the code checks if application of the old gradient scaled by the new gradient step size improves or not. This down scaling of the gradient step size is performed either until the convergence parameter improves again or until a minimum of the step size of  $1 \times 10^{-4}$  is reached. If application of the gradient is no longer able to improve the convergence parameter, the algorithm stops with a warning. Otherwise, the iteration is performed until convergence. For a successful application of this algorithm it is important that changes of the unitary transformation due to application of the energy gradient are not deteriorated by the a posteriori orthogonalization. Therefore, the orthogonalization procedure needs to maintain the direction of the unitary rotation of  $U_\sigma^{\text{no}}$  as close as possible. To this end, I recommend to use Löwdin's orthogonalization method that yields a unitary transformation  $U_\sigma^{(k+1)}$  as close as possible to  $U_\sigma^{\text{no}}$ .

In case of energy-gradient algorithms, at least two convergence parameters lend themselves to be used: (i) minimization of the total energy and (ii) reduction of the Pederson criterion below a given threshold. As the minimum of the energy is not known, this criterion needs to be exploited as a self-consistency criterion. Thus, energy convergence is reached if the energy changes of two consecutive iteration steps are lower than the corresponding convergence parameter. Typical energy convergence parameters are on the order of  $10^{-8}$  Ry. In the PARSEC implementation, both convergence parameters can be combined or used separately (see Table C.2). Moreover, the treatment of the convergence parameter in ground-state calculations and during time propagation can be chosen independently.

Numerical tests of this algorithm showed that it notably improves in terms of computation time until convergence is reached in comparison to the algorithm of Sec. C.1.1. Yet, due to the a posteriori orthogonalization large gradient steps are precluded. Therefore, in the next section I explain another idea that allows for large energy-gradient steps due to step-size optimization.

### C.1.3 Energy gradient and line-search optimization

The central idea of the third algorithm for unitary optimization of the SIC energy implemented in PARSEC is to optimize the application of the energy gradient so that no explicit a posteriori orthogonalization is needed and consequently step size optimization can be performed efficiently. It is based on a conjugate gradient (CG) method where the unitary constraint of the energy-minimizing transformation is taken into account explicitly [AEK09]. Here, for the sake of completeness, I give a short introduction and summary of this algorithm following the presentation of Pub3 where it is explained in more detail.

In contrast to the gradient of Sec. C.1.2, the energy gradient of this section is based on a different idea. Here, in each step ( $k$ ) of the iterative procedure one tries to find a unitary

transformation  $S_\sigma^{(k)}$  that determines a new orbital set  $\{\tilde{\varphi}_{i\sigma}^{(k+1)}\}$  according to

$$\tilde{\varphi}_{i\sigma}^{(k+1)}(\mathbf{r}) = \sum_{j=1}^{N_\sigma} S_{ij\sigma}^{(k)} \tilde{\varphi}_{j\sigma}^{(k)}(\mathbf{r}) \quad (\text{C.14})$$

with lower SIC energy starting from a previous optimized orbital set  $\{\tilde{\varphi}_{i\sigma}^{(k)}\}$ . Thus,  $S_\sigma^{(k)}$  also needs to modify the previous unitary transformation  $U_\sigma^{(k)}$  according to

$$U_{ij\sigma}^{(k+1)} = \sum_{n=1}^{N_\sigma} S_{in\sigma}^{(k)} U_{nj\sigma}^{(k)} \quad (\text{C.15})$$

so that  $U_\sigma^{(k+1)}$  yields the new optimized orbitals from the occupied KS orbitals

$$\tilde{\varphi}_{i\sigma}^{(k+1)}(\mathbf{r}) = \sum_{j=1}^{N_\sigma} U_{ij\sigma}^{(k+1)} \varphi_{j\sigma}(\mathbf{r}). \quad (\text{C.16})$$

In this case, one is interested in SIC energy changes due to small variations of the transformation  $S_\sigma$  from the unit matrix starting from a fixed orbital set  $\{\tilde{\varphi}_{j\sigma}^{(k)}\}$  [PFD<sup>+</sup>11]: Linear order changes of the SIC energy due to deviations of  $S_\sigma$  from the unit matrix are given by the anti-Hermitian gradient matrix

$$G_{ij\sigma}^{(k)} = \left. \frac{\partial E_{\text{xc}}^{\text{SIC}}[\{\tilde{\varphi}_{n\sigma}^{(k)}\}, S_{mn\sigma}]}{\partial S_{ij\sigma}^*} \right|_{S_{ij\sigma}^* = \delta_{ij}} = \langle \tilde{\varphi}_{j\sigma}^{(k)} | \tilde{v}_{i\sigma}^{\text{SIC}(k)}(\mathbf{r}) - \tilde{v}_{j\sigma}^{\text{SIC}(k)}(\mathbf{r}) | \tilde{\varphi}_{i\sigma}^{(k)} \rangle. \quad (\text{C.17})$$

The SIC potentials  $\tilde{v}_{j\sigma}^{\text{SIC}(k)}(\mathbf{r})$  are computed from the energy-minimizing orbitals  $\tilde{\varphi}_{j\sigma}^{(k)}(\mathbf{r})$ . The gradient of Eq. (C.17) coincides with the Pederson condition.

The idea of Ref. [AEK09] is to perform the gradient step in a reduced space where the unitarity constraint is guaranteed by choice of the parameter space [EAS98]. Thus, the optimization problem can be turned into an unconstrained one by suitable restriction of the parameter space to the Lie group of  $n \times n$  unitary matrices  $U(n)$  [AEK09]. Due to the anti-Hermiticity of the gradient matrix, the exponential map

$$S_\sigma^{(k)}(l_\sigma^{(k)}) = \exp\{-l_\sigma^{(k)} G_\sigma^{(k)}\} \quad (\text{C.18})$$

with step size  $l_\sigma^{(k)}$  constitutes a unitarity-conserving transformation when it is applied to the unitary transformation  $U_\sigma^{(k)}$  as in Eq. (C.15).  $G_\sigma^{(k)}$  corresponds to the steepest descent search direction, but due to the exponential map unitarity of  $S_\sigma^{(k)}$  is guaranteed. Thus, the problem of a posteriori orthogonalization is avoided.

The numerical performance of this unitarity-conserving application of the energy gradient can be increased by means of CGs and optimization of the gradient step size. The idea of the CG is to use not only the information of the search direction given by the energy gradient, but to also take information of the previous search direction into account. Thus, the new search direction  $H_\sigma^{(k)}$  is based on the current gradient  $G_\sigma^{(k)}$  and the search direction  $H_\sigma^{(k-1)}$  of the last step of the iteration. In the PARSEC CG implementation, I use the new search direction

$$H_{ij\sigma}^{(k)} = G_{ij\sigma}^{(k)} + \gamma_\sigma^{(k)} H_{ij\sigma}^{(k-1)}, \quad (\text{C.19})$$

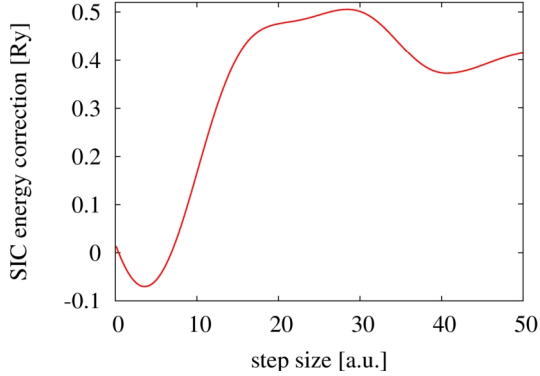


Figure C.1: Dependence of the SIC energy correction ( $E_{\text{xc}}^{\text{SIC}}[n] - E_{\text{xc}}^{\text{app}}[n]$  according to Eq. (3.3)) on the step size during the initial stage of the energy-minimizing unitary optimization in  $\text{Si}_4$  using the energy gradient with step-size optimization algorithm of Sec. C.1.3.

where  $\gamma_{\sigma}^{(k)}$  is the Polak-Ribière weighting factor [AEK09]

$$\gamma_{\sigma}^{(k)} = \frac{\langle G_{\sigma}^{(k)} - G_{\sigma}^{(k-1)}, G_{\sigma}^{(k)} \rangle}{\langle G_{\sigma}^{(k-1)}, G_{\sigma}^{(k-1)} \rangle}. \quad (\text{C.20})$$

The brackets are defined by

$$\langle X, Y \rangle = \frac{1}{2} \text{Re}\{\text{Tr}(XY^{\dagger})\}, \quad X, Y \in \mathbb{C}^{n \times n}. \quad (\text{C.21})$$

Finally, adaptation of the gradient step size  $l_{\sigma}^{(k)}$  gives further performance enhancement. As illustrated in Fig. C.1.3, the improvement of the SIC energy correction that can be obtained per iteration strongly depends on the value of the step size of Eq. (C.18): One observes an almost parabolic behavior of the energy correction for small step sizes and a large deviation from the optimum value of the correction for larger step sizes. Thus, the optimum step size can be estimated by a line search where the dependence of the SIC energy on  $l_{\sigma}^{(k)}$  via the transformation (C.18) is approximated to be a second order polynomial. Details of this line search, an overview of the algorithm, and more insight into its practical implementation are presented in Pub3.

The gradient line-search algorithm outperforms the two previous optimization algorithms in terms of numerical efficiency although per iteration step it requires twice the number of Poisson solver calls because of the step-size optimization. Yet, the number of iterations until convergence is reached is notably smaller. Therefore, using this algorithm GSIC calculations where unitary optimizations of molecules with up to one hundred electrons are performed and even TDGSIC propagation of such molecules are feasible.

## C.2 The unitary optimization algorithms in PARSEC

### C.2.1 Initialization of the optimization steps

Practical experience with the PARSEC code has shown that a high quality of the initial guess of the unitary transformation guarantees a fast solution of the unitary optimization problem per self-consistency iteration cycle. I pursue two strategies in PARSEC to find initial guesses: The first strategy is to determine the initial guess from algorithms and/or unitary

parameter name	type	options	explanation
<i>SIC_xc_type</i>	<i>string</i>	ca/pz/lda (D) pb/pbe pw/pw91	SIC of LDA, PZ parametrization SIC of PBE SIC of Perdew-Wang GGA functional
<i>Localization</i>	<i>bool</i>	false (D)	switch localization on/off
<i>Localization_Type</i>	<i>string</i>	fobo (D) pede grad  goly  grls  glso  inve  triv  trgo	Foster-Boys localization $E_{\min}$ , Fois <i>et al.</i> algorithm $E_{\min}$ , gradient algorithm, initial guess: Foster-Boys localization $E_{\min}$ , gradient algorithm, initial guess: previous transformation $E_{\min}$ , gradient line-search algorithm, initial guess: Foster-Boys localization $E_{\min}$ , gradient line-search algorithm, initial guess: previous transformation ground state: as “grad”, during propagation: $\{\tilde{\varphi}_{j\sigma}(\mathbf{r}, 0)\}$ fixed and $U_{ij\sigma}(t)$ computed from $\{\varphi_{i\sigma}(\mathbf{r}, t)\}$ ground state: as “grls”, propagation: fixed phase factors ground state: as “glso”, propagation: fixed phase factors
<i>FosterBoys_type</i>	<i>int</i>	1 (D)  2  3  4  5	Jacobi sweeps algorithm [ER63] propagation: fixed phase factors Fois <i>et al.</i> algorithm initial guess: previous transformation gradient algorithm initial guess: previous transformation gradient line-search algorithm initial guess: previous transformation gradient line-search algorithm, initial guess: previous transformation propagation: fixed phase factors
<i>Complex_Localization</i>	<i>bool</i>	false (D)	switch complex optimization on/off
<i>Use_last_trafo</i>	<i>bool</i>	false (D)	switch use of transformation of last step during propagation on/off
<i>Prop_use_KLI_mem</i>	<i>bool</i>	false (D)	switch use of memory term in TDGKLI propagation on/off

Table C.1: PARSEC input parameters related to GSIC calculations together with their data types, possible input options, and a short explanation. The shortcut “*int*” denotes integer and “*bool*” boolean data types. Moreover,  $E_{\min}$  abbreviates energy minimization. Default values are labeled by (D). The optimization algorithm of Fois *et al.* (Sec. C.1.1), the gradient algorithm (Sec. C.1.2), and the gradient line-search algorithm (Sec. C.1.3) are explained in the text.

optimization criteria that require lower numerical effort to perform the unitary optimization. To this end, the Foster-Boys criterion implemented with the Jacobi sweeps algorithm [ER63] lends itself to be used prior to more elaborate optimization algorithms like the ones presented before. Such Foster-Boys localizations start from the unit matrix. Here, I use a less restrictive convergence threshold for the Foster-Boys optimization and employ the resulting transformation as the starting point for subsequent optimizations. This strategy is always applied in the early stage of self-consistency iterations where changes of the integral over the charge weighted potential that is used as self-consistency residual error (SRE) has not dropped below 0.1. In spin-polarized calculations it needs to be lower than 0.1 in both spin channels.

The second strategy involves the optimized transformation of the last self-consistency iteration cycle. As the orbitals may change notably during the first steps of the self-consistency iteration, this strategy can only be applied after a couple of iterations when the SRE has dropped below 0.1. In this case, PARSEC compares all orbitals of the current cycle to the corresponding orbitals of the previous cycle. If the orbital overlap is larger than a given threshold, the previous transformation is used as initial guess for all orbitals. Currently this threshold is set to be 0.85. Note that during the diagonalization of the Hamiltonian the orbitals may change parity and in cases of close degeneracy the orbitals may change their order. Therefore, in cases where the orbitals do not match according to the comparison criterion, I check for sign changes and orbital swaps of orbitals with adjacent numbers. When such operations make the current orbitals match the orbitals of the previous cycle, the transformation needs to be adapted by changing signs, columns, and rows, respectively. Then, the modified transformation can be used as initial guess. In all other cases where no orbital matching can be obtained, the first strategy is applied and the initial guess is determined from the Foster-Boys criterion.

The only exceptions to these two strategies are the *Localization\_Type* “goly” and “glso” (see Tab. C.1) where always the transformation of the last self-consistency iteration cycle is used except for the first iteration. In the first iteration, PARSEC initializes the energy-minimizing transformation always by Foster-Boys localization.

## C.2.2 The PARSEC implementation

An overview of the PARSEC input parameters relevant for SIC and GSIC calculations is compiled in Tables C.1 and C.2 (see Sec. E.1 for more general information about the PARSEC input). These tables indicate possible input parameters and input values and highlight default settings. The xc functional upon which the SIC is performed is determined by *SIC\_xc\_type*. The unitary optimization of GSIC calculations is switched on and off by the flag *Localization*. All further parameters discussed in the following apply only in case of GSIC. The parameter *Localization\_Type* allows for the choice of unitary optimization algorithms and criteria. In case of Foster-Boys localization the algorithm needs to be specified by *FosterBoys\_Type*. The flag *Complex\_Localization* controls the use of complex-valued minimizing orbitals and corresponding transformations. Two further parameters are needed only for GSIC propagation. *Use\_last\_trafo* determines if the transformation of the last step during the propagation shall be used as initial transformation guess of the current time step. In all other cases the transformation is initialized or determined by phase factors according to the orbital eigenvalues (see Pub2 and Pub4). Finally with the input parameter

parameter name	type	options	explanation
<i>FosterBoys_Convergence</i>	<i>dp</i>	<i>c</i> (D)	Foster-Boys convergence criterion
<i>Pederson_Convergence</i>	<i>dp</i>	<i>s</i> (D)	Pederson convergence criterion
<i>Gradient_Convergence</i>	<i>dp</i>	<i>s</i> (D)	energy convergence criterion
<i>Adaptive_loc_tolerance</i>	<i>bool</i>	false (D)	switch use of localization tolerance adaptation on/off
<i>Orthogonalization</i>	<i>int</i>	0	Gram-Schmidt orthogonalization
		1 (D)	Löwdin orthogonalization
<i>Grad_step_max</i>	<i>dp</i>	500.0 (D)	maximum gradient step size in case of gradient algorithm
		0.01 (D)	trial step size in case of gradient line search algorithm
<i>Gradient_control_criterion</i>	<i>int</i>	1	check only Pederson criterion
		2	check only energy criterion
		3 (D)	either Pederson or energy criterion has to be fulfilled
		4	ground state: as in “3”, propagation: only energy criterion
		5	ground state: as in “3”, propagation: only Pederson criterion

Table C.2: PARSEC input parameters of the unitary optimization algorithms together with their data types, possible input options or default values, and a short explanation. The shortcut “*int*” denotes integer, “*dp*” double precision, and “*bool*” boolean data types. Moreover, *c* is the self-consistency convergence criterion and *s* the diagonalization-solver tolerance. Default values are labeled by (D).

*Prop\_use\_KLI\_mem* the usage of the memory term of the TDGKLI approximation can be switched on or off.

A second set of parameters (see Table C.2) is needed to control the unitary optimization algorithms. The convergence criteria can be set by three different input parameters: *FosterBoys\_Convergence*, *Pederson\_Convergence*, and *Gradient\_Convergence*. These input parameters are relevant for different settings of *Localization\_Type* and *FosterBoys\_Type*.

- The Foster-Boys criterion measures changes of the FOBO localization criterion per Jacobi sweep. Convergence is reached as soon as such changes are below the *FosterBoys\_Convergence* threshold. Typical numbers of this parameter are on the order of  $1 \times 10^{-20}$ . This parameter is used in case of “*FosterBoys\_Type* = 1” and if the transformation is initialized by Foster-Boys localization.
- The *Pederson\_Convergence* parameter specifies the threshold of the Pederson energy-minimization criterion. In this case, convergence is reached as soon as the absolute values of all elements of the Pederson criterion matrix drop below the *Pederson\_Convergence* threshold, typically on the order of  $1 \times 10^{-5}$  Ry. This parameter is used for all optimization algorithms except the ones indicated here explicitly.
- Using the parameter *Gradient\_Convergence*, changes of the SIC energy during the

minimization algorithms “*Localization\_Type = grad*” and “*Localization\_Type = goly*” are monitored and convergence is indicated as soon as these changes are lower than the input, typically on the order of  $1 \times 10^{-8}$  Ry. In those two cases, the use and combination of the *Pederson\_Convergence* and the *Gradient\_Convergence* parameters can be determined by the input parameter *Gradient\_control\_criterion* (see Tab. C.2).

The thresholds of the convergence parameters of the optimization algorithms can be adapted to the progress of the KS self-consistency iteration. Using this scheme, the convergence parameters are adapted according to the value of the SRE: The convergence thresholds are set to higher values when the SRE is notably larger than it is supposed to be at self-consistency. Only when the SRE is close to the self-consistency threshold, the preset values are used for the convergence parameters of the optimization algorithms. The adaptation scheme can be (de)activated by the flag *Adaptive\_loc\_tolerance*. (A similar convergence-parameter adaptation idea is presented in Sec. E.5.) The parameter *Grad\_step\_max* is needed for the gradient step size optimization in both gradient algorithms. In case of the energy gradient of Sec. C.1.2, the parameter sets the maximum size of the gradient step. Yet, in case of the gradient line-search algorithm of Sec. C.1.3, this parameter can be used to determine the size of the trial step. Here, I recommend to use the default values. Finally, using the parameter *Orthogonalization* one can choose between different types of orthogonalization algorithms during the unitary optimization, namely Gram-Schmidt or Löwdin orthogonalization.

## Appendix D

# Förster-type potentials and stochastic time-dependent density functional theory

This appendix is dedicated to the description of the PARSEC implementations that I performed related to the work on Pub1 and subsequent investigations that are presented in Chap. 5. First, I summarize in Sec. D.1 the Förster-type potential expansion ideas and their realization in PARSEC. These implementations were already performed during the work on Ref. [Hof08]. Second, I explain the determination of the coupling-matrix element from real-time propagation based on an off-resonant two-level model in Sec. D.2. Third, the appendix includes a description of the PARSEC extension of the standard closed quantum system KS propagation scheme to open quantum systems based on the stochastic Schrödinger equation. Some ideas about using the latter in the KS TDDFT framework, suggestions of bath operators for the single-particle approach, and more details about the PARSEC implementation are described in Sec. D.3.

### D.1 Förster-type potentials and grid partitioning

#### D.1.1 The Förster-type potential expansion in Donor-Acceptor systems

To investigate the coupling mechanism and check for Förster-type coupling behavior, I suggested in Pub1 a dipole coupling scheme that can be applied in the TDDFT context. In the following, I outline some of the theoretical background of this concept that is needed to explain the PARSEC implementation. For including a dipole-dipole coupling approximation in the KS framework, there are two valid starting points: the Hartree energy and the Hartree potential. Both routes involve a multipole expansion of the  $1/|\mathbf{r} - \mathbf{r}'|$  factor in the Hartree integral. Starting from the Hartree energy, one first performs the multipole expansion and then draws the functional derivative to obtain the corresponding potential (see Pub1 and Ref. [Hof08] for details). Along this route, one obtains the potential in dipole-dipole coupling approximation (superscript dd and superscript index E)

$$v_{\text{H}}^{\text{ddE}}[n^{\text{D}}, n^{\text{A}}] = (v_{\text{H}}[n^{\text{D}}] + v_{\text{H}}^{\text{ddE},\text{D}}[n^{\text{A}}])\Theta(-x) + (v_{\text{H}}[n^{\text{A}}] + v_{\text{H}}^{\text{ddE},\text{A}}[n^{\text{D}}])\Theta(x). \quad (\text{D.1})$$

The Heaviside function splits the entire real space into a D ( $\Theta(-x)$ ) and an A ( $\Theta(x)$ ) part (see Fig. 1 of Pub1). Hence, the superscripts D and A indicate properties that are computed only on the D or A side, respectively. Based on this notation,  $v_{\text{H}}[n^{\text{D(A)}}]$  is the Hartree potential of D(A) and  $v_{\text{H}}^{\text{ddE,D(A)}}[n^{\text{A(D)}}]$  is the potential resulting from the interaction between D and A in the D(A) half space. With the help of the multipole moments of the D(A) density,

$$\begin{aligned} N^i &= \int n^i(\mathbf{r}^i) d^3r^i, \\ \mathbf{d}^i &= \int \mathbf{r}^i n^i(\mathbf{r}^i) d^3r^i, \\ Q_{jk}^i &= \int n^i(\mathbf{r}^i) (3r_j^i r_k^i - r^{i2} \delta_{jk}) d^3r^i, \end{aligned} \quad (\text{D.2})$$

where  $i = \text{D, A}$ , the Förster potential that the D density generates in the half space of A is

$$\begin{aligned} v_{\text{H}}^{\text{ddE,A}}[n^{\text{D}}](\mathbf{r}^{\text{A}}) &= \frac{N^{\text{D}}}{|\mathbf{R}|} - \frac{(N^{\text{D}}\mathbf{r}^{\text{A}} - \mathbf{d}^{\text{D}}) \cdot \mathbf{R}}{|\mathbf{R}|^3} + \frac{\mathbf{r}^{\text{A}} \cdot \mathbf{d}^{\text{D}}}{|\mathbf{R}|^3} + \frac{N^{\text{D}}}{2} \sum_{j,k=1}^3 (3r_j^{\text{A}} r_k^{\text{A}} - r^{\text{A}2} \delta_{jk}) \frac{R_j R_k}{|\mathbf{R}|^5} \\ &+ \sum_{j,k=1}^3 \frac{Q_{jk}^{\text{D}} R_j R_k}{2|\mathbf{R}|^5} - \frac{3(\mathbf{R} \cdot \mathbf{r}^{\text{A}})(\mathbf{R} \cdot \mathbf{d}^{\text{D}})}{|\mathbf{R}|^5}. \end{aligned} \quad (\text{D.3})$$

The corresponding potential  $v_{\text{H}}^{\text{ddE,D}}[n^{\text{A}}](\mathbf{r}^{\text{D}})$  is obtained from equation (D.3) by interchanging D and A superscripts and replacing  $\mathbf{R}$  by  $-\mathbf{R}$ .

Alternatively, the multipole expansion can be inserted directly into the Hartree potential and one obtains the potential

$$v_{\text{H}}^{\text{ddv}}[n^{\text{D}}, n^{\text{A}}] = (v_{\text{H}}[n^{\text{D}}] + v_{\text{H}}^{\text{ddv,D}}[n^{\text{A}}])\Theta(-x) + (v_{\text{H}}[n^{\text{A}}] + v_{\text{H}}^{\text{ddv,A}}[n^{\text{D}}])\Theta(x) \quad (\text{D.4})$$

with the superscript index v that denotes the potential route, where

$$v_{\text{H}}^{\text{ddv,A}}[n^{\text{D}}] = \frac{N^{\text{D}}}{|\mathbf{r}^{\text{A}} + \mathbf{R}|} + \frac{\mathbf{d}^{\text{D}} \cdot (\mathbf{r}^{\text{A}} + \mathbf{R})}{|\mathbf{r}^{\text{A}} + \mathbf{R}|^3} + \sum_{j,k=1}^3 \frac{Q_{jk}^{\text{D}} R_j R_k}{2|\mathbf{r}^{\text{A}} + \mathbf{R}|^5} \quad (\text{D.5})$$

and

$$v_{\text{H}}^{\text{ddv,D}}[n^{\text{A}}] = \frac{N^{\text{A}}}{|\mathbf{r}^{\text{D}} - \mathbf{R}|} + \frac{\mathbf{d}^{\text{A}} \cdot (\mathbf{r}^{\text{D}} - \mathbf{R})}{|\mathbf{r}^{\text{D}} - \mathbf{R}|^3} + \sum_{j,k=1}^3 \frac{Q_{jk}^{\text{A}} R_j R_k}{2|\mathbf{r}^{\text{D}} - \mathbf{R}|^5}. \quad (\text{D.6})$$

Pub1 demonstrates that these two approaches result in potentials that differ qualitatively outside the regions where the density is high. From a comparison of the two potentials with the true Hartree potential, Pub1 concludes that  $v_{\text{H}}^{\text{ddv}}[n^{\text{D}}, n^{\text{A}}]$  is more appropriate as it exhibits the asymptotic decay to zero expected naturally from a physical potential.

Both ways of using Förster-type potentials are implemented in the PARSEC code. The Förster-type potential expansion feature can be (de)activated using the boolean flag `Use_foerster`. The input parameter `foerster_type` allows for the choice of the potential-determination route along the previous lines: “`foerster_type = 1`” is the default and uses Eq. (D.4), whereas “`foerster_type = 2`” uses Eq. (D.1). The separation of the grid into two half

spaces is always performed by the planes of the coordinate system that are perpendicular to the coordinate axes. To this end, one needs to indicate the desired coordinate axis “x”, “y”, or “z” via the input parameter *foerster\_half\_space* (*string*) and the partitioning is performed accordingly. To guarantee for consistent calculations, the selected scheme is used for the ground state and during real-time propagation throughout.

### D.1.2 Using Förster-type potentials in supermolecular systems

For the investigations on supermolecular systems of Chap. 5, I extended the Förster-type potential evaluation of the previous section to deal with more complicated molecular arrangements. This functionality may be (de)activated by the boolean flag *Use\_multi\_foerster* when “*Use\_foerster* = true”. The statements of the previous section concerning *foerster\_type* apply accordingly.

Two different types of arrangements, linear and circular ones, may be used to separate the entire grid into partitions, according to which one may place single molecules. These setups can be addressed by the integer input parameter *Foerster\_neighbor\_type*: numbers 1 to 3 correspond to linear arrangements, whereas numbers 10 and 11 imply circular setups. The PARSEC input block *Foerster\_centers* was implemented to define the position of the grid segments via the coordinates of their centers. For the sake of clearness, I use the term “hub” for these points in the following. Note that the hubs always need to be listed in consecutive order. In case of linear setups one additionally needs to specify the orientation of the alignment in terms of the coordinate axis using the parameter *foerster\_half\_space*. Then, the grid slicing is performed along each center line of neighboring hubs where center lines are perpendicular to the specified coordinate axis.

Circular setups are supposed to be arranged on a circle around the origin in the *x-y*-plane. The slicing is performed in terms of angles. If hubs are given via the input block *Foerster\_centers*, PARSEC computes the angles corresponding to the center lines that run through the origin and through the middle of all neighboring hubs. Here, the number of hubs should equal the number of wedges specified via the integer input parameter *Foerster\_wedge\_number*. The grid partitioning is performed along planes given by these center lines and the *z*-axis. When no hubs are defined, PARSEC performs an equidistant circular slicing while it assumes that the first molecule is positioned on the *x*-axis. In this case, one needs to give the number of wedges using the parameter *Foerster\_wedge\_number*.

Within each of these arrangements, one may choose between different ways of how the interaction between the subsystems is implemented. I start with the options that are available in the cases of linear arrangements. “*Foerster\_neighbor\_type* = 1” corresponds to an interaction between next neighbors only for all moments of the multipole series except for the monopole part. The latter contribution is by definition the most long-range one of the multipole series. It is important for reasonable absolute values of the potential and, therefore, needs to be applied also beyond next neighbors. In case of “*Foerster\_neighbor\_type* = 2”, PARSEC computes the pairwise interaction between all grid parts. “*Foerster\_neighbor\_type* = 3” models periodic boundary conditions: It computes the multipole moments of the last (first) molecule of linear arrangements and places a fictitious molecule with the same properties in front of the first (behind the last) molecule. The intermolecular interaction works only between next neighbors and assumes equidistant molecular spacing.

As this proceeding is just a crude approximation to periodic systems, the idea with

circular arrangements is to design “closed” systems where each molecule naturally has next neighbors on both sides and no explicit periodic boundary conditions need to be applied. In the circular setup of “*Foerster\_neighbor\_type* = 10”, the interaction contributions beyond the monopole term work only between next neighbors whereas monopole interaction applies between all molecules. “*Foerster\_neighbor\_type* = 11” uses pairwise interaction between all molecules of the setup.

### D.1.3 Partition-selective excitation and observation

For TD investigations, it may be relevant to excite only specific subsystems instead of the entire system. In cases where the previously explained partitioning is used, such subsystems can be related to partitions of the grid. In D-A systems where the separation is performed into two half spaces, such a feature can be controlled by the boolean flag *Use\_sel\_boost*. If “*Use\_sel\_boost* = true”, one may indicate via *boost\_half\_space* in which of the half spaces the excitation is supposed to work. This parameter reads a string with two positions where the first position discriminates between the negative (“n”) and the positive (“p”) side of the coordinate axis and the second position determines the axis (“x”, “y”, or “z”) along which the separation occurs.

A similar feature is implemented in case of more complex supermolecular systems by the integer input parameter *Excite\_center*. If “*Excite\_center* = 0”, the excitation is performed only in one of the half spaces of the grid, thus one additionally needs to specify *boost\_half\_space*. Alternatively, one may address the grid partition where excitation is performed via the hubs given by *Foerster\_centers*. To this end, one needs to set *Excite\_center* to the number corresponding to the position of the hub in the *Foerster\_centers* input list. Finally, the input option “*Excite\_center* = -1” deactivates selective excitation and the excitation process is applied in all partitions of the grid. Note that both space-selective excitation features may also be used independent of the Förster-type potential expansion.

In PARSEC calculations with multiple centers, some important observables are calculated not only in the entire system but also for each system partition separately. In cases of Förster-type potential approximations or selective excitation, the dipole moment and the integral over the density corresponding to each grid partition are written to the file “multi\_center.out” during time propagation. Here, the TD dipole moment is calculated relative to the centers of mass at the initial time  $t = 0$  corresponding to each grid partition.

## D.2 Unraveling the coupling strength with TDDFT

In this section, I briefly explain how the coupling strength and the energetic off-resonance in a system of one donor and one acceptor molecule manifest in the TD dipole moment. Note that the resonant coupling case was already discussed in Ref. [Hof08] and Pub1. The considerations employ a two-level model [Neu08] based on the assumption that the wave function of the total system can be separated into D and A parts due to negligible electronic coupling between D and A. To be able to employ the two-level picture, the excitation energies of interest of the true system need to be well separated from the energies of other excited states. Initially, the acceptor is in its ground state denoted by  $|A\rangle$  and the donor is in an excited state  $|D^*\rangle$ . This amounts to an initial product state  $|D^*A\rangle = |D^*\rangle|A\rangle = |1\rangle$ . The final wave function corresponds to the inverse situation, where  $|DA^*\rangle = |2\rangle$ . The states are

characterized by their eigenenergies  $E_1$  and  $E_2$ . One can measure the energetic off-resonances by the parameter

$$\Delta E = \frac{1}{2}(E_1 - E_2). \quad (\text{D.7})$$

The coupling between  $|1\rangle$  and  $|2\rangle$  is mediated by the Coulomb interaction  $V_C$ . It leads to the coupling-matrix element

$$V = \langle DA^* | V_C | D^* A \rangle. \quad (\text{D.8})$$

The time evolution of the two-state system with initial state  $|\Psi(0)\rangle = |1\rangle$  is given by

$$|\Psi(t)\rangle = a_1(t)|1\rangle + a_2(t)|2\rangle \quad (\text{D.9})$$

with the coefficients  $a_1(t)$  and  $a_2(t)$  [CTDF99],

$$\begin{aligned} |a_1(t)|^2 &= B + A \cos^2 \left( \sqrt{V^2 + \Delta E^2} t \right), \\ |a_2(t)|^2 &= A \sin^2 \left( \sqrt{V^2 + \Delta E^2} t \right), \end{aligned} \quad (\text{D.10})$$

where  $A = \frac{V^2}{V^2 + \Delta E^2}$  and  $B = \frac{\Delta E^2}{V^2 + \Delta E^2}$ . This time evolution of the coefficients corresponds to an incomplete oscillation with beat frequency  $\omega_{\text{beat}} = \sqrt{V^2 + \Delta E^2}$  that depends on the coupling between the initial and the final state as well as the energetic off-resonance: The occupation probability of the initial state varies around  $B$  with amplitude  $A$ , while the occupation probability of the final state oscillates with amplitude  $A$  around zero.

The TD dipole moment  $\mathbf{d}^A(t) = \langle \Psi(t) | \mathbf{r}^A | \Psi(t) \rangle$  of the acceptor, where I take the dipole operator  $\mathbf{r}^A$  in the space of the acceptor only, can be calculated as

$$\mathbf{d}^A(t) = |a_1(t)|^2 \langle A | \mathbf{r}^A | A \rangle + |a_2(t)|^2 \langle A^* | \mathbf{r}^A | A^* \rangle. \quad (\text{D.11})$$

Here, I exploited the orthogonality of  $|D\rangle$  and  $|D^*\rangle$ . If the static dipole moment  $\langle A | \mathbf{r}^A | A \rangle$  of  $A$  vanishes, Eq. (D.11) simplifies to

$$\mathbf{d}^A(t) = |a_2(t)|^2 \langle A^* | \mathbf{r}^A | A^* \rangle. \quad (\text{D.12})$$

Accordingly, with the assumption that the static  $D$  dipole moment vanishes, the TD donor dipole moment reads

$$\mathbf{d}^D(t) = |a_1(t)|^2 \langle D^* | \mathbf{r}^D | D^* \rangle. \quad (\text{D.13})$$

Thus, the resonance oscillation of the coefficients can be observed in the time evolution of the dipole moments  $\mathbf{d}^A(t)$  and  $\mathbf{d}^D(t)$ . In principle both Eqs. (D.12) and (D.13) can be used to determine  $V$ . Of special importance is Eq. (D.13) together with Eq. (D.10): A fit to the absolute of the extrema of the  $k$ -th component of the  $D$  dipole moment time evolution provides  $A p_k$ ,  $B p_k$ , and  $\omega_{\text{beat}}$ , where  $p_k = \langle D^* | r_k^D | D^* \rangle$ . It can be used to determine  $V$ ,  $\Delta E$ , and  $p_k$ . One obtains

$$V = \sqrt{\frac{A p_k}{A p_k + B p_k}} \omega_{\text{beat}} \quad (\text{D.14})$$

and

$$\Delta E = \sqrt{\frac{B p_k}{A p_k + B p_k}} \omega_{\text{beat}}. \quad (\text{D.15})$$

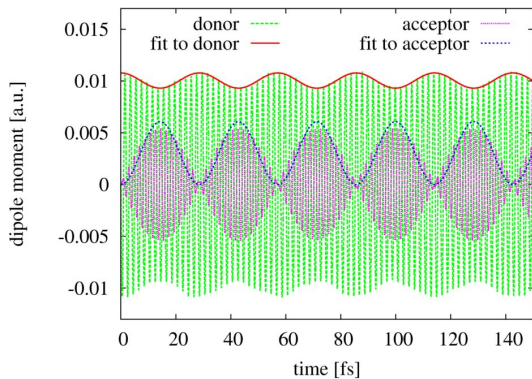


Figure D.1: Donor and acceptor dipole moment ( $z$ -component) in a setup of two  $\text{Na}_2$ , where the bond length of the acceptor  $\text{Na}_2$  is reduced by 0.5 bohr compared to the experimental bond length. I performed fits to the envelope of the oscillation according to the model discussed in the text.

A typical time evolution of the  $z$ -component of the D and A dipole moments of the model system is depicted in Fig. D.1 together with fits to the corresponding envelopes. Note that the two-level model qualitatively fits to the dipole oscillation of the off-resonant, coupled system of two molecules. However, the dipole moment envelopes do not perfectly follow the  $\sin^2$ - and  $\cos^2$ -shape. I understand these deviations as a consequence of the coupled system not being perfectly separable into D and A parts as one assumes in the model. Furthermore, although the second excitation of  $\text{Na}_2$  with polarization in  $z$ -direction is energetically far off and carries notably smaller oscillator strength,  $\text{Na}_2$  is not a perfect single level system. Therefore, the system of two sodium dimers does not perfectly fit into the two-level model. Nevertheless, the approach provides a tool to determine the coupling  $V$  and the energetic off-resonance  $\Delta E$ . The validity of the model can be checked by comparison of the thus obtained  $\Delta E$  to TDDFT excitation energies. Two different ways are available for calculating the latter: either from straight forward TDDFT propagation of one dimer with shifted bond length or along the just presented route. I performed both methods and found good agreement. Therefore, I assume reasonable quality of the coupling-matrix element results of Fig. 5.1.

## D.3 Stochastic time-dependent density functional theory

### D.3.1 An attempt towards a theoretical justification of stochastic time-dependent density functional theory with specific bath operators

Establishing an open quantum system scheme in the framework of TDDFT is highly relevant for studying large scale systems in contact with some effective environment. However, its theoretical foundation suffers from conceptual difficulties as I explain in Sec. 5.2.2. In this section, I supplement already existing approaches of proving open quantum system schemes in the TD(C)DFT framework. The underlying idea is based on the SSE and transparently illustrates how the range of possible bath operators is restricted to guarantee for the existence of an auxiliary system that reproduces the same density as the original interacting open quantum system of interest. The assumptions on the range of bath operators are guided by the attempt to avoid current density dependent contributions where  $v$ -representability is questionable [DV05]. The idea of proof was developed to establish the existence of a non-interacting open quantum system that reproduces the density of an interacting open quantum system for the bath operator that I introduced in Sec. 5.3.2. The applicability of

the idea of proof to this bath operator is discussed critically at the end of this section.

The attempt towards a proof of stochastic TDDFT starts from the system Hamiltonian

$$H_S = \sum_{i=1}^N \left[ \frac{\mathbf{p}_i^2}{2} + v_{\text{ext}}(\mathbf{r}_i, t) \right] + \sum_{i<j}^N W(\mathbf{r}_i - \mathbf{r}_j) \quad (\text{D.16})$$

without vector potentials. The initial state of the wave function  $\Psi$  at  $t = t_0$  is  $\Psi_0$ . I follow the reasoning of van Leeuwen [vL99] and consider the equations of motion of the ensemble-averaged density (see Eq. (5.13)) and of the ensemble-averaged current density

$$\partial_t \overline{j_k(\mathbf{r}, t)} = -\overline{n(\mathbf{r}, t)} \partial_k v_{\text{ext}}(\mathbf{r}, t) - \overline{\langle \psi(t) | \sum_{i=1}^3 \partial_i T_{ik}(\mathbf{r}) | \psi(t) \rangle} - \overline{\langle \psi(t) | W_k(\mathbf{r}) | \psi(t) \rangle} + \mathcal{G}_{Bk}(\mathbf{r}, t), \quad (\text{D.17})$$

where the  $k$ -th component of the current density modulation that is induced by the bath is described by

$$\mathcal{G}_{Bk}(\mathbf{r}, t) = \frac{1}{2} \overline{\langle 2S^\dagger j_k(\mathbf{r}, t) S - S^\dagger S j_k(\mathbf{r}, t) - j_k(\mathbf{r}, t) S^\dagger S \rangle}. \quad (\text{D.18})$$

Here, I adopted the notation of van Leeuwen [vL99] for the momentum-stress tensor  $T_{ik}(\mathbf{r})$  and the gradient of the particle-particle interaction  $W_k(\mathbf{r})$ . Moreover, I apply van Leeuwen's physical assumptions on the shape of the external potential and its analyticity in time [vL99]. By taking the time derivative of Eq. (5.13) and the divergence of Eq. (D.17) one obtains

$$\partial_t^2 \overline{n(\mathbf{r}, t)} = \nabla \left[ \overline{n(\mathbf{r}, t)} \nabla v_{\text{ext}}(\mathbf{r}, t) \right] + q(\mathbf{r}, t) - \nabla \mathcal{G}_B(\mathbf{r}, t) + \partial_t \mathcal{F}_B(\mathbf{r}, t), \quad (\text{D.19})$$

where

$$q(\mathbf{r}, t) = \overline{\langle \psi(t) | \sum_{i=1}^3 \sum_{k=1}^3 \partial_i \partial_k T_{ik}(\mathbf{r}) + \sum_{k=1}^3 \partial_k W_k(\mathbf{r}) | \psi(t) \rangle}. \quad (\text{D.20})$$

To investigate the one-to-one correspondence between the external potential and the ensemble-averaged density, I put some restrictions on the functional dependence of  $\mathcal{F}_B(\mathbf{r}, t)$  and  $\mathcal{G}_B(\mathbf{r}, t)$  on  $\overline{n(\mathbf{r}, t)}$  and  $\overline{\mathbf{j}(\mathbf{r}, t)}$ . I assume that  $\mathcal{F}_B(\mathbf{r}, t)$  depends on  $\overline{n(\mathbf{r}, t)}$  only and  $\mathcal{G}_B(\mathbf{r}, t)$  exhibits the general form

$$\mathcal{G}_B(\mathbf{r}, t) = a[\overline{n(\mathbf{r}, t)}](t) \overline{\mathbf{j}(\mathbf{r}, t)} + b[\overline{n(\mathbf{r}, t)}](t) \overline{\mathbf{j}(\mathbf{r}, t_0)} + \mathbf{c}[\overline{n(\mathbf{r}, t)}](\mathbf{r}, t). \quad (\text{D.21})$$

Here,  $a$  and  $b$  are arbitrary scalar functions that may depend on  $\overline{n(\mathbf{r}, t)}$  and  $t$ , whereas  $\mathbf{c}$  is a general vector that may depend on  $\overline{n(\mathbf{r}, t)}$ ,  $\mathbf{r}$ , and  $t$ . The question whether bath operators that fulfill these assumptions exist is discussed below. One obtains

$$\begin{aligned} \partial_t^2 \overline{n(\mathbf{r}, t)} = & \nabla \left[ \overline{n(\mathbf{r}, t)} \nabla v_{\text{ext}}(\mathbf{r}, t) \right] + q(\mathbf{r}, t) + \partial_t \mathcal{F}_B(\mathbf{r}, t) \\ & - a[\overline{n(\mathbf{r}, t)}](t) \nabla \overline{\mathbf{j}(\mathbf{r}, t)} - b[\overline{n(\mathbf{r}, t)}](t) \nabla \overline{\mathbf{j}(\mathbf{r}, t_0)} - \nabla \mathbf{c}[\overline{n(\mathbf{r}, t)}](\mathbf{r}, t) \end{aligned} \quad (\text{D.22})$$

by inserting  $\mathcal{G}_B(\mathbf{r}, t)$  of Eq. (D.21) into Eq. (D.19). Finally,  $\nabla \overline{\mathbf{j}(\mathbf{r}, t)}$  and  $\nabla \overline{\mathbf{j}(\mathbf{r}, t_0)}$  can be substituted using the continuity equation (5.13) and one arrives at

$$\begin{aligned} \partial_t^2 \overline{n(\mathbf{r}, t)} = & \nabla \left[ \overline{n(\mathbf{r}, t)} \nabla v_{\text{ext}}(\mathbf{r}, t) \right] + q(\mathbf{r}, t) + \partial_t \mathcal{F}_B(\mathbf{r}, t) \\ & + a[\overline{n(\mathbf{r}, t)}](t) \partial_t \overline{n(\mathbf{r}, t)} - a[\overline{n(\mathbf{r}, t)}](t) \mathcal{F}_B(\mathbf{r}, t) \\ & + b[\overline{n(\mathbf{r}, t)}](t) \left. \partial_t \overline{n(\mathbf{r}, t)} \right|_{t_0} - b[\overline{n(\mathbf{r}, t)}](t) \mathcal{F}_B(\mathbf{r}, t_0) - \nabla \mathbf{c}[\overline{n(\mathbf{r}, t)}](\mathbf{r}, t). \end{aligned} \quad (\text{D.23})$$

Equation (D.23) directly relates the external potential to the ensemble-averaged density without need for the current density.

Based on an equation similar to Eq. (D.23), van Leeuwen shows with his original proof that the density of a closed quantum system can be reproduced by an auxiliary system with Hamiltonian

$$H'_S = \sum_{i=1}^N \left[ \frac{\mathbf{p}_i^2}{2} + v'_{\text{ext}}(\mathbf{r}_i, t) \right] + \sum_{i<j}^N W'(\mathbf{r}_i - \mathbf{r}_j) \quad (\text{D.24})$$

which contains a different particle-particle interaction  $W'$  and external potential  $v'_{\text{ext}}$ . The auxiliary system starts from the initial state  $\Phi_0$  and the potential  $v'_{\text{ext}}$  vanishes at infinity as  $v_{\text{ext}}$  does. The van Leeuwen proof relies on some initial and boundary conditions for the density and current density: The density of both systems needs to be equal, i.e.,

$$\langle \Phi_0 | n(\mathbf{r}) | \Phi_0 \rangle = \langle \Psi_0 | n(\mathbf{r}) | \Psi_0 \rangle. \quad (\text{D.25})$$

Both systems need to start from the same time derivative of the density, i.e.,  $\partial_t n'(\mathbf{r}, t) = \partial_t n(\mathbf{r}, t)$  at  $t = t_0$ , and one obtains via the continuity equation

$$\langle \Phi_0 | \nabla \mathbf{j}(\mathbf{r}) | \Phi_0 \rangle = \langle \Psi_0 | \nabla \mathbf{j}(\mathbf{r}) | \Psi_0 \rangle. \quad (\text{D.26})$$

To apply the van Leeuwen construction scheme of the external potential of the auxiliary system in the open quantum system case with bath operator  $S'$ , I adopt equivalent initial and boundary conditions for the corresponding ensemble-averaged properties. However, due to the presence of  $\mathcal{F}_B(\mathbf{r}, t)$  and  $\mathcal{G}_B(\mathbf{r}, t)$ , some further requirements on the action of the bath operator need to be introduced in the auxiliary system. I assume that the modulations of the density equation of motion that are induced by the bath need to be both density dependent only and identical at  $t = t_0$ , i.e.,  $\mathcal{F}_B(\mathbf{r}, t_0) = \mathcal{F}'_B(\mathbf{r}, t_0)$ . Moreover,  $\mathcal{G}'_B(\mathbf{r}, t)$  needs to have the same structure as  $\mathcal{G}_B(\mathbf{r}, t)$ , so that

$$\mathcal{G}'_B(\mathbf{r}, t) = a'[\overline{n'(\mathbf{r}, t)}](t)\overline{\mathbf{j}'(\mathbf{r}, t)} + b'[\overline{n'(\mathbf{r}, t)}](t)\overline{\mathbf{j}'(\mathbf{r}, t_0)} + \mathbf{c}'[\overline{n'(\mathbf{r}, t)}](\mathbf{r}, t). \quad (\text{D.27})$$

Here,  $a'$ ,  $b'$ , and  $\mathbf{c}'$  correspond to the quantities of the original system in terms of their dependence on  $\overline{n'(\mathbf{r}, t)}$ ,  $\mathbf{r}$ , and  $t$ . These requirements imply that one needs to find a bath operator  $S'$  in the auxiliary system that leads to a density-only dependent  $\mathcal{F}'_B(\mathbf{r}, t)$  with initial condition  $\mathcal{F}_B(\mathbf{r}, t_0) = \mathcal{F}'_B(\mathbf{r}, t_0)$ , a linear current density dependence of  $\mathcal{G}'_B(\mathbf{r}, t)$ , and density dependent coefficients  $a'$ ,  $b'$ , and  $\mathbf{c}'$ . Thus, the auxiliary system follows the equation

$$\begin{aligned} \partial_t^2 \overline{n'(\mathbf{r}, t)} = & \nabla \left[ \overline{n'(\mathbf{r}, t)} \nabla v'_{\text{ext}}(\mathbf{r}, t) \right] + q'(\mathbf{r}, t) + \partial_t \mathcal{F}'_B(\mathbf{r}, t) \\ & + a'[\overline{n'(\mathbf{r}, t)}](t) \partial_t \overline{n'(\mathbf{r}, t)} - a'[\overline{n'(\mathbf{r}, t)}](t) \mathcal{F}'_B(\mathbf{r}, t) \\ & + b'[\overline{n'(\mathbf{r}, t)}](t) \left. \partial_t \overline{n'(\mathbf{r}, t)} \right|_{t_0} - b'[\overline{n'(\mathbf{r}, t)}](t) \mathcal{F}'_B(\mathbf{r}, t_0) - \nabla \mathbf{c}'[\overline{n'(\mathbf{r}, t)}](\mathbf{r}, t) \end{aligned} \quad (\text{D.28})$$

which is similar to Eq. (D.23) with all system specific properties being primed.

If one assumes that both systems have the same ensemble-averaged density, i.e.,  $\overline{n(\mathbf{r}, t)} = \overline{n'(\mathbf{r}, t)}$ , one obtains by subtracting Eqs. (D.23) and (D.28)

$$\nabla \left[ \overline{n(\mathbf{r}, t)} \nabla \omega(\mathbf{r}, t) \right] = \zeta(\mathbf{r}, t), \quad (\text{D.29})$$

where  $\omega(\mathbf{r}, t) = v_{\text{ext}}(\mathbf{r}, t) - v'_{\text{ext}}(\mathbf{r}, t)$  and

$$\begin{aligned} \zeta(\mathbf{r}, t) &= q'(\mathbf{r}, t) - q(\mathbf{r}, t) + \partial_t [\mathcal{F}'_{\text{B}}(\mathbf{r}, t) - \mathcal{F}_{\text{B}}(\mathbf{r}, t)] \\ &\quad + \left[ a'[\overline{n(\mathbf{r}, t)}](t) - a[\overline{n(\mathbf{r}, t)}](t) \right] \partial_t \overline{n(\mathbf{r}, t)} - a'[\overline{n(\mathbf{r}, t)}](t) \mathcal{F}'_{\text{B}}(\mathbf{r}, t) \\ &\quad + a[\overline{n(\mathbf{r}, t)}](t) \mathcal{F}_{\text{B}}(\mathbf{r}, t) + \left[ b'[\overline{n(\mathbf{r}, t)}](t) - b[\overline{n(\mathbf{r}, t)}](t) \right] \partial_t \overline{n(\mathbf{r}, t)} \Big|_{t_0} \\ &\quad - b'[\overline{n(\mathbf{r}, t)}](t) \mathcal{F}'_{\text{B}}(\mathbf{r}, t_0) + b[\overline{n(\mathbf{r}, t)}](t) \mathcal{F}_{\text{B}}(\mathbf{r}, t_0) \\ &\quad - \nabla \mathbf{c}'[\overline{n(\mathbf{r}, t)}](\mathbf{r}, t) + \nabla \mathbf{c}[\overline{n(\mathbf{r}, t)}](\mathbf{r}, t). \end{aligned} \quad (\text{D.30})$$

The first two terms of Eq. (D.30) equal the contributions of the van Leeuwen construction, whereas all other terms come from the influence of the bath and depend only on the ensemble-averaged density. Note that no explicitly current-density-dependent terms occur as I aimed at when setting up the assumptions for the structure of  $\mathcal{F}_{\text{B}}$  and  $\mathcal{G}_{\text{B}}$ . As Eq. (D.29) is of Sturm-Liouville type, a unique solution for  $\omega(\mathbf{r}, t)$  exists if  $\overline{n(\mathbf{r}, t)}$  and  $\zeta(\mathbf{r}, t)$  are known [vL99]. From here on, the idea is to follow the rationale of Ref. [vL99]: Solve Eq. (D.29) at  $t = t_0$  and consecutively compute its time derivatives to construct  $v'_{\text{ext}}(\mathbf{r}, t)$  from its Taylor series order by order in time within the convergence radius of the Taylor expansion. Note that the potential  $v'_{\text{ext}}(\mathbf{r}, t) + C(t)$  produces the same density as the system is not sensitive to a purely TD shift  $C(t)$  of the potential. In the van Leeuwen construction scheme [vL99], the choice of the boundary condition of  $\omega(\mathbf{r}, t)$  at infinity fixes a particular gauge of the potential  $v'_{\text{ext}}(\mathbf{r}, t)$ , thus determines the arbitrary constant  $C(t)$ .

In summary, the just presented rationale indicates: If one restricts the range of allowed bath operators and uses reasonable initial and boundary conditions the ensemble-averaged density  $\overline{n(\mathbf{r}, t)}$  obtained from an open quantum system with Hamiltonian  $H_{\text{S}}$ , bath operator  $S$ , and initial state  $\Psi_0$  can be reproduced by an auxiliary open quantum system with different particle-particle interaction  $W'$  and initial state  $\Phi_0$ . The external potential  $v'_{\text{ext}}(\mathbf{r}, t)$  – determined up to a purely TD function  $C(t)$  – is uniquely defined as long as the bath operator  $S'$  is chosen adequately. Thus, within the assumptions discussed above, a one-to-one correspondence between the external potential and  $\overline{n(\mathbf{r}, t)}$  exists, and the approach can be used for open quantum KS systems with a TDDFT Hamiltonian and a suitable external potential.

The potential obtained along this construction scheme may depend strongly on the choice of the bath operators  $S$  and  $S'$ . Therefore, I consider one special case of the previous assumptions where the density dependence of the action of the bath operator on the equation of motion of the ensemble-averaged density and current density is the same in the original and the auxiliary system, i.e.,  $\mathcal{F}_{\text{B}}(\mathbf{r}, t) = \mathcal{F}'_{\text{B}}(\mathbf{r}, t)$ ,  $a = a'$ ,  $b = b'$ , and  $\mathbf{c} = \mathbf{c}'$ . In this case Eq. (D.30) reduces to

$$\zeta(\mathbf{r}, t) = q'(\mathbf{r}, t) - q(\mathbf{r}, t), \quad (\text{D.31})$$

thus equals the term of van Leeuwen's closed quantum system proof, yet with ensemble-averaged quantities. Here, the potential  $v'_{\text{ext}}(\mathbf{r}, t)$  is determined by  $\zeta(\mathbf{r}, t)$  only, as both bath operators have by construction the same influence on the equations of motion of  $\overline{n(\mathbf{r}, t)}$  and  $\overline{\mathbf{j}(\mathbf{r}, t)}$  in the original and the primed system.

Finally, I discuss the practical value of the just presented strategy. To this end, I consider a bath operator in the original SSE that is motivated in analogy to the single-particle bath

operator of Sec. 5.3.2: The bath operator

$$S = \sqrt{\gamma}|\Psi(t_0)\rangle\langle\Psi(t)| \quad (\text{D.32})$$

induces relaxation of the excited system back to its ground state with the decay rate  $\gamma$ . Inserting  $S$  into the formula for  $\mathcal{F}_B(\mathbf{r}, t)$  yields

$$\mathcal{F}_B(\mathbf{r}, t) = \gamma \left[ \overline{\langle\Psi(t)|\Psi(t)\rangle\langle\Psi(t)|\Psi(t)\rangle} n(\mathbf{r}, t_0) - \overline{\langle\Psi(t)|\Psi(t)\rangle\langle\Psi(t)|n(\mathbf{r})|\Psi(t)\rangle} \right]. \quad (\text{D.33})$$

The wave functions that are solutions of the SSE are normalized only in the ensemble average up to fourth order in the coupling parameter  $\lambda$ , i.e., not every ensemble member itself is normalized. Therefore, focusing on the second term of Eq. (D.33), one cannot simply split the statistical average of this term in two factors because in general

$$\overline{\langle\Psi(t)|\Psi(t)\rangle\langle\Psi(t)|n(\mathbf{r})|\Psi(t)\rangle} \neq \overline{\langle\Psi(t)|\Psi(t)\rangle} \overline{\langle\Psi(t)|n(\mathbf{r})|\Psi(t)\rangle} = (1 + \mathcal{O}(\lambda^4)) \overline{\langle\Psi(t)|n(\mathbf{r})|\Psi(t)\rangle}. \quad (\text{D.34})$$

The same problem occurs also when setting up  $\mathcal{F}'_B(\mathbf{r}, t)$  using the KS reference system together with the bath operator

$$S' = \sqrt{\gamma}|\Phi(t_0)\rangle\langle\Phi(t)| \quad (\text{D.35})$$

that is supposed to model a bath mechanism that is equivalent to  $S$  in the stochastic TD KS equation (5.12) using the stochastic TDDFT KS Hamiltonian

$$H'_{\text{KS}}(\{\mathbf{r}_k\}, t) = \sum_{i=1}^N \left[ -\frac{\nabla_i^2}{2} + v'_H(\mathbf{r}_i, t) + v'_{\text{xc}}(\mathbf{r}_i, t) + v_{\text{ext}}(\mathbf{r}_i, t) \right], \quad (\text{D.36})$$

where  $v'_{\text{xc}}$  needs to be computed from  $v'_H$ ,  $v_{\text{ext}}$ , and the corresponding  $v'_{\text{ext}}$ .

For the connection between the bath operators  $S$  and  $S'$  and the idea of proof presented above, it remains to be argued that  $\mathcal{F}_B(\mathbf{r}, t)$  and  $\mathcal{F}'_B(\mathbf{r}, t)$  are pure functionals of the ensemble-averaged density, i.e., one needs to establish a relation like

$$\overline{\langle\Psi(t)|\Psi(t)\rangle\langle\Psi(t)|n(\mathbf{r})|\Psi(t)\rangle} = f[n(\mathbf{r}, t)] \overline{\langle\Psi(t)|n(\mathbf{r})|\Psi(t)\rangle} \quad (\text{D.37})$$

and corresponding relations for the KS system, where  $f$  is some unique functional of  $\overline{n(\mathbf{r}, t)}$ . An analogous problem appears also when one investigates the dependence of  $\mathcal{G}_B(\mathbf{r}, t)$  and  $\mathcal{G}'_B(\mathbf{r}, t)$  on the ensemble-averaged density and current density. Relations such as Eq. (D.37), similar relations for statistical correlations that emerge in  $\mathcal{G}_B(\mathbf{r}, t)$ , and the corresponding contributions in the KS system remain to be investigated.

From a practical point of view, one could consult the quantum-jump (qj) algorithm [DCM92, GPZ92, BP95, BP06] in order to get a grip on the problem with the statistical correlations. The piecewise deterministic evolution performed in the quantum-jump algorithm preserves the norm of each ensemble member  $\Psi^{\text{qj}}$ . Thus, the problem with the statistical correlations of the above discussion is avoided as  $\langle\Psi^{\text{qj}}(t)|\Psi^{\text{qj}}(t)\rangle = 1$  for each ensemble member.  $\mathcal{F}_B(\mathbf{r}, t)$ ,  $\mathcal{F}'_B(\mathbf{r}, t)$ ,  $\mathcal{G}_B(\mathbf{r}, t)$ , and  $\mathcal{G}'_B(\mathbf{r}, t)$  computed with  $S$  and  $S'$  would then exhibit the dependencies on  $n(\mathbf{r}, t)$  and  $\mathbf{j}(\mathbf{r}, t)$  required for the idea of proof.

For solving the open system KS equation (5.12) based on the stochastic TDDFT Hamiltonian of Eq. (D.36) with the quantum-jump algorithm, one needs to propagate the norm-preserving equation

$$i\partial_t\Phi = H'_{\text{KS}}\Phi - \frac{i}{2}S'^{\dagger}S'\Phi + \frac{i}{2}\|S'\Phi\|^2\Phi \quad (\text{D.38})$$

and simultaneously also the auxiliary equation

$$i\partial_t\Phi^{\text{aux}} = H'_{\text{KS}}\Phi^{\text{aux}} - \frac{i}{2}S'^{\dagger}S'\Phi^{\text{aux}}, \quad (\text{D.39})$$

where the norm of the auxiliary system decays. The scheme of Ref. [WT79] to transfer these equations to two sets of  $N$  single-particle equations applies when one uses  $S'$  of Eq. (D.35). One can demonstrate that the resulting equations equal the equations of the single-particle quantum-jump algorithm of Sec. 5.2.2 if one takes the single-particle bath operator

$$s'_i = \sqrt{\gamma}|\varphi_i(t_0)\rangle\langle\varphi_i(t)|. \quad (\text{D.40})$$

In summary, it is possible to find a single-particle version of the quantum-jump algorithm according to the scheme of Sec. 5.2.2 for simulating the open quantum system KS equation (5.12) when using the TDDFT Hamiltonian of Eq. (D.36) and the bath operator  $S'$  of Eq. (D.35). Note that the dipole-dependent factor of the single-particle bath operator of Eq. (5.19) can be included straight forwardly to this rationale by introducing a time-dependent damping factor  $\tilde{\gamma}(t) = \gamma|\mathbf{d}_k(t) - \mathbf{d}_k(t_0)|^2/D^2$  to  $s'_i$  instead of  $\gamma$  that takes the purely density-dependent dipole moment into account.

### D.3.2 Bath operators in the single-particle KS framework and related features

The choice of the bath operator is at the heart of the applicability of the open quantum system TDDFT scheme. On the one hand, the bath operator models the underlying physics of the bath mechanism, thus needs to be motivated by physical processes. On the other hand, it is important for the theoretical foundation of the open quantum system TDDFT framework and the existence of a single-particle scheme. Here, I introduce four heuristically motivated bath operators. All four bath operators are designed for the single-particle framework of KS TDDFT. They involve projection operators and induce relaxation of the entire excited system back to its ground state via projection to the occupied ground-state KS orbitals. The rationale behind these operators and their implementation is explained in the following.

The central idea behind the first bath operator is to interpret the differences between eigenvalues of occupied and unoccupied KS orbitals as excitation energies of the system. In this sense, one obtains, e.g., an excited state by replacing one of the occupied orbitals of the GS system by one of the higher lying unoccupied KS orbitals. Then, relaxation to the ground state may be performed if one detects the overlap of the time evolution of each orbital of this system with the space of all (or at least the most important) unoccupied orbitals and projects back to the ground state. To model this behavior with single-particle operators, the first bath operator  $s_i^{(1)}$  uses a large basis of  $M$  occupied and unoccupied KS orbitals, computes the overlap of all TD KS orbitals to these basis functions, and projects onto the corresponding GS orbital depending on the magnitude of the overlap [PDV08, ADV11]. This bath operator reads

$$s_i^{(1)} = \sqrt{\gamma} \sum_{j=i+1}^M |\varphi_i(t_0)\rangle\langle\varphi_j(t_0)|, \quad (\text{D.41})$$

where I use all KS eigenstates with an eigenvalue that is energetically above the eigenvalue of the reference orbital  $\varphi_i(t_0)$  and project back to the latter orbital. The factor  $\sqrt{\gamma}$  includes the

decay rate  $\gamma$  corresponding to the decay time  $\tau = 1/\gamma$ . Although this type of bath operator may be used to model interesting physics, to the best of my knowledge there is no explicit proof available that guarantees for its validity in the stochastic TDDFT framework of open quantum system theory. Therefore, I investigated alternative types of bath operators for the work that is presented in Sec. 5.3 and used  $s_i^{(1)}$  only for test calculations and implementing the algorithms.

The second class of bath operators induces relaxation of the excited system back to its ground state via projectors of the TD KS orbitals onto the corresponding GS orbitals. Such operators are motivated and introduced in Sec. 5.3.2. Here, I shortly outline a generalized version of this bath operator together with its implementation to the PARSEC code. The time constant of the decay process is given by the decay rate  $\gamma$ . One additional multiplicative factor renders this type of bath operator sensitive to variations of the multipole moments of the entire density or to such moments of particular subsystems. For reasons of a notation consistent with the PARSEC input that is explained in Sec. D.3.3, this bath operator is labeled by the superscript (4) and reads

$$s_i^{(4)} = \sqrt{\gamma} \frac{|\mathbf{d}_k(t) - \mathbf{d}_k(t_0)|}{D} |\varphi_i(t_0)\rangle \langle \varphi_i(t)|, \quad (\text{D.42})$$

where  $\gamma$  is an effective decay rate. The operator is proportional to variations  $|\mathbf{d}_k(t) - \mathbf{d}_k(t_0)|$  of the dipole moment  $\mathbf{d}_k(t) = \int \mathbf{r} n_k(\mathbf{r}, t) d^3r$  of the subsystem indicated by the index  $k$ . Here, the index  $k$  denotes a specific part of the grid using a particular partitioning scheme of the grid (see Sec. D.1 for further details about grid partition ideas). The density  $n_k(\mathbf{r}, t)$  is the density that corresponds only to subsystem  $k$ . Thus, this operator causes deexcitation of the entire system, but is sensitive to local changes of the dipole moment from the corresponding GS values during time propagation.  $D$  denotes a normalization factor of the dipole moment variations. In this approach, the time constant related to the rate  $\gamma$  of the dissipative mechanism is a free parameter, whereas  $D$  needs to be chosen reasonably as discussed in detail in Sec. 5.3.2. An attempt towards the theoretical justification of the use of this bath operator modulo the dipole-dependent factor in the framework of stochastic TDDFT using single-particle KS equations is outlined in Sec. D.3.1.

Another approach to define bath operators involves besides to the KS orbitals also localized orbitals  $\{\varphi_\kappa^{\text{loc}}(t_0)\}$ , where localization is performed according to the Foster-Boys criterion. The rationale behind this idea is to find bath operators that act in a restricted part of the grid. To this end, they measure the spatial localization in a specific region of the grid by calculating the overlap of the  $K$  localized orbitals  $\varphi_\kappa^{\text{loc}}(t_0)$  and the KS orbital onto which the operator acts. Here, the localized orbitals are dedicated and selected to represent orbitals that correspond to subsystems localized in particular parts of the entire grid. Therefore, instead of using the KS orbitals as in  $s_i^{(4)}$ , the bath operator  $s_i^{(2)}$  uses Foster-Boys orbitals in the projector that are computed from localization of the occupied ground-state KS orbitals and projects onto the corresponding ground-state KS orbital, i.e.,

$$s_i^{(2)} = \sum_{\kappa=1}^K \sqrt{\gamma} \frac{|\mathbf{d}_k(t) - \mathbf{d}_k(t_0)|}{D} |\varphi_i(t_0)\rangle \langle \varphi_\kappa^{\text{loc}}(t_0)|. \quad (\text{D.43})$$

The dipole-moment-sensitive factor guarantees for the dependence of the action of this bath operator on the dipole moment. Alternatively, bath operator  $s_i^{(3)}$  resembles the previous

operator, but does not include the dipole-moment-sensitive factor. Instead, it uses Foster-Boys orbitals computed not only from the occupied GS orbitals, but also takes unoccupied KS orbitals into account. Among these, PARSEC selects all  $Z$  orbitals  $\varphi_{\zeta}^{\text{loc}}(t_0)$  that are localized in a predefined part of the grid. The bath operator reads

$$s_i^{(3)} = \sum_{\zeta=1}^Z \sqrt{\gamma} |\varphi_i(t_0)\rangle \langle \varphi_{\zeta}^{\text{loc}}(t_0)|. \quad (\text{D.44})$$

Yet, to the best of my knowledge, the application of bath operators that rely on localized orbitals computed from ground-state KS orbitals in the context of stochastic TDDFT is not based on a solid theoretical proof. The first tests of these operators revealed difficulties that might be related to the interplay of localized Foster-Boys and delocalized KS orbitals in single-particle projection operators. Nevertheless, using localized orbitals to design spatially localized bath operators might be a promising route for further bath-operator development based on projection operator formalisms. In particular, it might be interesting to investigate the application of localized orbitals computed from the TD KS orbitals during time propagation.

For bath operators that relax the excited system back to its ground state, some practical advantages appear in the quantum-jump algorithm of Sec. 5.2.2: If no TD external perturbations occur after the initial excitation, the system remains in the ground state after each quantum jump. As a consequence, the time evolutions of all orbitals of the stochastic ensemble follow the same pattern: The KS system evolves deterministically until a quantum jump occurs. Then, back in the ground state, the system propagates trivially with TD phases according to the KS eigenvalues as acting with the bath operator on the ground state does not change the system. Therefore, the entire statistical ensemble can be generated from a single deterministic evolution of Eq. (5.16) alongside with the determination of the waiting-time distribution:

- (i) calculate a sufficiently long deterministic evolution together with the norm decay of the auxiliary system
- (ii) draw random numbers, find the points of time of a large number of quantum jumps, and determine the waiting-time distribution
- (iii) generate single trajectories of the ensemble where the time evolution up to the jump is determined by the deterministic evolution and GS values are used for the time after the jump

The physical quantities of interest follow from averaging over the observables calculated from the thus obtained statistical ensemble. Finally, note that I perform orthogonalization at the end of each time step as suggested in Ref. [ADV11] in case of bath operators  $s_i^{(1)}$  to  $s_i^{(3)}$ , whereas orthogonality is preserved in bath operator (4).

### D.3.3 PARSEC features and input parameters

The final section of this appendix is dedicated to an explanation of the PARSEC input parameters related to the stochastic TDDFT (STDDFT) implementation. Additional general remarks concerning the PARSEC input and especially the input data types are compiled in

Sec. E.1. All STDDFT functionalities may be (de)activated by the boolean flag *Use\_stdfft*. When STDDFT calculations are performed, the most important choice is the selection of the bath operator via the integer input parameter *Bath\_Type*. The numbers that specify the different operators correspond to the numbers in parenthesis that I used in the superscripts of Eqs. (D.41) to (D.44) to label the different operators in the previous section. One needs to specify these numbers using the integer input parameter *Bath\_operators* to choose among the bath operators. Yet, in the current version only a single type of bath operator can be used per PARSEC run. Either the decay rate or the decay time need to be set for this bath operator using the input parameters *Decay\_rate* (*double precision*) or *Decay\_time* (*physical*). In the cases of bath operators (2)-(4) that involve either dipole moments of local subsystems or Foster-Boys localized orbitals, one needs to specify the grid partition to which the bath operator is supposed to be sensitive. This information may be provided via the input block *Damping\_centers*, where PARSEC expects the index of the desired partition (see Sec. D.1) in the first column and, in the second column, the normalization factor *D* corresponding to the molecule that is located in the indicated partition. The determination of this normalization factor is explained in Sec. 5.3.2. If localized orbitals are involved, the localization threshold may be set via the parameter *Localization\_threshold* (*double precision*).

A partition-selective excitation may be performed as explained in Sec. D.1.3. Alternatively, in case of bath operator (1), excitation may be performed within the KS system by replacing one of the occupied orbitals of the KS GS configuration by one of the energetically higher lying unoccupied orbitals. The present PARSEC implementation provides means to replace the HOMO orbital by the LUMO. This feature can be (de)activated by the boolean flag *Switch\_orb*. A partition-selective observation (see Sec. D.1.3) is automatically active if partition-selective excitation or damping are used. Additionally, one may also request output of the time evolution of the projection of each TD KS orbital onto the GS KS orbitals via the boolean input flag *Overlap\_output*. This option is not active by default. More output can be generated during STDDFT calculations if one is interested also in details of the norm decaying auxiliary system. This output may be selected via the boolean flag *Decaying\_system\_output* but is inactive by default.

Last but not least, the determination of the quantum-jump times is based on random numbers. However, working with random numbers causes difficulties during the implementation phase of such a stochastic code as one likes to preform identical calculations to test the influence of changes in the code. Apart from this, for some of the calculations, I prefer to set up the random numbers outside the PARSEC code, thus perform PARSEC calculations with preset random numbers. For such cases, I introduced the integer input parameter *Random\_seed*, that can be used to specify the initialization and thus predetermine the outcome of the random number generator.

# Appendix E

## PARSEC miscellaneous

This appendix comprises a collection of PARSEC functionalities that I implemented during the work on this thesis and that do not belong to the topics covered in the previous appendices. Sections E.2 to E.4 contain PARSEC features related to the real-time propagation routines, whereas in Secs. E.5 and E.6 I present some implementations to the ground-state section of the code. For a more general introduction to the PARSEC input, see the PARSEC documentation and Ref. [KMT<sup>+</sup>06]. In the following section, I start with some general comments about the design of the PARSEC input script.

### E.1 General comments on the PARSEC input

The PARSEC input involves different structures and data types that may be used for a case-specific definition of input variables <sup>1</sup>. Therefore, in the following I briefly introduce the data types that are relevant for the input options added during the work on this thesis. Control parameters that determine specific functionalities of the code are typically based on the data types *integer* (*int*), *boolean* (*bool*), or *string*. For typical physical and numerical parameters, the data types *integer*, *double precision* (*dp*), and *physical* are used. The difference between *double* and *physical* is that in case of variables that are indicated to be *physical*, a physical unit corresponding to the specific input parameter may be added to the input value. If no physical unit is specified explicitly in the input file, PARSEC reads the parameter value nevertheless and assumes default units. The PARSEC input block structure (*block*) allows for the input of data arrays in terms of the lines and columns between the block-structure indicators. In such structures, all numbers are assumed to be of *double precision* value. If necessary, I indicate these data types during the explanations about the input parameters that are relevant for this work.

### E.2 Determining the midpoint Hamiltonian during propagation via extrapolation

To perform real-time propagation with the PARSEC code, two numerical realizations of the propagator [CMR04] are implemented [MKHM06, Mun07, Mun09]: the Taylor algorithm

---

<sup>1</sup>More information about the PARSEC input is available in the PARSEC User's Guide (<http://parsec.ices.utexas.edu>).

based on a fourth order Taylor expansion of the exponential function and the so-called split-operator algorithm where the KS Hamiltonian is split into Hartree and xc contributions on the one hand and kinetic and external contributions on the other hand. The advantage of the latter approach is that per time step only a single evaluation of each contribution to the total Hamiltonian is needed [Mun09]. Instead, the Taylor method relies on a Hamiltonian determination with a predictor scheme that first computes the so-called midpoint KS Hamiltonian  $h_{\text{KS}}(\mathbf{r}, t + \Delta t/2)$  after half of the time step and only then performs the full Taylor time step [CMR04, MKHM06, Mun07, Mun09]. This scheme requires two evaluations of the KS Hamiltonian. The prize one has to pay for the reduced numerical effort in the split-operator scheme is that numerical stability of this propagation method is not guaranteed and, therefore, the time step needs to be chosen small enough to avoid spurious self-excitation effects. The fourth order Taylor scheme is known to be conditionally stable [CMR04], yet numerically more involved.

However, during propagation of orbital functionals where the evaluation of the potential – especially its xc contribution – is the most cost-pushing factor, one likes to avoid as many potential evaluations as possible. Therefore, I implemented an extrapolation scheme that saves most of the potential evaluations for the midpoint Hamiltonian as it extrapolates the midpoint Hartree-xc potential  $v_{\text{Hxc}}(\mathbf{r}, t + \Delta t/2)$  from previous time steps via second order polynomial interpolation based on the polynomial

$$v_{\text{Hxc}}(\mathbf{r}, t + \Delta t) = m\Delta t^2 + n\Delta t + o. \quad (\text{E.1})$$

The coefficients  $m$ ,  $n$ , and  $o$  can be computed from the potentials of three previous time steps at  $t - 2\Delta t$ ,  $t - \Delta t$ , and  $t$  by solving the corresponding set of equations. One obtains

$$m = \frac{1}{2\Delta t^2} [v_{\text{Hxc}}(\mathbf{r}, t) + v_{\text{Hxc}}(\mathbf{r}, t - 2\Delta t) - 2v_{\text{Hxc}}(\mathbf{r}, t - \Delta t)], \quad (\text{E.2})$$

$$n = \frac{1}{2\Delta t} [v_{\text{Hxc}}(\mathbf{r}, t - 2\Delta t) - 4v_{\text{Hxc}}(\mathbf{r}, t - \Delta t) + 3v_{\text{Hxc}}(\mathbf{r}, t)], \quad (\text{E.3})$$

$$o = v_{\text{Hxc}}(\mathbf{r}, t). \quad (\text{E.4})$$

Inserting these coefficients into the interpolation formula of Eq. (E.1) yields the new midpoint potential

$$v_{\text{Hxc}}(\mathbf{r}, t + \Delta t/2) = 0.375v_{\text{Hxc}}(\mathbf{r}, t - 2\Delta t) - 1.25v_{\text{Hxc}}(\mathbf{r}, t - \Delta t) + 1.875v_{\text{Hxc}}(\mathbf{r}, t). \quad (\text{E.5})$$

In this procedure, all potentials at integer multiples of  $\Delta t$  are computed by explicit potential evaluation, whereas most of the midterm potentials are determined via Eq. (E.5). As this scheme requires at least two Hartree-xc potentials of times earlier than  $t$ , it can not be applied during the first two steps of the propagation. In this case, the midpoint potentials are computed explicitly by a predictor step [CMR04, MKHM06, Mun07, Mun09].

The extrapolation scheme can be (de)activated in the PARSEC input using the flag *Prop\_extrapolation*, which is of boolean data type. The default is “false”. It applies only for the Taylor propagation method. Numerical tests of the extrapolation procedure on  $\text{Na}_5$  revealed minor deviations to the original Taylor method of the dipole signal only at maxima and minima of the TD dipole moment. These deviations did not affect the Fourier transformation of the dipole signal. However, propagation times of orbital functionals are reduced to almost half of the propagation time of the full Taylor algorithm as now the most cost-intensive procedures need to be performed only once per time step.

### E.3 On the fly Fourier transformation of the time-dependent density

In this section, I explain how the customized PARSEC version determines transition densities introduced in Sec. 2.3, i.e., the Fourier transformations of the TD density. In principle, if one likes to compute the full frequency dependence of the density, one should compute a long enough time evolution of the latter, store the density with a reasonable time resolution on each grid point one is interested in, and finally perform a three dimensional Fourier transformation of the full signal. However, this proceeding is prohibitive as it would require a huge amount of memory to store all signal with a reasonable resolution. Therefore, to calculate transition densities corresponding to specific excitation energies, I implemented an on the fly procedure to compute the Fourier integral at preset frequencies during time propagation: I use a simple trapezoidal rule to integrate

$$\rho(\mathbf{r}, \omega_n) \propto \int_0^T (n(\mathbf{r}, t) - n(\mathbf{r}, 0)) e^{i\omega_n t} dt \quad (\text{E.6})$$

step by step during the time run at fixed frequencies  $\omega_n$ . Thus, one needs to store only  $\rho(\mathbf{r}, \omega_n)$ , i.e., one array over the entire grid for each frequency  $\omega_n$ . This frequency dependent Fourier transformation can be activated by the flag *TD\_Fourier\_Trafo\_number* that should equal the total number of frequencies where the Fourier transformation shall be performed. It is active when *TD\_Fourier\_Trafo\_number* is positive and differs from zero. The specific frequencies at which Fourier transformation is supposed to be performed can to be indicated using the PARSEC block structure *TD\_FT\_frequencies*. There, one needs to list all frequencies in eV units.

### E.4 Propagation miscellaneous

This final chapter on implementations to the propagation section of the PARSEC code includes all features that are not related to a concrete area or specific results of this thesis but were implemented to test some ideas and properties during propagation.

The first feature involves a test of how much the orbitals differ from the GS orbitals multiplied by the TD phase factor  $\exp(-i\varepsilon_j t)$  using the eigenvalue  $\varepsilon_j$  of each orbital  $j$ . To this end, when the option *Prop\_check\_linear\_response* (*boolean*) is activated, the code determines how much the TD orbitals  $\varphi_j(\mathbf{r}, t)$  differ from  $\varphi_j(\mathbf{r}, 0) \exp(-i\varepsilon_j t)$  in terms of the maximum difference, the integral of the absolute difference, and the integral over the absolute square of their difference. From the output per orbital, one can estimate how much the orbitals change during propagation due to some arbitrary excitation process.

The second propagation feature was implemented to test if enhancement of the efficiency of the propagation algorithm can be achieved by freezing some of the orbitals during propagation. This option may be (de)activated by the flag *Use\_sel\_orb\_prop* (*boolean*). I implemented the PARSEC block structures *Sel\_up\_orb\_prop\_block* and *Sel\_dn\_orb\_prop\_block* to be able to indicate the active and frozen orbitals separately for spin up and down. These block structures consist of two columns requiring the number that refers to orbitals in the PARSEC code in the first and indicators for the orbitals in the second column. Active orbitals, labeled by “1”, are propagated regularly by application of

the KS Hamiltonian and frozen orbitals that remain at their GS values need to be labeled by “0”. First numerical tests of orbital freezing on small molecules showed that as soon as one of the orbitals was frozen, the dipole signal differed notably from the true dipole moment time evolution. Yet, this idea was never checked for sizable molecules where potentially some of the lower lying orbitals contribute less to the TD dipole signal.

Finally, if one likes to use static electric fields in dipole approximation during time propagation, this may be achieved by choosing “*Laser\_shape* = rampnola” in the PARSEC input as implemented by Anne Klimach. In this case, the potential of the external field may grow to unphysically large numbers at the outer part of the real-space grid. Therefore, in some cases it may appear reasonable to set the external potential constant outside a certain volume around the system. To this end, I implemented the physical PARSEC input parameter *Const\_field\_radius*. It reads a distance to the origin of the grid that determines a boundary outside which the potential is set constant to the value of the potential on this boundary. Note that this feature works only if the polarization of the external field is chosen to point exactly into the direction of the coordinate system. This option is turned off (default) when *Const\_field\_radius* is set to be zero.

## E.5 Adaptation of the diagonalization tolerance during the ground-state procedure

Most of the computation time of the PARSEC ground-state iterations goes into the diagonalization of the Hamiltonian matrix. Comparison of the performances of PARSEC and the octopus code [MCBR03, CAO<sup>+</sup>06] in collaboration with Heiko Appel revealed that particularly much time gets lost in PARSEC when diagonalization is performed during the first iterations of the self-consistency procedure. There is one striking difference between PARSEC and octopus: To my understanding, the octopus code limits the maximum number of matrix times vector multiplications in the diagonalization routine <sup>2</sup>. Thus, with a reasonable choice of this limit, it accepts a reduction of the accuracy of the diagonalization during the first iteration steps where typically a larger number of matrix times vector multiplications are needed for high diagonalization accuracy. PARSEC performs high accuracy diagonalization from the first iteration step on. Yet, during the first steps of the KS self-consistency procedure, the KS Hamiltonian may notably deviate from the final self-consistent KS Hamiltonian. Hence, it appears worthless computing the orbitals already with the final diagonalization accuracy as they come from a Hamiltonian that is not converged.

Therefore, I implemented an adaptation scheme that adjusts the diagonalization tolerance to the self-consistency residual error measured via the integral over changes of the charge weighted potential. From the first iteration until the SRE drops below  $10^5$  times the preset convergence threshold  $c$ , a diagonalization solver tolerance  $t$  of  $1 \times 10^{-3}$  is used. Then, the diagonalization tolerance is reduced towards the final tolerance  $f$  in four steps  $i$  when the SRE drops below  $10^{5-i}c$  according to

$$t = 10^{-3 + \frac{i}{4}(3 + \log_{10}(f))}. \quad (\text{E.7})$$

---

<sup>2</sup>The information about the limitation of matrix times vector multiplications in the octopus code came up in discussions with Heiko Appel.

This choice of the SRE and the solver-tolerance thresholds relies on practical experience and yields reasonable performance enhancement, while for most systems the final results are not influenced by adaptive solver settings as long as sufficiently low convergence parameters are guaranteed in the end. Therefore, using this scheme the detection of the convergence of the self-consistency procedure is allowed only when the solver tolerance has dropped to its final value  $f$ . This diagonalization tolerance adaptation can be activated by the boolean flag *Adaptive\_diag\_tolerance*. Yet, it is deactivated automatically when the (G)OEP or GKLI are used, “*poissonsolver = 1*”, or Förster-type potential evaluation is applied, because in these cases experience shows that high accuracy of the diagonalization is preferable from the start.

## E.6 Ground-state miscellaneous

The last section of this appendix contains a list of extensions to the GS PARSEC code that are not covered by the previous appendices.

In the original version, PARSEC moves all nuclei of the system to center the outermost nuclei with respect to the planes of the coordinate system. Yet, for some applications this centering procedure of the nuclei positions is not desired. Therefore, I added the boolean flag *Centering\_atom\_position* to control the centering option. The position centering is applied, when the flag is set to its default value “true” and vice versa.

To investigate all contributions of the OEP potential and/or its KLI approximation separately, I implemented the option *OEP\_potential\_output* (boolean). When this flag is “true”, the OEP or KLI potential is split into Slater and all contributions beyond Slater. These are written to separate output files along all coordinate axis, on the planes of the coordinate system, and as a cube file on the three dimensional grid.

Last but not least, a static electric field in dipole approximation may be applied during GS calculations using the boolean flag *Apply\_electric\_field*. In the current implementation, this field applies only in  $x$ -direction of the coordinate system. The field strength may be defined by the physical PARSEC input parameter *Electric\_Field*.



# Acknowledgment

I am grateful to a lot of people who accompanied me on my way to this thesis. In gratitude for the encouragement, support, and inspiration that I have received, I would like to acknowledge in particular ...

... my supervisor Stephan Kümmel who guided my work with his suggestions and advice, by scrutinizing my findings, and by sharing his deep knowledge and understanding of physics in general and especially density functional theory with me. His enthusiasm for science has always been a great inspiration.

... the members and alumni of the Kümmel-group: Anne Klimach, Linn Leppert, Rodrigo Albuquerque, Richard Armiento, Matthias Dauth, Sebastian Frank, Andreas Karolewski, Markus Knoll, Thomas Körzdörfer, Philipp Schaffhauser, Tobias Schmidt, Mark Thiele, and Sebastian Wüstner. I appreciate great physics and private discussions with my office mates, critical questions and insight during our group seminars, and the friendly atmosphere in general. My thanks go to Linn, Andreas, Matthias, and Tobias for their proof reading and helpful comments on this manuscript.

... all friends and fellows of the Elite Study Program Macromolecular Science and the Graduiertenkolleg 1640 "Photophysics of Synthetic and Biological Multichromophoric Systems". Sharing science with you in many official and private occasions has always been a pleasure.

... my scientific partners and hosts: Massimiliano Di Ventra for insightful discussions on open quantum systems and stochastic Schrödinger equations in the context of TDDFT as well as his hospitality in San Diego; Heiko Appel, first for insight and support on the project of excitation-energy transfer and stochastic TDDFT, second for many handy linux hints, and third for the great time in San Diego; Or Cohen and Leor Kronik for helpful comments and sharing their experience on multigrid methods; Simon and Peter Klüpfel for sharing their knowledge about optimization methods for determining energy-minimizing unitary transformations; Miguel A. L. Marques for comments on TD propagation schemes.

... Monika Birkelbach, Claudia Masuch, Markus Hilt, and Bernhard Winkler for helping with administrative matters and solving all computer issues.

... all sports fellows who share my enthusiasm for Taekwondo and who have accompanied me for many years. I have always enjoyed practicing sports with you and relaxing my mind in the gym.

... my family for providing all the opportunities and challenges that I enjoyed, for lots of support and advice, and for the trust that I experienced.

... Karina Mees for her love, for her understanding of the many ups and downs during this thesis, for her support and advice in all matters of life, for her trust, and for sharing her life with me.



# List of publications and manuscripts

1. **D. Hofmann**, T. Körzdörfer, and S. Kümmel,  
Phys. Rev. A **82**, 012509 (2010):  
*Energy transfer and Förster's dipole coupling approximation investigated in a real-time Kohn-Sham scheme*
2. **D. Hofmann**, T. Körzdörfer, and S. Kümmel,  
Phys. Rev. Lett. **108**, 146401 (2012):  
*Kohn-Sham Self-Interaction Correction in Real Time*
3. **D. Hofmann**, S. Klüpfel, P. Klüpfel, and S. Kümmel,  
Phys. Rev. A **85**, 062514 (2012):  
*Using complex degrees of freedom in the Kohn-Sham self-interaction correction*
4. **D. Hofmann** and S. Kümmel,  
J. Chem. Phys. **137**, 064117 (2012):  
*Self-interaction correction in a real-time Kohn-Sham scheme: access to difficult excitations in time-dependent density functional theory*
5. **D. Hofmann** and S. Kümmel,  
Phys. Rev. Lett., submitted (2012):  
*Integer particle preference during charge transfer in Kohn-Sham theory*



# List of abbreviations, functionals, and methods

A	acceptor
ALDA	adiabatic local density approximation
a.u.	atomic units
B	bath
B3LYP	Becke three-parameter Lee-Yang-Parr hybrid functional
BLYP	semiempirical GGA functional that combines Becke88 exchange and Lee, Yang, and Parr correlation
CASPT2	complete active space perturbation theory of second order
CC	Coupled-Cluster
CCSD(T)	Coupled-Cluster (singles, doubles and perturbative triples)
CEDA	common energy denominator approximation
CG	conjugate gradient
CT	charge-transfer
D	donor
DFT	density functional theory
$e$	elementary electric charge
EA	electron affinity
EET	excitation-energy transfer
EXX	exact exchange
FOBO	Foster-Boys
FOBO-SIC	SIC functional implemented via the GKLI approximation using FOBO transformations
fs	femtosecond
GGA	generalized gradient approximation
GKLI	generalized Krieger, Li, and Iafrate approximation
GKLI-SIC	SIC functional implemented via the GKLI approximation using energy-minimizing transformations
GKS	generalized Kohn-Sham approach
GOEP	generalized optimized effective potential
GOEP-SIC	SIC functional implemented via the GOEP approximation using energy-minimizing transformations
GS	ground-state
GSIC	generalized self-interaction correction
GSLA	generalized Slater approximation

GSLA-SIC	SIC functional implemented via the GSLA approximation using energy-minimizing transformations
HF	Hartree-Fock
HK	Hohenberg-Kohn
HOMO, H	highest occupied molecular orbital
Hxc	Hartree-exchange-correlation
IP	ionization potential
KLI	Krieger, Li, and Iafrate approximation
KLI-EXX	EXX functional implemented via the KLI approximation
KLI-SIC	SIC functional implemented via the KLI approximation
KS	Kohn-Sham
LDA	local density approximation
LH	light-harvesting
LHF	localized Hartree-Fock
LHF-CEDA	localized Hartree-Fock - common energy denominator approximation
loc	localized
LSDA	local spin-density approximation
LUMO, L	lowest unoccupied molecular orbital
LYP	Lee, Yang, and Parr correlation functional
MG	multigrid
MPI	message passing interface
MP2	Møller-Plesset perturbation theory of second order
MP4	Møller-Plesset perturbation theory of fourth order
OEP	optimized effective potential
OEP-SIC	SIC functional implemented via the OEP approximation
PARSEC	pseudopotential algorithm for real-space electronic structure calculations
PBE	Perdew, Burke, and Ernzerhof functional approximation
PZ	Perdew-Zunger
qj	quantum-jump
RT	real-time
TD	time-dependent
TDCDFT	time-dependent current density functional theory
TDDFT	time-dependent density functional theory
TDGKLI	generalized Krieger, Li, and Iafrate approximation in TDDFT
TDGKLI-SIC	SIC functional implemented via the TDGKLI approximation using complex-valued energy-minimizing transformations
TDGSLA	generalized Slater approximation in TDDFT
TDGSLA-SIC	SIC functional implemented via the TDGSLA approximation using complex-valued energy-minimizing transformations
TDGSIC	generalized self-interaction correction in TDDFT
TDFOBO-SIC	SIC functional implemented via the TDGKLI approximation using spatially localizing transformations
TDKLI	Krieger, Li, and Iafrate approximation in TDDFT
TDL(S)DA	adiabatic local (spin) density approximation in TDDFT
TDOEP	time-dependent optimized effective potential
TDSL	Slater approximation in TDDFT

S	system
se	single-electron
SIC	self-interaction correction
SIE	self-interaction error
sl	semilocal
SLA	Slater approximation
SRE	self-consistency residual error
SSE	stochastic Schrödinger equation
STDDFT	stochastic time-dependent density functional theory
xc	exchange-correlation



# Bibliography

- [ADV09] H. Appel and M. Di Ventra, *Stochastic quantum molecular dynamics*, Phys. Rev. B **80** (2009), 212303.
- [ADV11] H. Appel and M. Di Ventra, *Stochastic quantum molecular dynamics for finite and extended systems*, Chem. Phys. **391** (2011), 27.
- [AEK09] T. Abrudan, J. Eriksson, and V. Koivunen, *Conjugate gradient algorithm for optimization under unitary matrix constraint*, Signal Processing **89** (2009), 1704.
- [AGB03] H. Appel, E. K. U. Gross, and K. Burke, *Excitations in Time-Dependent Density-Functional Theory*, Phys. Rev. Lett. **90** (2003), 043005.
- [AKK08] R. Armiento, S. Kümmel, and T. Körzdörfer, *Electrical response of molecular chains in density functional theory: Ultranonlocal response from a semilocal functional*, Phys. Rev. B **77** (2008), 165106.
- [Aut09] J. Autschbach, *Charge-Transfer Excitations and Time-Dependent Density Functional Theory: Problems and Some Proposed Solutions*, Chem. Phys. Chem. **10** (2009), 1757.
- [BCG05] K. Burke, R. Car, and R. Gebauer, *Density Functional Theory of the Electrical Conductivity of Molecular Devices*, Phys. Rev. Lett. **94** (2005), 146803.
- [BCOR04] R. A. Broglia, G. Colò, G. Onida, and H. E. Roman, *Solid State Physics of Finite Systems*, Springer, 2004.
- [Bec88] A. D. Becke, *Density-functional exchange-energy approximation with correct asymptotic behavior*, Phys. Rev. A **38** (1988), 3098.
- [Bec93] A. D. Becke, *A new mixing of Hartree-Fock and local density-functional theories*, J. Chem. Phys. **98** (1993), 1372.
- [BLS10] R. Baer, E. Livshits, and U. Salzner, *Tuned Range-Separated Hybrids in Density Functional Theory*, Annu. Rev. Phys. Chem. **61** (2010), 85.
- [Boy60] S. F. Boys, *Construction of Some Molecular Orbitals to Be Approximately Invariant for Changes from One Molecule to Another*, Rev. Mod. Phys. **32** (1960), 296.

- [BP95] H.-P. Breuer and F. Petruccione, *Stochastic dynamics of quantum jumps*, Phys. Rev. E **52** (1995), 428.
- [BP06] H.-P. Breuer and F. Petruccione, *The Theory of Open Quantum Systems*, Clarendon Press, 2006.
- [Bra81] A. Brandt, *Multigrid solvers on parallel computers*, Elliptic Problem Solvers, pp. 39 – 83, Academic Press New York, 1981.
- [BSK<sup>+</sup>03] W. R. Burdick, Y. Saad, L. Kronik, I. Vasiliev, M. Jain, and J. R. Chelikowsky, *Parallel implementation of time-dependent density functional theory*, Comput. Phys. Commun. **156** (2003), 22.
- [Büt86] M. Büttiker, *Four-Terminal Phase-Coherent Conductance*, Phys. Rev. Lett. **57** (1986), 1761.
- [BWLT07] P. Bauer, H. Wietasch, S. M. Lindner, and M. Thelakkat, *Synthesis and characterization of donor-bridge-acceptor molecule containing tetraphenylbenzidine and perylene bisimide*, Chem. Mater. **19** (2007), 88.
- [CA80] D. M. Ceperley and B. J. Alder, *Ground State of the Electron Gas by a Stochastic Method*, Phys. Rev. Lett. **45** (1980), 566.
- [CAO<sup>+</sup>06] A. Castro, H. Appel, M. Oliveira, C. A. Rozzi, X. Andrade, F. Lorenzen, M. A. L. Marques, E. K. U. Gross, and A. Rubio, *octopus: a tool for the application of time-dependent density functional theory*, physica status solidi (b) **243** (2006), 2465.
- [Cap02] K. Capelle, *A bird's-eye view of density-functional theory*, 2002.
- [Cas95] M. E. Casida, *Time-Dependent Density Functional Response Theory for Molecules*, Recent Advances in Density Functional Methods **1** (1995), 155.
- [Cas96] M. E. Casida, *Time-Dependent Density Functional Response Theory of Molecular Systems: Theory, Computational Methods, and Functionals*, Recent Developments and Applications in Modern Density-Functional Theory **4** (1996), 391.
- [CBKR07] K. Capelle, M. Borgh, K. Kärkkäinen, and S. M. Reimann, *Energy Gaps and Interaction Blockade in Confined Quantum Systems*, Phys. Rev. Lett. **99** (2007), 010402.
- [CEVV06] C.-L. Cheng, J. S. Evans, and T. Van Voorhis, *Simulating molecular conductance using real-time density functional theory*, Phys. Rev. B **74** (2006), 155112.
- [CF09] Y.-C. Cheng and G. R. Fleming, *Dynamics of Light Harvesting in Photosynthesis*, Annu. Rev. Phys. Chem. **60** (2009), 241.
- [CGB02] D. P. Chong, O. V. Gritsenko, and E. J. Baerends, *Interpretation of the Kohn-Sham orbital energies as approximate vertical ionization potentials*, J. Chem. Phys. **116** (2002), 1760.

- [CHG07] J.-D. Chai and M. Head-Gordon, *Systematic optimization of long-range corrected hybrid density functionals*, J. Chem. Phys. **128** (2007), 084106.
- [CHR12] M. E. Casida and M. Huix-Rotllant, *Progress in Time-Dependent Density Functional Theory*, Annu. Rev. Phys. Chem. **63** (2012), 287.
- [CK09] B. Champagne and B. Kirtman, *Polarizabilities and second hyperpolarizabilities of hydrogen chains using the spin-component-scaled Møller-Plesset second-order method*, Int. J. Quantum Chem. **109** (2009), 3103.
- [CMLM<sup>+</sup>09] C. Curutchet, A. Muñoz-Losa, S. Monti, J. Kongsted, G. D. Scholes, and B. Mennucci, *Electronic Energy Transfer in Condensed Phase Studied by a Polarizable QM/MM Model*, J. Chem. Theory Comput. **5** (2009), 1838.
- [CMR04] A. Castro, M. A. L. Marques, and A. Rubio, *Propagators for the time-dependent Kohn–Sham equations*, J. Chem. Phys. **121** (2004), 3425.
- [CMVA95] B. Champagne, D. H. Mosley, M. Vračko, and J.-M. André, *Electron-correlation effects on the static longitudinal polarizability of polymeric chains*, Phys. Rev. A **52** (1995), 178.
- [CRS97] F. Calvayrac, P. G. Reinhard, and E. Suraud, *Spectral Signals from Electronic Dynamics in Sodium Clusters*, Ann. Phys. **255** (1997), 125.
- [CTDF99] C. Cohen-Tannoudji, B. Diu, and F. Laloë, *Quantenmechanik Teil 1*, Walter de Gruyter, 1999.
- [CTS94] J. R. Chelikowsky, N. Troullier, and Y. Saad, *Finite-difference-pseudopotential method: Electronic structure calculations without a basis*, Phys. Rev. Lett. **72** (1994), 1240.
- [DCM92] J. Dalibard, Y. Castin, and K. Mølmer, *Wave-function approach to dissipative processes in quantum optics*, Phys. Rev. Lett. **68** (1992), 580.
- [DDV08] R. D’Agosta and M. Di Ventra, *Stochastic time-dependent current-density-functional theory: A functional theory of open quantum systems*, Phys. Rev. B **78** (2008), 165105.
- [DDV09] R. D’Agosta and M. Di Ventra, *Comment on “Time-dependent current-density functional theory for generalized open quantum systems” by J. Yuen-Zhou, C. Rodríguez-Rosario and A. Aspuru-Guzik*, arXiv:0911.3932v1 (2009).
- [DG90] R. M. Dreizler and E. K. U. Gross, *Density Functional Theory: An Approach to the Quantum Many-body Problem*, Springer, 1990.
- [DHG04] A. Dreuw and M. Head-Gordon, *Failure of Time-Dependent Density Functional Theory for Long-Range Charge-Transfer Excited States: The Zinbacteriochlorin-Bacteriochlorin and Bacteriochlorophyll-Spheroidene Complexes*, J. Am. Chem. Soc. **126** (2004), 4007.

- [DHL03] C. C. Douglas, G. Haase, and U. Langer, *A Tutorial on Elliptic PDE*, Society for Industrial and Applied Mathematics, 2003.
- [DKK<sup>+</sup>11] M. Dauth, T. Körzdörfer, S. Kümmel, J. Ziroff, M. Wiessner, A. Schöll, F. Reinert, M. Arita, and K. Shimada, *Interpretation of the Kohn-Sham orbital energies as approximate vertical ionization potentials*, Phys. Rev. Lett. **107** (2011), 193002.
- [DL11] I. Dreissigacker and M. Lein, *Adiabatic approximation within time-dependent density functional theory using inversion of the ground-state spin-density Kohn-Sham formalism*, Chem. Phys. **391** (2011), 143146.
- [DV05] R. D’Agosta and G. Vignale, *Non-V-representability of currents in time-dependent many-particle systems*, Phys. Rev. B **71** (2005), 245103.
- [DVD07] M. Di Ventra and R. D’Agosta, *Stochastic Time-Dependent Current-Density-Functional Theory*, Phys. Rev. Lett. **98** (2007), 226403.
- [DWHG03] A. Dreuw, J. Weisman, and M. Head-Gordon, *Long-range charge-transfer excited states in time-dependent density functional theory require non-local exchange*, J. Chem. Phys. **119** (2003), 2943.
- [EAS98] A. Eldemann, T. A. Arias, and S. T. Smith, *The Geometry of Algorithms with Orthogonality Constraints*, SIAM J. Matrix Anal. Appl. **20** (1998), 303.
- [EBF07] P. Elliott, K. Burke, and F. Furche, *Excited states from time-dependent density functional theory*, arXiv:cond-mat/0703590v1 (2007).
- [ER63] C. Edmiston and K. Ruedenberg, *Localized Atomic and Molecular Orbitals*, Rev. Mod. Phys. **35** (1963), 457.
- [EVV09] J. S. Evans, O. A. Vydrov, and T. Van Voorhis, *Exchange and correlation in molecular wire conductance: Nonlocality is the key*, J. Chem. Phys. **131** (2009), 034106.
- [FB60] J. M. Foster and S. F. Boys, *Canonical Configurational Interaction Procedure*, Rev. Mod. Phys. **32** (1960), 300.
- [FJ00] R. D. Falgout and J. E. Jones, *Multigrid on massively parallel architectures*, Multigrid Methods VI, pp. 101–107, Springer, 2000.
- [FKH<sup>+</sup>08] B. Fückel, A. Köhn, M. E. Harding, G. Diezemann, G. Hinze, T. Basché, and J. Gauss, *Theoretical investigation of electronic excitation energy transfer in bichromophoric assemblies*, J. Chem. Phys. **128** (2008), 074505.
- [FO05] G. W. Ford and R. F. O’Connell, *Limitations on the utility of exact master equations*, Ann. Phys. **319** (2005), 348.
- [För46] T. Förster, *Energiewanderung und Fluoreszenz*, Naturwiss. **33** (1946), 166.
- [För48] T. Förster, *Zwischenmolekulare Energiewanderung und Fluoreszenz*, Ann. Phys. **437** (1948), 55.

- [För65] T. Förster, *Delocalized Excitation and Excitation Transfer*, Modern Quantum Chemistry Part III: Action of light and organic crystals, pp. 93–138, Academic Press, 1965.
- [FPM93] E. S. Fois, J. I. Penman, and P. A. Madden, *Self-interaction corrected density functionals and the structure of metal clusters*, J. Chem. Phys. **98** (1993), 6352.
- [Fre90] W. R. Frensley, *Boundary conditions for open quantum systems driven far from equilibrium*, Rev. Mod. Phys. **62** (1990), 745.
- [FRM11] J. I. Fuks, A. Rubio, and N. T. Maitra, *Charge transfer in time-dependent density-functional theory via spin-symmetry breaking*, Phys. Rev. A **83** (2011), 042501.
- [GB01] O. V. Gritsenko and E. J. Baerends, *Orbital structure of the Kohn-Sham exchange potential and exchange kernel and the field-counteracting potential for molecules in an electric field*, Phys. Rev. A **64** (2001), 042506.
- [GB04] O. Gritsenko and E. J. Baerends, *Asymptotic correction of the exchange–correlation kernel of time-dependent density functional theory for long-range charge-transfer excitations*, J. Chem. Phys. **121** (2004), 655.
- [GDP96] E. K. U. Gross, J. F. Dobson, and M. Petersilka, *Density functional theory of time-dependent phenomena*, Top. Current. Chem. **181** (1996), 81.
- [GGB02] M. Grüning, O. V. Gritsenko, and E. J. Baerends, *Exchange potential from the common energy denominator approximation for the Kohn–Sham Green’s function: Application to (hyper)polarizabilities of molecular chains*, J. Chem. Phys. **116** (2002), 6435.
- [GGS09] P. Gori-Giorgi and A. Savin, *Study of the Discontinuity of the Exchange–Correlation Potential in an Exactly Soluble Case*, Int. J. Quantum Chem. **109** (2009), 2410.
- [GKG97] T. Grabo, T. Kreibich, and E. K. U. Gross, *Optimized Effective Potential for Atoms and Molecules*, Mol. Eng. **7** (1997), 27.
- [GKKG00] T. Grabo, T. Kreibich, S. Kurth, and E. K. U. Gross, *Orbital Functionals in Density Functional Theory: The Optimized Effective Potential Method*, Advances in Condensed Matter Science, pp. 203–297, Gordon and Breach Science Publishers, 2000.
- [GN99] P. Gaspard and M. Nagaoka, *Non-Markovian stochastic Schrödinger equation*, J. Chem. Phys. **111** (1999), 5676.
- [GND00] J. Garza, J. A. Nichols, and D. A. Dixon, *The optimized effective potential and the self-interaction correction in density functional theory: Application to molecules*, J. Chem. Phys. **112** (2000), 7880.

- [GPZ92] C. W. Gardiner, A. S. Parkins, and P. Zoller, *Wave-function quantum stochastic differential equations and quantum-jump simulation methods*, Phys. Rev. A **46** (1992), 4363.
- [GU97] S. Goedecker and C. J. Umrigar, *Critical assessment of the self-interaction-corrected-local-density-functional method and its algorithmic implementation*, Phys. Rev. A **55** (1997), 1765.
- [GvGSB00] O. V. Gritsenko, S. J. A. van Gisbergen, P. R. T. Schipper, and E. J. Baerends, *Origin of the field-counteracting term of the Kohn-Sham exchange-correlation potential of molecular chains in an electric field*, Phys. Rev. A **62** (2000), 012507.
- [GvLB94] O. V. Gritsenko, R. van Leeuwen, and E. J. Baerends, *Analysis of electron interaction and atomic shell structure in terms of local potentials*, J. Chem. Phys. **101** (1994), 8955.
- [Hac81] W. Hackbusch, *Bemerkungen zur iterierten Defektkorrektur und zu ihrer Kombination mit Mehrgitterverfahren*, Rev. Roumaine Math. Pures Appl. **26** (1981), 1319.
- [Hac85] W. Hackbusch, *Multi-Grid Methods and Applications*, Springer-Verlag, 1985.
- [HDRS98] X. C. Hu, A. Damjanovic, T. Ritz, and K. Schulten, *Architecture and mechanism of the light-harvesting apparatus of purple bacteria*, Proc. Natl. Acad. Sci. U.S.A. **95** (1998), 5935.
- [HFHGHG01] C.-P. Hsu, G. R. Fleming, M. Head-Gordon, and T. Head-Gordon, *Excitation energy transfer in condensed media*, J. Chem. Phys. **114** (2001), 3065.
- [HG12] M. Hellgren and E. K. U. Gross, *Discontinuities of the exchange-correlation kernel and charge-transfer excitations in time-dependent density-functional theory*, Phys. Rev. A **85** (2012), 022514.
- [HJ97] B. Heise and M. Jung, *Parallel solvers for nonlinear elliptic problems*, Parallel Computing **22** (1997), 1527.
- [HK64] P. Hohenberg and W. Kohn, *Inhomogeneous Electron Gas*, Phys. Rev. **136** (1964), B864.
- [HKMR05] F. Hülsemann, M. Kowarschik, M. Mohr, and U. Rüde, *Parallel geometric multigrid*, Numerical Solution of Partial Differential Equations on Parallel Computers, pp. 165–208, Springer, 2005.
- [Hof08] D. Hofmann, *Anregung und Energietransfer in molekularen Systemen*, Diplomarbeit, Universität Bayreuth, 2008.
- [HPB99] P. Hessler, J. Park, and K. Burke, *Several Theorems in Time-Dependent Density Functional Theory*, Phys. Rev. Lett. **82** (1999), 378.

- [Hsu03] C.-P. Hsu, *Theoretical Study of Photosynthetic Light-Harvesting Processes: Application of Time-Dependent Density Functional Theory*, J. Chin. Chem. Soc. **50** (2003), 745.
- [IF09] A. Ishizaki and G. R. Fleming, *On the adequacy of the Redfield equation and related approaches to the study of quantum dynamics in electronic energy transfer*, J. Chem. Phys. **130** (2009), 234110.
- [IHG10] A. Ipatov, A. Heßelmann, and A. Görling, *Molecular excitation spectra by TDDFT with the nonadiabatic exact exchange kernel*, Int. J. Quantum Chem. **110** (2010), 2202.
- [Jan78] J. F. Janak, *Proof that  $\partial E/\partial n_i = \varepsilon$  in density-functional theory*, Phys. Rev. B **18** (1978), 7165.
- [JCRE08] S. Jang, Y.-C. Cheng, D. R. Reichman, and J. D. Eaves, *Theory of coherent resonance energy transfer*, J. Chem. Phys. **129** (2008), 101104.
- [JFTL02] C. Jamorski, J. B. Foresman, C. Thilgen, and H.-P. Lüthi, *Assessment of time-dependent density-functional theory for the calculation of critical features in the absorption spectra of a series of aromatic donor-acceptor systems*, J. Chem. Phys. **116** (2002), 8761.
- [JJS02] S. Jang, Y.J. Jung, and R. J. Silbey, *Nonequilibrium generalization of Förster-Dexter theory for excitation energy transfer*, Chem. Phys. **275** (2002), 319.
- [Jou07] D. P. Joubert, *Alternative derivation of an exchange-only density-functional optimized effective potential*, Phys. Rev. A **76** (2007), 042503.
- [Jun97] M. Jung, *On the parallelization of multi-grid methods using a non-overlapping domain decomposition data structure*, Appl. Numer. Math. **23** (1997), 119.
- [KAK09] A. Karolewski, R. Armiento, and S. Kümmel, *Polarizabilities of Polyacetylene from a Field-Counteracting Semilocal Functional*, J. Chem. Theo. Comput. **5** (2009), 712.
- [KAR01] S. Kümmel, K. Andrae, and P.-G. Reinhard, *Collectivity in the optical response of small metal clusters*, Appl. Phys. B **73** (2001), 293.
- [KBE06] M. Koentopp, K. Burke, and F. Evers, *Zero-bias molecular electronics: Exchange-correlation corrections to Landauer's formula*, Phys. Rev. B **73** (2006), 121403.
- [KBY07] S.-H. Ke, H. U. Baranger, and W. Yang, *Role of the exchange-correlation potential in ab initio electron transport calculations*, J. Chem. Phys. **126** (2007), 201102.
- [KK06] S. Kümmel and L. Kronik, *Hyperpolarizabilities of molecular chains: A real-space approach*, Comput. Mater. Sci. **35** (2006), 321.

- [KK08] S. Kümmel and L. Kronik, *Orbital-dependent density functionals: Theory and applications*, Rev. Mod. Phys. **80** (2008), 3.
- [KK10] T. Körzdörfer and S. Kümmel, *Single-particle and quasiparticle interpretation of Kohn-Sham and generalized Kohn-Sham eigenvalues for hybrid functionals*, Phys. Rev. B **82** (2010), 155206.
- [KK11] T. Körzdörfer and S. Kümmel, *Self-interaction correction in the Kohn-Sham framework*, Theoretical and Computational Developments in Modern Density Functional Theory, chap. 9, Nova Science Publishers, 2011.
- [KKM08] T. Körzdörfer, S. Kümmel, and M. Mundt, *Self-interaction correction and the optimized effective potential*, J. Chem. Phys. **129** (2008), 014110.
- [KKMK09] T. Körzdörfer, S. Kümmel, N. Marom, and L. Kronik, *When to trust photoelectron spectra from Kohn-Sham eigenvalues: The case of organic semiconductors*, Phys. Rev. B **79** (2009), 201205.
- [KKP04] S. Kümmel, L. Kronik, and J. P. Perdew, *Electrical Response of Molecular Chains from Density Functional Theory*, Phys. Rev. Lett. **93** (2004), 213002.
- [KLI92] J. B. Krieger, Y. Li, and G. J. Iafrate, *Systematic approximations to the optimized effective potential: Application to orbital-density-functional theory*, Phys. Rev. A **46** (1992), 5453.
- [KMK08] T. Körzdörfer, M. Mundt, and S. Kümmel, *Electrical Response of Molecular Systems: The Power of Self-Interaction Corrected Kohn-Sham Theory*, Phys. Rev. Lett. **100** (2008), 133004.
- [KMT<sup>+</sup>06] L. Kronik, A. Makmal, M. L. Tiago, M. M. G. Alemany, M. Jain, X. Huang, Y. Saad, and J. R. Chelikowsky, *PARSEC - the pseudopotential algorithm for real-space electronic structure calculations: recent advances and novel applications to nano-structures*, Phys. status solidi B **243** (2006), 1063.
- [KN12] C. König and J. Neugebauer, *Quantum chemical description of absorption properties and excited-state processes in photosynthetic systems*, Chem. Phys. Chem. **13** (2012), 386.
- [KNOC11] A. Kolli, A. Nazir, and A. Olaya-Castro, *Electronic excitation dynamics in multichromophoric systems described via a polaron-representation master equation*, J. Chem. Phys. **135** (2011), 154112.
- [Kör09] T. Körzdörfer, *Self-interaction and charge transfer in organic semiconductors*, Ph.D. thesis, Universität Bayreuth, 2009.
- [Kör11] T. Körzdörfer, *On the relation between orbital-localization and self-interaction errors in the density functional theory treatment of organic semiconductors*, J. Chem. Phys. **134** (2011), 094111.

- [KP03a] S. Kümmel and J. P. Perdew, *Optimized effective potential made simple: Orbital functionals, orbital shifts, and the exact Kohn-Sham exchange potential*, Phys. Rev. B **68** (2003), 035103.
- [KP03b] S. Kümmel and J. P. Perdew, *Simple Iterative Construction of the Optimized Effective Potential for Orbital Functionals, Including Exact Exchange*, Phys. Rev. Lett. **90** (2003), 043004.
- [KP03c] S. Kümmel and J. P. Perdew, *Two avenues to self-interaction correction within Kohn-Sham theory: unitary invariance is the shortcut*, Mol. Phys. **101** (2003), 1363.
- [KS65] W. Kohn and L. J. Sham, *Self-Consistent Equations Including Exchange and Correlation Effects*, Phys. Rev. **140** (1965), A1133.
- [KSA<sup>+</sup>05] S. Kurth, G. Stefanucci, C.-O. Almbladh, A. Rubio, and E. K. U. Gross, *Time-dependent quantum transport: A practical scheme using density functional theory*, Phys. Rev. B **72** (2005), 035308.
- [KSBK11] A. Karolewski, T. Stein, R. Baer, and S. Kümmel, *Communication: Tailoring the optical gap in light-harvesting molecules*, J. Chem. Phys. **134** (2011), 151101.
- [KSK<sup>+</sup>10] S. Kurth, G. Stefanucci, E. Khosravi, C. Verdozzi, and E. K. U. Gross, *Dynamical Coulomb Blockade and the Derivative Discontinuity of Time-Dependent Density Functional Theory*, Phys. Rev. Lett. **104** (2010), 236801.
- [KSRS08] H. Köstler, R. Schmid, U. Rude, and C. Scheit, *A parallel multigrid accelerated Poisson solver for ab initio molecular dynamics applications*, Comput. Visual. Sci. **11** (2008), 115.
- [KSSB11] T. Körzdörfer, J. S. Sears, C. Sutton, and J.-L. Brédas, *Long-range corrected hybrid functionals for  $\pi$ -conjugated systems: Dependence of the range-separation parameter on conjugation length*, J. Chem. Phys. **135** (2011), 204107.
- [KTRH95] B. Kirtman, J. L. Toto, K. A. Robins, and M. Hasan, *Ab initio finite oligomer method for nonlinear optical properties of conjugated polymers. Hartree-Fock static longitudinal hyperpolarizability of polyacetylene*, J. Chem. Phys. **102** (1995), 5350.
- [Küh95] W. Kühlbrandt, *Many wheels make light work*, Nature **374** (1995), 497.
- [Lan57] R. Landauer, *Spatial variation of currents and fields due to localized scatterers in metallic conduction*, IBM J. Res. Dev. **1** (1957), 223.
- [LB07] E. Livshits and R. Baer, *A well-tempered density functional theory of electrons in molecules*, Phys. Chem. Chem. Phys. **9** (2007), 2932.

- [LBBS12] Z.-F. Liu, J. P. Bergfield, K. Burke, and C. A. Stafford, *Accuracy of density functionals for molecular electronics: The Anderson junction*, Phys. Rev. B **85** (2012), 155117.
- [LK05] M. Lein and S. Kümmel, *Exact Time-Dependent Exchange-Correlation Potentials for Strong-Field Electron Dynamics*, Phys. Rev. Lett. **94** (2005), 143003.
- [LM83] D. C. Langreth and M. J. Mehl, *Beyond the local-density approximation in calculations of ground-state electronic properties*, Phys. Rev. B **28** (1983), 1809.
- [Löw50] P.-O. Löwdin, *On the Non-Orthogonality Problem Connected with the Use of Atomic Wave Functions in the Theory of Molecules and Crystals*, J. Chem. Phys. **18** (1950), 365.
- [LYP88] C. Lee, W. Yang, and R. G. Parr, *Development of the Colle-Salvetti correlation-energy formula into a functional of the electron density*, Phys. Rev. B **37** (1988), 785.
- [Mai05] N. T. Maitra, *Undoing static correlation: Long-range charge transfer in time-dependent density-functional theory*, J. Chem. Phys. **122** (2005), 234104.
- [May02] I. Mayer, *On Löwdins Method of Symmetric Orthogonalization*, Int. J. Quantum Chem. **90** (2002), 63.
- [MB01] N. T. Maitra and K. Burke, *Demonstration of initial-state dependence in time-dependent density-functional theory*, Phys. Rev. A **63** (2001), 042501.
- [MBW02] N. T. Maitra, K. Burke, and C. Woodward, *Memory in Time-Dependent Density Functional Theory*, Phys. Rev. Lett. **89** (2002), 023002.
- [MCBR03] M. A. L. Marques, A. Castro, G. F. Bertsch, and A. Rubio, *octopus: a first-principles tool for excited electron-ion dynamics*, Comp. Phys. Comm. **151** (2003), 60.
- [MCR01] M. A. L. Marques, A. Castro, and A. Rubio, *Assessment of exchange-correlation functionals for the calculation of dynamical properties of small clusters in time-dependent density functional theory*, J. Chem. Phys. **115** (2001), 3006.
- [MDRS08] J. Messud, P. M. Dinh, P.-G. Reinhard, and E. Suraud, *Time-Dependent Density-Functional Theory with a Self-Interaction Correction*, Phys. Rev. Lett. **101** (2008), 096404.
- [MDRS09a] J. Messud, P. M. Dinh, P.-G. Reinhard, and E. Suraud, *On the exact treatment of time-dependent self-interaction correction*, Ann. Phys. (N.Y.) **324** (2009), 955.

- [MDRS09b] J. Messud, P. M. Dinh, P.-G. Reinhard, and E. Suraud, *Simplification of the time-dependent generalized self-interaction correction method using two sets of orbitals: Application of the optimized effective potential formalism*, Phys. Rev. A **80** (2009), 044503.
- [MDRS11] J. Messud, P. M. Dinh, P.-G. Reinhard, and E. Suraud, *The generalized SIC-OEP formalism and the generalized SIC-Slater approximation (stationary and time-dependent cases)*, Annalen der Physik **523** (2011), 270.
- [MG04] M. A. L. Marques and E. K. U. Gross, *Time-dependent density functional theory*, Annu. Rev. Phys. Chem. **55** (2004), 427.
- [Mit97] W. F. Mitchell, *A Parallel Multigrid Method Using the Full Domain Partition*, Electronic Transactions on Numerical Analysis **6** (1997), 224.
- [MK05] M. Mundt and S. Kümmel, *Derivative Discontinuities in Time-Dependent Density-Functional Theory*, Phys. Rev. Lett. **95** (2005), 203004.
- [MK06] M. Mundt and S. Kümmel, *Optimized effective potential in real time: Problems and prospects in time-dependent density-functional theory*, Phys. Rev. A **74** (2006), 022511.
- [MK07] M. Mundt and S. Kümmel, *Photoelectron spectra of anionic sodium clusters from time-dependent density-functional theory in real time*, Phys. Rev. B **76** (2007), 035413.
- [MKHM06] M. Mundt, S. Kümmel, B. Huber, and M. Moseler, *Photoelectron spectra of sodium clusters: The problem of interpreting Kohn-Sham eigenvalues*, Phys. Rev. B **73** (2006), 205407.
- [MKK11] A. Makmal, S. Kümmel, and L. Kronik, *Dissociation of diatomic molecules and the exact-exchange Kohn-Sham potential: The case of LiF*, Phys. Rev. A **83** (2011), 062512.
- [MKvLR07] M. Mundt, S. Kümmel, R. van Leeuwen, and P.-G. Reinhard, *Violation of the zero-force theorem in the time-dependent Krieger-Li-Iafrate approximation*, Phys. Rev. A **75** (2007), 050501.
- [MLCGM08] A. Muñoz-Losa, C. Curutchet, I. Fdez. Galván, and B. Mennucci, *Quantum mechanical methods applied to excitation energy transfer: A comparative analysis on excitation energies and electronic couplings*, J. Chem. Phys. **129** (2008), 034104.
- [MMN<sup>+</sup>12] M. A. L. Marques, N. T. Maitra, F. M. S. Nogueira, E. K. U. Gross, and A. Rubio (eds.), *Fundamentals of Time-Dependent Density Functional Theory*, Lecture Notes in Physics, Springer, 2012.
- [MNMB07] R. Metivier, F. Nolde, K. Müllen, and T. Basché, *Electronic excitation energy transfer between two single molecules embedded in a polymer host*, Phys. Rev. Lett. **98** (2007), 047802.

- [MSCY06] P. Mori-Sánchez, A. J. Cohen, and W. Yang, *Many-electron self-interaction error in approximate density functionals*, J. Chem. Phys. **125** (2006), 201102.
- [MSWY03] P. Mori-Sánchez, Q. Wu, and W. Yang, *Accurate polymer polarizabilities with exact exchange density-functional theory*, J. Chem. Phys. **119** (2003), 11001.
- [MT96] L. R. Matheson and R. E. Tarjan, *Parallelism in Multigrid Methods: How Much Is Too Much?*, Int. J. Parallel Program. **24** (1996), 397.
- [MT06] N. T. Maitra and D.G. Tempel, *Long-range excitations in time-dependent density functional theory*, J. Chem. Phys. **125** (2006), 184111.
- [Mul50] R. S. Mulliken, *Structures of Complexes Formed by Halogen Molecules with Aromatic and with Oxygenated Solvents*, J. Am. Chem. Soc. **72** (1950), 600.
- [MUN<sup>+</sup>06] M. A. L. Marques, C. A. Ullrich, F. Nogueira, A. Rubio, K. Burke, and E. K. U. Gross (eds.), *Time-Dependent Density Functional Theory*, Lecture Notes in Physics, Springer, 2006.
- [Mun07] M. Mundt, *Orbital functionals in time-dependent density-functional theory*, Ph.D. thesis, Universität Bayreuth, 2007.
- [Mun09] M. Mundt, *Real-time approach to time-dependent density-functional theory in the linear and nonlinear regime*, J. Theor. Comp. Chem. **8** (2009), 561.
- [MVO<sup>+</sup>11] M. A. L. Marques, J. Vidal, M. J. T. Oliveira, L. Reining, and S. Botti, *Density-based mixing parameter for hybrid functionals*, Phys. Rev. B **83** (2011), 035119.
- [Neu07] J. Neugebauer, *Couplings between electronic transitions in a subsystem formulation of time-dependent density functional theory*, J. Chem. Phys. **126** (2007), 134116.
- [Neu08] J. Neugebauer, *Photophysical properties of natural light-harvesting complexes studied by subsystem density functional theory*, J. Phys. Chem. B **112** (2008), 2207.
- [New91] M. D. Newton, *Quantum chemical probes of electron-transfer kinetics: the nature of donor-acceptor interactions*, Chem. Rev. **91** (1991), 767.
- [NFM03] F. Nogueira, C. Fiolhais, and M. A. L. Marques (eds.), *A Primer in Density Functional Theory*, Lecture Notes in Physics, Springer, 2003.
- [OCL97] S. Ögüt, J. R. Chelikowsky, and S. G. Louie, *Quantum Confinement and Optical Gaps in Si Nanocrystals*, Phys. Rev. Lett. **79** (1997), 1770.
- [ORR02] G. Onida, L. Reining, and A. Rubio, *Electronic excitations: density-functional versus many-body Green's-function approaches*, Rev. Mod. Phys. **74** (2002), 601.

- [PAZ01] S. Patchkovskii, J. Autschbach, and T. Ziegler, *Curing difficult cases in magnetic properties prediction with self-interaction corrected density functional theory*, J. Chem. Phys. **115** (2001), 26.
- [PBE96] J. P. Perdew, K. Burke, and M. Ernzerhof, *Generalized Gradient Approximation Made Simple*, Phys. Rev. Lett. **77** (1996), 3865.
- [PBHT08] M. J. G. Peach, P. Benfield, T. Helgaker, and D. J. Tozer, *Excitation energies in density functional theory: An evaluation and a diagnostic test*, J. Chem. Phys. **128** (2008), 044118.
- [PDV08] Y. V. Pershin, Y. Dubi, and M. Di Ventra, *Effective single-particle order- $N$  scheme for the dynamics of open noninteracting many-body systems*, Phys. Rev. B **78** (2008), 054302.
- [Per86] J. P. Perdew, *Density-functional approximation for the correlation energy of the inhomogeneous electron gas*, Phys. Rev. B **33** (1986), 8822.
- [Per90] J. P. Perdew, *Size-Consistency, Self-Interaction Correction, and Derivative Discontinuity in Density Functional Theory*, Adv. Quantum Chem. **21** (1990), 113.
- [PFD<sup>+</sup>11] C.-H. Park, A. Ferretti, I. Dabo, N. Poilvert, and N. Marzari, *Variational Minimization of Orbital-dependent Density Functionals*, arXiv:1108.5726v1 (2011).
- [PGG96] M. Petersilka, U. J. Gossmann, and E. K. U. Gross, *Excitation Energies from Time-Dependent Density-Functional Theory*, Phys. Rev. Lett. **76** (1996), 1212.
- [PHL84] M. R. Pederson, R. A. Heaton, and C. C. Lin, *Local-density Hartree-Fock theory of electronic states of molecules with self-interaction correction*, J. Chem. Phys. **80** (1984), 1972.
- [PHL85] M. R. Pederson, R. A. Heaton, and C. C. Lin, *Density-Functional Theory with self-interaction correction - application to the lithium molecule*, J. Chem. Phys. **82** (1985), 2688.
- [PL83] J. P. Perdew and M. Levy, *Physical Content of the Exact Kohn-Sham Orbital Energies: Band Gaps and Derivative Discontinuities*, Phys. Rev. Lett. **51** (1983), 1984.
- [PL88] M. R. Pederson and C. C. Lin, *Localized and canonical atomic orbitals in self-interaction corrected local density functional approximation*, J. Chem. Phys. **88** (1988), 1807.
- [PM89] J. Pipek and P. G. Mezey, *A fast intrinsic localization procedure applicable for ab initio and semiempirical linear combination of atomic orbital wave functions*, J. Chem. Phys. **90** (1989), 4916.

- [PPLB82] J. P. Perdew, R. G. Parr, M. Levy, and J. L. Balduz, *Density-Functional Theory for Fractional Particle Number: Derivative Discontinuities of the Energy*, Phys. Rev. Lett. **49** (1982), 1691.
- [PSB08] C. D. Pemmaraju, S. Sanvito, and K. Burke, *Polarizability of molecular chains: A self-interaction correction approach*, Phys. Rev. B **77** (2008), 121204(R).
- [PTVF92] W. H. Press, S. A. Teukolsky, W. T. Vetterling, and B. P. Flannery, *Numerical Recipes in FORTRAN*, Cambridge University Press, 1992.
- [PW92] J. P. Perdew and Y. Wang, *Accurate and simple analytic representation of the electron-gas correlation energy*, Phys. Rev. B **45** (1992), 13244.
- [PY86] J. P. Perdew and W. Yue, *Accurate and simple density functional for the electronic exchange energy: Generalized gradient approximation*, Phys. Rev. B **33** (1986), 8800.
- [PZ81] J. P. Perdew and A. Zunger, *Self-interaction correction to density-functional approximations for many-electron systems*, Phys. Rev. B **23** (1981), 5048.
- [RG84] E. Runge and E. K. U. Gross, *Density-Functional Theory for Time-Dependent Systems*, Phys. Rev. Lett. **52** (1984), 997.
- [RL98] M. Rohlfing and S. G. Louie, *Excitonic Effects and the Optical Absorption Spectrum of Hydrogenated Si Clusters*, Phys. Rev. Lett. **80** (1998), 3320.
- [RL00] M. Rohlfing and S. G. Louie, *Electron-hole excitations and optical spectra from first principles*, Phys. Rev. B **62** (2000), 4927.
- [RLG10] D. Rocca, D. Lu, and G. Galli, *Ab initio calculations of optical absorption spectra: Solution of the Bethe-Salpeter equation within density matrix perturbation theory*, J. Chem. Phys. **133** (2010), 164109.
- [RMAG09] P. Rebertus, M. Mohseni, and A. Aspuru-Guzik, *Role of Quantum Coherence and Environmental Fluctuations in Chromophoric Energy Transport*, J. Phys. Chem. B **113** (2009), 9942.
- [RPC<sup>+</sup>06] A. Ruzsinszky, J. P. Perdew, G. I. Csonka, O. A. Vydrov, and G. E. Scuseria, *Spurious fractional charge on dissociated atoms: Pervasive and resilient self-interaction error of common density functionals*, J. Chem. Phys. **125** (2006), 194112.
- [RPC<sup>+</sup>08] A. Ruzsinszky, J. P. Perdew, G. I. Csonka, G. E. Scuseria, and O. A. Vydrov, *Understanding and correcting the self-interaction error in the electrical response of hydrogen chains*, Phys. Rev. A **77** (2008), 060502(R).
- [RSA<sup>+</sup>06] P.-G. Reinhard, P. D. Stevenson, D. Almeded, J. A. Maruhn, and M. R. Strayer, *Role of boundary conditions in dynamic studies of nuclear giant resonances and collisions*, Phys. Rev. E **73** (2006), 036709.

- [Saa03] Y. Saad, *Iterative Methods for Sparse Linear Systems*, Society for Industrial and Applied Mathematics (2003), 187.
- [SAF98] L. Serrano-Andrés and M. P. Fülischer, *Theoretical Study of the Electronic Spectroscopy of Peptides. III. Charge-Transfer Transitions in Polypeptides*, J. Am. Chem. Soc. **120** (1998), 10912.
- [Sav95] A. Savin, *Beyond the Kohn-Sham Determinant*, Recent Advances in Density Functional Methods **1** (1995), 129.
- [Sch84] S. Schaffer, *Higher Order Multi-Grid Methods*, Math. Comp. **43** (1984), 89.
- [Sch03] G. D. Scholes, *Long-range resonance energy transfer in molecular systems*, Ann. Rev. Phys. Chem. **54** (2003), 57.
- [SDCF94] P. J. Stephens, F. J. Devlin, C. F. Chabalowski, and M. J. Frisch, *Ab Initio Calculation of Vibrational Absorption and Circular Dichroism Spectra Using Density Functional Force Fields*, J. Phys. Chem. **98** (1994), 11623.
- [SFK09] E. Sagvolden, F. Furche, and A. Köhn, *Förster Energy Transfer and Davydov Splittings in Time-Dependent Density Functional Theory: Lessons from 2-Pyridone Dimer*, J. Chem. Theory Comput. **5** (2009), 873.
- [SG01] F. Della Sala and A. Görling, *Efficient localized Hartree-Fock methods as effective exact-exchange Kohn-Sham methods for molecules*, J. Chem. Phys. **115** (2001), 5718.
- [SGV<sup>+</sup>96] A. Seidl, A. Görling, P. Vogl, J. A. Majewski, and M. Levy, *Generalized Kohn-Sham schemes and the band-gap problem*, Phys. Rev. B **53** (1996), 3764.
- [SH53] R. T. Sharp and G. K. Horton, *A Variational Approach to the Unipotential Many-Electron Problem*, Phys. Rev. **90** (1953), 317.
- [Sil11] R. Silbey, *Description of quantum effects in the condensed phase*, Procedia Chemistry **3** (2011), 188.
- [SKB09a] T. Stein, L. Kronik, and R. Baer, *Prediction of charge-transfer excitations in coumarin-based dyes using a range-separated functional tuned from first principles*, J. Am. Chem. Soc. **131** (2009), 244119.
- [SKB09b] T. Stein, L. Kronik, and R. Baer, *Reliable Prediction of Charge Transfer Excitations in Molecular Complexes Using Time-Dependent Density Functional Theory*, J. Am. Chem. Soc. **131** (2009), 2818.
- [Sla51] J. C. Slater, *A Simplification of the Hartree-Fock Method*, Phys. Rev. **81** (1951), 385.
- [SP08] E. Sagvolden and J. P. Perdew, *Discontinuity of the exchange-correlation potential: Support for assumptions used to find it*, Phys. Rev. A **77** (2008), 012517.

- [SPB<sup>+</sup>06] C. Scharf, K. Peter, P. Bauer, C. Jung, M. Thelakkat, and J. Köhler, *Towards the characterization of energy-transfer processes in organic donor-acceptor dyads based on triphenyldiamine and perylenebisimides*, Chem. Phys. **328** (2006), 403.
- [Spe96] S. Speiser, *Photophysics and Mechanisms of Intramolecular Electronic Energy Transfer in Bichromophoric Molecular Systems: Solution and Supersonic Jet Studies*, Chem. Rev. **96** (1996), 1953.
- [SS83] L. J. Sham and M. Schlüter, *Density-Functional Theory of the Energy Gap*, Phys. Rev. Lett. **51** (1983), 1888.
- [ŠT03] M. Šterk and R. Trobec, *Parallel Performances of a Multigrid Poisson Solver*, International Symposium on Parallel and Distributed Computing (2003), 238.
- [Ste78] H. J. Stetter, *The Defect Correction Principle and Discretization Methods*, Numer. Math. **29** (1978), 425.
- [Str78] L. Stryer, *Fluorescence energy-transfer as a spectroscopic ruler*, Ann. Rev. Biochem. **47** (1978), 819.
- [SV09] N. Schuch and F. Verstraete, *Computational complexity of interacting electrons and fundamental limitations of density functional theory*, Nat. Phys. **5** (2009), 732.
- [TAH<sup>+</sup>99] D. J. Tozer, R. D. Amos, N. C. Handy, B. O. Roos, and L. Serrano-Andrés, *Does density functional theory contribute to the understanding of excited states of unsaturated organic compounds?*, Mol. Phys. **97** (1999), 859.
- [TC98a] X.-M. Tong and S.-I. Chu, *Time-dependent density-functional theory for strong-field multiphoton processes: Application to the study of the role of dynamical electron correlation in multiple high-order harmonic generation*, Phys. Rev. A **57** (1998), 452.
- [TC98b] X.-M. Tong and S.-I. Chu, *Time-dependent density-functional theory with optimized effective potential and self-interaction correction: Application to the study of coherent control of multiple high-order harmonic generation of He atoms in mixed laser fields*, Int J. Quantum Chem. **69** (1998), 293.
- [TFSB05] C. Toher, A. Filippetti, S. Sanvito, and K. Burke, *Self-Interaction Errors in Density-Functional Calculations of Electronic Transport*, Phys. Rev. Lett. **95** (2005), 146402.
- [TK09] M. Thiele and S. Kümmel, *Photoabsorption spectra from adiabatically exact time-dependent density-functional theory in real time*, Phys. Chem. Chem. Phys. **11** (2009), 4631.
- [TM91] N. Troullier and J. L. Martins, *Efficient pseudopotentials for plane-wave calculations*, Phys. Rev. B **43** (1991), 1993.

- [TMM09] D. G. Tempel, T. J. Martínez, and N. T. Maitra, *Revisiting Molecular Dissociation in Density Functional Theory: A Simple Model*, J. Chem. Theo. Comput. **5** (2009), 770.
- [TOS01] U. Trottenberg, C. W. Oosterlee, and A. Schüller, *Multigrid*, Academic Press, 2001.
- [Toz03] D. J. Tozer, *Relationship between long-range charge-transfer excitation energy error and integer discontinuity in Kohn-Sham theory*, J. Chem. Phys. **119** (2003), 12697.
- [TS76] J. D. Talman and W. F. Shadwick, *Optimized effective atomic central potential*, Phys. Rev. A **14** (1976), 36.
- [TS07] C. Toher and S. Sanvito, *Efficient Atomic Self-Interaction Correction Scheme for Nonequilibrium Quantum Transport*, Phys. Rev. Lett. **99** (2007), 056801.
- [TS08] C. Toher and S. Sanvito, *Effects of self-interaction corrections on the transport properties of phenyl-based molecular junctions*, Phys. Rev. B **77** (2008), 155402.
- [TTdM+95] T. T. Toto, J. L. Toto, C. P. de Melo, M. Hasan, and B. Kirtman, *Ab initio finite oligomer method for nonlinear optical properties of conjugated polymers. Effect of electron correlation on the static longitudinal hyperpolarizability of polyacetylene*, Chem. Phys. Lett. **244** (1995), 59.
- [UGG95] C. A. Ullrich, U. J. Gossmann, and E. K. U. Gross, *Time-dependent optimized effective potential*, Phys. Rev. Lett. **74** (1995), 872.
- [vBH72] U. von Barth and L. Hedin, *A local exchange-correlation potential for the spin polarized case: I*, J. Phys. C **5** (1972), 1629.
- [vFdBvL+02] M. van Faassen, P. L. de Boeij, R. van Leeuwen, J. A. Berger, and J. G. Snijders, *Ultranonlocality in Time-Dependent Current-Density-Functional Theory: Application to Conjugated Polymers*, Phys. Rev. Lett. **88** (2002), 186401.
- [vGSG+99] S. J. A. van Gisbergen, P. R. T. Schipper, O. V. Gritsenko, E. J. Baerends, J. G. Snijders, B. Champagne, and B. Kirtman, *Electric Field Dependence of the Exchange-Correlation Potential in Molecular Chains*, Phys. Rev. Lett. **83** (1999), 694.
- [Vig95] G. Vignale, *Center of Mass and Relative Motion in Time Dependent Density Functional Theory*, Phys. Rev. Lett. **74** (1995), 3233.
- [Vig04] G. Vignale, *Mapping from current densities to vector potentials in time-dependent current density functional theory*, Phys. Rev. B **70** (2004), 201102.
- [vK07] N. G. van Kampen, *Stochastic Processes in Physics and Chemistry*, Elsevier, 2007.

- [vL98] R. van Leeuwen, *Causality and Symmetry in Time-Dependent Density-Functional Theory*, Phys. Rev. Lett. **80** (1998), 1280.
- [vL99] R. van Leeuwen, *Mapping from Densities to Potentials in Time-Dependent Density-Functional Theory*, Phys. Rev. Lett. **82** (1999), 3863.
- [vL01] R. van Leeuwen, *Key concepts in time-dependent density-functional theory*, Int. J. Mod. Phys. B **15** (2001), 1969.
- [vLGB95] R. van Leeuwen, O. V. Gritsenko, and E. J. Baerends, *Step structure in the atomic Kohn-Sham potential*, Z. Phys. D **33** (1995), 229.
- [VOC02] I. Vasiliev, S. Ögüt, and J. R. Chelikowsky, *First-principles density-functional calculations for optical spectra of clusters and nanocrystals*, Phys. Rev. B **65** (2002), 115416.
- [VOC06] I. Vasiliev, S. Ögüt, and J. R. Chelikowsky, *Optical excitations in organic molecules, clusters, and defects studied by first-principles Green's function methods*, Phys. Rev. B **73** (2006), 205334.
- [VS06] O. A. Vydrov and G. E. Scuseria, *Assessment of a long-range corrected hybrid functional*, J. Chem. Phys. **125** (2006), 234109.
- [VSP<sup>+</sup>06] O. A. Vydrov, G. E. Scuseria, J. P. Perdew, A. Ruzsinszky, and G. I. Csonka, *Scaling down the Perdew-Zunger self-interaction correction in many-electron regions*, J. Chem. Phys. **124** (2006), 094108.
- [VSP07] O. A. Vydrov, G. E. Scuseria, and J. P. Perdew, *Tests of functionals for systems with fractional electron number*, J. Chem. Phys. **126** (2007), 154109.
- [Wei08] U. Weiss, *Quantum Dissipative Systems*, World Scientific, 2008.
- [WT79] C.-Y. Wong and H. H. K. Tang, *Dynamics of nuclear fluid. V. Extended time-dependent Hartree-Fock approximation illuminates the approach to thermal equilibrium*, Phys. Rev. C **20** (1979), 1419.
- [WU08] H. O. Wijewardane and C. A. Ullrich, *Real-Time Electron Dynamics with Exact-Exchange Time-Dependent Density-Functional Theory*, Phys. Rev. Lett. **100** (2008), 056404.
- [YB96] K. Yabana and G. F. Bertsch, *Time-dependent local-density approximation in real time*, Phys. Rev. B **54** (1996), 4484.
- [YB99a] K. Yabana and G. F. Bertsch, *Optical response of small silver clusters*, Phys. Rev. A **60** (1999), 3809.
- [YB99b] K. Yabana and G. F. Bertsch, *Time-dependent local-density approximation in real time: Application to conjugated molecules*, Int. J. Quantum Chem. **75** (1999), 55.

- [YF02] M. Yang and G. R. Fleming, *Influence of phonons on exciton transfer dynamics: comparison of the Redfield, Förster, and modified Redfield equations*, Chem. Phys. **275** (2002), 355.
- [YTH04] T. Yanai, D. P. Tew, and N. C. Handy, *A new hybrid exchange-correlation functional using the Coulomb-attenuating method (CAM-B3LYP)*, Chem. Phys. Lett. **393** (2004), 51.
- [YZTRRAG10] J. Yuen-Zhou, D. G. Tempel, C.A. Rodríguez-Rosario, and A. Aspuru-Guzik, *Time-Dependent Density Functional Theory for Open Quantum Systems with Unitary Propagation*, Phys. Rev. Lett. **104** (2010), 043001.
- [ZS80] A. Zangwill and P. Soven, *Density-functional approach to local-field effects in finite systems: Photoabsorption in the rare gases*, Phys. Rev. A **21** (1980), 1561.
- [ZSK<sup>+</sup>09] T. Ziegler, M. Seth, M. Krykunov, J. Autschbach, and F. Wang, *Is charge transfer transitions really too difficult for standard density functionals or are they just a problem for time-dependent density functional theory based on a linear response approach*, J. Mol. Struct.: THEOCHEM **914** (2009), 106.
- [ZY98] Y. Zhang and W. Yang, *A challenge for density functionals: Self-interaction error increases for systems with a noninteger number of electrons*, J. Chem. Phys. **109** (1998), 2604.



# Erklärung

Hiermit erkläre ich, dass ich die vorliegende Arbeit selbstständig verfasst und keine anderen als die angegebenen Quellen und Hilfsmittel verwendet habe. Die Arbeit wurde weder in gleicher noch in ähnlicher Form bei anderen Prüfungsbehörden zur Erlangung eines akademischen Grades vorgelegt.

Ich erkläre, dass ich keine Hilfe von gewerblichen Promotionsberatern bzw. -vermittlern oder ähnlichen Dienstleistern in Anspruch genommen habe und auch nicht beabsichtige diese zukünftig in Anspruch zu nehmen.

Weiterhin erkläre ich, dass ich bisher keinen anderweitigen Promotionsversuch unternommen habe.

Bayreuth, den 06. September 2012

Dirk Hofmann



## Publication 1

# Energy transfer and Förster's dipole coupling approximation investigated in a real-time Kohn-Sham scheme

D. Hofmann, T. Körzdörfer, and S. Kümmel

*Physikalisches Institut, Universität Bayreuth, D-95440 Bayreuth, Germany*

Physical Review A **82**, 012509 (2010)

©2010 The American Physical Society

DOI: 10.1103/PhysRevA.82.012509

available at: <http://link.aps.org/doi/10.1103/PhysRevA.82.012509>

### ABSTRACT

We present a scheme to investigate energy transfer by real-time propagation of the Kohn-Sham equations. The scheme's purpose is to check and go beyond the dipole coupling approximation underlying a Förster-type energy transfer, and to obtain information about the coupling on the grounds of the density-functional theory. We observe deviations from the dipole coupling approximation for small molecules.



## Energy transfer and Förster's dipole coupling approximation investigated in a real-time Kohn-Sham scheme

D. Hofmann, T. Körzdörfer, and S. Kümmel

*Physikalisches Institut, Universität Bayreuth, D-95440 Bayreuth, Germany*

(Received 19 April 2010; published 23 July 2010)

We present a scheme to investigate energy transfer by real-time propagation of the Kohn-Sham equations. The scheme's purpose is to check and go beyond the dipole coupling approximation underlying a Förster-type energy transfer, and to obtain information about the coupling on the grounds of the density-functional theory. We observe deviations from the dipole coupling approximation for small molecules.

DOI: [10.1103/PhysRevA.82.012509](https://doi.org/10.1103/PhysRevA.82.012509)

PACS number(s): 31.15.ee, 31.70.Hq, 82.20.Rp, 82.20.Wt

### I. ENERGY TRANSFER AND TIME-DEPENDENT DENSITY FUNCTIONAL THEORY

Energy transfer is one of the most fundamental processes on the molecular scale, governing light-harvesting in biological systems [1,2] and energy conversion in electronic devices such as organic solar cells [3–5] or light-emitting diodes [6]. The design principles of natural light-harvesting complexes [7–9] have found considerable interest, as hopes are high that the principles realized in nature can be mimicked in the design of artificial organic devices [3,10,11].

One standard method to interpret experimental data of excitation energy transfer between a donor (D) and an acceptor (A) molecule separated by the distance  $R$  is the so-called Förster resonance energy transfer (FRET) theory [9–21]. Förster theory describes the nonradiative energy transfer mediated by a (quantum-mechanical) coupling between the transition dipoles of the donor and acceptor molecules [13–15]. One of the central assumptions in FRET is that the coupling between D and A can be described by a (point)-dipole-dipole interaction, falling as  $1/R^3$ . Furthermore, FRET theory is formulated for the weak coupling regime (i.e., the isolated D and A excited states do not change significantly on coupling). Based on these assumptions Förster derived an expression for the energy transfer rate showing a characteristic  $R^{-6}$  distance dependence, with the nuclear vibrations being subsumed into a spectral overlap factor between donor emission and acceptor absorption spectra. The resulting, rather simple expression for the energy transfer rate, see Sec. II for details, allows for determining the intermolecular distance  $R$  by spectroscopy of the coupled D-A system, and D as well as A individually.

Thus, FRET has gained tremendous importance as it establishes a spectroscopic ruler on the nanoscale [22,23]. Typically it is applied in a range of distances from about 10 to 100 Å [24,25]. However, in recent years the applicability of the dipole coupling approximation underlying FRET has been questioned in many applications [25–33] as frequently the intermolecular distance  $R$  is comparable to the molecules' extension, or the D and A molecules are connected by bridging units.

Theoretical insight into the validity of the dipole coupling approximation is, therefore, of great importance. As the molecules of practical relevance often contain many electrons, (time-dependent) density functional theory (TD)DFT appears as a natural choice to study the problem on a first-principles scale at bearable computational cost. Recently,

TDDFT has been applied to Förster-type excitation energy transfer questions [34–41] in the Casida-type linear response formalism [42]. As a complementary approach to the Casida formalism, real-time implementations [43–52] of TDDFT are finding increasing attention due to their accuracy and favorable scaling, which allows one to apply them to large systems [53–55]. In addition, they do not require computation of the exchange-correlation kernel, which can be advantageous when advanced functionals that explicitly employ the orbitals are used [47,49,56–58].

In the following we present a real-time TDDFT scheme for investigating energy transfer and the dipole coupling approximation. After shortly reviewing the pertinent concepts of FRET theory in Sec. II, we discuss in Sec. III how the dipole coupling can be incorporated into the real-time methodology. This leads to a very general scheme for qualitatively checking the validity of the dipole coupling approximation, as demonstrated in Sec. IV. Under certain conditions that are explained in Sec. V one can also determine the coupling matrix element quantitatively. We stress that in all instances we deliberately do not use the Kohn-Sham Slater determinant as an approximation to the true wave function, staying truly on TDDFT grounds.

### II. THE DIPOLE COUPLING APPROXIMATION

In the following we briefly review the aspects of Förster theory that are crucial for the further considerations. Starting with Fermi's Golden Rule, the energy transfer rate  $k^{\text{ET}}$  can be written as [15]

$$k^{\text{ET}} = 2\pi |V|^2 \int_0^\infty d\epsilon J(\epsilon), \quad (1)$$

where  $J(\epsilon)$  is the spectral overlap between the normalized donor emission and acceptor absorption spectra. Hartree atomic units are used throughout.  $V$  is the electronic coupling matrix element

$$V = \langle DA^* | \hat{V}^C | D^* A \rangle, \quad (2)$$

where the Coulomb interaction  $\hat{V}^C$  mediates between the initial and final wave functions. Förster theory is based on the assumption that the wave function of the total system can be separated into D and A parts due to negligible electronic coupling between D and A. Initially, the acceptor is in its ground state denoted by  $|A\rangle$  and the donor is in an excited

state  $|D^*\rangle$ . The final wave function corresponds to the inverse situation. Thus, the states in Eq. (2) are written as

$$\begin{aligned} \langle DA^*| &= \frac{1}{\sqrt{2}}(\langle \widetilde{DA}^*| - \langle \widetilde{A^*D}|), \\ |D^*A\rangle &= \frac{1}{\sqrt{2}}(|\widetilde{D^*A}\rangle - |\widetilde{A\widetilde{D}^*}\rangle), \end{aligned} \quad (3)$$

where  $|\widetilde{DA}^*\rangle$  abbreviates the product state  $|D\rangle|A^*\rangle$ , respectively. Accordingly, the coupling matrix element splits into the Coulomb contribution (i.e.,  $D$  and  $D^*$  having the same coordinates)

$$V^C = \langle \widetilde{DA}^*| \hat{V}^C | \widetilde{D^*A}\rangle \quad (4)$$

and the so-called exchange contribution

$$V^x = \langle \widetilde{A^*D}| \hat{V}^C | \widetilde{D^*A}\rangle \quad (5)$$

(i.e.,  $A^*$  and  $D^*$  having the same coordinates) [14,59,60]. As the overlap between states falls exponentially with increasing  $R$ ,  $V^x$  is neglected in FRET and only the Coulomb term contributes to the Förster rate-of-excitation energy transfer. (The exchange contribution gives the so-called Dexter-type energy transfer [59].)

Under the assumption that the extension of the D and A molecules is small compared to  $R$

$$\frac{|\mathbf{r}^A|}{|\mathbf{R}|} \ll 1 \quad \text{and} \quad \frac{|\mathbf{r}^D|}{|\mathbf{R}|} \ll 1, \quad (6)$$

(see Fig. 1 for the notation), the Coulomb interaction between the electrons of D and A is expanded in a multipole series. Expanding up to powers  $R^{-3}$ , the interaction is written as

$$\begin{aligned} &\sum_{j,k} \frac{1}{|\mathbf{R} + (\mathbf{r}_k^A - \mathbf{r}_j^D)|} \\ &= \sum_{j,k} \left\{ \frac{1}{|\mathbf{R}|} - \frac{(\mathbf{r}_k^A - \mathbf{r}_j^D)\mathbf{R}}{|\mathbf{R}|^3} + \frac{3}{2} \frac{[(\mathbf{r}_k^A - \mathbf{r}_j^D)\mathbf{R}]^2}{|\mathbf{R}|^5} \right. \\ &\quad \left. - \frac{(\mathbf{r}_k^A - \mathbf{r}_j^D)^2}{2|\mathbf{R}|^3} + \dots \right\}, \end{aligned} \quad (7)$$

where the  $k$  sum runs over all electrons of the acceptor, and the  $j$  sum runs over all electrons in the donor. Introducing the orientation factor

$$\kappa^{DA} = \hat{e}^D \hat{e}^A - 3(\hat{e}^D \mathbf{R})(\hat{e}^A \mathbf{R}), \quad (8)$$

with the vectors  $\hat{e}^i = \frac{\mathbf{r}^i}{|\mathbf{r}^i|}$ , the transition dipole moments

$$\begin{aligned} \boldsymbol{\mu}^D &= \langle D| \sum_j \mathbf{r}_j^D |D^*\rangle \\ \boldsymbol{\mu}^A &= \langle A| \sum_k \mathbf{r}_k^A |A^*\rangle, \end{aligned} \quad (9)$$

and assuming orthogonality of D and A states, one finds the coupling matrix element of FRET theory

$$V^{\text{FRET}} = \kappa^{DA} \frac{|\boldsymbol{\mu}^A| |\boldsymbol{\mu}^D|}{|\mathbf{R}|^3}. \quad (10)$$

$V^{\text{FRET}}$  features the characteristic  $R^{-3}$  dependence of Förster theory. Together with Eq. (1) this yields the rate of the Förster-type excitation energy transfer.

### III. A DIPOLE COUPLING SCHEME IN THE TDDFT CONTEXT

The previously presented concept relies on using the states  $|A\rangle$  and  $|D\rangle$ . For the typical molecules of interest involving tens to hundreds of electrons, the computational cost of calculating these many-particle states with *ab initio* wave function methods is prohibitive. (TD)DFT allows one to determine the electronic structure of systems of that size, yet again, the many-particle states are not accessible: Even if the ultimate exchange-correlation functional were known, there is no reason to believe that generally the Kohn-Sham Slater determinant will be close to the true correlated wave function. Therefore, a TDDFT scheme that is intended to investigate the dipole coupling approximation that is inherent to Förster theory must be based solely on the variable that is reliable in (TD)DFT, namely the density. One way of how this can be achieved is presented in the following.

The real-time formalism of TDDFT that we want to apply is based on the time-dependent Kohn-Sham (KS) equations [43,45,48,50]

$$i \frac{\partial}{\partial t} \varphi_j(\mathbf{r}, t) = h_{\text{KS}}(\mathbf{r}, t) \varphi_j(\mathbf{r}, t), \quad (11)$$

where  $h_{\text{KS}}$  is the time-dependent KS Hamiltonian given by

$$h_{\text{KS}}(\mathbf{r}, t) = -\frac{\nabla^2}{2} + v_{\text{H}}(\mathbf{r}, t) + v_{\text{xc}}(\mathbf{r}, t) + v_{\text{ext}}(\mathbf{r}, t). \quad (12)$$

The potential  $v_{\text{ext}}(\mathbf{r}, t)$  represents all external contributions (e.g., nuclei and a laser field). The electron interaction is taken into account via the Hartree potential

$$v_{\text{H}}[n](\mathbf{r}, t) = \int \frac{n(\mathbf{r}', t)}{|\mathbf{r} - \mathbf{r}'|} d^3 r' \quad (13)$$

and the exchange-correlation (xc) potential  $v_{\text{xc}}(\mathbf{r}, t)$ . Whereas  $v_{\text{H}}[n](\mathbf{r}, t)$  is known explicitly as the functional derivative of the classical Hartree energy

$$E_{\text{H}}[n] = \frac{1}{2} \int \frac{n(\mathbf{r}, t) n(\mathbf{r}', t)}{|\mathbf{r} - \mathbf{r}'|} d^3 r d^3 r', \quad (14)$$

the xc potential has to be approximated as its exact form is unknown.

The real-time KS equations lend themselves very naturally to a general and straightforward scheme for checking the dipole coupling approximation that is at the heart of FRET: One can explicitly implement the multipole expansion of Förster into the TDDFT equations and compare the orbital propagation with the multipole expansion to another one without (i.e., with the usual full KS Hamiltonian). The details of this strategy are explained in the following.

In accordance with the assumption of an appreciable spatial separation of the D and A systems that is underlying FRET theory, we divide the full density into a D and an A part. For the sake of being as explicit in our notation as possible, we assume in all of the following that the D and A densities

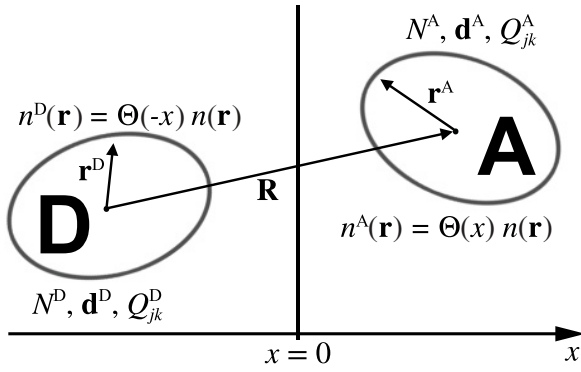


FIG. 1. Donor and acceptor are separated by the distance  $R = |\mathbf{R}|$  and can thus be localized in the half-spaces with negative and positive  $x$  coordinate, for the sake of an explicit notation. Each system is characterized by its multipole moments  $N^i$ ,  $\mathbf{d}^i$  and  $Q_{jk}^i$ , where  $i = \{D, A\}$  labels the system, respectively. Distances with respect to the center of D and A, respectively, are denoted by  $\mathbf{r}^D$  and  $\mathbf{r}^A$ .

are localized in the half spaces of negative and positive  $x$  coordinates, respectively, as shown in Fig. 1

$$\begin{aligned} n^D(\mathbf{r}) &= \Theta(-x)n(\mathbf{r}), \\ n^A(\mathbf{r}) &= \Theta(x)n(\mathbf{r}), \end{aligned} \quad (15)$$

where  $\Theta(x)$  is the Heaviside step function.

As reviewed previously, Förster's concept is based on using the exact states for the separate molecules, but only taking the classical (Hartree) interaction between the transition dipoles of D and A into account for the intermolecular coupling. Consequently, a TDDFT analog of Förster's approach should take all electron interaction effects into account [i.e., use  $v_H$  and the (unknown) exact  $v_{xc}$ ] within each molecule, but use only the Hartree potential for the coupling between D and A, and the latter only to low order in a multipole expansion.

In the following we describe how this expansion can be incorporated into a TDDFT scheme in practice, and we start by noting that there are two possible paths to implement the dipole coupling approximation for the Hartree coupling. The first is to start with the Hartree energy of Eq. (14), perform the multipole expansion, and then take the functional derivative to obtain the potential. The second is to start from the Hartree potential itself and perform the dipole approximation on the level of Eq. (13).

Following the first route, the Hartree energy splits into three components

$$E_H[n] = E_H[n^D] + E_H[n^A] + \int \frac{n^A(\mathbf{r})n^D(\mathbf{r}')}{|\mathbf{r} - \mathbf{r}'|} d^3r d^3r', \quad (16)$$

where the first two contributions separate in D and A, whereas the third term contains the interaction between the D and A systems. The expansion (7) is used in the third term on the right-hand side (rhs) of Eq. (16) to obtain the Hartree energy  $E_H^{dd}$  in the dipole coupling approximation. Calculating the functional derivative of Eq. (16) we use the functional

chain rule to take the separation in D and A densities into account

$$v_H[n](\mathbf{r}) = \sum_{i=D,A} \int \frac{\delta E_H^{dd}[n^D, n^A]}{\delta n^i(\mathbf{r}')} \frac{\delta n^i(\mathbf{r}')}{\delta n(\mathbf{r})} d^3r'. \quad (17)$$

Consequently, the potential in the dipole coupling approximation (superscript  $dd$ ) as derived from the energy (thus superscript index E) can be written as

$$\begin{aligned} v_H^{dde}[n^D, n^A] &= (v_H[n^D] + v_H^{dde,D}[n^A])\Theta(-x) \\ &\quad + (v_H[n^A] + v_H^{dde,A}[n^D])\Theta(x), \end{aligned} \quad (18)$$

where  $v_H[n^{D(A)}]$  is the Hartree potential of D(A) and  $v_H^{dde,D(A)}[n^{A(D)}]$  is the potential resulting from the third term of Eq. (16) in the D(A) half-space. With the help of the multipole moments of the D(A) density,

$$\begin{aligned} N^i &= \int n^i(\mathbf{r}^i) d^3r^i, \quad \mathbf{d}^i = \int \mathbf{r}^i n^i(\mathbf{r}^i) d^3r^i, \\ Q_{jk}^i &= \int n^i(\mathbf{r}^i) (3r_j^i r_k^i - r^{i2} \delta_{jk}) d^3r^i, \end{aligned} \quad (19)$$

where  $i = D, A$ , the Förster potential that the donor density generates in the half space of A (cf. Fig. 1) is

$$\begin{aligned} v_H^{dde,A}[n^D](\mathbf{r}^A) &= \frac{N^D}{|\mathbf{R}|} - \frac{(N^D \mathbf{r}^A - \mathbf{d}^D) \mathbf{R}}{|\mathbf{R}|^3} + \frac{\mathbf{r}^A \mathbf{d}^D}{|\mathbf{R}|^3} \\ &\quad + \frac{N^D}{2} \sum_{j,k=1}^3 (3r_j^A r_k^A - r^{A2} \delta_{jk}) \frac{R_j R_k}{|\mathbf{R}|^5} \\ &\quad + \sum_{j,k=1}^3 \frac{Q_{jk}^D R_j R_k}{2|\mathbf{R}|^5} - \frac{3(\mathbf{R} \mathbf{r}^A)(\mathbf{R} \mathbf{d}^D)}{|\mathbf{R}|^5}. \end{aligned} \quad (20)$$

The corresponding potential  $v_H^{dde,D}[n^A](\mathbf{r}^D)$  is obtained from Eq. (20) by interchanging the D and A superscripts and replacing  $\mathbf{R}$  by  $-\mathbf{R}$ .

As an alternative to this derivation we can take the second route. To this end we start directly at the level of the potential and write the Hartree potential on the A side as

$$v_H^A[n_D, n_A] = \int \frac{n^A(\mathbf{r}')}{|\mathbf{r}^A - \mathbf{r}'|} d^3r' + \int \frac{n^D(\mathbf{r}^D)}{|\mathbf{r}^A + \mathbf{R} - \mathbf{r}^D|} d^3r^D. \quad (21)$$

This expression leads to another natural way of translating Förster's Hartree dipole coupling concept into a TDDFT scheme: The contribution from the A density to the Hartree potential in A's own half space is taken into account fully, whereas the contribution from the D density to the Hartree potential in A's half space [the second term on the rhs of Eq. (21)] is expanded in analogy to Eq. (7). The latter leads to the potential

$$v_H^{ddv,A}[n^D] = \frac{N^D}{|\mathbf{r}^A + \mathbf{R}|} + \frac{\mathbf{d}^D(\mathbf{r}^A + \mathbf{R})}{|\mathbf{r}^A + \mathbf{R}|^3} + \sum_{j,k=1}^3 \frac{Q_{jk}^D R_j R_k}{2|\mathbf{r}^A + \mathbf{R}|^5}, \quad (22)$$

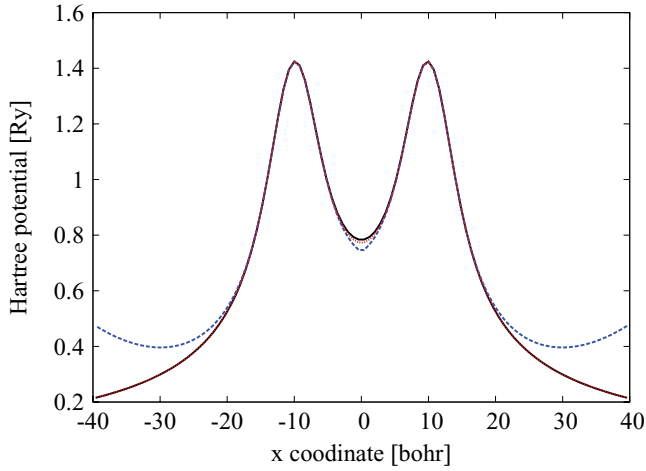


FIG. 2. (Color online) Comparison of the usual Hartree potential  $v_H[n]$  (black solid line) with the Hartree potentials  $v_H^{ddv}[n_D, n_A]$  (red dotted line) and  $v_H^{dde}[n_D, n_A]$  (blue dashed line). The potentials are plotted along the axis that runs through the centers of the two sodium dimers, while the position of the molecules is  $-10$  and  $+10$  bohr.

on the A side (where the superscript index  $v$  indicates that we approximated the potential directly, not the energy as in route 1). The corresponding potential on the D side is

$$v_H^{ddv,D}[n^A] = \frac{N^A}{|\mathbf{r}^D - \mathbf{R}|} + \frac{\mathbf{d}^A(\mathbf{r}^D - \mathbf{R})}{|\mathbf{r}^D - \mathbf{R}|^3} + \sum_{j,k=1}^3 \frac{Q_{jk}^A R_j R_k}{2|\mathbf{r}^D - \mathbf{R}|^5}. \quad (23)$$

Using these expressions instead of  $v_H^{dde,A}$  and  $v_H^{dde,D}$  in Eq. (18) defines the potential  $v_H^{ddv}$ .

Let us pause for a moment to compare the two routes. The first one, starting from the energy, appears more natural if one has in mind Förster's original work, which was based on the energy. However, the second one, directly using the potential, seems to be more natural in the context of KS (TD)DFT in which the potential is readily available. However, both are valid translations of Förster's concept into a real-time TDDFT context, and it is thus not clear *a priori* which one should be preferred. To get a better understanding of the differences between  $v_H^{dde}$  and  $v_H^{ddv}$  we plot them in Fig. 2 for a transparent example, a system of two sodium dimers [61] aligned in parallel and separated by  $R = 20$  a.u..

While  $v_H^{ddv}$  is rather similar to the full Hartree potential, the potential  $v_H^{dde}$  is considerably too low in the central region between the dimers and rises unphysically far away from the dimers. This behavior can be traced back to the fact that, in calculating  $v_H^{dde}$ , we always divide by powers of the fixed  $R$  [see denominators of Eq. (20)] while the numerators rise with growing distance  $r$  to the corresponding molecule. In contrast, in potential  $v_H^{ddv}$  the distance  $r$  enters in the denominator. Therefore,  $v_H^{ddv}$  decays with the growing distance to the corresponding dimer. As this is the behavior one naturally expects from a potential, we used  $v_H^{ddv}$  in our calculations [62].

#### IV. REAL-TIME INVESTIGATION OF THE DIPOLE COUPLING APPROXIMATION

Our focus so far was on the conceptual work of translating Förster's dipole coupling idea into the (TD)DFT context. For using the scheme in practical calculations, we have to address the question of which influences the approximation that is used for the description of the xc effects will have.

The excitation spectrum of two identical molecules at a separation large enough for the individual molecular densities to not overlap can qualitatively be described as being similar to the spectrum of a single molecule, but with possibly an energetic splitting of the monomer excitations (Davydov splitting, see Sec. V), and with additional charge-transfer excitations from one monomer to the other that carry practically zero oscillator strength.

It is a well known problem of many commonly used density functional, in particular (semi)local ones, that they seriously underestimate the energy of charge-transfer excitations. In the KS framework, this failure is closely related to the absence of step-like structures in the xc potential that result from discontinuities [63] in TDDFT, see Ref. [64] for a detailed discussion. It has been shown that xc approximations using a large fraction of exact exchange [39], or range-separated hybrid functionals [65], or self-interaction corrections [66] can describe charge transfer well. Using a functional that accurately describes charge transfer is mandatory for an accurate description of two monomers at close distance [67].

In the propagation setup the movement of charge is recorded in real-time and this can be used to directly monitor for charge transfer from one molecule to the other. This built-in warning allows one to check against leaving the "large separation" situation which was described in Sec. II and which is the focus of interest here [68]. At large separation, the energy transfer is completely dominated by the Hartree coupling. It remains mandatory in any case that the xc functional approximation one uses describes the excitation spectrum of the single molecules with reasonable accuracy, as otherwise the time-dependent density and transition dipoles will be incorrect.

Starting from two molecules at a large separation  $R$  and decreasing the distance, our aim is to check when the dipole coupling approximation breaks down. Our calculations are performed with our real-time TDDFT extension [51,52] of the real-space code PARSEC [69]. The two molecules are placed in two different half-spaces of the real-space grid. All investigations are performed in the so-called supermolecular approach [70], where we consider D and A as a combined system. To distinguish between a coupling of excited states that fulfills the assumptions leading to expansion (7) and a coupling that does not, we compare the time-dependent dipole moments of D and A obtained by a DFT plus TDDFT run with the full Hartree potential, to the ones obtained in a second run using the potential  $v_H^{ddv}$ . The dipole moments are calculated using the D and A centers of density in the DFT ground state as reference points.

Our proceeding is as follows: (1) determine the spectrum of one single molecule, (2) choose the excitation of interest, (3) perform a real-time TDDFT calculation using the full Hartree potential with a short laser pulse as the initial excitation, (4) repeat step (3) with  $v_H^{ddv}$ , (5) compare the

time-dependent dipole moments obtained in steps (3) and (4). The laser pulse is added as an external potential during the first steps of the real-time propagation only within the half-space of D. The frequency, length, and shape of the pulse are tuned to excite the system only in a narrow frequency band around the excitation chosen in step (2). (See Appendix A for details.)

In the following we demonstrate the use of this approach in calculations for dimers of  $\text{Na}_2$  and  $\text{C}_7\text{H}_6\text{O}$ , respectively. These systems are transparent enough to allow for a clear explanation and demonstration of our concept and they are established reference systems [36,71]. We employ the time-dependent local density approximation (TDLDA) as it well describes the excitations of  $\text{Na}_2$  and  $\text{C}_7\text{H}_6\text{O}$  [72,73] that are of interest in our study. The possible underestimation of charge-transfer excitations that was discussed at the beginning of this section is not of concern here as we are specifically interested in the major excitations carrying dipole oscillator strength. These are described well by TDLDA for the systems that we study.

We first investigate the coupling between two sodium dimers with parallel alignment of the two  $\text{Na}_2$  axes as a function of the distance  $R$  between the two  $\text{Na}_2$  molecules. As the excitation of interest we choose the one that is at 2.1 eV in the  $\text{Na}_2$  spectrum [71,72]. A typical time evolution of the acceptor dipole moment is shown in Fig. 3. At the chosen distance,  $R = 15$  bohr, there are obvious deviations between the time-dependent dipole moment that is obtained using the full Hartree potential and the one that is obtained using  $v_H^{ddv}$ .

The deviations are a manifestation of the breakdown of the dipole coupling approximation at 15 bohr. A systematic analysis of the deviations in the dipole moment at a range of distances from 45 to 15 bohr is depicted in Fig. 4. Qualitatively, we see in Fig. 4 three regimes: For very large distances (45 and 35 bohr) the differences vanish and one is clearly in the dipole regime. At smaller distances (around 25 bohr in the

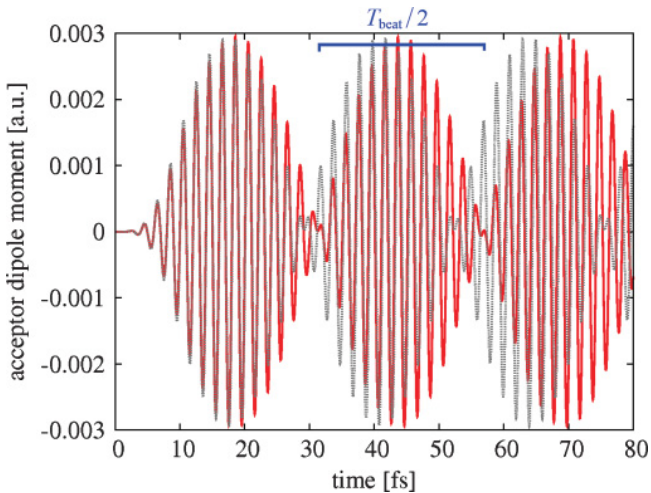


FIG. 3. (Color online) Acceptor dipole moment along the  $\text{Na}_2$  molecular axis, recorded as a function of time, for a system of two  $\text{Na}_2$  with a separation of  $R = 15$  bohr. The time evolution was calculated using the full Hartree potential (solid, red) and the potential  $v_H^{ddv}$  (dotted, black). The coupling between D and A manifests itself in the beat frequency  $\omega_{\text{beat}}$  of an oscillation between D and A (cf. Sec. V). This beat frequency can be extracted from the A dipole moment via  $\omega_{\text{beat}} = 2\pi/T_{\text{beat}}$ .

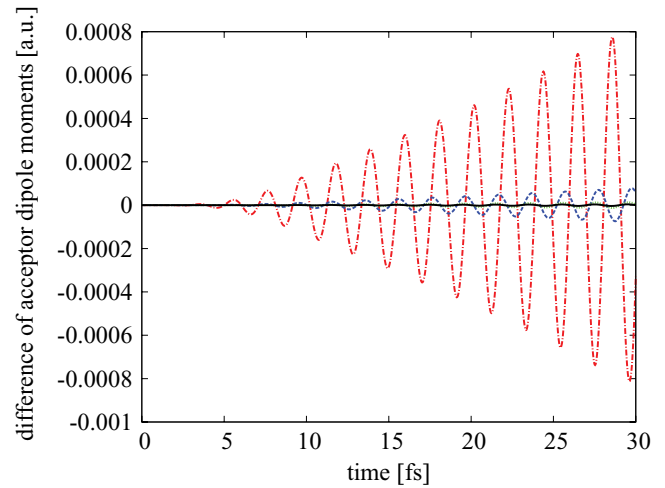


FIG. 4. (Color online) Difference between the acceptor dipole moments obtained in a calculation using the full Hartree potential and another one using  $v_H^{ddv}$  for an  $\text{Na}_2$  dimer, for different values of  $R$ : 15 bohr (dot dashed, red), 25 bohr (dashed, blue), 35 bohr (dotted, green) and 45 bohr (solid, black).

present example) one starts to observe deviations, and for yet smaller distances (15 bohr) the dipole moments differ very significantly during their time evolution—although the density overlap is still small. Here the dipole approximation clearly fails and higher multipoles are relevant.

The same effects are seen in the second example in which we examine the coupling between two  $\text{C}_7\text{H}_6\text{O}$  molecules that are aligned in parallel as depicted in Fig. 5. We again focus on the lowest excitation with appreciable oscillator strength. The dipole moment time evolution was calculated for a range of distances from  $R = 40$  bohr to  $R = 12$  bohr, again using the two different potentials as discussed previously. Characteristic results (distances of 24 to 12 bohr) are shown in Fig. 6. The differences at  $R = 12$  bohr and  $R = 16$  bohr significantly exceed the differences at the larger separations. Therefore, one can argue qualitatively that up to 16 bohr separation one cannot speak of a Förster-type coupling. From 20 bohr on, the differences in the dipole moment time evolution are notably smaller and the Förster-type dipole approximation can be considered valid [74].

As our analysis has so far focused on the total dipole moments, it is rather general and the concept can

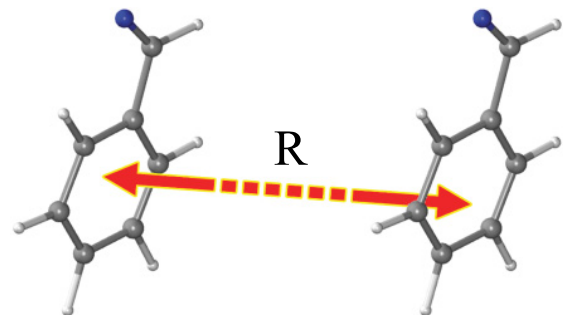


FIG. 5. (Color online) System of two  $\text{C}_7\text{H}_6\text{O}$  molecules, where the distance  $R$  is varied from 40 to 12 bohr.

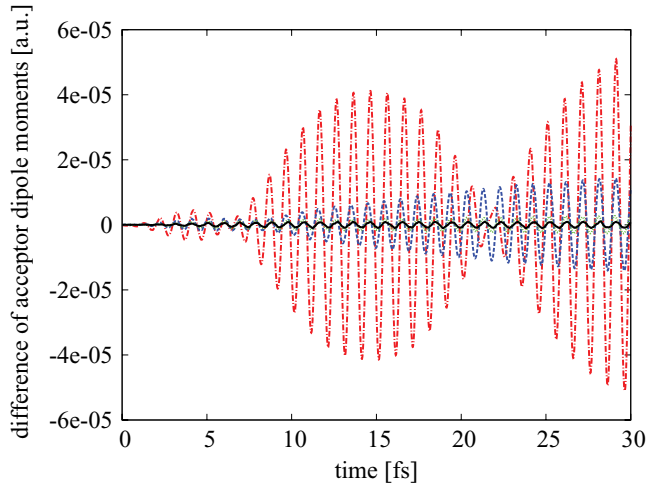


FIG. 6. (Color online) Difference of acceptor dipole moment in a system of two  $C_7H_6O$  between a calculation using the full Hartree potential and another one with the potential  $v_H^{dhw}$ . The molecules are separated by 12 bohr (dot dashed, red), 16 bohr (dashed, blue), 20 bohr (dotted, green), and 24 bohr (solid, black).

straightforwardly be extended, e.g. to unequal dimers. Comparing characteristic features of the dipole moment evolution obtained with full coupling and with dipole coupling, one can assess the trust range of the dipole approximation.

If the excitations of interest have the special feature of being rather well separated from all other excitations so that one can think about the coupling as a coupling in a two-level system, then one can also determine the coupling matrix element quantitatively from the TDDFT calculation—despite the fact that one does not explicitly know the states in TDDFT. This is the topic of the next section.

## V. EXTRACTING THE COUPLING MATRIX ELEMENT FROM A REAL-TIME PROPAGATION

A coupling matrix element of type (2) enters the energy transfer rate (1), and it is a close-lying question whether and how it can be evaluated. In principle, one could calculate the initial and final states and evaluate Eq. (2) directly. However, as discussed previously, the states are hard to compute from first principles and there is no rigorous reason to identify the KS Slater determinant with the true wave function. Therefore, if one wants to stay on the safe formal grounds of (TD)DFT by not using the KS Slater determinant as an approximation to the true wave function, one has to think about alternative ways to determine the coupling matrix element.

The Davydov splitting [75–77] is such an alternative [34–39,41]. In the case of two equal molecules, the Davydov splitting  $\Delta\Omega$  equals the energy splitting  $\Delta E$  of the (nearly) degenerate excitation energies of the monomers in the supermolecule [34,36,37,39]. In the discussed situation  $\Delta\Omega$  is proportional to the coupling matrix element (2)

$$V = \frac{\Delta\Omega}{2}. \quad (24)$$

This observation can be exploited in TDDFT by calculating the spectrum [50,78–80] and deducing the coupling matrix

element from the energy splitting. In the real-time approach to TDDFT spectra are usually determined by initially exciting the system with a momentum boost [45,81], propagating the time-dependent KS equations [82] using the dipole moment as observable, and calculating the dipole spectrum via a Fourier transformation [81]. As the energy splitting is typically much smaller than the excitation energies themselves, high resolution and thus comparably long propagation times are needed to resolve the splitting.

Therefore, we consider an alternative way of extracting the relevant information by observing the D and A dipole moments separately. It considerably reduces the computational load. We note that the Davydov splitting  $\Delta\Omega$  and consequently also the coupling matrix element  $V$  manifests itself as a frequency  $\omega_{\text{beat}}$  in the time-dependent D (and A) dipole moment. This frequency can be extracted as a beat frequency  $\omega_{\text{beat}}$  of an oscillation between D and A. (See Appendix B for details.) From it one obtains

$$V = \omega_{\text{beat}}. \quad (25)$$

Apart from the beat the dipole moment of the system oscillates only at frequencies close to the laser frequency that was used for the excitation. Hence the beat frequency can be determined easily from the D and A dipole moments (see Fig. 3). The essential observation now is that for doing so, the dipole moment time evolution only has to be recorded long enough to capture one half cycle of the beat. This is a much shorter time than the time needed to obtain an accurate spectrum from the Fourier transformation. Thus, the coupling strength can be determined with moderate simulation times.

We used this approach to determine the coupling of the lowest excitation of the two sodium dimers. Figure 7 shows the thus obtained distance dependence of the coupling matrix element. One observes significant differences from the dipole

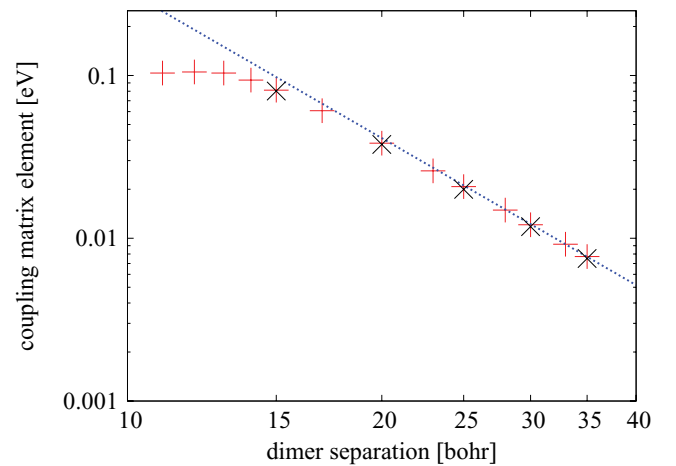


FIG. 7. (Color online) Coupling matrix element between the excited states at 2.1 eV of two  $Na_2$  versus the dimer separation. Red crosses show the results from our real-time and real-space implementation. As a guide to the eye we plotted a dotted line with slope  $-3$  which corresponds to a Förster-type coupling. As a confirmation of our implementation we also report results that we obtained using linear response TDDFT from a commercial program package [83–85] (black crosses).

coupling behavior for distances below 20 bohr. Above 25 bohr the coupling falls with the expected  $1/R^{-3}$  dependence.

As a test of our real-time and real-space implementation we followed Ref. [39] and computed linear response TDDFT spectra for a couple of dimer distances with the TURBOMOLE package [83–85] using the local density approximation and Fully Optimized Contracted Gaussian Basis Sets of Triple Zeta Valence Quality (def2-TZVP) [86]. The coupling matrix elements (see Fig. 7) are calculated according to Eq. (24) exploiting the Davydov splitting. The agreement between the two methods is very good and the observed small differences can be attributed to technical differences such as the use of pseudopotentials and basis sets versus real space.

For putting our findings into perspective one should compare the distance of 25 bohr to the bond length of the sodium dimer, which is 5.78 bohr. The ratio of the extension of the molecular systems to their separation indicates that one has to be careful in relying on the dipole coupling approximation for extended systems that are not very far apart.

## VI. CONCLUSION

We have presented a qualitative and a quantitative scheme for investigating the coupling behavior of two molecules within the real-time approach to TDDFT. The approach allows one to distinguish between a Förster-type dipole coupling and a non-dipole coupling on very general grounds. If the coupled excitations that are of interest can be considered as a two-level system (i.e., large energetic separation from other excitations), then the coupling matrix element can be determined efficiently in the real-time scheme by evaluating the Davydov splitting from a beat frequency.

Already the small molecules investigated in this manuscript show notable deviations from the Förster-type dipole coupling at moderate distances. For larger molecules such as typically used for spectroscopic labeling or in molecular electronics, the question at which distances FRET can be relied on is thus of great significance. Theoretical tools such as the one discussed here can play an important role, as they enable us to check whether the FRET dipole coupling approximation can be applied or not.

## ACKNOWLEDGMENTS

Financial support by the DFG and the Elitestudienprogramm “Macromolecular Science” is gratefully acknowledged.

## APPENDIX A: EXCITATION WITH A LASER PULSE

Here we briefly explain how we excite the system by a laser pulse in the real-time investigation of the dipole coupling

approximation in Sec. IV. The laser acts as a time-dependent external potential in dipole approximation

$$E_L(t) = E_{\text{env}}(t) \sin(\omega_L t), \quad (\text{A1})$$

where  $E_{\text{env}}(t)$  is the pulse envelope. The frequency  $\omega_L$  of the pulse was chosen to equal the excitation energy we were interested in. We used the envelope  $E_{\text{env}}(t) = E_{\text{max}} \sin^2(\frac{\pi t}{T_L})$  as this form leads to a Fourier spectrum in which the side maxima are much lower than the main peak (typically the height of the first side maximum is less than 3% of the height of the main peak). The length  $T_L$  of the pulse is tuned by comparing the Fourier spectrum of the pulse with the excitation spectrum of the molecule:  $T_L$  was chosen such that the first side maximum of the pulse's spectrum lay closer to the pulse's main frequency than the neighboring peak in the molecule's excitation spectrum. In all cases we investigated, the excitations of the single molecules were sufficiently separated from each other to dominantly excite just one excited state of the system. This could be verified from the time-dependent dipole signal.

## APPENDIX B: BEAT OSCILLATION IN THE TIME-DEPENDENT ACCEPTOR DIPOLE MOMENT

In this Appendix we briefly explain why  $\omega_{\text{beat}}$  can be extracted from the dipole moment. We start by noting that Eq. (24) is derived in a two-state model [35,36], where  $|\widetilde{D}^*A\rangle$  and  $|\widetilde{D}A^*\rangle$  are a pair of resonant states. The time evolution

$$|\Psi(t)\rangle = a_1(t)|\widetilde{D}^*A\rangle + a_2(t)|\widetilde{D}A^*\rangle, \quad (\text{B1})$$

of the two-state system with initial state  $|\Psi(0)\rangle = |\widetilde{D}^*A\rangle$  is given by the coefficients  $a_1(t)$  and  $a_2(t)$  [87]

$$\begin{aligned} |a_1(t)|^2 &= \cos^2(Vt), \\ |a_2(t)|^2 &= \sin^2(Vt). \end{aligned} \quad (\text{B2})$$

The coefficients oscillate with the beat frequency  $\omega_{\text{beat}}$ , see Eq. (25). The corresponding time-dependent dipole moment  $\mathbf{d}^A(t) = \langle \Psi(t) | \mathbf{r}^A | \Psi(t) \rangle$  on the A side can be calculated as

$$\mathbf{d}^A(t) = |a_1(t)|^2 \langle A | \mathbf{r}^A | A \rangle + |a_2(t)|^2 \langle A^* | \mathbf{r}^A | A^* \rangle, \quad (\text{B3})$$

where we exploited the orthogonality of  $|D\rangle$  and  $|D^*\rangle$ . If the static dipole moment  $\langle A | \mathbf{r}^A | A \rangle$  of A vanishes, (B3) simplifies to

$$\mathbf{d}^A(t) = |a_2(t)|^2 \langle A^* | \mathbf{r}^A | A^* \rangle. \quad (\text{B4})$$

Therefore, the resonance oscillation of the coefficients can be observed in the time evolution of the dipole moment  $\mathbf{d}^A(t)$ . Both Eqs. (B3) and (B4) can be used to determine the coupling matrix element  $V$  via the beat frequency (25).

- 
- [1] Y.-C. Cheng and G. R. Fleming, *Annu. Rev. Phys. Chem.* **60**, 241 (2009).  
 [2] S. Tretiak and S. Mukamel, *Chem. Rev.* **102**, 3171 (2002).  
 [3] B. Kippelen and J.-L. Brédas, *Energy Environ. Sci.* **2**, 251 (2009).

- [4] C. W. Tang, *Appl. Phys. Lett.* **48**, 183 (1986).  
 [5] J. I. Basham, G. K. Mor, and C. A. Grimes, *ACS Nano* **4**, 1253 (2010).  
 [6] R. H. Friend *et al.*, *Nature (London)* **397**, 121 (1999).  
 [7] G. D. Scholes, *Chem. Phys.* **275**, 373 (2002).

- [8] G. D. Scholes and G. R. Fleming, *J. Phys. Chem. B* **104**, 1854 (2000).
- [9] X. Hu, A. Damjanović, T. Ritz, and K. Schulten, *Proc. Natl. Acad. Sci. USA* **95**, 5935 (1998).
- [10] M. D. Newton, *Chem. Rev.* **91**, 767 (1991).
- [11] S. Speiser, *Chem. Rev.* **96**, 1953 (1996).
- [12] Th. Förster, *Naturwiss.* **33**, 166 (1946).
- [13] Th. Förster, *Ann. Phys. (NY)* **437**, 55 (1948).
- [14] Th. Förster, in *Modern Quantum Chemistry*, edited by O. Sinnanoglu (Academic Press, New York, 1965), Vol. 3, pp. 93–137.
- [15] G. D. Scholes, *Annu. Rev. Phys. Chem.* **54**, 57 (2003).
- [16] R. Métivier, F. Nolde, K. Müllen, and T. Basché, *Phys. Rev. Lett.* **98**, 047802 (2007).
- [17] Ch. Scharf *et al.*, *Chem. Phys.* **328**, 403 (2006).
- [18] P. Bauer, H. Wietasch, S. M. Lindner, and M. Thelakkat, *Chem. Mater.* **19**, 88 (2007).
- [19] T. Körzdörfer, S. Tretiak, and S. Kümmel, *J. Chem. Phys.* **131**, 034310 (2009).
- [20] F. Laquai, Y.-S. Park, J.-J. Kim, and T. Basché, *Macromol. Rapid Commun.* **30**, 1203 (2009).
- [21] D. Beljonne, C. Curutchet, G. D. Scholes, and R. J. Silbey, *J. Phys. Chem. B* **113**, 6583 (2009).
- [22] L. Stryer and R. P. Haugland, *Proc. Natl. Acad. Sci. USA* **58**, 719 (1967).
- [23] L. Stryer, *Annu. Rev. Biochem.* **47**, 819 (1978).
- [24] R. Ziessel, M. A. H. Alamiry, K. J. Elliott, and A. Harriman, *Angew. Chem. Int. Ed.* **48**, 2772 (2009).
- [25] S. E. Braslavsky *et al.*, *Photochem. Photobiol. Sci.* **7**, 1444 (2009).
- [26] K. F. Wong, B. Bagchi, and P. J. Rossky, *J. Phys. Chem. A* **108**, 5752 (2004).
- [27] H. Singh and B. Bagchi, *Curr. Sci.* **89**, 1710 (2005).
- [28] Y. R. Khan, T. E. Dykstra, and G. D. Scholes, *Chem. Phys. Lett.* **461**, 305 (2008).
- [29] E. Dolgih *et al.*, *J. Phys. Chem. A* **113**, 4639 (2009).
- [30] S. Saini, H. Singh, and B. Bagchi, *J. Chem. Sci.* **118**, 23 (2006).
- [31] S. Saini, S. Bhowmick, V. B. Shenoy, and B. Bagchi, *J. Photochem. Photobiol. A: Chem.* **190**, 335 (2007).
- [32] R. Baer and E. Rabani, *J. Chem. Phys.* **128**, 184710 (2008).
- [33] H. Tamura, J.-M. Mallet, M. Oheim, and I. Burghardt, *J. Phys. Chem. C* **113**, 7548 (2009).
- [34] C.-P. Hsu, G. R. Fleming, M. Head-Gordon, and T. Head-Gordon, *J. Chem. Phys.* **114**, 3065 (2000).
- [35] C.-P. Hsu, *J. Chin. Chem. Soc.* **50**, 745 (2003).
- [36] J. Neugebauer, *J. Chem. Phys.* **126**, 134116 (2007).
- [37] J. Neugebauer, *J. Phys. Chem. B* **112**, 2207 (2008).
- [38] B. Fückel *et al.*, *J. Chem. Phys.* **128**, 074505 (2008).
- [39] E. Sagvolden, F. Furche, and A. Köhn, *J. Chem. Theory Comput.* **5**, 873 (2009).
- [40] A. Muñoz-Losa, C. Curutchet, I. F. Galván, and B. Mennucci, *J. Chem. Phys.* **129**, 034104 (2008).
- [41] C. Curutchet *et al.*, *J. Chem. Theory Comput.* **5**, 1838 (2009).
- [42] M. E. Casida, in *Recent Advances in Density Functional Methods, Part I*, edited by D. P. Chong (World Scientific, Singapore, 1995), Vol. 1, Chap. 5, pp. 155–192.
- [43] E. K. U. Gross, J. F. Dobson, and M. Petersilka, in *Density Functional Theory*, edited by R. F. Nalewajski, *Top. Curr. Chem.* (Springer, Berlin, 1996), Vol. 181, p. 81.
- [44] C. A. Ullrich, S. Erhard, and E. K. U. Gross, in *Super Intense Laser Atom Physics IV*, Nato ASI series 3/13, edited by H. G. Muller and M. V. Fedorov (Kluwer, Dordrecht, 1996), p. 267.
- [45] K. Yabana and G. F. Bertsch, *Phys. Rev. B* **54**, 4484 (1996).
- [46] U. Saalmann and R. Schmidt, *Z. Phys. D: At. Mol. Clusters* **38**, 153 (1996).
- [47] X.-M. Tong and S.-I. Chu, *Phys. Rev. A* **55**, 3406 (1997).
- [48] K. Yabana and G. F. Bertsch, *Int. J. Quantum Chem.* **75**, 55 (1999).
- [49] F. Calvayrac, P.-G. Reinhard, E. Suraud, and C. A. Ullrich, *Phys. Rep.* **337**, 493 (2000).
- [50] M. A. L. Marques and E. K. U. Gross, *Annu. Rev. Phys. Chem.* **55**, 427 (2004).
- [51] M. Mundt and S. Kümmel, *Phys. Rev. B* **76**, 035413 (2007).
- [52] M. Mundt, *J. Theor. Comput. Chem.* **8**, 561 (2009).
- [53] J. R. Chelikowsky, L. Kronik, and I. Vasiliev, *J. Phys. Condens. Matter* **15**, R1517 (2003).
- [54] M. A. L. Marques, X. Lopez, D. Varsano, A. Castro, and A. Rubio, *Phys. Rev. Lett.* **90**, 258101 (2003).
- [55] M. A. L. Marques, A. Castro, G. F. Bertsch, and A. Rubio, *Comput. Phys. Commun.* **151**, 60 (2003).
- [56] M. A. L. Marques, A. Castro, and A. Rubio, *J. Chem. Phys.* **115**, 3006 (2001).
- [57] M. Mundt and S. Kümmel, *Phys. Rev. A* **74**, 022511 (2006).
- [58] H. O. Wijewardane and C. A. Ullrich, *Phys. Rev. Lett.* **100**, 056404 (2008).
- [59] D. L. Dexter, *J. Chem. Phys.* **21**, 836 (1953).
- [60] C.-P. Hsu, *Acc. Chem. Res.* **42**, 509 (2009).
- [61] Norm conserving pseudopotentials of Troullier-Martins [N. Troullier and J. L. Martins, *Phys. Rev. B* **43**, 1993 (1991)] type were used.
- [62] In test calculations the actual differences that we observed in the dynamics when using either  $v_H^{ddv}$  or  $v_H^{ddE}$  were rather small. This was a consequence of low density in the regions of space where the two approximations differ.
- [63] M. Mundt and S. Kümmel, *Phys. Rev. Lett.* **95**, 203004 (2005).
- [64] S. Kümmel and L. Kronik, *Rev. Mod. Phys.* **80**, 3 (2008).
- [65] T. Stein, L. Kronik, and R. Baer, *J. Am. Chem. Soc.* **131**, 2818 (2009).
- [66] T. Körzdörfer, M. Mundt, and S. Kümmel, *Phys. Rev. Lett.* **100**, 133004 (2008).
- [67] Charge-transfer states may also play a role at large separation if they enter, e.g., as pathways that are not optically excited. In our study here we focus on optical excitation.
- [68] As local approximations always underestimate the charge-transfer excitation energy, one will see the charge transfer earlier when using local functionals than it occurs in nature (i.e., one will be warned when monitoring the charge in the real-time approach).
- [69] L. Kronik *et al.*, *Phys. Status Solidi B* **243**, 1063 (2006).
- [70] D. Beljonne *et al.*, *J. Chem. Phys.* **112**, 4749 (2000).
- [71] I. Vasiliev, S. Ögüt, and J. R. Chelikowsky, *Phys. Rev. Lett.* **82**, 1919 (1999).
- [72] S. Kümmel, K. Andrae, and P.-G. Reinhard, *Appl. Phys. B* **73**, 293 (2001).
- [73] The change in the excitation energies when going from TDLDA to a functional including a percentage of exact exchange [time-dependent Becke three-parameter Lee-Yang-Parr hybrid

- functional (TDB3LYP)] are of the order of 0.2 eV for the excitations of C<sub>7</sub>H<sub>6</sub>O that carry appreciable oscillator strength. As charge-transfer excitations would be more sensitive to the fraction of the Fock exchange this is another confirmation for the fact that we are not looking at charge-transfer excitations.
- [74] We checked up to a separation of 40 bohr that the differences in the dipole moment decrease continuously.
- [75] A. S. Davydov, *Quantenmechanik* (Dt. Verl. der Wiss., Berlin, 1967), p. 519.
- [76] A. S. Davydov, *Phys. Status Solidi* **30**, 357 (1968).
- [77] M. Kasha, H. R. Rawls, and M. Ashraf El-Bayoumi, *Pure Appl. Chem.* **11**, 371 (1965).
- [78] M. Petersilka, U. J. Gossmann, and E. K. U. Gross, *Phys. Rev. Lett.* **76**, 1212 (1996).
- [79] H. Appel, E. K. U. Gross, and K. Burke, *Phys. Rev. Lett.* **90**, 043005 (2003).
- [80] P. Elliott, K. Burke, and F. Furche, [arXiv:cond-mat/0703590](https://arxiv.org/abs/cond-mat/0703590).
- [81] F. Calvayrac, P. G. Reinhard, and E. Suraud, *Ann. Phys.* **255**, 125 (1997).
- [82] A. Castro, M. A. L. Marques, and A. Rubio, *J. Chem. Phys.* **121**, 3425 (2004).
- [83] TURBOMOLE V6.0 2009, a development of the University of Karlsruhe and Forschungszentrum Karlsruhe GmbH, 1989–2007, TURBOMOLE GmbH, since 2007; available from [<http://www.turbomole.com>].
- [84] R. Ahlrichs, M. Baer, M. Haeser, H. Horn, and C. Koelmel, *Chem. Phys. Lett.* **162**, 165 (1989).
- [85] F. Furche and D. Rappoport, in *Computational Photochemistry*, Theoretical and Computational Chemistry, edited by M. Olivucci (Elsevier, Amsterdam, 2005), Vol. 16, Chap. III.
- [86] A. Schäfer, C. Huber, and R. Ahlrichs, *J. Chem. Phys.* **100**, 5829 (1994).
- [87] C. Cohen-Tannoudji, B. Diu, and F. Laloë, *Quantenmechanik Band 1* (Walter de Gruyter, Berlin, 2009) p. 374.



## Publication 2

# Kohn-Sham Self-Interaction Correction in Real Time

D. Hofmann, T. Körzdörfer, and S. Kümmel

*Theoretical Physics IV, University of Bayreuth, D-95440 Bayreuth, Germany*

Physical Review Letters **108**, 146401 (2012)

©2012 The American Physical Society

DOI: 10.1103/PhysRevLett.108.146401

available at: <http://link.aps.org/doi/10.1103/PhysRevLett.108.146401>

### ABSTRACT

We present a solution scheme for the time-dependent Kohn-Sham self-interaction correction. Based on the generalized optimized effective potential approach, the multiplicative Kohn-Sham potential is constructed in real time and real space for the self-interaction corrected local density approximation. Excitations of different character, including charge-transfer excitations that had been regarded as prime examples for the failure of standard time-dependent density functionals, are described correctly by this approach. We analyze the time-dependent exchange-correlation potential and density, revealing features that are decisive for the correct description of the response.



## Kohn-Sham Self-Interaction Correction in Real Time

D. Hofmann, T. Körzdörfer, and S. Kümmel

*Theoretical Physics IV, University of Bayreuth, D-95440 Bayreuth, Germany*

(Received 9 November 2011; published 2 April 2012)

We present a solution scheme for the time-dependent Kohn-Sham self-interaction correction. Based on the generalized optimized effective potential approach, the multiplicative Kohn-Sham potential is constructed in real time and real space for the self-interaction corrected local density approximation. Excitations of different character, including charge-transfer excitations that had been regarded as prime examples for the failure of standard time-dependent density functionals, are described correctly by this approach. We analyze the time-dependent exchange-correlation potential and density, revealing features that are decisive for the correct description of the response.

DOI: 10.1103/PhysRevLett.108.146401

PACS numbers: 71.15.Mb, 31.15.ee, 31.70.Hq

In the rapidly evolving fields of nano science and molecular electronics, progress has been fueled by the interplay between experiment and first principles calculations. Time-dependent density functional theory (TDDFT) has emerged as one of the most powerful and most frequently used theories for calculating electronic excitations. TDDFT's success rests on its excellent ratio between accuracy and computational cost, allowing us to predict and understand electron dynamics in systems of experimentally relevant complexity [1,2]. However, the many great successes of TDDFT based on commonly used exchange-correlation (xc) approximations such as the time-dependent adiabatic local density approximation (TD-LDA) or global hybrid functionals are overshadowed by serious and systematic failures. Excitations that involve orbitals that experience the long-range behavior of the Kohn-Sham (KS) potential, excitonic excitations, and excitations of charge-transfer (CT) character are in error even qualitatively when calculated with commonly used xc functionals. In particular, the failure to describe CT excitations is a very serious limitation, as it precludes TDDFT's use in many of the most exciting areas of nano science such as light harvesting [3] and transport [2].

The source of these failures is well understood, as the time-dependent xc potential of functionals such as the TD-LDA is qualitatively wrong in several ways. It has no memory—i.e.,  $v_{xc}(\mathbf{r}, t)$  does not depend on the density  $n(\mathbf{r}, t')$  for  $t' \leq t$  [4,5]—it does not show the proper  $1/r$  asymptotic decay, and it lacks the steplike structures that reflect particle number discontinuities [6,7]. The close relation between the latter and the proper description of charge transfer has repeatedly been stressed [2,8–10] and points to the ultimate origin of the problem: The absence or existence of a physically meaningful particle number discontinuity is closely tied to electronic self-interaction or its absence, respectively [11].

Based on this insight, it appears very natural to generalize the idea of a self-interaction correction (SIC) from ground-state DFT [12], where it typically is

written in the form  $E_{xc}^{SIC}[n_{\uparrow}, n_{\downarrow}] = E_{xc}^{LDA}[n_{\uparrow}, n_{\downarrow}] - \sum_{\sigma=\uparrow,\downarrow} \sum_{i=1}^{N_{\sigma}} (E_H[n_{i\sigma}] + E_{xc}[n_{i\sigma}, 0])$ , to the TD case. Here,  $E_H$  and  $E_{xc}$  are Hartree and xc energy, respectively, and  $N_{\sigma}$  occupied orbitals  $\{\varphi_{i\sigma}\}$  define  $n_{i\sigma} = |\varphi_{i\sigma}|^2$  and  $n_{\sigma} = \sum_{i=1}^{N_{\sigma}} n_{i\sigma}$ . TD-SIC schemes have been developed successfully in the past [13–16] and are straightforward, in principle: The orbital-specific potentials  $u_{xcj\sigma}(\mathbf{r}, t) = v_{j\sigma}^{SIC}(\mathbf{r}, t) / \varphi_{j\sigma}^*(\mathbf{r}, t)$ , where

$$v_{j\sigma}^{SIC}(\mathbf{r}, t) = \frac{\delta E_{xc}^{SIC}[\{\varphi_{k\tau}\}]}{\delta \varphi_{j\sigma}(\mathbf{r}, t)}, \quad (1)$$

are evaluated with the time-dependent orbitals obtained from propagation and then are used either as separate, orbital-specific potentials [16] or as ingredients to construct the TD Krieger-Li-Iafate (KLI) approximation to the optimized effective potential (OEP) [13–15]. TD-SIC has many attractive features: It is parameter-free, nonempirical, and driven by the clear physical concept of relating orbitals and electrons [17], which is approximate but in practice very powerful [18,19].

However, SIC also has quite problematic aspects. As integrating the full TD-OEP equation is possible but very demanding already in one spatial dimension [20], and as a generally applicable, three-dimensional TD-OEP scheme is missing [21], KS TD-SIC calculations so far relied on the KLI or even Slater approximations. However, there are systems for which these approaches violate the zero-force theorem seriously enough to prevent a stable propagation [22]. Worse yet, comparison of OEP and KLI calculations for SIC revealed that already the KLI ground-state electronic structure can be seriously in error [23]. These problems may be less relevant for atoms and small molecules in very strong external fields, i.e., the situations that were mostly studied with TD-SIC so far. However, they preclude the use of KLI TD-SIC for more general cases and, in particular, for the CT problem. The problems can be sidestepped by using TD-SIC in a non-KS way with

orbital-specific potentials, yet such approaches have their own set of challenges [16].

In this work, we focus on the KS realization of TD-SIC. By explicitly taking into account the unitary variance of the SIC expression via the generalized OEP (GOEP) formalism [17], we arrive at an accurate KS TD-SIC scheme. We demonstrate that excitations of different character—from the collective response of small metal particles, to excitations that have been described as excitonic, up to challenging CT excitations—are described reliably by KS TD-SIC. Working with the KS potential not only allows us to exploit technical advantages and thus apply TD-SIC to systems of a complexity that was out of the range of previous TD-SIC schemes, it also enables us to transparently analyze the time-dependent response: The TD xc potential in CT systems develops a pronounced field-counteracting behavior and exhibits a complicated response at high frequencies. By analysis of transition densities, we show that KS TD-SIC puts the response peaks at the appropriate energies and represents the correct excitation structure.

The fact that SIC is not unitarily invariant [12] has been regarded as a weakness of SIC. Yet this weakness can be turned into a strength. We first explain the idea in words and then detail the approach with equations.

The well known problems with propagations using the usual KLI approximation [16,22] are ultimately a consequence of the KLI potential not being a functional derivative; i.e., the KLI solution is not variationally stable. However, for unitarily variant functionals such as SIC, an additional degree of freedom can be exploited to increase the stability of the propagation. As different sets of orbitals can yield the same density but different SIC energies, there is more than one way to construct a rigorous KS SIC potential. As has previously been explained for the ground-state case [17], the most general KS approach for unitarily variant functionals includes a unitary transformation among the occupied orbitals into the chain rule derivation of the OEP. This leads to the GOEP equation. By taking the usual steps [24,25], the GOEP can straightforwardly be extended to TD situations. Thus also the generalized KLI (GKLI) approximation is readily extended to TD-GKLI. The crucial advantage here is that, for the SIC, GKLI is a much better approximation to the GOEP than the usual KLI is to the usual OEP. This is a consequence of the additional minimizing step via the unitary transformation. The quality of the GKLI potential has been confirmed for the ground state [17,18], and the advantages of the generalized approach directly carry over to the TD case. Thus, although the GKLI is still an approximation, it is so close to the GOEP that for our practical purposes it is not a limitation. However, obtaining a sufficiently stable numerical propagation depends on performing all steps in the propagation and, in particular, the unitary rotation very accurately, as described in the following.

The usual TD-KLI potential [21,24] is defined by

$$u_{xc\sigma}^{\text{TD-SIC}}(\mathbf{r}, t) = \frac{1}{2n_{\sigma}(\mathbf{r}, t)} \left\{ \sum_{j=1}^{N_{\sigma}} n_{j\sigma}(\mathbf{r}, t) \{ u_{xcj\sigma}(\mathbf{r}, t) + [\bar{v}_{xcj\sigma}^{\text{TD-SIC}}(t) - \bar{u}_{xcj\sigma}(t)] \} \right\} + \text{c.c.}, \quad (2)$$

where a bar denotes an orbital average, e.g.,  $\bar{v}_{xcj\sigma}^{\text{TD-SIC}}(t) = \int \varphi_{j\sigma}^*(\mathbf{r}, t) v_{xc\sigma}^{\text{TD-SIC}}(\mathbf{r}, t) \varphi_{j\sigma}(\mathbf{r}, t) d^3r$ . Equation (2) goes over into the TD-GKLI by replacing all orbital-specific potentials  $u_{xcj\sigma}$  by the generalized orbital-specific potentials

$$u_{xcj\sigma}^{\text{G}}(\mathbf{r}, t) = \frac{1}{\varphi_{j\sigma}^*(\mathbf{r}, t)} \sum_i^{N_{\sigma}} U_{ij}^{\sigma}(t) \tilde{v}_{i\sigma}^{\text{SIC}}(\mathbf{r}, t). \quad (3)$$

Here,  $\tilde{v}_{i\sigma}^{\text{SIC}}$  is defined in analogy to Eq. (1) but evaluated for the set of orbitals  $\{\tilde{\varphi}_{i\sigma}\}$  that is obtained from the occupied KS orbitals  $\{\varphi_{j\sigma}\}$  by

$$\tilde{\varphi}_{i\sigma}(\mathbf{r}, t) = \sum_{j=1}^{N_{\sigma}} U_{ij}^{\sigma}(t) \varphi_{j\sigma}(\mathbf{r}, t), \quad (4)$$

where the unitary transformation  $U_{ij}^{\sigma}(t)$  is determined at each time step to minimize the instantaneous SIC energy. This criterion is fulfilled when the equations

$$\langle \tilde{\varphi}_{i\sigma}(\mathbf{r}, t) | \frac{\tilde{v}_{i\sigma}^{\text{SIC}}(\mathbf{r}, t)}{\tilde{\varphi}_{i\sigma}^*(\mathbf{r}, t)} - \frac{\tilde{v}_{j\sigma}^{\text{SIC}}(\mathbf{r}, t)}{\tilde{\varphi}_{j\sigma}^*(\mathbf{r}, t)} | \tilde{\varphi}_{j\sigma}(\mathbf{r}, t) \rangle = 0 \quad \forall t \quad (5)$$

are satisfied [26] for all occupied orbitals. For a given set of  $\{\varphi_{j\sigma}\}$ ,  $U_{ij}^{\sigma}$  can be found iteratively [27]. Such a TD-SIC calculation thus proceeds by propagating the KS orbitals a finite step  $\Delta t$  (starting from the ground state), then determining the unitary transformation according to Eq. (5), and finally calculating the new xc potential from Eq. (2) with  $u_{xcj\sigma}$  replaced by  $u_{xcj\sigma}^{\text{G}}$  from Eq. (3). For clear spectral signals in the linear response that is of interest here, this sequence has to be repeated until ca. 40 fs of propagation time are completed after an initial boost.

The approach thus appears like a straightforward extension of the ground-state concept to the time domain. However, a huge challenge is hidden in the above description. Stability of the propagation hinges crucially on the accuracy with which the transformation of Eq. (4) can be calculated, because the latter contributes decisively to keeping the propagation in the variationally stable regime. Calculating  $U_{ij}^{\sigma}$  is already expensive for ground-state situations [26,27]. Yet, the general KS TD-SIC that we aim at should be applicable to systems with tens of orbitals for many ten thousands of time steps, at each of which Eqs. (4) and (5) must be solved. The situation is further complicated by the finding that  $U_{ij}^{\sigma}(t + \Delta t)$  is not well approximated by  $U_{ij}^{\sigma}(t)$ . Therefore, using the known ground-state algorithms [26,27] for solving Eqs. (4) and (5) with the

accuracy that is needed for the TD case would basically render KS TD-SIC useless for larger and complex systems. This problem can be overcome by realizing that the numerical effort for iteratively finding the unitary transformation at time  $t$  can be significantly reduced by using the ground-state KS eigenvalues  $\epsilon_j$  to generate an initial guess

$$U_{ij}^\sigma(t) = e^{i\epsilon_j \Delta t} U_{ij}^\sigma(t - \Delta t). \quad (6)$$

Here, we take into account the transformation from the previous time step *and* the phase factors that the KS orbitals would acquire if the Hamiltonian were time-independent. By using this algorithm, KS TD-SIC becomes applicable to systems of a size and complexity that has not been reached with previous TD-SIC schemes.

As a first test, we checked the stability of the propagation for the Na<sub>5</sub> cluster, which is established as a difficult system for obtaining a stable propagation [22,27], e.g., showing serious instabilities for the  $x$ -only KLI potential and yet worse instabilities for regular KLI TD-SIC. We find the two lowest pronounced excitation peaks at 2.0 and 2.2 eV. For this as well as for all other systems discussed below, the desired spectral resolution is achieved without being compromised by propagation instabilities.

Turning to systems that are physically more interesting, we next investigate small hydrogenated Si clusters. These are known for being only poorly described by the TD-LDA, and it has been argued that an accurate description of excitonic effects as, e.g., obtained from the Bethe-Salpeter equation (GW-BSE), is needed. For SiH<sub>4</sub> and Si<sub>2</sub>H<sub>6</sub> several GW-BSE reference calculations are available [28–30]. The left part of Fig. 1 shows the square root of our dipole power spectrum [31], i.e., peaks reflect excitation energies for TD-LDA and KS TD-SIC. Black lines visualize the position of the GW-BSE excitation

energies [28–30,32]. Whereas the TD-LDA spectrum does not resemble the GW-BSE results at all, the KS TD-SIC excitation energies do and are well within the uncertainty limits that the GW-BSE calculations themselves have [32]. Also for Si<sub>2</sub>H<sub>6</sub> the KS TD-SIC excitations at 7.8 and 9.1 eV compare favorably to the GW-BSE excitations at 7.6 and 9.0 eV [28].

Finally, we turn our attention to the most interesting test cases: the CT systems. It has been shown that range-separated hybrids implemented in the non-KS way can describe CT excitations [33–36] but at the cost of introducing fit parameters that can lead to failures in nonstandard situations [36] or tuned parameters that render the functionals non-size-consistent [35,36]. An improvement of long-range CT excitations can typically also be achieved by a hybrid mixing with large amounts of exact exchange yet at the cost of reducing accuracy for more local excitations. KS TD-SIC is size-consistent and parameter-free. These are strong advantages from a fundamental perspective. However, in the light of the above, two issues that are important for practical purposes must be checked: Does KS TD-SIC describe long-range CT accurately, and does it not spoil accuracy for more short-ranged excitations?

We first address the latter question by studying a paradigm case. In the 4-(*N,N*-dimethylamino)benzonitrile molecule [37], a local excitation that is seen experimentally at 4.25 eV and an excitation that has been classified as being of short-range CT character [38] at 4.56 eV are described with moderate but acceptable accuracy by standard functionals. The time-dependent Perdew-Burke-Ernzerhof generalized gradient approximation, e.g., yields excitations at 4.02 and 4.30 eV [37], respectively. Here, KS TD-SIC, if it works properly, should not ruin the accuracy achieved at the local xc level. The right part of Fig. 1 shows in the upper half the excitation spectrum obtained in TD-LDA and KS TD-SIC. Both spectra show two peaks in the relevant range: a rather small one reflecting the local excitation and a higher one reflecting the CT. KS TD-SIC shifts the 3.9 and 4.2 eV TD-LDA peaks to 4.1 and 4.4 eV, respectively. Thus, the KS TD-SIC not only does not spoil the local xc accuracy but improves agreement with experiment further.

One may wonder whether KS TD-SIC really describes the correct physics beyond just yielding reasonably looking energies. It is known that the character of the CT excitation in 4-(*N,N*-dimethylamino)benzonitrile is correctly described by local xc functionals, and it is desirable to check whether KS TD-SIC preserves this feature. At first sight, one may think that this is impossible in the real-time approach, because the propagation does not yield an excitation's decomposition into orbital transitions as in explicit linear response [4]. However, we can analyze the transition density

$$\rho_\omega(\mathbf{r}) \propto -\text{Im}\{\delta n(\mathbf{r}, \omega)\} \quad (7)$$

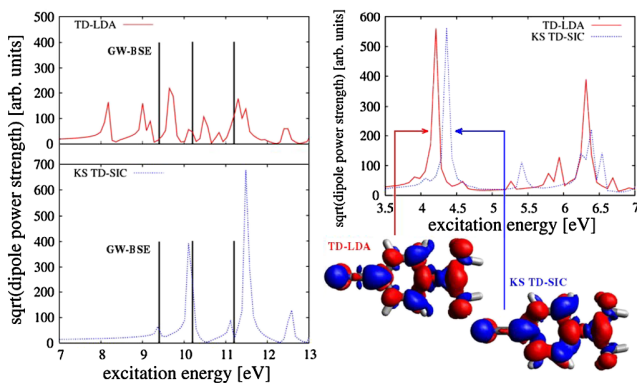


FIG. 1 (color online). Left: Peaks denote excitation energies in TD-LDA (top) and KS TD-SIC (bottom) for SiH<sub>4</sub>; black vertical lines indicate GW-BSE excitation energies. Right: Comparison of TD-LDA and KS TD-SIC spectra for the 4-(*N,N*-dimethylamino)benzonitrile molecule; transition densities (bottom) confirm that the character of the CT excitation is similar for both.

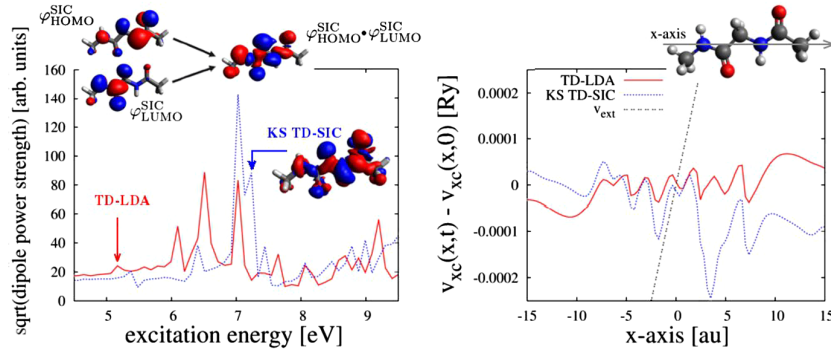


FIG. 2 (color online). Left: TD-LDA and KS TD-SIC spectrum of the dipeptide and KS TD-SIC CT transition density. Small inset: The orbital product  $\varphi_{\text{HOMO}}^{\text{SIC}}(\mathbf{r})\varphi_{\text{LUMO}}^{\text{SIC}}(\mathbf{r})$  approximates the transition density well and shows the CT character. Right: Snapshots of external, TD-LDA xc, and TD-SIC xc potential.

by taking the Fourier transform  $\delta n(\mathbf{r}, \omega)$  of the time-dependent density fluctuations  $\delta n(\mathbf{r}, t) = n(\mathbf{r}, t) - n(\mathbf{r}, 0)$  [39]. The transition densities evaluated at the respective CT frequencies are shown in Fig. 1. KS TD-SIC clearly preserves the character correctly.

Having seen the accuracy for short-range CT excitations, we proceed to investigating long-range CT, again using a paradigm test case. The dipeptide molecule has become a benchmark for the description of CT and a hallmark example for the severe failure of usual TDDFT [37,40,41]. It is known [41] that the dipeptide in addition to lower local excitations shows a clear CT excitation from one peptide to the other at 7.18 eV (complete active space perturbation theory of second order reference). This excitation is badly underestimated by ca. 2 eV by (semi)local xc functionals [41].

Identifying this CT excitation in the spectra from real-time calculations (left part of Fig. 2) is possible with the help of the transition density. In an orbital picture the CT excitation would correspond to a highest occupied molecular orbital—lowest unoccupied molecular orbital transition (if the SIC orbital ordering is used). The upper inset in the left part of Fig. 2 shows these orbitals and their product. The latter would correspond to the transition density for an idealized transition between static orbitals. We compare it to the true  $\rho_{\omega}(\mathbf{r})$  that we calculated from the TD density [Eq. (7)] for all peaks in the spectrum up to 8 eV. There is unambiguously one  $\rho_{\omega}(\mathbf{r})$  that corresponds to the highest occupied molecular orbital—lowest unoccupied molecular orbital CT picture: In KS TD-SIC it appears at 7.2 eV (blue arrow in Fig. 2) and in TD-LDA at 5.2 eV (red arrow). Thus, we have identified the CT excitation and see that KS TD-SIC yields a very realistic CT energy.

Taking advantage of working with a local potential, we can analyze  $v_{\text{xc}}(\mathbf{r}, t)$  to reveal the reason for this success. The right half of Fig. 2 shows snapshots of the external potential  $v_{\text{ext}}(\mathbf{r}, t)$ ,  $v_{\text{xc}}^{\text{TD-LDA}}(\mathbf{r}, t)$ , and  $v_{\text{xc}}^{\text{TD-SIC}}(\mathbf{r}, t)$  of the dipeptide at  $t = 5.2$  fs during a sinusoidal dipole excitation with 0.2 eV. There is a striking difference: TD-LDA

works with the external field, and KS TD-SIC works against it. The TD field-counteracting behavior of  $v_{\text{xc}}^{\text{TD-SIC}}$  explains why KS TD-SIC correctly shifts the CT excitations to higher energies, while CT is too easy in TD-LDA. For stronger excitations (not shown in the plot for clarity), TD-LDA still shows its simple behavior, and  $v_{\text{xc}}^{\text{TD-SIC}}$  develops additional structures that depend on excitation details and may reflect nonadiabatic effects.

It has also been shown that SIC can benefit from spin-symmetry breaking which may effectively model long-range correlation [42,43]. In cases of broken spin symmetry, the role or need of step structures in  $v_{\text{xc}}$  is unclear. However, in the cases studied here, spin symmetry is not broken and the step structures in  $v_{\text{xc}}$  are decisive. Revealing in detail how such features and the fractional particle number concept are linked to the unitary transformation of the GOEP, possibly identifying nonadiabatic effects by comparison with the adiabatically exact approximation [44], and possibly identifying semilocal mechanisms for modeling step structures [45] are worthwhile tasks for future work.

In summary, TD Kohn-Sham SIC based on the GOEP reliably describes excitations of very different character, from typical local excitations, over excitations that have been described as excitonic, up to challenging charge-transfer excitations. Analysis of the TD xc potential showed that TD-SIC leads to qualitatively new features such as a TD field-counteracting term that is absent in local functionals. KS TD-SIC thus appears as a promising, parameter-free approach for calculating excitations from first principles.

Financial support by DFG, GRK 1640 (S. K.), the GIF (S. K.), and AvH (T. K.) is gratefully acknowledged.

- 
- [1] M. A. L. Marques, X. López, D. Varsano, A. Castro, and A. Rubio, *Phys. Rev. Lett.* **90**, 258101 (2003).  
 [2] C. Toher, A. Filippetti, S. Sanvito, and K. Burke, *Phys. Rev. Lett.* **95**, 146402 (2005).

- [3] A. Dreuw and M. Head-Gordon, *J. Am. Chem. Soc.* **126**, 4007 (2004).
- [4] E. K. U. Gross, J. F. Dobson, and M. Petersilka, in *Density Functional Theory*, edited by R. F. Nalewajski, Topics in Current Chemistry Vol. 181 (Springer, Berlin, 1996), p. 81.
- [5] N. T. Maitra, K. Burke, and C. Woodward, *Phys. Rev. Lett.* **89**, 023002 (2002).
- [6] J. P. Perdew, R. G. Parr, M. Levy, and J. L. Balduz, Jr., *Phys. Rev. Lett.* **49**, 1691 (1982).
- [7] M. Mundt and S. Kümmel, *Phys. Rev. Lett.* **95**, 203004 (2005).
- [8] D. J. Tozer, *J. Chem. Phys.* **119**, 12 697 (2003).
- [9] N. T. Maitra, *J. Chem. Phys.* **122**, 234104 (2005).
- [10] M. Hellgren and E. K. U. Gross, *Phys. Rev. A* **85**, 022514 (2012).
- [11] J. P. Perdew, *Adv. Quantum Chem.* **21**, 113 (1990).
- [12] J. P. Perdew and A. Zunger, *Phys. Rev. B* **23**, 5048 (1981).
- [13] X.-M. Tong and S.-I. Chu, *Phys. Rev. A* **57**, 452 (1998); S.-I. Chu, *J. Chem. Phys.* **123**, 062207 (2005).
- [14] C. A. Ullrich, P.-G. Reinhard, and E. Suraud, *J. Phys. B* **31**, 1871 (1998).
- [15] M. A. L. Marques, A. Castro, and A. Rubio, *J. Chem. Phys.* **115**, 3006 (2001).
- [16] J. Messud, P. M. Dinh, P.-G. Reinhard, and E. Suraud, *Phys. Rev. Lett.* **101**, 096404 (2008).
- [17] T. Körzdörfer, S. Kümmel, and M. Mundt, *J. Chem. Phys.* **129**, 014110 (2008).
- [18] T. Körzdörfer, S. Kümmel, N. Marom, and L. Kronik, *Phys. Rev. B* **79**, 201205(R) (2009); **82**, 129903(E) (2010).
- [19] M. Dauth, T. Körzdörfer, S. Kümmel, J. Ziroff, M. Wiessner, A. Schöll, F. Reinert, M. Arita, and K. Shimada, *Phys. Rev. Lett.* **107**, 193002 (2011).
- [20] H. O. Wijewardane and C. A. Ullrich, *Phys. Rev. Lett.* **100**, 056404 (2008).
- [21] M. Mundt and S. Kümmel, *Phys. Rev. A* **74**, 022511 (2006).
- [22] M. Mundt, S. Kümmel, R. van Leeuwen, and P.-G. Reinhard, *Phys. Rev. A* **75**, 050501(R) (2007).
- [23] T. Körzdörfer, M. Mundt, and S. Kümmel, *Phys. Rev. Lett.* **100**, 133004 (2008).
- [24] C. A. Ullrich, U. J. Gossmann, and E. K. U. Gross, *Phys. Rev. Lett.* **74**, 872 (1995).
- [25] R. van Leeuwen, *Phys. Rev. Lett.* **80**, 1280 (1998).
- [26] M. R. Pederson, R. A. Heaton, and C. C. Lin, *J. Chem. Phys.* **80**, 1972 (1984); **82**, 2688 (1985).
- [27] J. Messud, P. M. Dinh, P.-G. Reinhard, and E. Suraud, *Ann. Phys. (N.Y.)* **324**, 955 (2009).
- [28] M. Rohlfing and S. G. Louie, *Phys. Rev. Lett.* **80**, 3320 (1998).
- [29] M. Rohlfing and S. G. Louie, *Phys. Rev. B* **62**, 4927 (2000).
- [30] M. L. Tiago and J. R. Chelikowsky, *Phys. Rev. B* **73**, 205334 (2006).
- [31] M. Mundt and S. Kümmel, *Phys. Rev. B* **76**, 035413 (2007).
- [32] First GW-BSE SiH<sub>4</sub> excitations range between 9.0 [28], 9.16 [29], and 9.4 eV [30]. We regard the real-space approach of Ref. [30] as closest to our implementation.
- [33] T. Yanai, D. P. Tew, and N. C. Handy, *Chem. Phys. Lett.* **393**, 51 (2004).
- [34] J.-D. Chai and M. Head-Gordon, *J. Chem. Phys.* **128**, 084106 (2008).
- [35] T. Stein, L. Kronik, and R. Baer, *J. Am. Chem. Soc.* **131**, 2818 (2009).
- [36] A. Karolewski, T. Stein, R. Baer, and S. Kümmel, *J. Chem. Phys.* **134**, 151101 (2011).
- [37] M. J. G. Peach, P. Benfield, T. Helgaker, and D. J. Tozer, *J. Chem. Phys.* **128**, 044118 (2008).
- [38] C. Jamorski, J. B. Foresman, C. Thilgen, and H.-P. Lüthi, *J. Chem. Phys.* **116**, 8761 (2002).
- [39] R. A. Broglia, G. Coló, G. Onida, and H. E. Roman, *Solid State Physics of Finite Systems* (Springer, Berlin, 2004); M. Thiele and S. Kümmel, *Phys. Chem. Chem. Phys.* **11**, 4631 (2009).
- [40] L. Serrano-Andrés and M. P. Fülscher, *J. Am. Chem. Soc.* **120**, 10 912 (1998); D. J. Tozer, R. D. Amos, N. C. Handy, B. O. Roos, and L. Serrano-Andrés, *Mol. Phys.* **97**, 859 (1999).
- [41] D. Rocca, D. Lu, and G. Galli, *J. Chem. Phys.* **133**, 164109 (2010).
- [42] J. I. Fuks, A. Rubio, and N. T. Maitra, *Phys. Rev. A* **83**, 042501 (2011).
- [43] I. Dreissigacker and M. Lein, *Chem. Phys.* **391**, 143 (2011).
- [44] M. Thiele, E. K. U. Gross, and S. Kümmel, *Phys. Rev. Lett.* **100**, 153004 (2008).
- [45] R. Armiento, S. Kümmel, and T. Körzdörfer, *Phys. Rev. B* **77**, 165106 (2008); A. Karolewski, R. Armiento, and S. Kümmel, *J. Chem. Theory Comput.* **5**, 712 (2009).



## Publication 3

# Using complex degrees of freedom in the Kohn-Sham self-interaction correction

D. Hofmann<sup>1</sup>, S. Klüpfel<sup>2</sup>, P. Klüpfel<sup>2</sup>, and S. Kümmel<sup>1</sup>

<sup>1</sup>*Theoretical Physics IV, University of Bayreuth, D-95440 Bayreuth, Germany*

<sup>2</sup>*Science Institute, VR-III, University of Iceland, Reykjavik, Iceland*

Physical Review A **85**, 062514 (2012)

©2012 The American Physical Society

DOI: 10.1103/PhysRevA.85.062514

available at: <http://link.aps.org/doi/10.1103/PhysRevA.85.062514>

### ABSTRACT

The Perdew-Zunger self-interaction correction (SIC) to local and semilocal density functionals systematically underestimates molecular bond lengths, yet improves many other ground-state properties. An alternative definition of a SIC is reached by using the Perdew-Zunger energy with a global, multiplicative Kohn-Sham potential instead of the orbital-specific potentials of traditional SIC. Due to the unitary variance of the SIC energy, the most general construction of the SIC Kohn-Sham potential involves a unitary transformation of the Kohn-Sham orbitals. We systematically investigate the Kohn-Sham version of the SIC, in particular with respect to the bond-length question, and present a detailed analysis of the influence of different unitary transformations. Using a complex-valued energy-minimizing transformation appears to be the most favorable approach, and we explain this result by analyzing orbital densities. We discuss how to calculate the transformations efficiently.



## Using complex degrees of freedom in the Kohn-Sham self-interaction correction

D. Hofmann,<sup>1</sup> S. Klüpfel,<sup>2</sup> P. Klüpfel,<sup>2</sup> and S. Kümmel<sup>1</sup>

<sup>1</sup>Theoretical Physics IV, University of Bayreuth, D-95440 Bayreuth, Germany

<sup>2</sup>Science Institute, VR-III, University of Iceland, Reykjavik, Iceland

(Received 30 March 2012; published 25 June 2012)

The Perdew-Zunger self-interaction correction (SIC) to local and semilocal density functionals systematically underestimates molecular bond lengths, yet improves many other ground-state properties. An alternative definition of a SIC is reached by using the Perdew-Zunger energy with a global, multiplicative Kohn-Sham potential instead of the orbital-specific potentials of traditional SIC. Due to the unitary variance of the SIC energy, the most general construction of the SIC Kohn-Sham potential involves a unitary transformation of the Kohn-Sham orbitals. We systematically investigate the Kohn-Sham version of the SIC, in particular with respect to the bond-length question, and present a detailed analysis of the influence of different unitary transformations. Using a complex-valued energy-minimizing transformation appears to be the most favorable approach, and we explain this result by analyzing orbital densities. We discuss how to calculate the transformations efficiently.

DOI: [10.1103/PhysRevA.85.062514](https://doi.org/10.1103/PhysRevA.85.062514)

PACS number(s): 31.15.E-, 31.15.ae, 33.15.Fm, 71.15.Mb

### I. INTRODUCTION

Numerous applications of density functional theory (DFT) during the past decades document its power in predicting ground-state properties of atoms, molecules, and other large-scale many-particle systems at a reasonable computational cost. However, DFT using local or semilocal density functionals is also well known for some notorious failures [1–23]: wrong prediction of dissociation limits [6,7] and chemical reaction barriers [8,9], as well as missing Rydberg series and instability of anions [10,11]. Standard functionals tend to overestimate charge-transfer properties, as, for example, polarizabilities of molecular chains [12,13,24–27] and charge transport in molecular devices [14–16]. Moreover, local and semilocal DFT show deficiencies with regard to electron localization effects in transition metals and their oxides [17–20] and molecular semiconductors [21–23].

These shortcomings do not come as a surprise if one keeps in mind that the reliability of DFT in predicting ground-state properties strongly depends on the quality of the used exchange-correlation (xc) density functional. The previously mentioned drawbacks of commonly used xc functional approximations are frequently ascribed to the self-interaction error (SIE) of such density functionals. Getting a handle on the SIE is considered as one promising route to improve the performance of approximate functionals. Therefore, the desire to find a correction scheme to this error and assess its predictive power in many-particle systems is great.

Correction of the SIE, however, is not a unique concept, as many different approaches to self-interaction correction (SIC) have been proposed [1,28–39]. The first well-established correction scheme is the SIC introduced by Perdew and Zunger (PZ) [1]:

$$E_{xc}^{SIC}[n_{\uparrow}, n_{\downarrow}] = E_{xc}^{app}[n_{\uparrow}, n_{\downarrow}] - \sum_{\sigma=\uparrow, \downarrow} \sum_{j=1}^{N_{\sigma}} (E_H[n_{j\sigma}] + E_{xc}^{app}[n_{j\sigma}, 0]). \quad (1)$$

Here,  $E_H$  is the Hartree energy, orbital densities  $n_{j\sigma}(\mathbf{r})$  can be calculated from the  $N_{\sigma}$  occupied orbitals  $\varphi_{j\sigma}(\mathbf{r})$  according to  $n_{j\sigma}(\mathbf{r}) = |\varphi_{j\sigma}(\mathbf{r})|^2$ , and spin densities are defined as

$n_{\sigma} = \sum_{j=1}^{N_{\sigma}} n_{j\sigma}$ . The PZ correction can be applied to any arbitrary xc functional approximation  $E_{xc}^{app}[n_{\uparrow}, n_{\downarrow}]$ . In practice, the first PZ SIC calculations were performed by direct minimization of the energy functional with respect to the orbitals. This results in a set of single-particle Schrödinger equations with an orbital-specific potential.

Within the framework of the traditional PZ approach, a variety of comprehensive studies on ground-state properties are available [1,40–47]. It is a general finding that PZ SIC is capable of improving ground-state properties if it is built on top of the local spin-density approximation (LSDA). Vydrov *et al.* [45] showed the advantages of self-interaction corrected LSDA (LSDA-SIC) explicitly for total energies of atoms, atomization energies, barrier heights of chemical reactions, ionization potentials, and electron affinities. In contrast, PZ SIC of semilocal functionals such as generalized gradient approximations (GGAs) tends to be more unfavorable, since mean deviations from experiment for representative test sets have a tendency to be larger for the corrected functional than for its uncorrected version [44,45].

However, new insights into the SIC have emerged recently from different perspectives. On the one hand, the generalized optimized effective potential (GOEP) equation [4] makes it possible to bring the SIC functional rigorously under the Kohn-Sham umbrella while explicitly taking into account the unitary variance of the energy expression by a unitary transformation in the space of occupied orbitals. This can be seen as the formal Kohn-Sham foundation of earlier works that combined a global SIC potential with localizing transformations [31,32]. On the other hand, using complex orbitals in the unitary transformation has appeared as a necessity [47,48]. Accurate time-dependent SIC calculations, in which the orbitals become complex due to the propagation, revealed that also the ground state must be calculated with complex orbitals because otherwise one observes a sudden decrease of the energy even in a stationary propagation [48]. Focusing on ground-state properties a detailed study [47] recently included complex unitary transformations in the PZ SIC. It was shown that this procedure yields total energies and highest occupied orbital eigenvalues for atoms from

H to Ar in better agreement with experiment than those obtained using real orbitals if the SIC is applied to the Perdew, Burke, and Ernzerhof (PBE) functional [49] (PBE-SIC) [47]. Thus, the performance of the SIC in ground-state calculations must clearly be re-evaluated under several points of view: How different is GOEP SIC, which is formally a different density functional, in practice from traditional Perdew-Zunger SIC? How do SIC results change when complex- instead of real-valued unitary transformations are used? Was the earlier reported finding of the poor performance of PBE-SIC generally just a consequence of the restriction to real-valued orbital transformations?

In this paper we address these questions. We are, in particular, investigating molecular bond lengths, as these represent a well-examined paradigm example of a ground-state property where PZ LSDA-SIC is inferior to bare LSDA [40,41,45]. Bare LSDA bond lengths are in astonishingly good agreement with the experiment, with errors of typically less than 0.05 bohrs [50]. As a general trend LSDA slightly overestimates bonds between hydrogen and main-group elements and underestimates bonds between nonhydrogens [50]. Looking at a GGA one notes that the PBE, for example, is known to have a slight tendency to overestimate bond lengths, while PBE-SIC, in general, yields too-short bonds [45]. However, to the best of our knowledge, all SIC-related bond-length investigations focused on the PZ SIC implementation with orbital-specific potentials and no information is available for (G)OEP SIC.

With this paper we start filling this gap. To this end, we first discuss the peculiarities of the theoretical concept of SIC in KS DFT. We give an overview of SIC in the standard KS and the GOEP KS method and describe three different choices of the unitary transformation that is part of the scheme. More insight into the practical implementation of our algorithm for the determination of the corresponding transformations is given in Appendix B. On this theoretical basis we then investigate the influence of different SIC approaches and unitary transformation choices on total energies and bond lengths of a test set of dimers and small molecules that covers different bonding situations. We employ the SIC for both the LSDA and the PBE functional. A comparison and assessment of the total energies and bond lengths shows that real and complex transformations lead to different results: Complex transformations give lower total energies than real ones and improve bond lengths of double- and triple-bond systems. Finally, we provide insight into these differences by analyzing the orbital densities obtained from the different approaches.

## II. KOHN-SHAM SELF-INTERACTION CORRECTION

From a Kohn-Sham [51] DFT perspective, implementation of the SIC of Perdew and Zunger is far from trivial. First, one has to deal with a functional that depends on the orbitals explicitly and therefore is only an implicit functional of the density. In KS DFT, such explicit, orbital-dependent functionals can be handled by the OEP method [2,3]. Second, the SIC energy functional of Eq. (1) is not invariant under unitary transformation of the orbitals. This means that starting from a given set of occupied orbitals one can construct further orbital sets by unitary transformations that give the same density but result in different SICs. The GOEP scheme [4]

takes this ambiguity into account by considering the freedom of unitary transformations in the space of occupied orbitals in the derivation of the OEP equation. The generalization manifests itself in the existence of two sets of orbitals [4], where the occupied canonical KS orbitals  $\{\varphi_{j\sigma}(\mathbf{r})\}$  solve the KS equations and a second orbital set  $\{\tilde{\varphi}_{i\sigma}(\mathbf{r})\}$  is used to set up the SIC xc energy and the corresponding potential. Both orbital sets are connected by a unitary transformation  $U_{ij\sigma}$  according to

$$\tilde{\varphi}_{i\sigma}(\mathbf{r}) = \sum_{j=1}^{N_\sigma} U_{ij\sigma} \varphi_{j\sigma}(\mathbf{r}). \quad (2)$$

Note that for our investigations we always choose real canonical KS orbitals  $\{\varphi_{j\sigma}(\mathbf{r})\}$  without loss of generality.

To take the unitary transformation into account in the GOEP method one has to add an additional step in the derivation of the OEP potential by virtue of the functional chain rule (for details, see Ref. [4]). This leads to the generalized OEP integral equation, where, compared to the standard OEP equation, the orbital-specific potentials  $u_{xcj\sigma}(\mathbf{r})$  are replaced with the generalized orbital-specific potentials,

$$u_{xcj\sigma}^G(\mathbf{r}) = \frac{1}{\varphi_{j\sigma}^*(\mathbf{r})} \sum_{i=1}^{N_\sigma} U_{ij\sigma} \tilde{\varphi}_{i\sigma}^*(\mathbf{r}) \tilde{v}_{i\sigma}^{\text{SIC}}(\mathbf{r}), \quad (3)$$

where

$$\tilde{v}_{i\sigma}^{\text{SIC}}(\mathbf{r}) = \frac{\delta E_{xc}^{\text{SIC}}[\{\tilde{n}_{k\tau}\}]}{\delta \tilde{n}_{i\sigma}(\mathbf{r})}. \quad (4)$$

Reference [4] shows that solutions of the GOEP equation can be obtained with well-known methods invented for the standard OEP case. Yet, finding solutions can be a numerically expensive task. Therefore, often the approximation of Krieger, Lee, and Iafrate [52] is used, where  $u_{xcj\sigma}(\mathbf{r})$  has to be replaced by the generalized  $u_{xcj\sigma}^G(\mathbf{r})$  to obtain the generalized KLI (GKLI) potential,

$$v_{xc\sigma}^{\text{GKLI}}(\mathbf{r}) = v_{xc\sigma}^{\text{GSL}}(\mathbf{r}) + \frac{1}{2n_\sigma(\mathbf{r})} \sum_{j=1}^{N_\sigma} n_{j\sigma}(\mathbf{r}) \times [(\bar{v}_{xcj\sigma}^{\text{GKLI}} - \bar{u}_{xcj\sigma}^G) + \text{c.c.}]. \quad (5)$$

Here, the orbital-density averaged potentials are given by

$$\bar{v}_{xcj\sigma}^{\text{GKLI}} = \int d^3r \varphi_{j\sigma}^*(\mathbf{r}) v_{xc\sigma}^{\text{GKLI}}(\mathbf{r}) \varphi_{j\sigma}(\mathbf{r}) \quad (6)$$

and

$$\bar{u}_{xcj\sigma}^G = \int d^3r \varphi_{j\sigma}^*(\mathbf{r}) u_{xcj\sigma}^G(\mathbf{r}) \varphi_{j\sigma}(\mathbf{r}). \quad (7)$$

The first term of Eq. (5) is the generalized Slater contribution

$$v_{xc\sigma}^{\text{GSL}}(\mathbf{r}) = \frac{1}{2n_\sigma(\mathbf{r})} \sum_{j=1}^{N_\sigma} n_{j\sigma}(\mathbf{r}) [u_{xcj\sigma}^G(\mathbf{r}) + u_{xcj\sigma}^{G*}(\mathbf{r})], \quad (8)$$

whereas the second term is the response potential with the characteristic  $(\bar{v}_{xcj\sigma}^{\text{GKLI}} - \bar{u}_{xcj\sigma}^G)$  contribution.

However, still the question about how to treat the unitary transformation remains. First considerations of incorporating a unitary transformation into the PZ SIC scheme go back to Pederson, Heaton, and Lin [53–55]. In their original work,

they suggested an energy-minimization criterion for the total energy  $E^{\text{tot}}$ ,

$$\left( \frac{\partial E^{\text{tot}}}{\partial S_{ij\sigma}} \right)_{S_{ij\sigma}=\delta_{ij}} = 0 \quad \forall i, j \text{ occupied}, \quad (9)$$

to pinpoint the unitary transformation. Here,  $S_{ij\sigma}$  is a trial transformation that takes the set  $\{\tilde{\varphi}_{j\sigma}\}$  to a test set  $\{\tilde{\varphi}'_{i\sigma}\}$  and deviates only slightly from the unit matrix abbreviated by the Kronecker symbol  $\delta_{ij}$ . The criterion can be reformulated [53] and leads to a set of equations,

$$\langle \tilde{\varphi}_{i\sigma} | \tilde{v}_{i\sigma}^{\text{SIC}}(\mathbf{r}) - \tilde{v}_{j\sigma}^{\text{SIC}}(\mathbf{r}) | \tilde{\varphi}_{j\sigma} \rangle = 0 \quad \forall i, j \text{ occupied}, \quad (10)$$

that are fulfilled only when the SIC energy is minimized. This strategy of Pederson *et al.* can also be applied in KS DFT [4,56]. The central idea is to find an orbital set  $\{\tilde{\varphi}_{i\sigma}\}$  and the corresponding unitary transformation that leaves the density unchanged, minimizes the energy, and determines the xc potential. Using real canonical KS orbitals and taking definitions (2) and (9) into consideration, there are two possible choices of the orbitals  $\{\tilde{\varphi}_{i\sigma}\}$  and the transformation  $U_{ij\sigma}$ : They can be chosen either both real or both complex. At the same time, the potential remains a real potential in GOEP, as well as in its GKLI approximation. The two different sets of numbers valid for the orbitals and the transformation lead to two definitions of the unitary transformation:  $U_{ij\sigma}$  is defined according to Eq. (9) with numbers either restricted to be real or free to be complex.

A further definition of the unitary transformation is based on the observation that typically real energy-minimizing orbitals are much more localized in space than KS orbitals are [4]. This is because the Hartree contribution to the SIC in Eq. (1) increases with increasing degree of localization of the orbitals [23], while the SIE vanishes only at a certain degree of localization that strongly depends on the system. Therefore, spatially localizing transformations introduced by Foster and Boys [57,58], Edminton and Ruedenberg [59], and Pipek and Mezey [60] were suggested as a numerically less expensive alternative to the energy-minimizing transformations. The corresponding orbitals are typically called localizing or Foster-Boys orbitals. Reference [4] already investigated the difference between spatially localizing and real energy-minimizing orbitals and found good agreement for the studied cases and observables.

In summary, we consider four different versions of the SIC: one version (1) based on the standard KLI approach (KLI-SIC) and three versions (2–4) based on the GKLI concept. The three different versions of the GKLI approach result from three different definitions of the unitary transformation: (2) a real spatially localizing (FOBO), (3) a real energy-minimizing (real  $E_{\text{min}}$ ), and (4) a complex energy-minimizing transformation (complex  $E_{\text{min}}$ ). All approaches are implemented in the Bayreuth version [61] of the PARSEC real-space program package [62]. In PARSEC, core electrons are treated by the pseudopotential (PP) approximation (see Appendix A for details). We use a gradient algorithm with an optimized step size that takes the unitary constraint of the transformation into account explicitly to determine the energy-minimizing unitary transformations and corresponding orbitals (see Appendix B).

The Foster-Boys localization is carried out by a method of Edminton and Ruedenberg [59].

Having established the conceptual basis of our study, we finally note that Ref. [4] already assessed the performance of the GKLI approximation compared to full GOEP and concluded that both approaches yield ground-state energies and spin densities in close agreement. Since those are the properties needed in our investigations, for computational reasons, all results presented in the following were obtained by the GKLI approach.

### III. RESULTS AND DISCUSSION

We applied the standard KLI and the GKLI to investigate the total energy and bond-length situation for a test set of dimers and small molecules. The test set comprises  $\text{H}_2\text{O}$  and  $\text{CH}_4$  as typical single-bond representatives,  $\text{O}_2$  with a bond order of two, and the triple-bond representatives  $\text{CO}$  and  $\text{N}_2$ . We determined the lowest-energy configuration by means of bond-length variation followed by quadratic interpolation around the minimum [45]. During this procedure, the bond angles of  $\text{H}_2\text{O}$  and  $\text{CH}_4$  were kept constant at the experimental value. The results are compiled in Table I. The quadratic fit of the applied interpolation procedure leads to errors less than 0.001 bohrs. Possible uncertainties due to the use of PPs are discussed in Appendix A.

As a first aspect of our work, we discuss total energy results of our test set of molecules at experimental geometries. To this end, total energies relative to the corresponding LSDA result are shown in Fig. 1(a) for the four different LSDA-SIC implementations discussed in Sec. II. At first glance we can distinguish between two situations: In case of  $\text{H}_2\text{O}$  and  $\text{CO}$  all total energy results decrease in the order LSDA, standard, FOBO, real  $E_{\text{min}}$ , and complex  $E_{\text{min}}$  SIC, whereas for  $\text{CH}_4$ ,  $\text{O}_2$ , and  $\text{N}_2$  we first observe a total energy increase from LSDA to KLI-SIC followed again by a decrease of the total energy in the preceding order. Moreover, all total energies calculated with a localizing or energy-minimizing transformation are lower than the uncorrected LSDA result. The total energy decrease does not come as a surprise if one keeps in mind that in the given order additional variational degrees of freedom play a role. While LSDA is an explicit density functional that is derived from the homogeneous density limit, in the SIC scheme variation of the orbitals provides additional means for energy minimization. Beyond that, in the GKLI approach the unitary transformation can be used to further reduce the total energy. Here, localizing orbitals yield total energies that are almost equal to the ones obtained from real energy-minimizing orbitals. Finally, due to the additional complex degrees of freedom the space of variational energy minimization grows further and allows for another reduction of the total energy. This energy decrease is less pronounced only in the case of  $\text{CH}_4$ . The thus unexpected increase of KLI-SIC total energies for  $\text{CH}_4$ ,  $\text{O}_2$ , and  $\text{N}_2$ , however, reflects the problem of the SIC functional being unitarily variant and the KLI potential not being a functional derivative of the original energy expression. In case of the SIC energy functional, this can lead to pronounced differences between KLI SIC and OEP SIC results [4,26]. Deviations between KLI SIC and OEP SIC total energies, where the KLI LSDA-SIC result is larger than

TABLE I. Comparison of bond lengths (bohrs) of several dimers and small molecules calculated with LSDA, PBE, and different SIC implementations of the two functionals. GKLI SIC calculations are performed with three different definitions of the unitary transformation (see text). As a reference, experimental (Expt.) bond lengths are given.

Molecule	LSDA-SIC						PBE	PBE-SIC						Expt.
	LSDA	KLI-SIC	FOBO	real $E_{\min}$	complex $E_{\min}$	PZ SIC		KLI-SIC	FOBO	real $E_{\min}$	complex $E_{\min}$	PZ SIC		
H <sub>2</sub> O	1.829	1.769	1.758	1.758	1.750	1.759 [40]	1.825	1.799	1.787	1.786	1.774		1.809 [65]	
CH <sub>4</sub>	2.073	2.044	2.009	2.009	2.009	2.002 [40]	2.072	2.083	2.046	2.045	2.045	2.043 [45]	2.052 [66]	
O <sub>2</sub>	2.289	2.090	2.157	2.159	2.163	2.155 [45]	2.326	2.140	2.204	2.205		2.196 [45]	2.281 [67]	
CO	2.152	2.006	2.068	2.070	2.086	2.032 [40]	2.169	2.019	2.104	2.107	2.129	2.083 [45]	2.132 [67]	
N <sub>2</sub>	2.080	1.999	1.994	1.993	2.006	1.984 [40]	2.091	2.037	2.023	2.023	2.039	2.026 [45]	2.074 [67]	

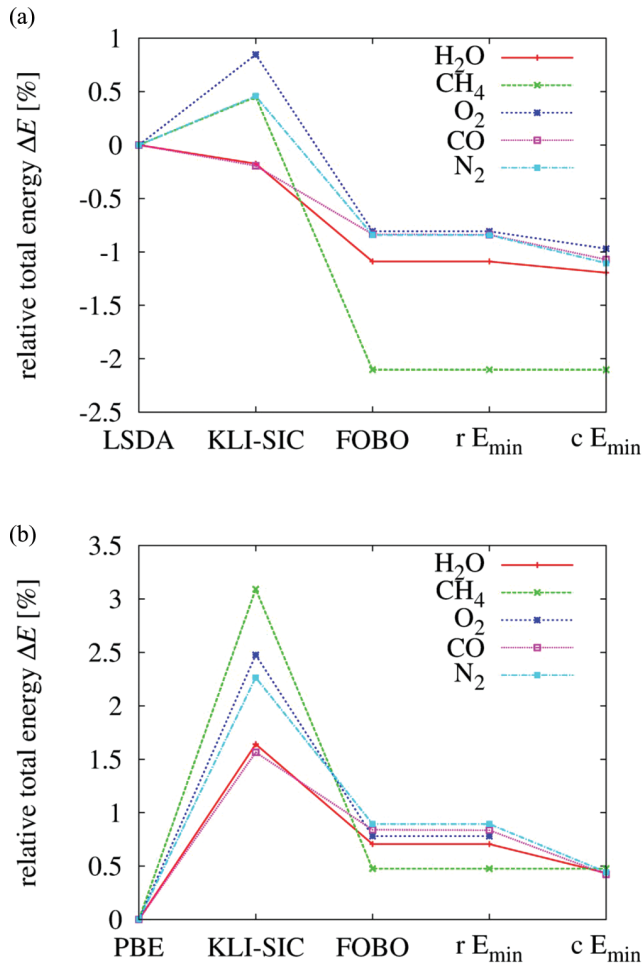


FIG. 1. (Color online) Panel (a) shows the relative total energy  $\Delta E = (E^{\text{func}} - E^{\text{LSDA}})/|E^{\text{LSDA}}|$  for the four different definitions of a KS SIC to the LSDA energy [63]. On the horizontal axis are the following functionals (func) from left to right: LSDA, KLI SIC without unitary transformation (KLI-SIC), GKLI SIC with FOBO transformation (FOBO), GKLI SIC with real-valued energy-minimizing transformation ( $r E_{\min}$ ), and GKLI SIC with complex-valued energy-minimizing transformation ( $c E_{\min}$ ), as introduced in Sec. II. For each of these functionals the total energy has been calculated for the five molecules listed in the inset. The lines serve only as a guide for the eye. Panel (b) shows the corresponding relative total energies for the PBE GGA functional and the corresponding four versions of a KS SIC to the PBE energy. All calculations were performed at experimental bond lengths (see Table I).

the LSDA one, are known in the literature [4]. Therefore, our results point once more toward the need of a generalized KLI scheme with an additional localizing or energy-minimizing transformation if KLI SIC calculations are performed.

One notable difference to this picture appears in the PBE-SIC case in Fig. 1(b). Whereas LSDA total energies are above all GKLI LSDA-SIC results, bare PBE gives the lowest total energies followed by an increase to KLI PBE-SIC and a subsequent decrease to GKLI PBE-SIC results. This finding may reflect the fact that for all systems investigated here, PBE yields total energies that are lower than coupled-cluster [singles, doubles and perturbative triples, CCSD(T)] reference results, as one can check using, for example, the NIST Computational Chemistry Comparison and Benchmark Database [64]. Therefore, the positive PBE-SIC energy correction points toward the right direction and the additional variational degrees of freedom of the unitary transformation guarantee for energy minimization within the PBE-SIC approach. The differences between LSDA, PBE, and the corresponding SIC schemes are a manifestation of the different theoretical concepts behind LSDA and PBE and are discussed more extensively at the end of this section.

We stress that our implementation in the PARSEC program package is based on real-space grids. Therefore, it can be excluded that differences due to real and complex numbers appear just as a consequence of basis set effects. They represent true features of the GOEP approach. Thus, as a first result of our paper, we conclude that complex energy-minimizing transformations need to be considered if one wants to perform the most rigorous energy-minimizing SIC calculations in KS DFT.

We now turn our discussion to the bond lengths and begin with the LSDA and LSDA-SIC results in Table I. Note that bare LSDA gives the overall best results in good agreement with previous findings based on all-electron (AE) calculations [45]. Possible deviations between PP and AE bond lengths can be explained by the PP approximation and are discussed in further detail in Appendix A. As previously found for PZ SIC, an underestimation of the bond lengths can be observed also in KS SIC. Here, however, one has to keep in mind that KLI-SIC suffers from unitary variance problems and the KLI not being a functional derivative. Because of that and because of the different numerical approaches of PPs and AE calculations, a direct comparison of the PZ SIC and our KS standard KLI SIC results is difficult.

A classification into two groups of results occurs if one examines the trend while passing through the different levels

of the SIC implementation. In the case of single-bond systems one observes a decrease in bond length when going from KLI-SIC via FOBO SIC and real  $E_{\min}$  SIC to complex  $E_{\min}$  SIC. Yet, in the same order, the trend is reversed for the double- and triple-bond systems. Here FOBO and real  $E_{\min}$  SIC improve upon standard SIC while a further increase toward the experimental result can be obtained with complex  $E_{\min}$  SIC. The only result that breaks ranks here is the  $N_2$  KLI-SIC bond length that is between real  $E_{\min}$  and complex  $E_{\min}$  SIC results. This observation, however, is likely to occur again as an artifact of the KLI-SIC approach. Moreover, as already observed in the total energies, there is no difference in the  $CH_4$  results for different definitions of the unitary transformation.

In case of the PBE our results show a bond-length overestimation in accordance with previous findings in the literature. The LSDA classification into two groups of results reoccurs in PBE-SIC and again the  $N_2$  KLI-SIC bond length is outside the general trend. Comparing LSDA-SIC and PBE-SIC results one observes that PBE-SIC bond lengths are all larger than the corresponding LSDA-SIC values. This finding cannot be explained by an overall shift that equals the difference between bare LSDA and PBE bond lengths. Interestingly, the changes from real energy-minimizing transformations to complex ones appear to be larger in PBE-SIC calculations than in LSDA-SIC. Therefore, we conclude that there are intricate differences in how the SIC acts on the LSDA and the PBE functional, respectively, and that these differences are also related to the use of real or complex transformations. Furthermore, we observe, in accordance with previous findings, that FOBO SIC and real  $E_{\min}$  SIC results for the bond lengths of all systems and both functionals investigated are in good agreement. This is one further confirmation of the use of FOBO SIC as a reasonable approximation to the real  $E_{\min}$  SIC procedure.

Note that in the case of  $O_2$  with complex  $E_{\min}$  PBE-SIC, we faced convergence problems and therefore are not able to give a well-founded number for the corresponding bond length: Although the system converges well up to 0.01% of the total energy, the remaining uncertainties in the total energy are still on the order of energy changes due to bond-length variation. We understand this problem as a delicate interplay between degeneracies in the  $O_2$  KS system and the KLI expression itself not being invariant with respect to unitary transformations of the canonical KS orbitals. The missing invariance of the KLI potential was already observed in Ref. [68] in the context of the exact exchange (EXX) functional, where the Slater contribution is invariant but the KLI response potential may change due to unitary transformations of the orbitals. However, in case of SIC the problem is even more involved: In standard KLI SIC, the unitary variance appears already on the level of the Slater potential. While this problem is solved in the generalized Slater approximation because  $v_{xc\sigma}^{GSL}(\mathbf{r})$  is invariant under unitary transformations among KS orbitals as long as the transformed orbitals yield the same minimizing orbitals  $\{\tilde{\varphi}_{i\sigma}(\mathbf{r})\}$ , the KLI response term remains variant in SIC and in all three GSIC versions.

At first glance, this does not seem to be an issue as the KS orbitals are fixed by solution of the KS equation. However, the problem with the unitary variance of the KLI potential is that, in the case of degeneracies, arbitrary unitary transformations can be performed within the space of degenerate KS orbitals

without changing the structure of the KS system. As a consequence, the variant KLI potential may be ill defined in such situations. In the spin-polarized  $O_2$ , twofold degeneracies occur at the highest occupied orbitals in both spin channels. Additionally, with complex  $E_{\min}$  PBE-SIC an almost threefold degeneracy appears at energetically lower-lying orbitals in one of the spin channels, where the orbital eigenvalues differ by only 0.002 Ry. Moreover, we observe rotations of (almost) degenerate orbitals during the self-consistency iteration. Additional convergence problems can be introduced by limitations in the numerical accuracy with which the minimizing unitary transformation is calculated. However, in our calculations, we carefully minimized such influencing factors by examination of a broad range of numerical parameters. Thus, we find that the convergence problems in  $O_2$  complex  $E_{\min}$  PBE-SIC are related to the missing invariance of the KLI potential under unitary transformations of degenerate occupied orbitals.

We further note that already the complex  $E_{\min}$  LDA-SIC exhibits difficult convergence in terms of the charge-weighted potential that we use as a self-consistency measure [62]. However, in contrast to the PBE-SIC case, the convergence issue here is less severe as the total energy converges up to an accuracy way below the variations due to changes of the bond length. The energetic spread of the three almost degenerate orbitals is about 0.013 Ry and thus about one order of magnitude larger than in PBE-SIC. Furthermore, the convergence problem does not occur in case of standard KLI, FOBO, and real  $E_{\min}$  SIC because, due to a different structure of the KS system, there is no almost threefold degeneracy and the twofold degeneracies do not seem to be problematic.

Finally, comparing our KS SIC to the PZ SIC results from the literature we find that the complex  $E_{\min}$  SIC yields the closest agreement with experimental bond lengths for double- and triple-bond systems of all self-interaction corrected functionals considered here. For single-bond systems complex  $E_{\min}$  SIC overcorrects even more and yields less favorable bond lengths. Therefore, as a second result of our work, we find that application of a complex energy-minimizing transformation leads to notable shifts in the bond length compared to real transformations. In a double- and triple-bond situation the bond-length shifts point toward the experimental result and therefore improve upon standard KLI-SIC and real transformation GKLI SIC approaches.

In order to examine the difference between real [69] and complex energy-minimizing orbitals further, we compare isosurface plots of the corresponding orbital densities [47] illustrated with the CO dimer in Fig. 2. While the energy-minimizing orbital densities 1 and 5 in Fig. 2 are qualitatively similar, striking differences are observed for orbital densities 2–4. Real  $E_{\min}$  orbital densities 2–4 show pronounced nodal planes, whereas complex  $E_{\min}$  orbital densities do not. The order of the energy-minimizing orbitals does not have any physical significance as they are not eigenfunctions of the Hamiltonian. We introduced the energy-minimizing orbital numbering just for the sake of being explicit in our assignment. Real orbitals need to form nodal planes in order to make orthogonality between different orbitals possible. These nodal planes are passed on to the corresponding orbital densities. If, however, complex degrees of freedom are permitted, the complex numbers can be exploited to guarantee for

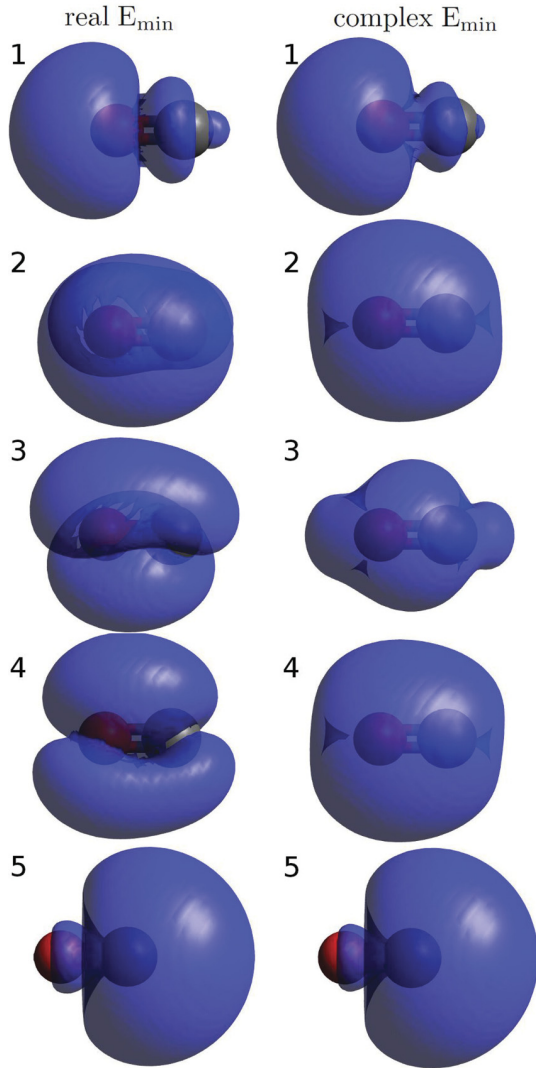


FIG. 2. (Color online) Orbital densities of real and complex energy-minimizing orbitals of CO at the experimental bond length of 2.132 bohrs.

orthogonality without or with reduced nodal planes, and thus nodal planes are also avoided in the corresponding orbital densities [47,70]. Our investigations indicate as a further result of our work that the complex energy-minimizing transformation in the generalized SIC KS approach leads to notably smoother energy-minimizing orbital densities where nodal planes are avoided compared to the real  $E_{\min}$  case. The smoother orbital densities without nodal planes are much closer to true electron densities and therefore closer to the realm where (semi-)local functionals as, for example, the LSDA and the PBE, are considered to be appropriate [45–47,70]. This gives an idea why complex  $E_{\min}$  LSDA-SIC and PBE-SIC, where smoother orbital densities are used, result in an improved energy minimization. Moreover, it also gives an explanation for the more pronounced changes from real to complex transformations in PBE-SIC than LSDA-SIC: The PBE functional is more sensitive to changes of the (orbital) density due to its gradient terms [49]. Notable density changes, however, occur close to nodal planes. Therefore, the PBE functional is expected to

show a more pronounced reaction on emerging or vanishing nodal planes than the LSDA does [47,70].

#### IV. CONCLUSIONS

In conclusion, we recapitulated the implementation of the SIC functional with a unitary transformation in the KS world of DFT and discussed three possible definitions of the transformation. The GCLI approach was applied to determine the total energy and bond length of a representative set of dimers and small molecules. We found that additional degrees of freedom corresponding to different definitions of the SIC approach lead to decreasing total energies. Complex degrees of freedom in the energy-minimizing transformation play a prominent role. The key difference between real and complex energy-minimizing orbitals seems to be the formation of nodal plains. Real energy-minimizing orbitals form nodal plains also in the corresponding orbital densities, while complex orbitals give smoother orbital densities. This allows for further energy minimization in the cases of LSDA-SIC and PBE-SIC. We confirmed in KS DFT the general notion that SIC underestimates bond lengths. However, whereas in the case of single-bond systems SIC with increasing degrees of freedom leads to increasing underestimation, for double- and triple-bond systems complex energy-minimizing generalized KS SIC yields the best self-interaction corrected results. This reduces standard SIC bond-length underestimation. Our results show that, in general, both the xc functional as well as the definition of the unitary transformation have a strong influence on the performance of SIC. In this spirit, one can conclude that the unitary transformation is a worthwhile starting point for improving self-interaction corrected DFT.

#### ACKNOWLEDGMENTS

We acknowledge discussions with J. P. Perdew on the topic of why the PBE functional may benefit less from a SIC than LSDA. We thank E. Engel for providing the EXX PPs. S.K. acknowledges financial support by DFG SFB 840 and the German-Israeli Foundation. P.Kl. acknowledges support from a grant from the Icelandic Research Fund and S.Kl. acknowledges a graduate student fellowship from the University of Iceland’s Research Fund.

#### APPENDIX A: PSEUDOPOTENTIALS

Throughout the paper we use norm-conserving PPs of Troullier-Martins [71] type for all atoms except hydrogen. The LSDA and all LSDA-SIC calculations were carried out with LSDA PPs, while we used PBE PPs for the PBE and PBE-SIC calculations. For hydrogen a Giannozzi-type PP according to Gygi [72] was used.

Since the PPs were constructed consistently only for the corresponding LSDA or PBE functional their performance in combination with the self-interaction corrected functionals is not clear at first glance. However, the applicability of LSDA PPs together with other xc energy functionals was investigated before [40,73]. Goedecker *et al.* [40] examined the application of PPs in the context of traditional PZ LSDA-SIC and found close similarity between LSDA and LSDA-SIC PPs. They report that without major effects on their results,

TABLE II. Core cutoff radii  $r_c$  of the LSDA and PBE PPs of C, N, and O in bohrs.

	LSDA-PP		PBE-PP	
	$2s r_c$	$2p r_c$	$2s r_c$	$2p r_c$
C	1.09	1.09	1.09	1.09
N	0.99	0.99	0.99	0.99
O	1.09	1.09	1.09	1.09

LSDA-SIC PPs could be substituted by LSDA PPs in LSDA-SIC calculations [40]. Based on this finding, we used PPs from (semi-)local functionals with small core cutoff radii  $r_c$  to keep the influence of the PPs low. The core cutoff radii of the PPs used in our calculations are compiled in Table II.

However, an influence on bond-length results can be expected from the PP construction itself. Therefore, we compare the bond lengths obtained from the bare LSDA and PBE functionals using the PPs of Table II to AE calculations from the literature in Table III.

While differences between PP and AE results are negligible for the single-bond systems, we observe deviations between the two approaches of 0.026 bohrs at the maximum for the double- and triple-bond systems. Deviations of that size can be expected due to the PP construction. Therefore, we further estimated the influence of the PP parameters on the bond lengths by repeating the bond-length investigations using different PPs constructed with different core cutoff radii. In case of the CO molecule, for instance, we can perfectly reproduce the AE LSDA result using a softer C ( $2s r_c = 1.29$  and  $2p r_c = 1.29$ ) and O ( $2s r_c = 1.45$  and  $2p r_c = 1.45$ ) PP. Here, also all LSDA-SIC results are shifted downward by about 0.02 bohrs and, most importantly, all trends discussed in Sec. III remain. PP parameters with a similar behavior can be found for N<sub>2</sub> and O<sub>2</sub>.

In order to further assess the influence of the PPs on bond-length results, we repeated all calculations using PPs constructed for the EXX functional (EXX-PP) in the KS OEP scheme [74] and compared to our previous results. EXX-PPs were proven to yield reliable KS band gaps in the OEP and KLI scheme [75–77]. One may argue that the EXX functional represents the extreme case of a perfectly self-interaction free functional without correlation. Therefore, if LSDA-PPs and EXX-PPs both yield results in good agreement one would be rather safe in assuming that all PPs also give reasonable results in the explicitly self-interaction corrected LSDA calculations. In practical application, however, we find that the convergence

TABLE III. LSDA and PBE bond lengths (bohrs) obtained from our PP approach in comparison to AE calculations, respectively.

	LSDA		PBE	
	LSDA-PP	AE	PBE-PP	AE
H <sub>2</sub> O	1.829		1.825	
CH <sub>4</sub>	2.073	2.073 [45]	2.072	2.071 [45]
O <sub>2</sub>	2.289	2.274 [45]	2.326	2.300 [45]
CO	2.152	2.130 [45]	2.169	2.147 [45]
N <sub>2</sub>	2.080	2.071 [45]	2.091	2.085 [45]

behavior of EXX-PP LSDA-SIC calculations is, by far, less favorable and leads to errors up to 0.01 bohrs in the bond-length interpolation procedure. Moreover, already LSDA bond lengths from EXX PPs are in error by 0.031 bohrs at the maximum. Deviations of this size can be explained by the construction procedure of EXX-PPs, where long-range effects of the EXX functional are treated explicitly [74]. Our investigations indicate that EXX-PPs cannot be transferred carelessly to calculations with other functionals because they are tailored to the peculiarities of the EXX functional. Yet, the general trends of bond-length shifts due to different SIC implementations are clearly visible also in the EXX-PP LSDA-SIC results.

In summary, we estimate an absolute bond-length error (excluding core-valence interaction effects) due to the use of PPs of 0.02 bohrs in this study. This error is on the scale where also other details of the numerical implementation start to matter. Results beyond the given accuracy are outside the interest of our investigation. The trends discussed in Sec. III are very robust and can thus be regarded as a valid general finding.

## APPENDIX B: UNITARILY CONSTRAINED ALGORITHM FOR THE ENERGY-MINIMIZING TRANSFORMATION

The purpose of this appendix is the description of the algorithm that we use in PARSEC for the determination of the energy-minimizing unitary transformation. The algorithm is based on a conjugate gradient (CG) method where the unitary constraint of the energy-minimizing transformation is taken into account explicitly. To this end, we apply an algorithm of Abrudan *et al.* [78] that exploits the group properties of unitary matrices [79] and was recently proposed for application in self-interaction corrected DFT [80,81]. In this algorithm, the computational cost can be reduced notably by optimizing the search direction and step size by means of CGs and a line search on the Lie group of unitary matrices. A general overview of the CG algorithm is provided in Table III of Ref. [78]. We describe the application of this algorithm in the context of SIC in two steps: First, we explain the basic algorithm that performs energy minimization constrained to unitary transformations of the occupied orbitals. In a second step, we illustrate performance enhancements of the basic algorithm by using CGs and step-size optimization.

The algorithm discussed in the following is supposed to minimize the SIC energy functional of Eq. (1) with respect to its freedom of unitary transformations. It starts from a fixed set of occupied orbitals  $\{\varphi_{j\sigma}^{(0)}\}$  determined by the initial unitary transformation  $U_{\sigma}^{(0)}$ . For this initial guess, multiple options are possible: (i) Take the occupied KS orbitals where  $U_{ij\sigma}^{(0)} = \delta_{ij}$ , (ii) use the minimizing transformation of the previous step of the KS self-consistency procedure, or (iii) determine the initial orbitals and transformation by a criterion different to energy minimization, for example, the FOBO localization. We find that as long as the orbitals do not change much during a KS self-consistency iteration, best performance can be obtained by the energy-minimizing transformation of the last KS step. In all other cases, we use FOBO localizing orbitals as an initial guess.

In each step ( $k$ ) of our iterative procedure we need to find a unitary transformation  $S_\sigma^{(k)}$  that determines a new orbital set  $\{\tilde{\varphi}_{i\sigma}^{(k+1)}\}$ ,

$$\tilde{\varphi}_{i\sigma}^{(k+1)}(\mathbf{r}) = \sum_{j=1}^{N_\sigma} S_{ij\sigma}^{(k)} \tilde{\varphi}_{j\sigma}^{(k)}(\mathbf{r}), \quad (\text{B1})$$

with lower SIC energy. Thus,  $S_\sigma^{(k)}$  also needs to modify the unitary transformation  $U_\sigma^{(k)}$  according to

$$U_{ij\sigma}^{(k+1)} = \sum_{n=1}^{N_\sigma} S_{in\sigma}^{(k)} U_{nj\sigma}^{(k)} \quad (\text{B2})$$

so that  $U_\sigma^{(k+1)}$  yields the new energy-minimizing orbitals from the occupied KS orbitals,

$$\tilde{\varphi}_{i\sigma}^{(k+1)}(\mathbf{r}) = \sum_{j=1}^{N_\sigma} U_{ij\sigma}^{(k+1)} \varphi_{j\sigma}(\mathbf{r}). \quad (\text{B3})$$

Therefore, as a first step we determine how the SIC energy changes due to small variations of the transformation  $S_\sigma$  from the unit matrix starting from a fixed orbital set  $\{\tilde{\varphi}_{j\sigma}^{(k)}\}$  [81]: Linear order changes of the SIC energy due to deviations of  $S_\sigma$  from the unit matrix are given by the anti-Hermitian gradient matrix,

$$G_{ij\sigma}^{(k)} = \left. \frac{\partial E_{\text{xc}}^{\text{SIC}}[\{\tilde{\varphi}_{n\sigma}^{(k)}\}, S_{mn\sigma}]}{\partial S_{ij\sigma}^*} \right|_{S_{ij\sigma}^* = \delta_{ij}} = \langle \tilde{\varphi}_{j\sigma}^{(k)} | \tilde{v}_{i\sigma}^{\text{SIC}(k)}(\mathbf{r}) - \tilde{v}_{j\sigma}^{\text{SIC}(k)}(\mathbf{r}) | \tilde{\varphi}_{i\sigma}^{(k)} \rangle. \quad (\text{B4})$$

Here, the SIC potentials  $\tilde{v}_{j\sigma}^{\text{SIC}(k)}(\mathbf{r})$  are computed from the energy-minimizing orbitals  $\tilde{\varphi}_{j\sigma}^{(k)}(\mathbf{r})$ .

The gradient can be applied straightforwardly as a steepest descent search direction with a step size  $l_\sigma^{(k)}$  to find the new transformation  $\tilde{U}_{ij\sigma}^{(k+1)} = U_{ij\sigma}^{(k)} - l_\sigma^{(k)} G_{ij\sigma}^{(k)}$ . Note that the step size carries a spin index and the iteration number as later we perform optimization of the step size per spin channel in each step of the iteration. Here, the step size is a fixed real number. However, this application of the energy gradient violates the unitary constraint and unitarity of  $\tilde{U}_\sigma^{(k+1)}$  has to be reconstituted *a posteriori*. To this end, in the first version of our algorithm we used the so-called Löwdin-orthogonalization method [82] that yields a unitary transformation  $U_\sigma^{(k+1)}$  as close as possible to  $\tilde{U}_\sigma^{(k+1)}$ . The *a posteriori* orthogonalization, however, renders an optimization of the step size difficult.

Therefore, the idea of Ref. [78] is to perform the gradient step in a reduced space, where the unitarity constraint is guaranteed by choice of the parameter space [79]. Thus, the optimization problem can be turned into an unconstrained one by suitable restriction of the parameter space to the Lie group of  $n \times n$  unitary matrices  $U(n)$  [78]. Due to the anti-Hermiticity of the gradient matrix, the exponential map

$$S_\sigma^{(k)}(l_\sigma^{(k)}) = \exp\{-l_\sigma^{(k)} G_\sigma^{(k)}\} \quad (\text{B5})$$

with step size  $l_\sigma^{(k)}$  constitutes a unitarity conserving transformation when it is applied to the unitary transformation  $U_\sigma^{(k)}$  as in Eq. (B2). Here,  $G_\sigma^{(k)}$  corresponds to the steepest descent search direction but due to the exponential map unitarity of  $S_\sigma^{(k)}$  is guaranteed. The exponential map of Eq. (B5) needs to be

interpreted by the series expansion of the exponential function. In practical calculations, we compute the unitary matrix  $M_\sigma^{(k)}$  and the diagonal matrix  $D_{om\sigma}^{(k)} = \lambda_{m\sigma}^{(k)} \delta_{om}$  with eigenvalues  $\lambda_{m\sigma}^{(k)}$  [81] by diagonalization of the Hermitian matrix

$$-iG_\sigma^{(k)} = M_\sigma^{(k)\dagger} D_\sigma^{(k)} M_\sigma^{(k)}. \quad (\text{B6})$$

Hence, Eq. (B2) can be reformulated as

$$U_{ij\sigma}^{(k+1)} = \sum_{n,m=1}^{N_\sigma} M_{mi\sigma}^{(k)*} \exp\{-il_\sigma^{(k)} \lambda_{m\sigma}^{(k)}\} M_{mn\sigma}^{(k)} U_{nj\sigma}^{(k)}. \quad (\text{B7})$$

So far we have described the basic steepest descent algorithm where the unitary constraint is taken into account explicitly. It allows for the determination of the energy-minimizing unitary transformation by iteration of Eq. (B7) together with the gradient of Eq. (B4), the orbitals of Eq. (B3), and the diagonalization of Eq. (B6).

Yet, the numerical performance of this algorithm can be notably increased. In the following, we describe how such a performance enhancement can be obtained by using CGs and an optimization of the gradient step size. The idea of the CG approach [78] is to determine the new search direction  $H_\sigma^{(k)}$  based on the current gradient  $G_\sigma^{(k)}$  and the search direction  $H_\sigma^{(k-1)}$  of the last step of the iteration. In the PARSEC CG implementation, we employ the new search direction,

$$H_{ij\sigma}^{(k)} = G_{ij\sigma}^{(k)} + \gamma_\sigma^{(k)} H_{ij\sigma}^{(k-1)}, \quad (\text{B8})$$

where  $\gamma_\sigma^{(k)}$  is the Polak-Ribière weighting factor [78],

$$\gamma_\sigma^{(k)} = \frac{\langle G_\sigma^{(k)} - G_\sigma^{(k-1)}, G_\sigma^{(k)} \rangle}{\langle G_\sigma^{(k-1)}, G_\sigma^{(k-1)} \rangle}. \quad (\text{B9})$$

The brackets are defined by

$$\langle X, Y \rangle = \frac{1}{2} \text{Re}\{\text{Tr}(XY^\dagger)\}, \quad X, Y \in \mathbb{C}^{n \times n}. \quad (\text{B10})$$

To constitute the CG version of our iterative algorithm, the new conjugate search direction of Eq. (B8) replaces the gradient  $G_\sigma^{(k)}$  in the basic steepest descent algorithm. For a transparent overview, we summarized our CG algorithm together with the initialization of the algorithm in Table IV. Note that in some cases the CG of the iterative procedure does not perform better than the steepest descent. Comments and a criterion about when the CG should be abandoned can be found in Ref. [78].

Thus far, the gradient step  $l_\sigma^{(k)}$  was chosen to be a fixed real number. However, an optimization of  $l_\sigma^{(k)}$  further improves the numerical performance. To this end, we approximate the energy as a function of  $l_\sigma^{(k)}$  by a second-order polynomial and use the step size corresponding to the minimum of the polynomial as an optimum step size  $l_\sigma^{\text{opt}(k)}$ . The optimum can be calculated from the slope

$$m_\sigma^{(k)}(l_\sigma^{(k)}) = \left. \frac{dE_{\text{xc}}^{\text{SIC}}(l_\sigma)}{dl_\sigma} \right|_{l_\sigma=l_\sigma^{(k)}} \quad (\text{B11})$$

of the polynomial at  $l_\sigma^{(k)} = 0$  and after some trial step  $l_\sigma^{(k)} = l_\sigma^{\text{trial}}$  according to

$$l_\sigma^{\text{opt}(k)} = \frac{-m_\sigma^{(k)}(0) l_\sigma^{\text{trial}}}{m_\sigma^{(k)}(l_\sigma^{\text{trial}}) - m_\sigma^{(k)}(0)}. \quad (\text{B12})$$

TABLE IV. CG algorithm with step-size optimization for the minimization of the SIC energy functional. The CG version of the algorithm without step-size optimization can be obtained by neglecting steps (2 iii), (4), and (5) and choosing a fixed step size  $l_\sigma$  in the beginning.

(1)	Initialization: (i) $k = 0$ , $H_{ij\sigma}^{(-1)} = 0$ , $\tilde{\varphi}_{i\sigma}^{(0)}(\mathbf{r}) = \sum_{j=1}^{N_\sigma} U_{ij\sigma}^{(0)} \varphi_{j\sigma}(\mathbf{r})$ (ii) set real number $l^{\text{trial}}$
(2)	Compute: (i) $G_{ij\sigma}^{(k)} = \langle \tilde{\varphi}_{i\sigma}^{(k)}   \tilde{v}_{i\sigma}^{\text{SIC}(k)}(\mathbf{r}) - \tilde{v}_{j\sigma}^{\text{SIC}(k)}(\mathbf{r})   \tilde{\varphi}_{i\sigma}^{(k)} \rangle$ (ii) $H_{ij\sigma}^{(k)} = G_{ij\sigma}^{(k)} + \gamma_\sigma H_{ij\sigma}^{(k-1)}$ (iii) $m_\sigma^{(k)}(0) = -2 \langle H_\sigma^{(k)}, G_\sigma^{(k)} \rangle$
(3)	Determine $M_\sigma^{(k)}$ and $D_{om\sigma}^{(k)} = \lambda_{m\sigma}^{(k)} \delta_{om}$ from diagonalization of $-i H_\sigma^{(k)} = M_\sigma^{(k) \dagger} D_\sigma^{(k)} M_\sigma^{(k)}$
(4)	Perform the trial step with step size $l^{\text{trial}}$ and compute: (i) $U_{ij\sigma}^{\text{trial}} = \sum_{n,m=1}^{N_\sigma} M_{mi\sigma}^{(k)*} \exp\{-i l^{\text{trial}} \lambda_{m\sigma}^{(k)}\} M_{mn\sigma}^{(k)} U_{nj\sigma}^{(k)}$ (ii) $\tilde{\varphi}_{i\sigma}^{\text{trial}}(\mathbf{r}) = \sum_{j=1}^{N_\sigma} U_{ij\sigma}^{\text{trial}} \varphi_{j\sigma}(\mathbf{r})$ and $\{\tilde{v}_{i\sigma}^{\text{SIC trial}}\}$ (iii) $G_{ij\sigma}^{\text{trial}} = \langle \tilde{\varphi}_{i\sigma}^{\text{trial}}   \tilde{v}_{i\sigma}^{\text{SIC trial}}(\mathbf{r}) - \tilde{v}_{j\sigma}^{\text{SIC trial}}(\mathbf{r})   \tilde{\varphi}_{i\sigma}^{\text{trial}} \rangle$ (iv) $m_\sigma^{(k)}(l^{\text{trial}}) = -2 \langle H_\sigma^{(k)}, G_\sigma^{\text{trial}} \rangle$ (v) $l_\sigma^{\text{opt}(k)} = \frac{-m_\sigma^{(k)}(0) l^{\text{trial}}}{m_\sigma^{(k)}(l^{\text{trial}}) - m_\sigma^{(k)}(0)}$
(5)	Determine the step size: compute $l_\sigma^{\text{cut}(k)} = \frac{\pi}{2 \times \text{maximum of } \{\lambda_{m\sigma}^{(k)}\}}$ ; If $0 \leq l_\sigma^{\text{opt}(k)} \leq l_\sigma^{\text{cut}(k)}$ : choose $l_\sigma^{(k)} = l_\sigma^{\text{opt}(k)}$ Else: choose $l_\sigma^{(k)} = 0.2 l_\sigma^{\text{cut}(k)}$
(6)	Perform a CG step with step size $l_\sigma^{(k)}$ and compute: (i) $U_{ij\sigma}^{(k+1)} = \sum_{n,m=1}^{N_\sigma} M_{mi\sigma}^{(k)*} \exp\{-i l_\sigma^{(k)} \lambda_{m\sigma}^{(k)}\} M_{mn\sigma}^{(k)} U_{nj\sigma}^{(k)}$ (ii) $\tilde{\varphi}_{i\sigma}^{(k+1)}(\mathbf{r}) = \sum_{j=1}^{N_\sigma} U_{ij\sigma}^{(k+1)} \varphi_{j\sigma}(\mathbf{r})$ and $\{\tilde{v}_{i\sigma}^{\text{SIC}(k+1)}\}$
(7)	Check convergence: If convergence is fulfilled: stop Else: $k := k + 1$ and go to step (2)

We obtain the needed slopes based on the derivative of the energy with respect to  $l_\sigma$  in two steps [81]

$$m_\sigma^{(k)}(l_\sigma^{(k)}) = \sum_{i,j=1}^{N_\sigma} \left. \frac{\partial E_{xc}^{\text{SIC}}(l_\sigma^{(k)})}{\partial S_{ij\sigma}} \right|_{S_{ij\sigma}=\delta_{ij}} \left. \frac{dS_{ij\sigma}(l_\sigma)}{dl_\sigma} \right|_{l_\sigma=0}, \quad (\text{B13})$$

where the first factor represents the gradient and the second factor the negative search direction at  $l_\sigma = 0$ . The gradient needs to be computed at  $l_\sigma^{(k)} = 0$  and after the trial step at  $l_\sigma^{(k)} = l^{\text{trial}}$ . In case of the CG method, the second factor gives  $H_\sigma^{(k)}$  for the search direction and one obtains

$$m_\sigma^{(k)}(0) = -2 \langle H_\sigma^{(k)}, G_\sigma^{(k)} \rangle, \quad (\text{B14})$$

$$m_\sigma^{(k)}(l^{\text{trial}}) = -2 \langle H_\sigma^{(k)}, G_\sigma^{\text{trial}} \rangle, \quad (\text{B15})$$

where we used the bracket of Eq. (B10).

Numerical tests of this polynomial line search revealed that it is advisable to introduce an upper limit of the optimized step size. We determine this upper limit based on the observation that the exponential map of Eq. (B5) results in an almost periodic variation of the transformation with frequencies determined by the eigenvalues  $\lambda_{m\sigma}^{(k)}$  [78,81]. The idea is to avoid periodic oscillations by choosing step sizes that are smaller than the first quarter of the period of the highest-frequency component given by  $\lambda_\sigma^{\text{max}(k)} = \text{maximum of } \{\lambda_{m\sigma}^{(k)}\}$

$$0 \leq l_\sigma^{(k)} \leq l_\sigma^{\text{cut}(k)}, \quad l_\sigma^{\text{cut}(k)} = \frac{\pi}{2 \lambda_\sigma^{\text{max}(k)}}. \quad (\text{B16})$$

If the step size violates this condition, we choose  $l_\sigma^{(k)} = 0.2 l_\sigma^{\text{cut}(k)}$ .

Finally, we determine the convergence of our algorithm by monitoring the Pederson criterion of Eq. (10). Convergence is reached when the absolute value of the largest matrix element of the matrix in Eq. (10) is smaller than a given threshold which is typically less than  $10^{-5}$  Ry. In all calculations for the present paper we used a threshold of  $10^{-6}$  Ry. The CG algorithm with step-size optimization is summarized in Table IV.

We applied the gradient line search unitary optimization algorithm also for systems that are much larger than the ones studied in this paper. For instance, applying it to molecular semiconductors where SIC plays an important role [22,83] yields notably reduced computation times as compared to the algorithm used previously by some of us [4,22,83]. A further detailed presentation and numerical assessment of the new algorithm including, for example,  $C_{20}$  and diamond will be given elsewhere [84].

Note that the algorithm described here can also be used to optimize the Foster-Boys [57,58] spatial localization criterion in the form [60,85]

$$B[\{\tilde{\varphi}_{j\sigma}\}] = \sum_{i=1}^{N_\sigma} [\langle \tilde{\varphi}_{i\sigma} | \mathbf{r}^2 | \tilde{\varphi}_{i\sigma} \rangle - \langle \tilde{\varphi}_{i\sigma} | \mathbf{r} | \tilde{\varphi}_{i\sigma} \rangle^2] \quad (\text{B17})$$

under the constraint of unitary transformations. To this end, one needs to substitute the energy gradient of Eq. (B4) with the gradient of the Foster-Boys criterion,

$$\begin{aligned} G_{ij\sigma}^{(k)} &= \left. \frac{\partial B[\{\tilde{\varphi}_{n\sigma}^{(k)}\}, S_{mn\sigma}]}{\partial S_{ij\sigma}^*} \right|_{S_{ij\sigma}^*=\delta_{ij}} \\ &= \langle \tilde{\varphi}_{j\sigma}^{(k)} | \tilde{v}_{i\sigma}^{\text{FOBO}(k)}(\mathbf{r}) - \tilde{v}_{j\sigma}^{\text{FOBO}(k)}(\mathbf{r}) | \tilde{\varphi}_{i\sigma}^{(k)} \rangle, \end{aligned} \quad (\text{B18})$$

where

$$\tilde{v}_{i\sigma}^{\text{FOBO}(k)}(\mathbf{r}) = \mathbf{r}^2 - 2\mathbf{r} \cdot \langle \tilde{\varphi}_{i\sigma}^{(k)} | \mathbf{r} | \tilde{\varphi}_{i\sigma}^{(k)} \rangle. \quad (\text{B19})$$

[1] J. P. Perdew and A. Zunger, *Phys. Rev. B* **23**, 5048 (1981).

[2] T. Grabo, T. Kreibich, and E. K. U Gross, in *Strong Coulomb Correlation in Electronic Structure: Beyond the Local Density Approximation*, edited by V. Anisimov (Gordon & Breach, Tokyo, 2000).

[3] S. Kümmel and L. Kronik, *Rev. Mod. Phys.* **80**, 3 (2008).

[4] T. Körzdörfer, S. Kümmel, and M. Mundt, *J. Chem. Phys.* **129**, 014110 (2008).

[5] A. J. Cohen, P. Mori-Sánchez, and W. Yang, *Science* **321**, 792 (2008).

- [6] Y. Zhang and W. Yang, *J. Chem. Phys.* **109**, 2604 (1998).
- [7] A. Ruzsinszky, J. P. Perdew, G. I. Csonka, O. A. Vydrov, and G. E. Scuseria, *J. Chem. Phys.* **126**, 104102 (2007).
- [8] K. D. Dobbs and D. A. Dixon, *J. Phys. Chem.* **98**, 12584 (1994).
- [9] T. N. Truong and W. Duncan, *J. Chem. Phys.* **101**, 7408 (1994).
- [10] K. Schwarz, *Chem. Phys. Lett.* **57**, 605 (1978).
- [11] H. B. Shore, J. H. Rose, and E. Zaremba, *Phys. Rev. B* **15**, 2858 (1977).
- [12] S. J. A. van Gisbergen, P. R. T. Schipper, O. V. Gritsenko, E. J. Baerends, J. G. Snijders, B. Champagne, and B. Kirtman, *Phys. Rev. Lett.* **83**, 694 (1999).
- [13] S. Kümmel, L. Kronik, and J. P. Perdew, *Phys. Rev. Lett.* **93**, 213002 (2004).
- [14] C. Toher, A. Filippetti, S. Sanvito, and K. Burke, *Phys. Rev. Lett.* **95**, 146402 (2005).
- [15] C. Toher and S. Sanvito, *Phys. Rev. Lett.* **99**, 056801 (2007).
- [16] S.-H. Ke, H. U. Baranger, and W. Yang, *J. Chem. Phys.* **126**, 201102 (2007).
- [17] D. Glötzl, *J. Phys. F* **8**, L163 (1978).
- [18] A. Svane and O. Gunnarsson, *Phys. Rev. B* **37**, 9919(R) (1988).
- [19] A. Svane and O. Gunnarsson, *Phys. Rev. Lett.* **65**, 1148 (1990).
- [20] W. M. Temmerman, Z. Szotek, and H. Winter, *Phys. Rev. B* **47**, 11533 (1993).
- [21] P. Mori-Sánchez, A. J. Cohen, and W. Yang, *Phys. Rev. Lett.* **100**, 146401 (2008).
- [22] T. Körzdörfer, S. Kümmel, N. Marom, and L. Kronik, *Phys. Rev. B* **79**, 201205(R) (2009); **82**, 129903(E) (2010).
- [23] T. Körzdörfer, *J. Chem. Phys.* **134**, 094111 (2011).
- [24] C. D. Pemmaraju, S. Sanvito, and K. Burke, *Phys. Rev. B* **77**, 121204(R) (2008).
- [25] A. Ruzsinszky, J. P. Perdew, G. I. Csonka, G. E. Scuseria, and O. A. Vydrov, *Phys. Rev. A* **77**, 060502(R) (2008).
- [26] T. Körzdörfer, M. Mundt, and S. Kümmel, *Phys. Rev. Lett.* **100**, 133004 (2008).
- [27] R. Armiento, S. Kümmel, and T. Körzdörfer, *Phys. Rev. B* **77**, 165106 (2008); A. Karolewski, R. Armiento, and S. Kümmel, *J. Chem. Theory Comput.* **5**, 712 (2009).
- [28] P. Cortona, *Phys. Rev. A* **34**, 769 (1986).
- [29] M. A. Whitehead, in *Recent Advances in Density Functional Methods, Part II*, edited by D. P. Chong (World Scientific, Singapore, 1997).
- [30] C. A. Ullrich, P.-G. Reinhard, and E. Suraud, *Phys. Rev. A* **62**, 053202 (2000).
- [31] J. Garza, J. A. Nichols, and D. A. Dixon, *J. Chem. Phys.* **112**, 7880 (2000).
- [32] S. Patchkovskii, J. Autschbach, and T. Ziegler, *J. Chem. Phys.* **115**, 26 (2001).
- [33] U. Lundin and O. Eriksson, *Int. J. Quantum Chem.* **81**, 247 (2001).
- [34] H.-J. Unger, *Phys. Lett. A* **284**, 124 (2001).
- [35] C. Legrand, E. Suraud, and P.-G. Reinhard, *J. Phys. B: At. Mol. Opt. Phys.* **35**, 1115 (2002).
- [36] S. Kümmel and J. P. Perdew, *Mol. Phys.* **101**, 1363 (2002).
- [37] A. Filippetti and N. A. Spaldin, *Phys. Rev. B* **67**, 125109 (2003).
- [38] Paula Mori-Sánchez, A. J. Cohen, and W. Yang, *J. Chem. Phys.* **125**, 201102 (2006).
- [39] D. Vieira and K. Capelle, *J. Chem. Theory Comput.* **6**, 3319 (2010).
- [40] S. Goedecker and C. J. Umrigar, *Phys. Rev. A* **55**, 1765 (1997).
- [41] G. I. Csonka and B. G. Johnson, *Theor. Chem. Acc.* **99**, 158 (1998).
- [42] J. Gräfenstein, E. Kraka, and D. Cremer, *Phys. Chem. Chem. Phys.* **6**, 1096 (2004).
- [43] O. A. Vydrov and G. E. Scuseria, *J. Chem. Phys.* **121**, 8187 (2004).
- [44] O. A. Vydrov and G. E. Scuseria, *J. Chem. Phys.* **122**, 184107 (2005).
- [45] O. A. Vydrov, G. E. Scuseria, J. P. Perdew, A. Ruzsinszky, and G. I. Csonka, *J. Chem. Phys.* **124**, 094108 (2006).
- [46] O. A. Vydrov and G. E. Scuseria, *J. Chem. Phys.* **124**, 191101 (2006).
- [47] S. Klüpfel, P. Klüpfel, and Hannes Jónsson, *Phys. Rev. A* **84**, 050501(R) (2011).
- [48] D. Hofmann, diploma thesis, University of Bayreuth, 2008; D. Hofmann, T. Körzdörfer, and S. Kümmel, *Phys. Rev. Lett.* **108**, 146401 (2012).
- [49] J. P. Perdew, K. Burke, and M. Ernzerhof, *Phys. Rev. Lett.* **77**, 3865 (1996).
- [50] R. M. Dickson and A. D. Becke, *J. Chem. Phys.* **99**, 3898 (1993).
- [51] W. Kohn and L. J. Sham, *Phys. Rev.* **140**, A1133 (1965).
- [52] J. B. Krieger, Y. Li, and G. J. Iafrate, *Phys. Rev. A* **46**, 5453 (1992).
- [53] M. R. Pederson, R. A. Heaton, and C. C. Lin, *J. Chem. Phys.* **80**, 1972 (1984).
- [54] M. R. Pederson, R. A. Heaton, and C. C. Lin, *J. Chem. Phys.* **82**, 2688 (1985).
- [55] M. R. Pederson and C. C. Lin, *J. Chem. Phys.* **88**, 1807 (1988).
- [56] J. Messud, P. M. Dinh, P.-G. Reinhard, and E. Suraud, *Phys. Rev. A* **80**, 044503 (2009).
- [57] S. F. Boys, *Rev. Mod. Phys.* **32**, 296 (1960).
- [58] J. M. Foster and S. F. Boys, *Rev. Mod. Phys.* **32**, 300 (1960).
- [59] C. Edminton and K. Ruedenberg, *Rev. Mod. Phys.* **35**, 457 (1963).
- [60] J. Pipek and P. G. Mezey, *J. Chem. Phys.* **90**, 4916 (1989).
- [61] M. Mundt, S. Kümmel, B. Huber, and M. Moseler, *Phys. Rev. B* **73**, 205407 (2006).
- [62] L. Kronik, A. Makmal, M. L. Tiago, M. M. G. Alemany, M. Jain, X. Huang, Y. Saad, and J. R. Chelikowsky, *Phys. Status Solidi B* **243**, 1063 (2006).
- [63] The absolute total energies of complex  $E_{\min}$  SIC are  $-34.76$  Ry for  $\text{H}_2\text{O}$ ,  $-16.42$  Ry for  $\text{CH}_4$ ,  $-64.35$  Ry for  $\text{O}_2$ ,  $-43.76$  Ry for  $\text{CO}_2$ , and  $-40.21$  Ry for  $\text{N}_2$ .
- [64] NIST Computational Chemistry Comparison and Benchmark Database, NIST Standard Reference Database Number 101, Release 15b, August 2011, edited by Russell D. Johnson III, [<http://cccbdb.nist.gov/>].
- [65] J. H. Callomon, E. Hirota, K. Kuchitsu, W. J. Lafferty, A. G. Maki, and C. S. Pote, in *Structure Data of Free Polyatomic Molecules*, edited by K.-H. Hellwege and A. M. Hellwege, Landolt-Börnstein, New Series, Group II, Vol. 7 (Springer, Berlin, 1976).
- [66] D. L. Gray and A. G. Robiette, *Mol. Phys.* **37**, 1901 (1979).
- [67] K. P. Huber and G. Herzberg, *Molecular Spectra and Molecular Structure IV: Constants of Diatomic Molecules* (Van Nostrand Reinhold, New York, 1979).
- [68] F. Della Sala and A. Görling, *J. Chem. Phys.* **115**, 5718 (2001).
- [69] Due to the close similarity of FOBO and real  $E_{\min}$  SIC we focus our discussion only on the comparison between real  $E_{\min}$  and complex  $E_{\min}$  orbital densities.

- [70] J. P. Perdew, Communication at the workshop “Self-Interaction Correction: State of the Art and Future Directions”, Chester, UK, 2011.
- [71] N. Troullier and J. L. Martins, *Phys. Rev. B* **43**, 1993 (1991).
- [72] F. Gygi, *Phys. Rev. B* **48**, 11692 (1993).
- [73] Y.-H. Kim, M. Städele, and R. M. Martin, *Phys. Rev. A* **60**, 3633 (1999).
- [74] E. Engel, A. Hock, R. N. Schmid, R. M. Dreizler, and N. Chetty, *Phys. Rev. B* **64**, 125111 (2001).
- [75] A. Makmal, R. Armiento, E. Engel, L. Kronik, and S. Kümmel, *Phys. Rev. B* **80**, 161204(R) (2009).
- [76] E. Engel, *Phys. Rev. B* **80**, 161205(R) (2009).
- [77] M. Betzinger, C. Friedrich, S. Blügel, and A. Görling, *Phys. Rev. B* **83**, 045105 (2011).
- [78] T. Abrudan, J. Eriksson, and V. Koivunen, *Signal Process.* **89**, 1704 (2009).
- [79] A. Eldemann, T. A. Arias, and S. T. Smith, *SIAM J. Matrix Anal. Appl.* **20**, 303 (1998).
- [80] P. Klüpfel, S. Klüpfel, K. Tsemekhman, and H. Jónsson, *Lect. Notes Comput. Sci.* **7134**, 23 (2012).
- [81] C.-H. Park, A. Ferretti, I. Dabo, N. Poilvert, and N. Marzari, *arXiv:1108.5726v1*.
- [82] I. Mayer, *Int. J. Quantum Chem.* **90**, 63 (2002).
- [83] M. Dauth, T. Körzdörfer, S. Kümmel, J. Ziroff, M. Wiessner, A. Schöll, F. Reinert, M. Arita, and K. Shimada, *Phys. Rev. Lett.* **107**, 193002 (2011).
- [84] S. Klüpfel, H. Jónsson, and P. Klüpfel (unpublished).
- [85] J. Messud, P. M. Dinh, P.-G. Reinhard, and E. Suraud, *Ann. Phys.* **523**, 270 (2011).



## Publication 4

# Self-interaction correction in a real-time Kohn-Sham scheme: access to difficult excitations in time-dependent density functional theory

D. Hofmann and S. Kümmel

*Theoretical Physics IV, University of Bayreuth, D-95440 Bayreuth, Germany*

The Journal of Chemical Physics **137**, 064117 (2012)

©2012 American Institute of Physics

DOI: 10.1063/1.4742763

available at: <http://link.aip.org/link/?JCP/137/064117>

### ABSTRACT

We present a real-time Kohn-Sham propagation scheme for the self-interaction correction (SIC). The multiplicative Kohn-Sham potential is constructed in real-time and real-space based on the generalized optimized effective potential equation. We demonstrate that this approach yields promising results for a wide range of test systems, including hydrogen terminated silicon clusters, conjugated molecular chains, and molecular charge-transfer systems. We analyze the nature of excitations by calculating transition densities from the time evolution and by evaluating the time-dependent exchange-correlation potential. A properly constructed Kohn-Sham SIC potential shows a time-dependent field-counteracting behavior. These favorable characteristics of the exchange-correlation potential may be lost in approximations such as the SIC-Slater potential.

Reprinted with permission from J. Chem. Phys. 137, 064117 (2012).  
Copyright 2012, American Institute of Physics.



# Self-interaction correction in a real-time Kohn-Sham scheme: Access to difficult excitations in time-dependent density functional theory

D. Hofmann and S. Kümmel<sup>a)</sup>*Theoretische Physik IV, Universität Bayreuth, D-95440 Bayreuth, Germany*

(Received 19 May 2012; accepted 23 July 2012; published online 14 August 2012)

We present a real-time Kohn-Sham propagation scheme for the self-interaction correction (SIC). The multiplicative Kohn-Sham potential is constructed in real-time and real-space based on the generalized optimized effective potential equation. We demonstrate that this approach yields promising results for a wide range of test systems, including hydrogen terminated silicon clusters, conjugated molecular chains, and molecular charge-transfer systems. We analyze the nature of excitations by calculating transition densities from the time evolution and by evaluating the time-dependent exchange-correlation potential. A properly constructed Kohn-Sham SIC potential shows a time-dependent field-counteracting behavior. These favorable characteristics of the exchange-correlation potential may be lost in approximations such as the SIC-Slater potential. © 2012 American Institute of Physics. [<http://dx.doi.org/10.1063/1.4742763>]

## I. INTRODUCTION

Predicting and understanding the electronic structure and excitations of nanoscale materials requires reliable first-principles approaches. In principle, (time-dependent) density functional theory ((TD)DFT) appears as the ideal choice for this task due to its attractive ratio of accuracy to computational effort. However, most standard density functionals suffer from deficiencies that limit their applicability. The wrong asymptotic behavior of the potential,<sup>1</sup> the incorrect prediction of dissociation limits,<sup>2</sup> and the overestimation of the static electric response<sup>3</sup> are well-known problems. In semiconductor nanoclusters, where quantum confinement and excitonic effects are known to play an important role,<sup>4-9</sup> standard functionals tend to underestimate low-lying optical excitations.<sup>10</sup> Charge transfer (CT) is overestimated in transport<sup>11</sup> and the energy of long-range CT excitations is badly underestimated.<sup>12,13</sup> These problems are particularly severe as questions of CT play a decisive role in the efforts to tap new sources of energy by constructing artificial light-harvesting systems.

There is a close relation between these deficiencies and the self-interaction error of density functionals. Accurate response properties, e.g., polarizabilities of molecular chains, can be obtained with Kohn-Sham (KS) DFT using the exact exchange (EXX) functional.<sup>14</sup> Partial inclusion of exact exchange as, for example, in range-separated hybrid functionals improves CT excitations.<sup>15-19</sup> In the latter approaches, a careful adjustment of the range-separation parameter seems to be necessary for accurate results.<sup>20</sup> Tuning<sup>17,18</sup> instead of fitting can be a successful non-empirical way of determining the range-separation parameter. Unfortunately, the tuning procedure violates the size consistency requirement.<sup>21</sup>

Promising improvements of response properties<sup>22-24</sup> were also obtained with a Perdew-Zunger (PZ) self-

interaction correction (SIC).<sup>1</sup> In particular, when used within KS theory SIC polarizabilities were found to be very accurate.<sup>24</sup> Besides its appealing feature of being parameter free and non-empirical, PZ SIC fulfills important exact constraints on the xc energy functional as it is exact for one-electron densities and for uniform spin-densities. Moreover, PZ SIC includes full Hartree self-interaction correction. The potential of self-interaction corrected functionals shows the correct  $1/r$  asymptotic decay<sup>1,25</sup> and develops step-like structures that reflect particle number discontinuities.<sup>3,14,24,26-28</sup> The SIC approach leads to orbital functionals and therefore, when used in TDDFT, introduces an explicit dependence on the TD orbitals. Since the TD orbitals at time  $t$  depend on the entire history of the density  $n(\mathbf{r}, t')$  for  $t' \leq t$ ,<sup>29</sup> KS orbital functionals in principle contain so-called memory effects in a natural way.<sup>29-31</sup> The particle number discontinuity is crucial for the proper description of CT, and it has also been argued that memory effects play a role.<sup>11,13,29,32-34</sup> As both are in principle included in TD KS SIC, the latter is a promising candidate for curing the well-known deficiencies of TDDFT, while at the same time keeping a qualitatively correct description of many ground-state (GS) properties.<sup>35</sup>

In this paper, we demonstrate that TD SIC in the KS framework can noticeably improve the TDDFT based description of even difficult excitations. We first discuss the concept of GS SIC in Sec. II, followed by a description of TD SIC in Sec. III. Section IV presents real-time (RT) TDDFT calculations of absorption spectra. There, we also introduce an analysis tool based on the transition density that allows to analyze absorption spectra and to visualize the nature of electronic excitations. Section V A gives an overview of how the methods that were introduced before perform for the established test case of hydrogen chains. Finally, we report and discuss results obtained for typical real systems of different character: small metal particles in Sec. V B, semiconducting hydrogenated silicon clusters in Sec. V C,  $\pi$ -conjugated polyacetylene chains in Sec. V D, and molecular CT systems in Sec. V E. These

<sup>a)</sup>URL: <http://www.tp4.uni-bayreuth.de>.

results demonstrate that our SIC scheme shows appealing features, e.g., a TD field-counteracting behavior of the xc potential, and that it is able to correctly predict excitations that were considered too difficult for standard TDDFT.

## II. THE SELF-INTERACTION CORRECTION IN DENSITY FUNCTIONAL THEORY

### A. The self-interaction correction energy expression

In their seminal work, Perdew and Zunger<sup>1</sup> introduced a self-interaction correction where single orbital densities  $n_{j\sigma}(\mathbf{r}) = |\varphi_{j\sigma}(\mathbf{r})|^2$  of  $N_\sigma$  occupied orbitals  $\{\varphi_{j\sigma}(\mathbf{r})\}$  from a DFT single particle approach are interpreted to represent the  $N_\sigma$  electrons of the system. The idea of the correction is to subtract the energy of the interaction of every electron with itself from the xc energy of some xc functional approximation  $E_{xc}^{\text{app}}[n_\uparrow, n_\downarrow]$  according to

$$E_{xc}^{\text{SIC}}[n_\uparrow, n_\downarrow] = E_{xc}^{\text{app}}[n_\uparrow, n_\downarrow] - \sum_{\sigma=\uparrow,\downarrow} \sum_{j=1}^{N_\sigma} [E_{\text{H}}[n_{j\sigma}] + E_{xc}^{\text{app}}[n_{j\sigma}, 0]]. \quad (1)$$

Here,  $E_{\text{H}}$  is the classical Hartree energy and  $\sigma$  denotes the spin index.

This scheme has long been known, yet it has aspects that have rarely been discussed in the past. First, it has frequently been assumed that the SIC vanishes for the ultimate  $E_{xc}$ . However, the exchange-correlation energy is defined for GS densities, and these are typically smooth and nodeless. This is not necessarily true for orbital densities, which may exhibit complicated nodal structures. Therefore, the statement that the SIC of Eq. (1) vanishes for the ultimate xc functional implies the additional assumption that the orbital densities that are used in Eq. (1) are GS densities of some potential.

Second, one might wonder if the relation between orbital densities and electrons is a unique one. Indeed a peculiarity is built into the SIC energy functional as it is not invariant under unitary transformation of the orbitals. This means that starting from a given set of occupied orbitals, one can construct further orbital sets by unitary transformations that give the same density but result in different orbital densities. Different orbital densities, however, represent different identifications of orbitals with electrons and therefore yield different self-interaction corrections. Suggestions to solve this ‘‘unitary variance problem’’ emerged in the past and are based on two orbital sets<sup>35–42</sup> that take different roles:<sup>43</sup> The canonical orbital set  $\{\varphi_{j\sigma}(\mathbf{r})\}$  of  $N_\sigma$  occupied orbitals solves the single particle equations and a second orbital set  $\{\tilde{\varphi}_{j\sigma}(\mathbf{r})\}$  is used to set up the SIC xc energy (1) uniquely. By definition, both orbital sets give the same density and, therefore, are connected by a unitary transformation  $U_{ij}^\sigma$  according to

$$\tilde{\varphi}_{i\sigma}(\mathbf{r}) = \sum_{j=1}^{N_\sigma} U_{ij}^\sigma \varphi_{j\sigma}(\mathbf{r}). \quad (2)$$

We call such approaches generalized SIC (GSIC) schemes.

At first sight, the unitary variance of the SIC energy functional appears to be a weakness of the SIC approach. Yet, this

weakness can be turned into a strength in GSIC as the degrees of freedom of the unitary transformation provide means to include additional constraints into the energy functional. Exploiting this feature, promising improvements have been obtained in GS DFT.<sup>35–38,44</sup> In the present TDDFT context, we explain the idea of exploiting the unitary degrees of freedom in Sec. III B and then detail the approach with equations from Sec. III C throughout to Sec. III E.

Recent investigations of GSIC schemes<sup>45,46</sup> stress the importance of complex orbitals and unitary transformations in GS DFT. Therefore, throughout the paper we used real GS canonical orbitals without loss of generality, but complex TD canonical orbitals, complex unitary transformations, and complex orbitals  $\{\tilde{\varphi}_{j\sigma}\}$ .

### B. Local density approximation (LDA) vs generalized gradient approximation (GGA) SIC

As the SIC can, in principle, be applied to all xc functional approximations, the question arises on top of which approximate  $E_{xc}^{\text{app}}[n_\uparrow, n_\downarrow]$  SIC should be performed. Perdew and Zunger already advocated the use of the LDA as it is on average a good model for the xc hole and exactly satisfies the related sum rule.<sup>1,47</sup> The combination of GGAs with SIC using real orbitals in GS calculations has been reported to be doubtful.<sup>48</sup> The GS SIC applied to GGAs gives more promising results if complex orbitals and unitary transformations are taken into account.<sup>45,46</sup> Yet, the strong spatial variations of TD orbital densities may be ill suited for being combined with the gradient corrections that were derived for the much smoother GS total densities. Therefore, for the TD case that is of interest here we focus exclusively on self-interaction corrected LDA.

### C. Perdew-Zunger vs Kohn-Sham approach

The SIC xc energy expression depends explicitly on the orbitals and not on the density itself, i.e., it is an implicit density functional. Therefore, there are two options for choosing a single-particle scheme: first, the traditional PZ scheme, where one performs variations  $\delta/\delta\varphi_{i\sigma}^*(\mathbf{r})$  with respect to the canonical orbitals, and second, the KS scheme, where the functional derivative is performed with respect to the density, i.e.,  $\delta/\delta n(\mathbf{r})$ . The traditional scheme is close to Hartree-Fock theory in its variational ansatz and one ends up with orbital-specific potentials that can be computationally tedious. In contrast, the KS approach results in a local multiplicative potential, raising hopes that the approach is not as ‘‘Hartree-Fock like’’ as traditional PZ SIC.<sup>28</sup> Moreover, the KS approach has further advantages: it leads to Janak’s theorem,<sup>49</sup> exact KS eigenvalues are good approximations to relaxed vertical ionization potentials,<sup>50</sup> using a local potential has numerical advantages, and the local multiplicative potential allows for a transparent analysis of the response behavior and interpretability of orbitals and eigenvalues.<sup>44</sup> Yet, it must also be said that the construction of the local potential is not free from difficulties as it requires use of the optimized effective potential (OEP) method<sup>25,51</sup> or the generalized OEP (GOEP) formalism.<sup>35</sup>

### III. TIME-DEPENDENT KOHN-SHAM SELF-INTERACTION CORRECTION

#### A. Time-dependent optimized effective potential

Already in GS DFT determining the OEP is an involved procedure, and the TDOEP equation<sup>52</sup> is yet more demanding to solve.<sup>53,54</sup> One attempt at a solution scheme in RT was inspired by the GS concept of using the so-called orbital shifts.<sup>55</sup> With the help of these, the standard TDOEP equation can be transformed into a set of coupled partial-differential equations for the occupied TD KS orbitals and their corresponding TD orbital shifts. Yet, propagating the coupled equations showed numerical instabilities. A successful RT solution of the TDOEP equation was achieved in Ref. 54 by direct integration, but the calculation was restricted to a one-dimensional model problem. RT implementations of orbital functionals for more complex systems so far relied on the extension of the Krieger-Li-Iafrate (KLI) approximation<sup>56</sup> to the TD case.<sup>52,53</sup> The time-dependent KLI (TDKLI) potential, however, can be problematic in terms of stability,<sup>57</sup> as discussed in detail later.

#### B. Adiabatic interpretation of the time-dependent generalized self-interaction correction

Tong and Chu<sup>58,59</sup> already extended the GS SIC method to the TD (propagation) case. They used the SIC in an orbital-adiabatic sense with the SIC (KLI) potential derived from the GS SIC energy. However, as in the GS case, TD SIC suffers from not being invariant under unitary transformations. Moreover, the usual KLI approximation and particularly the SIC approach are well known for suffering from stability problems during time propagation<sup>57,60–62</sup> (see also the Appendix). The instability of the KLI approximation is a consequence of the KLI potential not being a functional derivative and the SIC functional not being unitarily invariant. In GS DFT, the generalized KLI (GKLI) approximation compares well to the full GOEP, whereas the standard KLI is a poor approximation to the standard OEP for SIC.<sup>35,63</sup> Therefore, it appears natural to treat the unitary variance problem in TD situations in analogy to the GS case, i.e., extend the GOEP approach of GS DFT to TDDFT by using the GS formalism at every instant of time.

With the GSIC approach, we use the degrees of freedom that are provided by the unitary transformation for increasing the propagation stability. The KLI propagation instability manifests itself, e.g., in energy variations that occur even when no external field is applied. Thus, during time propagation the system leaves the path of the lowest energy evolution. In the GS case, the unitary transformation helps to obtain the lowest energy configuration. In the same spirit, the unitary transformation can be exploited in TD situations to keep the system on a stable energy path during propagation. This approach is orbital-adiabatic in the same sense as the SIC functional is, if the definition of the unitary transformation at every instant of time depends on the orbitals at the same instant of time. Such definitions of the unitary transformation are discussed in Sec. III E.

#### C. Generalized time-dependent SIC potential

In this section, we recapitulate the time-dependent KLI approximation and introduce our generalization of the TDKLI scheme to deal with unitarily variant functionals. TD SIC calculations of the orbital-adiabatic kind<sup>10,58,59,64–66</sup> have been carried out successfully based on the TDKLI potential<sup>53,58,59</sup>

$$v_{xc\sigma}^{\text{TDKLI}}(\mathbf{r}, t) + f_{\sigma}(\mathbf{r}, t) = \frac{1}{2n_{\sigma}(\mathbf{r}, t)} \left\{ \sum_{j=1}^{N_{\sigma}} n_{j\sigma}(\mathbf{r}, t) [u_{xcj\sigma}(\mathbf{r}, t) + (\bar{v}_{xcj\sigma}^{\text{TDKLI}}(t) - \bar{u}_{xcj\sigma}(t))] \right\} + \text{c.c.}, \quad (3)$$

where

$$f_{\sigma}(\mathbf{r}, t) = -\frac{i}{4n_{\sigma}(\mathbf{r}, t)} \sum_{j=1}^{N_{\sigma}} \nabla^2 n_{j\sigma}(\mathbf{r}, t) \times \int_{-\infty}^t dt' (\bar{u}_{xcj\sigma}(t') - \bar{u}_{xcj\sigma}^*(t')) \quad (4)$$

and the orbital density averaged potentials are given by

$$\bar{v}_{xcj\sigma}^{\text{TDKLI}}(t) = \int d^3r \varphi_{j\sigma}^*(\mathbf{r}, t) v_{xc\sigma}^{\text{TDKLI}}(\mathbf{r}, t) \varphi_{j\sigma}(\mathbf{r}, t) \quad (5)$$

and

$$\bar{u}_{xcj\sigma}(t) = \int d^3r \varphi_{j\sigma}^*(\mathbf{r}, t) u_{xcj\sigma}(\mathbf{r}, t) \varphi_{j\sigma}(\mathbf{r}, t). \quad (6)$$

In the standard TDKLI approach to SIC, the orbital-specific potentials  $u_{xcj\sigma}$  equal the SIC potentials

$$v_{j\sigma}^{\text{SIC}}(\mathbf{r}, t) = \frac{\delta E_{xc}^{\text{SIC}}[\{n_{k\tau}\}]}{\delta n_{j\sigma}(\mathbf{r}, t)}. \quad (7)$$

The first term on the right-hand side of Eq. (3) plus its complex conjugate is commonly denoted as the Slater (SLA) approximation<sup>60–62,67,68</sup>

$$v_{xc\sigma}^{\text{TDSL A}}(\mathbf{r}, t) = \frac{1}{2n_{\sigma}(\mathbf{r}, t)} \times \sum_{j=1}^{N_{\sigma}} n_{j\sigma}(\mathbf{r}, t) [u_{xcj\sigma}(\mathbf{r}, t) + u_{xcj\sigma}^*(\mathbf{r}, t)] \quad (8)$$

to the TDOEP potential.

The central idea of the generalization in case of unitarily variant functionals is to replace the orbital-specific potentials  $u_{xcj\sigma}$  by the generalized orbital-specific potentials<sup>60,69</sup>

$$u_{xcj\sigma}^{\text{G}}(\mathbf{r}, t) = \frac{1}{\varphi_{j\sigma}^*(\mathbf{r}, t)} \sum_i^{N_{\sigma}} U_{ij}^{\sigma}(t) \tilde{\varphi}_{i\sigma}^*(\mathbf{r}, t) \tilde{v}_{i\sigma}^{\text{SIC}}(\mathbf{r}, t) \quad (9)$$

in the TDKLI Eq. (3), where

$$\tilde{v}_{i\sigma}^{\text{SIC}}(\mathbf{r}, t) = \frac{\delta E_{xc}^{\text{SIC}}[\{\tilde{n}_{k\tau}\}]}{\delta \tilde{n}_{i\sigma}(\mathbf{r}, t)} \quad (10)$$

using the orbital densities  $\{\tilde{n}_{k\tau}(\mathbf{r}, t)\}$ . The generalized orbital-specific potentials of Eq. (9) are known from GS GOEP, but need to be evaluated with TD orbitals here. Moreover, in the

generalized TD approach the transformation  $U_{ij}^\sigma(t)$  turns into a TD function that connects the two orbital sets according to

$$\tilde{\varphi}_{i\sigma}(\mathbf{r}, t) = \sum_{j=1}^{N_\sigma} U_{ij}^\sigma(t) \varphi_{j\sigma}(\mathbf{r}, t). \quad (11)$$

In summary, Eq. (3) together with Eqs. (9) and (11) constitute our TD SIC GKLI (TDGKLI) scheme. A generalized Slater (GSLA) approximation<sup>60</sup> is introduced by substituting  $u_{xcj\sigma}^G$  into Eq. (8).

## D. Memory contributions in the time-dependent potential

The function  $f_\sigma(\mathbf{r}, t)$  of Eq. (4) depends on the full history of  $\bar{u}_{xcj\sigma}(t')$ , i.e., on all times  $t' \leq t$  and therefore introduces a memory dependence into the TDKLI scheme. Yet, for a large class of xc functionals, where the orbital dependence appears only via combinations  $\varphi_{j\sigma}^*(\mathbf{r}, t) \varphi_{j\sigma}(\mathbf{r}', t)$ , as, e.g., in the EXX and the SIC functional, this memory dependence vanishes.<sup>30,52,53,58,59</sup> It should be kept in mind, though, that a memory dependence in terms of the density  $n(\mathbf{r}, t')$  remains due to the use of the KS orbitals<sup>29–31</sup> in the TD SIC KLI potential, as stated in Sec. I.

However, one peculiarity occurs in TDGKLI: It is not clear from the start that the memory dependence in the TDKLI of Eqs. (3) and (4) vanishes. The use of the second orbital set in the GSIC scheme introduces a mixing of KS orbitals via the unitary transformation of Eq. (9) and; therefore, the previous argument using orbital combinations  $\varphi_{j\sigma}^*(\mathbf{r}, t) \varphi_{j\sigma}(\mathbf{r}', t)$  does not hold. Thus, the explicit memory contribution survives in the TDGKLI and Eq. (4) gives

$$f_\sigma(\mathbf{r}, t) = -\frac{1}{2n_\sigma(\mathbf{r}, t)} \sum_{j=1}^{N_\sigma} \nabla^2 n_{j\sigma}(\mathbf{r}, t) \int_{-\infty}^t dt' \int d^3r' \times \text{Im} \left( \varphi_{j\sigma}(\mathbf{r}', t') \sum_{k=1}^{N_\sigma} U_{kj}^\sigma(t') \tilde{\varphi}_{k\sigma}^*(\mathbf{r}', t') \tilde{v}_{k\sigma}^{\text{SIC}}(\mathbf{r}', t') \right). \quad (12)$$

## E. Definitions of the unitary transformation

In order to complete the TD GSIC scheme, we need to specify how the unitary transformation is defined during the time evolution. In the following, we discuss and classify several possibilities.

### 1. Energy-minimization criterion

To pinpoint the unitary transformation in GS DFT, Pederson *et al.*<sup>36–38</sup> suggested energy minimization of the total energy  $E^{\text{tot}}$  with respect to changes of  $U_{ij}^\sigma$ . This criterion leads to the set of equations

$$\langle \tilde{\varphi}_{i\sigma}(\mathbf{r}) | \tilde{v}_{i\sigma}^{\text{SIC}}(\mathbf{r}) - \tilde{v}_{j\sigma}^{\text{SIC}}(\mathbf{r}) | \tilde{\varphi}_{j\sigma}(\mathbf{r}) \rangle = 0 \quad (13)$$

for all  $i$  and  $j$  of occupied orbitals.<sup>36,46</sup> The equations are fulfilled only when the SIC energy is minimized. The very same criterion was also introduced as a symmetry condition in a recent implementation of original PZ SIC with orbital-specific

potentials.<sup>41,42</sup> The strategy of Pederson *et al.* can also be applied in KS DFT.<sup>35,43,60</sup> The idea is to find an orbital set  $\{\tilde{\varphi}_{j\sigma}(\mathbf{r})\}$  and the corresponding unitary transformation that leaves the density unchanged, minimizes the energy, and determines the xc potential. Orbitals  $\{\tilde{\varphi}_{j\sigma}\}$  obtained from the Pederson criterion are called energy-minimizing orbitals.

As we intend to support variational stability by a suitable choice of the TD unitary transformation it appears natural to fix  $U_{ij}^\sigma(t)$  by an extension of the Pederson energy-minimization criterion to the TD case, i.e.,

$$\langle \tilde{\varphi}_{i\sigma}(\mathbf{r}, t) | \tilde{v}_{i\sigma}^{\text{SIC}}(\mathbf{r}, t) - \tilde{v}_{j\sigma}^{\text{SIC}}(\mathbf{r}, t) | \tilde{\varphi}_{j\sigma}(\mathbf{r}, t) \rangle = 0 \quad (14)$$

for all  $i$  and  $j$  of occupied orbitals and all times  $t$ .<sup>69</sup> With this choice, the total energy  $E^{\text{tot}}(t)$  is minimized at every instant of time in the spirit of the orbital-adiabatic TD SIC approach, cf. Sec. III B. In the following, we name this SIC propagation scheme with energy minimization at every instant of time ‘‘GKLI.’’

The energy-minimization criterion has an interesting influence on the memory term of the TDGKLI potential.<sup>60</sup> With Eq. (14) the memory term vanishes. To demonstrate this explicitly, we start from Eq. (4) and calculate the difference

$$\bar{u}_{xcj\sigma}^G(t') - \bar{u}_{xcj\sigma}^{G*}(t') = \langle \varphi_{j\sigma}(\mathbf{r}, t') | u_{xcj\sigma}^G(\mathbf{r}, t') - u_{xcj\sigma}^{G*}(\mathbf{r}, t') | \varphi_{j\sigma}(\mathbf{r}, t') \rangle \quad (15)$$

using definition (6). Then, insert the orbital-specific potentials of Eq. (9), replace all KS orbitals by

$$\varphi_{j\sigma}(\mathbf{r}, t) = \sum_{i=1}^{N_\sigma} U_{ij}^\sigma(t) \tilde{\varphi}_{i\sigma}(\mathbf{r}, t), \quad (16)$$

and obtain

$$\begin{aligned} \bar{u}_{xcj\sigma}^G(t') - \bar{u}_{xcj\sigma}^{G*}(t') &= \sum_{k=1}^{N_\sigma} \sum_{i=1}^{N_\sigma} (U_{ij}^{\sigma*}(t') U_{kj}^\sigma(t') \langle \tilde{\varphi}_{k\sigma}(\mathbf{r}, t') | \tilde{v}_{k\sigma}^{\text{SIC}}(\mathbf{r}, t') | \tilde{\varphi}_{i\sigma}(\mathbf{r}, t') \rangle \\ &\quad - U_{ij}^\sigma(t') U_{kj}^{\sigma*}(t') \langle \tilde{\varphi}_{i\sigma}(\mathbf{r}, t') | \tilde{v}_{k\sigma}^{\text{SIC}}(\mathbf{r}, t') | \tilde{\varphi}_{k\sigma}(\mathbf{r}, t') \rangle). \end{aligned} \quad (17)$$

By switching indices  $i$  and  $k$  of the second term, we find

$$\begin{aligned} \bar{u}_{xcj\sigma}^G(t') - \bar{u}_{xcj\sigma}^{G*}(t') &= \sum_{k=1}^{N_\sigma} \sum_{i=1}^{N_\sigma} U_{ij}^{\sigma*}(t') U_{kj}^\sigma(t') \langle \tilde{\varphi}_{k\sigma}(\mathbf{r}, t') | \tilde{v}_{k\sigma}^{\text{SIC}}(\mathbf{r}, t') \\ &\quad - \tilde{v}_{i\sigma}^{\text{SIC}}(\mathbf{r}, t') | \tilde{\varphi}_{i\sigma}(\mathbf{r}, t') \rangle. \end{aligned} \quad (18)$$

If the Pederson criterion is fulfilled for all times, Eq. (18) vanishes and with it the memory dependence. Thus, starting from a consistent energy-minimizing GSIC GS, the Pederson criterion and related memory dependencies vanish from the initial time on.

For ensuring that the memory contribution vanishes, it is essential to converge the energy-minimization condition (14) below a threshold chosen so small that the remaining deviations from zero are of no physical and numerical relevance. Yet, already in GS calculations optimization of the Pederson criterion requires notable numerical effort.<sup>36,42,70</sup> In the TD

case, high quality of  $U_{ij}^\sigma(t)$  is required to keep the propagation in the variationally stable regime and Eq. (14) must be fulfilled at each time step for a total time of ca. 40 fs. A time evolution of this length is required for obtaining a reasonable spectral resolution after Fourier transformation of the TD dipole signal.

In order to reduce the computational effort for determining the unitary transformation in the TD case we developed a special scheme.<sup>69</sup> The unitary transformation can be determined notably more efficiently during propagation when we use

$$U_{ij}^\sigma(t) = e^{i\varepsilon_j \Delta t} U_{ij}^\sigma(t - \Delta t) \quad (19)$$

as an initial guess for the numerical unitary optimization. (The numerical optimization is discussed below.) This initial guess takes the transformation from the previous time step  $U_{ij}^\sigma(t - \Delta t)$  and phase factors with the KS eigenvalues  $\varepsilon_j$  into account. The choice is motivated by considering a time propagation of the GS orbitals without external perturbation: For this case, Eq. (19) provides the exact transformation. Or, stated the other way round: If one would fix the GS unitary transformation and would not take the phase factors into account in  $U_{ij}^\sigma(t)$  when propagating, then the orbitals  $\{\tilde{\varphi}_{j\sigma}\}$  would change immediately. This would lead to spurious changes of the xc potential and therefore to deviations from the GS. As a consequence, spurious self-excitation and propagation instability would occur.

## 2. Foster-Boys localization scheme

Alternatives to the energy-minimization condition can be obtained by using other definitions for  $U_{ij}^\sigma(t)$  than Eq. (14). It is known from the GS GOEP approach that spatial localization according to Foster and Boys<sup>71,72</sup> (FOBO) is numerically less expensive, but close to real-valued energy-minimizing transformations.<sup>35,46</sup> Therefore, we introduce FOBO localization in the generalized TD SIC approach. The Foster-Boys criterion<sup>62,73</sup> measures the spatial extent of the localizing or FOBO orbitals. In analogy to the energy-minimization case, we enforce the FOBO criterion at each time step of the propagation starting from a SIC GS with FOBO localization. In the FOBO scheme, the TDGKLI memory contribution does not vanish as explained before. Moreover, already in the GS the FOBO orbitals do not fulfill the Pederson criterion and thus even at the initial time the contribution of the memory term is unclear as the time integral in the memory term starts at minus infinity. Therefore, we define the FOBO propagation scheme such that we set  $f_\sigma(\mathbf{r}, t) = 0$ . The initial guess of Eq. (19) can again be used. Thus, the abbreviation FOBO in the following refers to a (TD)GKLI propagation with Foster-Boys localization in the GS and at every instant of time, and  $f_\sigma(\mathbf{r}, t) = 0$ .

## 3. Fixed phase factor approximation

Equation (19) can serve as the basis for yet another TD SIC scheme. Starting from an energy-minimizing GS transformation, one can use Eq. (19) without subsequent unitary optimization to define  $U_{ij}^\sigma(t)$ . We call this approach the fixed

phase factor TD transformation approximation (GKLI<sup>pf</sup>). It is motivated by the hope that in the linear response regime the KS orbitals and potential may stay close to their respective GS values, except for trivial phase factors in the orbitals. Therefore, the unitary transformation of Eq. (19) may yield a TD transformation close to the true energy-minimizing transformation. As linear order changes of the KS orbitals lead to linear order changes in the potential, and as higher order effects due to  $U_{ij}^\sigma(t)$  are excluded, the phase factor TD transformation may be seen as a linear response approximation to the true energy-minimizing transformation. However, since the memory contribution again does not vanish, one has to make a choice. Either one takes the memory term into account by time integration of Eq. (12), or one neglects the memory contribution completely. We discuss differences between the two options in the Appendix but mostly focus on the  $f_\sigma(\mathbf{r}, t) = 0$  scheme.

## 4. Discussion

From a theoretical point of view using the energy-minimizing  $U_{ij}^\sigma(t)$  at every time step appears as the most rigorous of the various schemes for several reasons. First, it is consistent with the energy-minimizing GS. Second, it follows the lines of the orbital-adiabatic definition and thus hopefully leads to propagation along a stable minimal energy path. Third, the memory contribution vanishes and, therefore, the history of the orbital-specific potentials  $u_{xcj\sigma}^G(\mathbf{r}, t)$  does not need to be calculated. From this perspective, the FOBO and the GKLI<sup>pf</sup> schemes appear as approximations to the energy-minimizing TDGKLI that are motivated by their lower computational costs. However, the practical performance of the different schemes needs to be investigated. Therefore, we assess the different approaches in Sec. V.

## IV. ANALYZING THE REAL-TIME RESPONSE

### A. Time-dependent self-interaction correction propagation scheme

One of the most important applications of TDDFT is the determination of optical excitation spectra. In RT TDDFT, one calculates dipole spectra from the Fourier transformation of the TD dipole moment.<sup>74,75</sup> To determine the dipole moment time evolution, we propagate the KS system after an initial boost excitation within the linear response regime. The GSIC propagation scheme for such calculations based on two orbital sets is implemented in the Bayreuth version<sup>76,77</sup> of the PARSEC program package.<sup>78</sup> In our approach, the following steps have to be taken at each time step: (i) propagate the KS orbitals a finite time step  $\Delta t$  using the KS potential of the previous time step, (ii) determine the unitary transformation according to Eq. (14), (iii) calculate the new potential using Eq. (3) together with Eqs. (9) and (12). This general propagation scheme can be refined by propagation techniques explained in Ref. 79. We employ a fourth-order Taylor expansion combined with the exponential midpoint rule,<sup>76,77</sup> where the potential needs to be determined twice per time step. The unitary optimization of the Pederson criterion

can be performed iteratively and we implemented algorithms of Fois *et al.*,<sup>80</sup> Messud *et al.*,<sup>42</sup> and Abrudan *et al.*<sup>81</sup> Whereas first GSIC propagations<sup>69</sup> used the former two approaches, we now obtain the best performance with the algorithm of Abrudan *et al.*,<sup>81</sup> based on minimizing the SIC energy contribution via conjugate gradients and a line search for gradient step-size optimization (for more details, see Ref. 46). For the FOBO unitary optimization, we use the same algorithm tailored to the FOBO criterion.<sup>46</sup>

The stability of propagation schemes using the TDKLI potential has been a topic of debate as the occurrence of instabilities is well known in the particularly difficult case of Na<sub>5</sub>.<sup>57,60–62</sup> We find that our GSIC propagation scheme using the TDGKLI approximations improves upon this drawback of the standard TDKLI.<sup>60,69</sup> We discuss the stability issue for the special case of Na<sub>5</sub> in the Appendix. For all other systems studied here, no notable instability occurs on the relevant time scales. Summarizing our experience from a practical point of view we can state that a time evolution of about 40 fs is needed for a reasonable spectral resolution of ca. 0.1 eV. Generally speaking, all GSIC variants remain remarkably stable during propagation within this time range if the numerical parameters are chosen reasonably. This distinguishes the TD GKLI approaches from standard TDKLI for which we could not calculate a clean spectrum in some cases.

## B. Transition density diagnostic tool

When a system's response is calculated from the analytically linearized TDDFT equations,<sup>82</sup> one readily obtains the decomposition of each excitation into occupied to unoccupied orbital transitions. Analysis of these orbital transitions and their associated weighting factors gives insight into the nature of an excitation, helping, e.g., in identifying CT excitations. In principle, the same information is available in the RT propagation and could be extracted from the explicitly TD orbitals. However, the technical and computational effort to do so is non-negligible. Therefore, we here introduce a relatively easy to implement RT evaluation tool that also allows to explore the nature of excitations. It is based on the transition density, which is directly related to the TD density and thus well defined in the framework of TDDFT.<sup>83–85</sup>

We exemplify this idea with the 4-(*N,N*-dimethylamino)benzoni- trile (DMABN) (Refs. 86, 87, and 88) adiabatic TD LDA dipole power spectrum<sup>76,89–91</sup> shown in Fig. 1, where we used the geometry of Ref. 88. The transition density  $\rho_\omega(\mathbf{r})$  corresponding to an excitation at frequency  $\omega$  is proportional to the negative of the imaginary part of the Fourier transformation  $\delta n(\mathbf{r}, \omega)$  of the TD density fluctuations  $\delta n(\mathbf{r}, t) = n(\mathbf{r}, t) - n(\mathbf{r}, 0)$ ,<sup>84,85</sup> i.e.,

$$\rho_\omega(\mathbf{r}) \propto -\text{Im}\{\delta n(\mathbf{r}, \omega)\}. \quad (20)$$

Thus, it can be calculated readily from RT propagation and is depicted in the right part of Fig. 1 for the two lowest excitations of DMABN, which are at 3.9 eV and 4.2 eV with the TD LDA. We calculated the Fourier transformation step by step during time propagation for preset frequencies. The obtained transition densities are a fingerprint of the corresponding excitation.

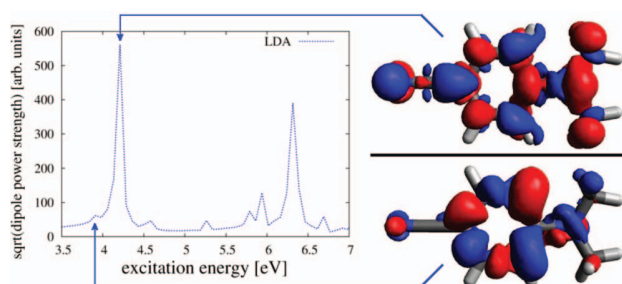


FIG. 1. DMABN spectrum and transition densities from density propagation.

The transition density can alternatively be calculated as the weighted sum of occupied and unoccupied orbital products<sup>84</sup>

$$\rho_\omega(\mathbf{r}) \propto \sum_i^{\text{occup.}} \sum_j^{\text{unoccup.}} a_{ij}^\omega \varphi_i(\mathbf{r}) \varphi_j^*(\mathbf{r}) \quad (21)$$

with weighting factors  $a_{ij}^\omega$ . In the DMABN system, the character of the excitations is well described by (semi)local xc functionals and well known to be dominated by transitions from one occupied to one unoccupied orbital.<sup>87</sup> One of the low lying transitions is understood to be a highest occupied molecular orbital (HOMO) to lowest unoccupied molecular orbital (LUMO) transition, whereas the other excitation is dominantly of HOMO to LUMO+1 character. The corresponding orbital products are shown in Fig. 2.

Comparing the transition densities from RT propagation and the ones calculated from orbital products clearly shows

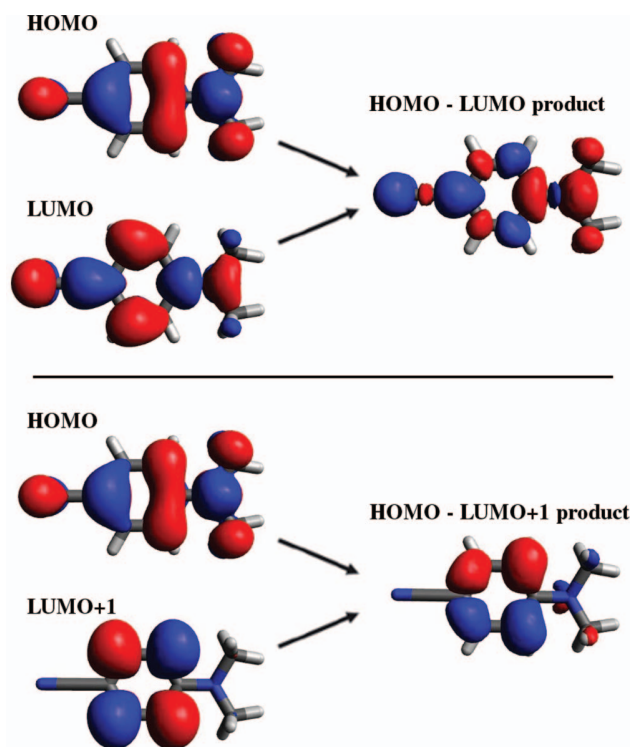


FIG. 2. Orbital products calculated from LDA GS orbitals of the DMABN molecule.

that the excitation at 3.9 eV is of HOMO to LUMO+1 and the excitation at 4.2 eV of HOMO to LUMO type. In the DMABN system, the HOMO-LUMO+1 excitation has been characterized as being local and the HOMO-LUMO excitation as short-range CT.<sup>87,88</sup>

Close inspection reveals that especially in the 3.9 eV excitation case the agreement between the HOMO-LUMO+1 product and the transition density from RT density evolution is not perfect. There are at least two possible explanations for this finding. A first technical aspect is related to the resolution of the Fourier transformation: It is limited by the length of the numerical density time evolution. Here, the two peaks are energetically very close and, therefore, the signal of the lower peak at 3.9 eV may be “contaminated” by the response of the close lying higher peak at 4.2 eV. Second, from a physical point of view, the transition is not necessarily of pure “one occupied to one unoccupied orbital” character. However, even with these small differences, the signal is clear enough to unambiguously distinguish between the two excitations.

In an attempt to allow for an objective transition density comparison that goes beyond “visual inspection” we introduce quantitative criteria. As the transition density carries information about the oscillator strength and, therefore, cannot be normalized easily, we suggest two different comparison criteria. First, we define

$$\kappa_1 = \frac{\int d^3r \rho_{\omega_1} \rho_{\omega_2}}{\int d^3r |\rho_{\omega_1} \rho_{\omega_2}|} \quad (22)$$

as a criterion that is not sensitive to the proportionality factors of Eqs. (20) and (21) but analyzes the spatial pattern of the corresponding transition densities. It varies between  $-1 < \kappa_1 < 1$  and takes its maximum value  $\kappa_1 = 1$  only if the spatial structure of the transition densities  $\rho_{\omega_1}$  and  $\rho_{\omega_2}$  is equal. Note that proportionality factors do not affect the fingerprint pattern but influence the absolute values. However, absolute values of transition densities would be influenced by the excitation process and are not our aim here anyhow as we do not calculate the weighting factors of Eq. (21). Instead we rely on the fact that in the cases that we study here the transition density is always dominated by a single occupied to unoccupied transition.

As a second comparison criterion, we use

$$\kappa_2 = \int d^3r |\rho_{\omega_1} \rho_{\omega_2}|, \quad (23)$$

which measures the absolute overlap of transition densities. The  $\kappa_2$ -value is useful for comparisons in which one transition density is fixed and one would like to compare this transition density to several others that have all been calculated by the same method. For example, one may want to test which of several TD transition densities that have all been obtained by the same excitation process is closest to a certain product of GS orbitals.

As an example Table I lists  $\kappa_1$  and  $\kappa_2$  for several DMABN excitations. The  $\kappa_1$  criterion confirms the transition density correspondence that we had found before by looking at transition density iso-surface plots. Corresponding transition densities show a  $\kappa_1$  greater than 0.9, whereas non-corresponding transition densities show  $\kappa_1$  lower than 0.6.

TABLE I. Quantitative transition density comparison for DMABN molecule excitations using the criteria  $\kappa_1$  of Eq. (22) and  $\kappa_2$  of Eq. (23). Labels TD followed by an excitation energy denote transition densities obtained from RT propagation (Eq. (20)), whereas labels GS followed by letters H, L, etc., denote transition densities calculated as a GS orbital product. H stands for HOMO and L for LUMO.

$\rho_{\omega_1}$	$\rho_{\omega_2}$	$\kappa_1$	$\kappa_2 (\times 10^{-5})$
TD 3.93 eV	GS H-L+1	0.91044	0.5582
TD 4.21 eV	GS H-L	0.92061	4.6795
TD 3.93 eV	GS H-L	0.57421	0.4739
TD 4.21 eV	GS H-L+1	-0.03861	1.4217
GS H-L	GS H-L+1	-0.01571	0.1601
TD 3.93 eV	TD 4.21 eV	0.59535	3.6365

The  $\kappa_1$  values of almost 0.6 that are seen in Table I are in line with the previously made argument that the excitations at 3.93 eV and 4.21 eV show some similarity. Yet, the difference between  $\kappa_1 = 0.6$  and  $\kappa_1 = 0.9$  is noticeable enough to allow for a clear identification of the corresponding transitions. We also see that the HOMO-LUMO and the HOMO-LUMO+1 orbital products are clearly identified as being dissimilar with a  $\kappa_1$  of less than 0.02.

Table I further shows why the bare  $\kappa_2$  criterion is limited in its predictive power:  $\kappa_2$  exhibits the same picture as  $\kappa_1$  when comparing the GS HOMO-LUMO transition density to the TD transition densities, but it fails when comparing the GS HOMO-LUMO+1 to the TD transition densities. The reason for this failure is the notably higher signal strength of the TD transition density at 4.21 eV that leads to a greater total overlap with the HOMO-LUMO+1 transition density, although the spatial structure is obviously different. Nevertheless, in cases of consistent excitation processes, similar signal strength, and similar  $\kappa_1$  values,  $\kappa_2$  can help to clarify complicated situations. One example of this kind is discussed in Sec. V E. Consequently, in the following we base our investigations on  $\kappa_1$  and use  $\kappa_2$  only if  $\kappa_1$  alone does not give a clear picture.

## V. RESULTS AND DISCUSSION

In the following, we apply the methods introduced so far to study different systems: on the one hand systems that allow for transparently analyzing the response and xc effects, on the other hand systems that are practically relevant and known to be challenging for TDDFT. We first investigate hydrogen chains and assess response features of SIC and GSIC in TD situations. Then, we address real systems that are paradigm examples for different types of excitations: metal clusters with a comparatively homogeneous density and “collective” excitations, semiconductor clusters that exhibit effects that were classified as excitonic, oligo-acetylene chains with extended  $\pi$ -conjugation, and molecular chromophores with CT excitations.

### A. Dynamical effects in hydrogen chains

We first investigate the SIC and GSIC TD response of hydrogen chains with alternating H-distances of 2 bohrs and 3

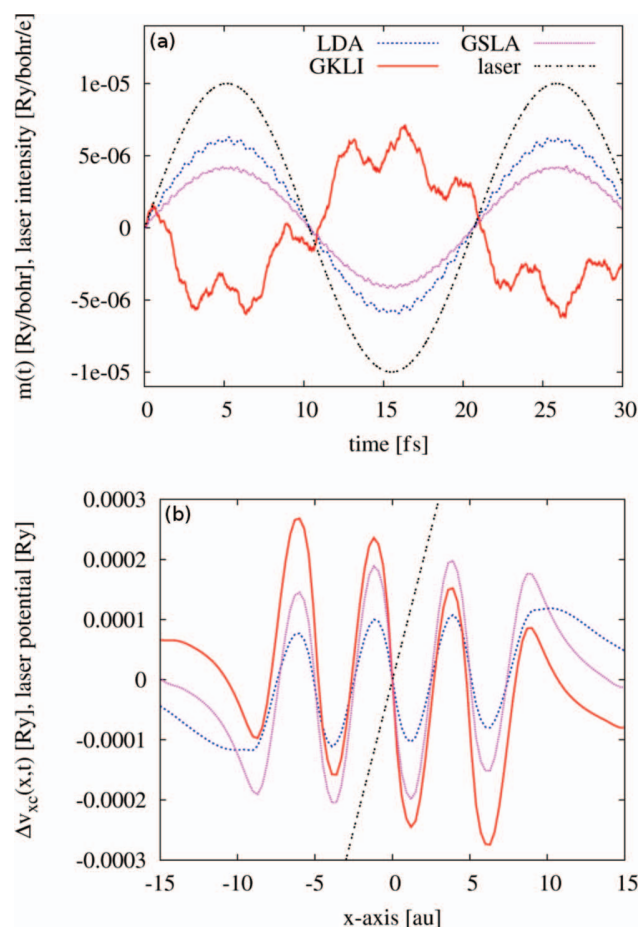


FIG. 3. (a) Slope  $m(t)$  of  $\Delta v_{xc}(x, t)$  for an electrical field (“laser”) excitation of frequency  $0.2 \text{ eV}/\hbar$  for LDA, GKLI, and GS LA. The field was scaled by a factor of 0.1 for the plot. (b) Corresponding snapshot of  $\Delta v_{xc}(x, t)$  along the H8 chain ( $x$ -direction) at the first maximum of the field at 5.2 fs.

bohrs.<sup>89–91</sup> Such chains have frequently been studied in GS DFT (Refs. 3, 14, 22–24, 28, and 92–97) and it has been shown that a field-counteracting term in the xc potential is decisive for the description of static response properties such as polarizabilities.<sup>3, 14, 24, 97</sup> Therefore, we are now interested in such spatial structures in the dynamical response. We study the linear TD response by applying an external sinusoidal electrical field of  $10^{-4} \text{ Ry/bohr/e}$  with different frequencies. The field is along the backbone of a H8 chain. For a transparent analysis, we need to reduce the data of  $v_{xc}(\mathbf{r}, t)$  to a manageable amount. Therefore, for each instant of time, we compute the slope  $m(t)$  of the difference

$$\Delta v_{xc}(x, t) = v_{xc}(x, t) - v_{xc}(x, 0) \quad (24)$$

by least squares linear regression along the H8 backbone ( $x$ -direction). Figure 3(a) shows the result obtained for an excitation of frequency  $0.2 \text{ eV}/\hbar$  and different xc potential approximations. The bottom panel shows snapshots of  $\Delta v_{xc}(x, t)$  at the first maximum of the field at 5.2 fs. The slope  $m(t)$  clearly reveals the general trend of the potential’s response to the external perturbation. For the low frequency excitation studied here the TD LDA and GS LA potentials unambiguously follow the external field, while the TD GKLI potential shows a

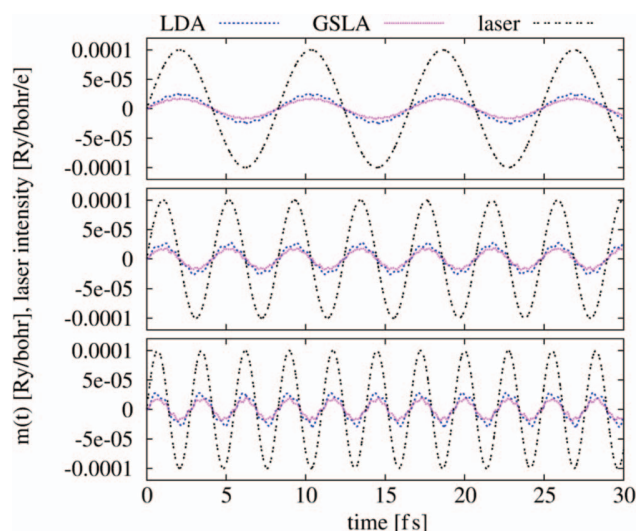


FIG. 4. Slope  $m(t)$  of  $\Delta v_{xc}(x, t)$  of the LDA and GS LA potential together with the electrical field amplitude for different excitation frequencies:  $0.5 \text{ eV}/\hbar$  (upper panel),  $1.0 \text{ eV}/\hbar$  (middle panel), and  $1.5 \text{ eV}/\hbar$  (lower panel).

field-counteracting behavior, in analogy to the GS case. The snapshots in Fig. 3(b) confirm this finding.

Analysis of the frequency dependence of the response of the xc potential reveals that the LDA and GS LA xc potentials follow the external potential also at higher frequencies. We exemplify this finding for frequencies of  $0.5 \text{ eV}/\hbar$ ,  $1.0 \text{ eV}/\hbar$ , and  $1.5 \text{ eV}/\hbar$  in Fig. 4. Yet, the GKLI response changes notably at higher excitation frequencies (see Fig. 5): While at low frequencies the GKLI xc potential clearly works against the external field, the response structure develops complicated features at higher frequencies. For the  $1.0 \text{ eV}$  excitation for instance, the GKLI potential is no longer in phase with the external potential and the slope of  $\Delta v_{xc}(x, t)$  increases notably in time. At  $1.5 \text{ eV}$   $v_{xc}^{\text{GKLI}}(\mathbf{r}, t)$  seems to work with the external

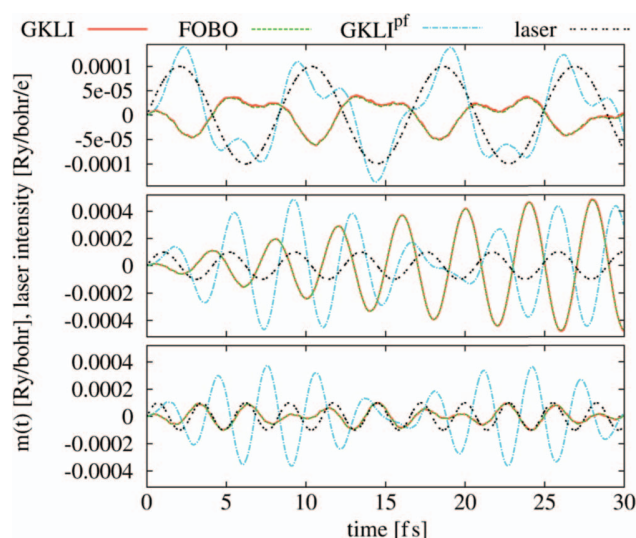


FIG. 5. Slope  $m(t)$  of  $\Delta v_{xc}(x, t)$  of the GKLI, the FOBO, and the GKLI<sup>pf</sup> potential together with the electrical field amplitude for different excitation frequencies as in Fig. 4.  $m(t)$  is almost identical for the GKLI and FOBO response.

field and is, apart from minor deviations, in phase with the external perturbation.

Figure 5 also demonstrates that the field-counteracting behavior at low frequencies is lost if one applies the fixed phase factor TD transformation approximation of Sec. III E 3: In the first quarter cycle of the external field  $\text{GKLI}^{\text{pf}}$  always works with the field for all excitation frequencies considered here. At low frequencies, also the overall trend of the xc potential response follows the external perturbation. At higher frequencies it develops complicated structures with phase shifts and elevated amplitude.

Using FOBO localization during the propagation at every instant of time does not spoil the field-counteracting trend of GKLI at low frequencies. Even at higher excitation frequencies, the overall trend of the FOBO potential is very similar to the GKLI one (see Fig. 5). Yet, analysis of the FOBO potential along the chain axis at single time steps reveals differences in the details of the potential response compared to the GKLI. FOBO localization implemented with fixed phase factors does not show the favorable behavior of the full TD FOBO scheme and, therefore, is not investigated further in the following.

Also the standard KLI potential shows a field-counteracting behavior during propagation at low frequencies. However, we did not investigate KLI in detail as the propagation had serious stability problems<sup>57</sup> already after 15 fs (see also the Appendix).

We believe that the field-counteracting behavior is an important feature of the xc potential and necessary for a proper description of response properties especially in situations where the density distribution changes notably, as it is the case in CT. Without the field-counteracting term response properties will be overestimated and CT will be too easy. The analysis in this section reveals that two features of the potential are important for the proper response: (i) The potential needs to include the response term that makes the difference between KLI and SLA. (ii) The unitary transformation criterion has to be enforced at every instant of time. As the GKLI with an energy-minimizing transformation at each time step is a well defined scheme that fulfills these criteria, we regard the GKLI approach as the best justified and most trustworthy (G)SIC implementation in TDDFT. Our investigations on hydrogen chains reveal that FOBO localization applied at every instant of time is a promising alternative to the energy minimization as it is computationally less expensive and close to the GKLI performance. Therefore, FOBO needs to be investigated further in the following.

We now turn to the determination of the lowest excitation energy of short hydrogen chains. The results are reported in Table II and can be categorized into three groups: First, the LDA numbers which confirm TD LDA's known trend to underestimate excitation energies in confined chain like systems.<sup>99</sup> Second, the KLI results that show an erroneous downward shift of about 0.3 eV to 0.5 eV with respect to the LDA excitation energies. We had to estimate many of the KLI excitation energies from a relatively short time propagation due to early onset of propagation instability. Third, all generalized SIC schemes which correct the LDA result towards higher energies by about 0.3 eV to 0.5 eV. There is a small

TABLE II. Lowest excitation energy of hydrogen chains with alternating H atom distances of 2 bohrs and 3 bohrs. Listed are results for LDA, KLI, and GKLI as well as for three approximations to the GKLI: FOBO, GSLA, and  $\text{GKLI}^{\text{pf}}$ . B3LYP and CC2 excitation energies are given as a reference.<sup>a</sup>

	LDA	KLI	GKLI	FOBO	GSLA	$\text{GKLI}^{\text{pf}}$	B3LYP	CC2
H <sub>4</sub>	7.70	7.45	8.30	8.25	8.30	8.35	8.36	9.26
H <sub>6</sub>	6.75	6.4 <sup>a</sup>	7.10	7.05	7.10	7.10	7.33	8.47
H <sub>8</sub>	6.00	5.5 <sup>a</sup>	6.35	6.30	6.35	6.40	6.70	8.00
H <sub>10</sub>	5.50	5.1 <sup>a</sup>	5.85	5.85	5.85	5.90	6.29	7.70
H <sub>12</sub>	5.15	4.8 <sup>a</sup>	5.60	5.50	5.55	5.60	6.01	7.50

<sup>a</sup>Numbers are estimated from a time evolution of notably less than 40 fs as obvious propagation instability occurred already within this time span.

trend of rising excitation energies from FOBO via GKLI and GSLA to  $\text{GKLI}^{\text{pf}}$ , but overall all GSIC energies are similar. In view of the earlier observed differences between the different GSIC schemes the similarity of the results here may come as a surprise. However, the similarity is explained by the special nature of the excitation that we study here. It is build from local contributions on each of the H<sub>2</sub> segments and has almost no component of CT from one H<sub>2</sub> unit to the next. Thus, the situation is notably different from the previous case where the TD external field could generate a charge flow along the chain's backbone.

To finally assess our GSIC schemes in comparison to other methods, we computed Becke three-parameter Lee-Yang-Parr hybrid functional (B3LYP) and approximate coupled-cluster singles-and-doubles model (CC2) (Ref. 98) excitation energies with TURBOMOLE (Refs. 100 and 101) using Gaussian basis sets of quadruple zeta valance quality (def2-QZVP).<sup>102</sup> We find that B3LYP gives higher excitation energies than GSIC with differences between B3LYP and GSIC on the order of about 0.3 eV. However, B3LYP and all GSIC schemes are off the CC2 numbers by at least 0.9 eV with rising deviation for larger chains. Although we are aware of possible deviations between CC2 and higher level reference calculations,<sup>103</sup> we interpret this finding as being in line with earlier observations of the peculiar nature of the hydrogen chains. Already in earlier works it has been observed, e.g., that current DFT taking ultranonical xc effects into account leads to large improvements for real conjugated polymers, whereas in hydrogen chain models the improvements are small.<sup>104</sup> Moreover, in hydrogen chains only full OEP SIC gives polarizabilities close to the coupled-cluster reference while one observes notable differences between GKLI and full OEP.<sup>28</sup> Thus, although hydrogen chains are a transparent test system, they are only a limited indicator for functional performance in realistic situations for true molecules and solids. Therefore, we draw two conclusions from the hydrogen chain tests. First, due to the favorable features that the GKLI  $v_{\text{xc}}$  showed for the hydrogen chains, hopes are high that GKLI may also describe real molecules well. Second, however, we are aware of the limitations of the hydrogen chain test and, therefore, have to assess the trustworthiness of GKLI thoroughly for real molecules. This is what we do in Secs. V B–V E.

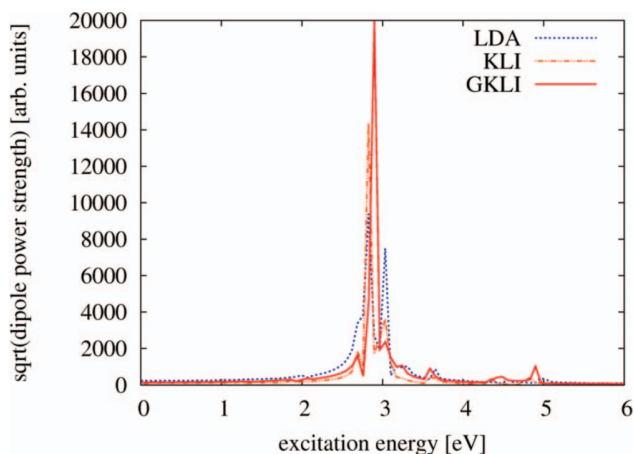


FIG. 6.  $\text{Na}_3^+$  spectrum calculated with LDA, standard KLI, and GKLI.

## B. Metal clusters

Metal clusters are known for their collective response properties that are well described with (semi)local xc functionals. Here, we focus on  $\text{Na}_3^+$  that was reported to be well described by both the TD LDA and TD EXX functional.  $\text{Na}_5$  as a more difficult case is discussed in the Appendix.

The  $\text{Na}_3^+$  time propagation behaves well in terms of propagation stability and excitation spectra can be determined easily.<sup>89–91</sup> The spectra obtained from LDA, standard KLI, and GKLI are compared in Fig. 6. All three spectra show similar excitation features. The only difference occurs at the main peak, where LDA and standard KLI give an excitation energy of 2.8 eV and GKLI gives 2.9 eV. Thus, the SIC approach does not spoil the good accuracy that TD LDA reaches for  $\text{Na}_3^+$ , i.e., it behaves as hoped for. Similar observations are made for other Na clusters.

## C. Hydrogenated silicon clusters

Hydrogen terminated silicon cluster<sup>4–10,105</sup> belong to a class of confined systems where the excitations have been described as being of excitonic nature. In these systems, the qualitative shift of the lowest excitation to lower energies with increasing cluster size is well described with (semi)local functionals.<sup>8</sup> However, for small hydrogenated silicon clusters (semi)local functionals considerably underestimate the position of the lowest excitation peak in comparison to GW Bethe-Salpeter equation (GW-BSE) and experimental results. This discrepancy vanishes with increasing cluster size.<sup>9</sup> It has further been reported that for silane ( $\text{SiH}_4$ ) and disilane ( $\text{Si}_2\text{H}_6$ ) the standard KLI SIC does not improve the spectrum, but underestimates excitation energies and distorts the structure of some excitation peaks,<sup>10</sup> whereas EXX within the TD-KLI yields reasonable excitation energies.<sup>10</sup>

We first discuss our results for silane<sup>89–91</sup> and compare to results obtained from GW-BSE (Refs. 6, 7, and 9) and the experimental spectrum.<sup>106</sup> Consistent with previous findings,<sup>10</sup> we confirm that the standard KLI SIC spectrum does not improve upon LDA. However, GSIC shifts the total spectrum to higher energies in agreement with the GW-BSE results. Dif-

ferent GW-BSE results have been reported in the literature for the first excitation energy of  $\text{SiH}_4$ : 9.0 eV,<sup>6</sup> 9.16 eV,<sup>7</sup> and 9.4 eV.<sup>9</sup> We regard the real-space approach of Ref. 9 conceptually closest to our real-space implementation, and our TD GSIC results indeed come close to it. A comparison to the experiment<sup>106</sup> shows that the GKLI reproduces the experimentally observed trends and compared to TD LDA also greatly improves the peak positions. Yet, there remains a discrepancy of about 0.5 eV between theoretical and experimental excitation energies (experimental peaks are reported at 8.8 eV, 9.7 eV, and 10.7 eV (Refs. 6 and 106)). We performed our calculations with the experimental geometry of Ref. 107, yet also assessed the influence of the Si–H bond length on excitation energies. We found that an increase of the bond length can explain a couple of 0.1 eV shift downwards in the excitation energies. As the experimental spectrum is rather broad and molecular vibration effects may play a role in silane, we believe that the significance of the comparison to the experiment is limited and rather focus on the comparison to GW-BSE. There we find good agreement and TD GKLI excitations are within the uncertainty limits that the GW-BSE calculations themselves have.<sup>9</sup>

The situation is qualitatively similar for disilane ( $\text{Si}_2\text{H}_6$ ). The spectra shown in Fig. 8 were obtained<sup>89–91</sup> for the experimental geometry.<sup>108</sup> Experimental excitation energies are reported at 7.6 eV, 8.4 eV, and 9.5 eV.<sup>106</sup> Whereas TD LDA and KLI SIC excitation energies are systematically too low, TD GKLI shifts the total spectrum to higher energies, thus greatly improving the agreement with GW-BSE and the experiment. Our excitation energies at 7.8 eV and 9.1 eV compare favorably to the GW-BSE excitations at 7.6 eV and 9.0 eV. However, in the GKLI approach a low intensity peak appears at 8.5 eV. Such a peak has not been reported for the GW-BSE. On the other hand, there is a GKLI excitation at 9.9 eV with almost vanishing signal strength that is close to the 9.7 eV GW-BSE excitation.

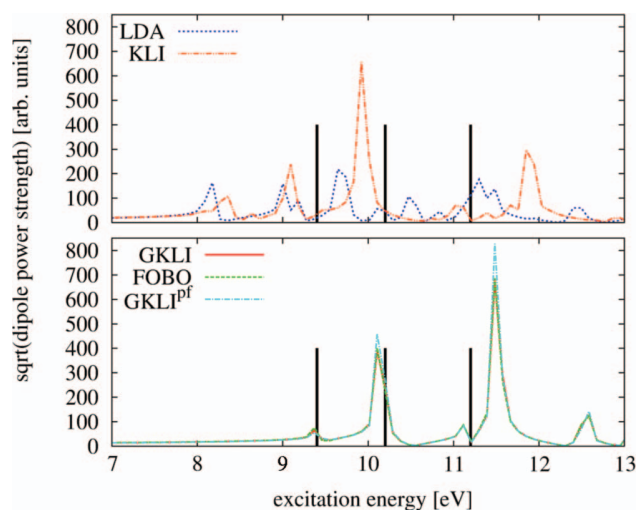


FIG. 7.  $\text{SiH}_4$  spectra calculated with different functionals. Black vertical lines indicate GW-BSE excitation energies at 9.4 eV,<sup>9</sup> 10.2 eV,<sup>6</sup> and 11.2 eV.<sup>6</sup> The upper panel shows LDA and standard KLI SIC, whereas in the lower panel we compare GKLI, FOBO, and  $\text{GKLI}^{\text{pf}}$ .

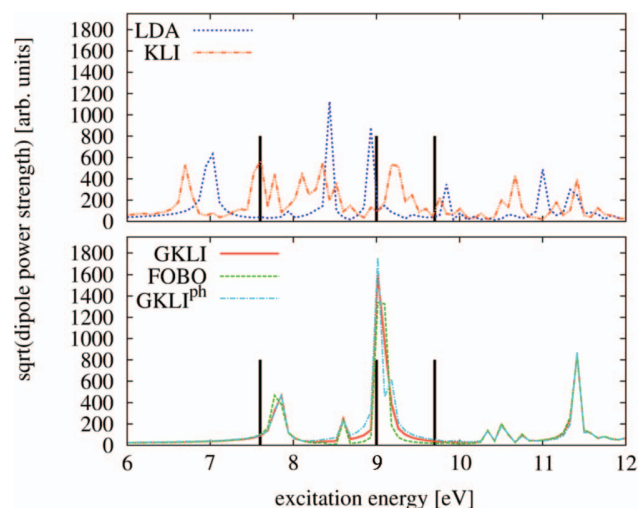


FIG. 8.  $\text{Si}_2\text{H}_6$  spectra calculated with different functionals. Black vertical lines indicate GW-BSE excitation energies at 7.6 eV, 9.0 eV, and 9.7 eV.<sup>6</sup> The upper panel shows LDA and standard KLI SIC, where in the lower panel we compare GKLI, FOBO, and  $\text{GKLI}^{\text{ph}}$ .

For silane and disilane, we included also spectra of GKLI with phase factor approximation and FOBO in Figs. 7 and 8. Generally speaking, all three methods yield very similar results. However, a deviation occurs at the 9.1 eV disilane excitation: GKLI has one pronounced peak, while  $\text{GKLI}^{\text{ph}}$  gives an additional structure at 9.2 eV. We observe such spurious features of the phase factor approximation in different systems, and see this is another reason for cautioning against the use of  $\text{GKLI}^{\text{ph}}$ .

#### D. Polyacetylene chains

Table III presents excitation energies for polyacetylene (PA). PA played a prominent role in the early work on conducting polymers<sup>109,110</sup> and is a paradigm system for strong confinement in two directions, but  $\pi$ -conjugated delocalized electrons in the third (along the chain's backbone). PA has been used for testing for deficiencies of (semi)local DFT and TDDFT in previous studies.<sup>99,111-113</sup>

The lowest excitation energy of acetylene oligomers decreases with increasing chain length because of an increase of the conjugated electronic system, but saturates at some finite chain length.<sup>99</sup> The qualitative trend for small chains is reproduced by the TD LDA. This indicates that the excitation studied here is not of the pronounced CT character which TD LDA

TABLE III. Lowest excitation energy of short polyacetylene chains. The table compares TD LDA and SIC results to linear response TDDFT calculations of Varsano *et al.*<sup>99</sup> (Va) and to B3LYP excitation energies calculated with TURBOMOLE using the def2-QZVP basis set.

	LDA	KLI	GKLI	FOBO	$\text{GKLI}^{\text{ph}}$	Va	B3LYP
$\text{C}_4\text{H}_6$	5.45	5.31	5.68	5.85	5.72	5.75	5.67
$\text{C}_6\text{H}_8$	4.47	4.41	4.62	4.75	4.55,4.69	4.83	4.71
$\text{C}_8\text{H}_{10}$	3.86	3.79	3.93	4.00	3.99	4.12	4.09
$\text{C}_{10}\text{H}_{12}$	3.38	3.31	3.42	3.52	3.45	3.67	3.66

severely underestimates. Judging the quality of the absolute numbers is not as easy, as comparison with experiment<sup>114-117</sup> is notoriously difficult and there is no established theoretical benchmark. One may take the TDDFT calculations of Varsano *et al.*<sup>99</sup> as a reference. The latter employed an xc kernel that was developed based on input from the BSE and yields excitations that are close to the ones obtained with the B3LYP functional. TD LDA excitations are lower than these references by about 0.3 eV. TD GKLI stays somewhat below the B3LYP results, but shifts the excitations upwards as expected.

We use the PA oligomers to further test the performance of different approximations to the GKLI. In accordance with our previous findings, we observe that standard TD KLI SIC erroneously reduces the TD LDA excitation energies. FOBO on the other hand gives broad and slightly higher excitation energies than the energy-minimizing GKLI. As the Foster-Boys criterion enforces spatial localization, this result may indicate that spatial localization effects play a role in the description of the excitations of the PA segments. The  $\text{GKLI}^{\text{ph}}$  results are very close to the GKLI ones but show a peculiarity for  $\text{C}_6\text{H}_8$ : The prominent first excitation peak of the spectrum is split into two peaks separated by 0.14 eV.

#### E. Molecular charge-transfer systems

Finally, we come to the most challenging test for the TD GKLI schemes and investigate CT excitations. First, we take up the DMABN example of Sec. IV B. The second lowest DMABN excitation is of HOMO to LUMO type and exhibits short-range CT character. The CT transition is understood to promote one electron from the methyl group as the donor to the nitrogen side of the benzene ring as the acceptor<sup>87</sup> (see the transition density in the upper panel of Figs. 2 and 9). The lowest excitation is described as a HOMO to LUMO+1 excitation localized on the benzene ring. Experimentally, the local excitation is seen at 4.25 eV and the CT excitation at 4.56 eV.<sup>88</sup> LDA underestimates both excitations by about 0.35 eV. Semilocal functionals improve upon LDA. The TD Perdew, Burke, and Ernzerhof functional,<sup>118</sup> e.g., yields excitation energies of 4.02 eV and 4.30 eV (Ref. 88) for the two lowest DMABN excitations. It is also known that the character of the excitations in DMABN is well described by (semi)local functionals.

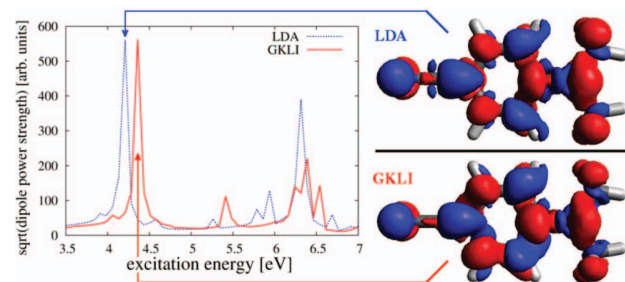


FIG. 9. TD LDA and GKLI SIC spectra of DMABN and transition densities calculated from RT propagation.

TABLE IV. Quantitative transition density comparison of DMABN using  $\kappa_1$  and  $\kappa_2$  of Sec. IV B. We indicate the functional and the method of calculation as in Table I.

$\rho_{\omega_1}$	$\rho_{\omega_2}$	$\kappa_1$	$\kappa_2 (\times 10^{-5})$
LDA GS H-L	GKLI GS H-L	0.99994	0.8945
GKLI TD 4.40 eV	GKLI GS H-L	0.92145	4.0776

The GKLI spectrum of Fig. 9 for the low lying excitations is similar to the LDA spectrum, but shifted to higher energies by about 0.2 eV. Thus, the GKLI spectrum looks very promising. Yet, we need to check whether the TD GKLI spectrum only superficially “looks right,” or whether the character of the transition is truly preserved. The transition density analysis of Sec. IV B offers the ideal tool for that purpose. Figure 9 shows iso-surface plots of the short-range CT transition densities obtained from LDA and GKLI in RT propagation. The picture shows a striking similarity between the LDA and GKLI transition densities.

For a quantitative comparison, we further compiled the values of  $\kappa_1$  and  $\kappa_2$  in Table IV. Comparing the GS HOMO to LUMO transition from LDA with the corresponding GKLI transition, one finds almost perfect agreement. This shows that the GS LDA orbitals, i.e., their shape and energetic ordering, are not changed by the SIC procedure. We further find that the  $\kappa_1$  criterion for the TD transition density of GKLI at 4.40 eV and the GKLI GS HOMO to LUMO transition indicates as good an agreement as the corresponding  $\kappa_1$  in LDA. In conclusion, the DMABN excitation energies are improved by the GKLI SIC approach, while the good description of the character of the transition that is reached with (semi)local functionals is correctly preserved by TD GKLI.

Note that we did not include FOBO data in our discussion as propagation with FOBO minimization at every instant of time spoils the spectrum of DMABN. The problem that arises in the FOBO propagation can be related to the fact that FOBO localization is not necessarily energy minimizing. In the case of DMABN, we observe energy fluctuations during the propagation that are by at least a factor of two larger than similar fluctuations in energy-minimizing or fixed phase factor propagation. These fluctuations can be related uniquely to the influence of the FOBO minimization. They spuriously drive the system and lead to artificial peaks in the spectrum. As a side remark, we note that the combination of FOBO localization in the GS and fixed phase factors during the propagation calculation gives a reasonable spectrum for DMABN with peaks at 4.3 eV and 4.6 eV.

In contrast to the DMABN molecule, which is described with moderate but acceptable accuracy by semi-local functionals, the model dipeptide that is our final test case is a hallmark example for the serious CT failure of standard density functionals. Polypeptides<sup>119</sup> show transitions of interpeptide CT character between 7.3 eV and 7.5 eV, and intrapeptide excitations near 5.6 eV and 6.5 eV. In the dipeptide model system of Refs. 69, 88, 105, 119, and 120, the calculated position of the CT state depends on the functional used. The (semi)local functionals strongly underestimate the CT excitation energy. B3LYP upshifts the CT states, but still leads to

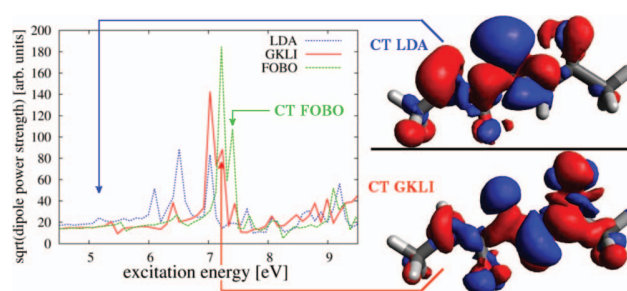


FIG. 10. LDA, GKLI, and FOBO spectra of the dipeptide model system with LDA and GKLI CT transition densities (see text).

a notable underestimation with respect to the complete active space with second-order perturbation theory (CASPT2) reference values and experimental findings. CASPT2 finds the lowest CT state at 7.18 eV.<sup>88</sup>

We calculated spectra of the model dipeptide<sup>89–91, 121, 123</sup> by RT propagation. The corresponding Fig. 10 clearly shows that TD LDA yields a significant signal already from 5.1 eV on, while the lowest excitation in the TD GKLI spectrum can be found at about 5.36 eV and higher excitations differ largely between the two approaches. It is of particular interest that a noticeable feature appears around 7.2 eV in the GKLI spectrum. However, based on the LDA and GKLI spectra alone, well founded characterizations of the excitations and conclusions about the description of CT states are not possible. Therefore, we once again resort to analysis of the transition densities.

We determined and examined the transition densities of all peaks in the spectral range of interest of the LDA and GKLI spectra according to Eq. (20). The transition density corresponding to the first peak in the LDA spectrum that carries notable oscillator strength is shown in Fig. 10. When comparing the iso-surface plot of this TD LDA RT transition density to the plots of occupied to unoccupied orbital transitions between LDA GS orbitals, one finds that there is a close similarity to the LDA HOMO-1 to LUMO transition. This LDA transition corresponds to an excitation from the occupied HOMO-1 that is mainly localized on one of the peptide units to the unoccupied LUMO that is mainly localized on the other peptide unit (see Fig. 11). Thus, it is of interpeptide CT character.

However, the labeling of the orbitals as HOMO-1 and LUMO depends on the functional used to determine the GS: the order of HOMO and HOMO-1 changes if one goes from a LDA to a GKLI calculation, and changes again when one goes from GKLI to FOBO. In Fig. 11, we used the GKLI orbital ordering. Note that GKLI HOMO and LUMO have the same spatial distribution as LDA HOMO-1 and LUMO. HOMO and HOMO-1 eigenvalues are close in energy in the GSIC calculations, and this explains why the ordering changes again when going from GKLI to FOBO. Our assignment of which transition is to be identified with the interpeptide CT excitation is supported by the transition density comparison criteria in Table V. For example, the criteria indicate close similarity between the LDA 5.15 eV RT transition density and the LDA GS HOMO-1 to LUMO transition, and there is no match with

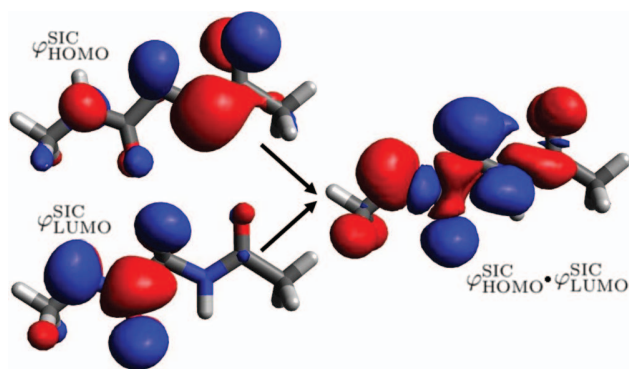


FIG. 11. HOMO to LUMO transition density in the dipeptide model system calculated from the GKLI GS KS orbitals. This corresponds to a HOMO-1 to LUMO transition in LDA and FOBO.

any of the other transition densities up to 7.4 eV. Furthermore, the discussed transition can be identified with the lowest CT transition of the CASPT2 calculations<sup>88</sup> based on the orbital assignment. There is thus no doubt that the lowest CT transition of the dipeptide that we are interested in is found at 5.15 eV in the LDA spectrum<sup>122</sup> and corresponds to the GKLI HOMO-LUMO transition.

Having thus identified the CT excitation and TD LDA's failure we now proceed to investigate how TD GKLI performs in this case. To this end, we analyzed the RT transition densities of all excitations found in the GKLI RT propagation and compared them to the GKLI HOMO-LUMO GS orbital transition density. Looking at the iso-surface plots shows that the GKLI excitation that appears at 7.22 eV (see Fig. 10) is associated with a transition density that is similar to the HOMO-LUMO one. In an effort to make sure that we are not fooled by just "visual similarity" we again evaluated the quantitative comparison criteria  $\kappa_1$  and  $\kappa_2$ . Table V shows that only the excitation at 7.22 eV yields significant overlap, i.e., high val-

TABLE V. Transition density comparison of the low lying dipeptide excitations calculated from RT propagation and orbital to orbital transitions with LDA, GKLI, and FOBO. We use the criteria  $\kappa_1$  and  $\kappa_2$  of Sec. IV B and indicate the functional and the method of calculation as in Table I.

$\rho_{\omega_1}$	$\rho_{\omega_2}$	$\kappa_1$	$\kappa_2 (\times 10^{-5})$
GKLI GS H-L	LDA GS H-1-L	0.9997	0.3021
GKLI GS H-L	FOBO GS H-1-L	0.9997	0.3156
LDA TD 5.15 eV	LDA GS H-1-L	0.9212	0.1656
LDA TD 6.07 eV	LDA GS H-1-L	-0.8774	0.1124
LDA TD 6.55 eV	LDA GS H-1-L	0.0213	0.8355
LDA TD 7.02 eV	LDA GS H-1-L	0.1240	0.8304
LDA TD 7.38 eV	LDA GS H-1-L	-0.2598	0.0876
GKLI TD 5.36 eV	GKLI GS H-L	0.2290	0.3346
GKLI TD 6.37 eV	GKLI GS H-L	-0.2045	1.2824
GKLI TD 6.95 eV	GKLI GS H-L	0.6845	0.4200
GKLI TD 7.22 eV	GKLI GS H-L	0.7536	1.3437
GKLI TD 7.53 eV	GKLI GS H-L	0.4432	0.2456
GKLI TD 7.22 eV	LDA TD 5.15 eV	0.7404	0.9516
FOBO TD 7.20 eV	FOBO GS H-1-L	-0.4218	2.4135
FOBO TD 7.40 eV	FOBO GS H-1-L	0.9086	1.2322
GKLI TD 7.22 eV	FOBO TD 7.40 eV	0.9356	13.346

ues, in both  $\kappa_1$  and  $\kappa_2$ . We can, therefore, truly identify the TD GKLI peak at 7.22 eV with the CT excitation.

This finding bears at least two messages. First and most importantly, it shows that TD GKLI can well describe even "difficult" CT excitations: The TD GKLI excitation energy is in very good agreement with the CASPT2 reference. Second, we note that in the TD description the excitation is no longer of a character that can purely be associated with a transition between static orbitals: There is a clear correspondence between the dynamical TD GKLI transition density at 7.22 eV and the GKLI GS HOMO-LUMO transition, but there are also differences. The dynamical transition density of TD GKLI shows more structure, and this finding is in line with our expectations about what TDDFT should do.

Finally, we again shortly assess the performance of approximations to the energy-minimizing TD GKLI scheme. The FOBO spectrum is shifted by about 0.2 eV with respect to the GKLI spectrum, yet qualitatively similar. For the FOBO scheme, we find the CT excitation energy at 7.40 eV and the calculations again support our assignment via the transition density comparison (see Table V): The FOBO transition density clearly corresponds to the GKLI transition density at 7.22 eV as well as the CT transition density calculated from static KS orbitals.

## VI. CONCLUSIONS

In conclusion, we have presented a generalized SIC time-dependent KS scheme using the TDGKLI approximation. In the TD GKLI approach, a TD unitary transformation guarantees for energy minimization at every instant of time. We further discussed and tested several computationally less expensive approximations. The numerical stability of the schemes was investigated.

Our TD GSIC approach was tested for a range of paradigm test systems that exhibit very different sorts of excitations. First, we investigated model hydrogen chains. A reliable description of the static polarizabilities of these systems is known to be related to the field-counteracting behavior of the xc potential. In dynamical situations, we observed a similar field-counteracting trend of the TD GKLI potential at low excitation frequencies. For higher frequency excitations the response develops complicated structures. We showed that approximations to the TD GKLI do not necessarily show the same positive features and the field-counteracting term is lost, e.g., in the generalized Slater approximation. Of all the possible approximations that we tested the FOBO approach comes closest to the energy-minimizing scheme.

Our further tests comprised small sodium clusters, hydrogenated silicon clusters, short segments of polyacetylene, and molecular charge-transfer systems. We showed that transition densities can be a powerful tool for analyzing real-time calculations. Our results demonstrate that Kohn-Sham TD GSIC yields reliable results also for excitations for which standard functionals fail badly, such as so-called excitonic excitations and difficult CT situations. It is thus an attractive, parameter free approach for predicting electronic excitations with TDDFT.

## ACKNOWLEDGMENTS

We thank D. Varsano for providing polyacetylene excitation energy reference values and A. Karolewski for providing polyacetylene geometries. Financial support by the German Research Foundation (DFG) Graduiertenkolleg 1640 and the German-Israeli Foundation is gratefully acknowledged.

## APPENDIX: STABILITY ANALYSIS OF THE PROPAGATION SCHEME FOR $\text{Na}_5$

The calculations presented in the main body of the paper demonstrated that our RT SIC approach based on the TDGKLI equation is numerically stable and efficient enough to be a truly powerful tool for investigating the optical response. Yet, in this Appendix we want to take a careful look at propagation stability for a particularly malevolent system. This is done with the aim of discussing a worst case scenario which may be of little relevance for many practical applications, but which is studied here nevertheless for the sake of completeness.

The small metal cluster  $\text{Na}_5$  has developed a sort of history as a problematic system for propagation approaches. When investigating propagation of the KS equations with the TDKLI potential corresponding to the exact-exchange functional it was found that the propagation was not stable for  $\text{Na}_5$ , and it was pointed out that the (TD)KLI potential violates the zero-force theorem.<sup>57</sup> Stability problems were also discussed for other approaches.<sup>60–62</sup> Yet, in some sense  $\text{Na}_5$  appears as a “pathological case” because for many other systems standard TDKLI calculations have been reported without mentioning problems.<sup>10,58,64,65,124</sup> However, as violation of the zero-force theorem and corresponding energy-conservation problems are in principle expected for any potential that is not a functional derivative, stability problems may occur for potentials that only approximate the true functional derivatives OEP or GOEP, such as the KLI and GKLI approximations, or model potentials.<sup>113,125</sup> The good news of this Appendix is that although  $\text{Na}_5$  continues to be a problematic case, all GSIC propagation schemes greatly improve stability as compared to the plain TDKLI scheme even for this system. This may be attributed to the energy-minimization condition (14) that is enforced at every time step.

As a first and serious<sup>57</sup> test, we propagated the  $\text{Na}_5$  GS without additional perturbation using different SIC versions based on the regular TDKLI and our TDGKLI approximation. In this case, during the time evolution all physical properties should remain at their GS values. We observe in Fig. 12(a) that already after about 30 fs, the KLI SIC total energy notably deviates from the GS energy. The onset and size of this KLI SIC instability is worse than the KLI instability observed earlier for  $\text{Na}_5$  with the EXX functional.<sup>57</sup>

Great improvements are obtained with all GSIC propagation schemes, and a time span of several tens of fs can be safely covered. Yet, deviation from energy conservation occurs at later times. Details of the time evolution and the onset of propagation instability depend on the way how the unitary transformation is treated during the time propagation.

For the question of stability it is worthwhile to first take a close look at the  $\text{GKLI}^{\text{pf}}$  and explicit treatment of the memory contribution ( $\text{GKLI}^{\text{pf}}$  mem) approximations. The fixed phase factor approximation by construction should be correct for the GS propagation situation: It is designed such that the xc potential should not change during propagation without excitation. Moreover, we start from a GS that was calculated quite accurately with the Pederson criterion guaranteed to be fulfilled below a threshold of  $1 \times 10^{-7}$  Ry. Thus on the scale given by this threshold also the memory contribution vanishes. This coincides with the finding that up to a propagation time of about 200 fs no noticeable differences between  $\text{GKLI}^{\text{pf}}$  and  $\text{GKLI}^{\text{pf}}$  mem occur. Yet after about 200 fs, the  $\text{GKLI}^{\text{pf}}$  calculation starts to show energy deviations. In  $\text{GKLI}^{\text{pf}}$  mem, we observe a first drift of the total energy that is larger than the energy scale set by the Pederson criterion after about 300 fs. In both cases, if all the numerics were conducted with perfect accuracy, no deviations from the GS energy should appear. Therefore, we understand the instability of  $\text{GKLI}^{\text{pf}}$  and  $\text{GKLI}^{\text{pf}}$  mem as a delicate interplay between unavoidable numerical inaccuracies and the GKLI potential not being a functional derivative.

This interplay is crucial here because  $\text{Na}_5$  is a very special system in so far as the zero-force theorem is quite noticeably violated already in the (G)KLI GS. Small deviations from the GS potential, even if they are caused only by the numerics, may result in spurious self-excitation. The  $\text{GKLI}^{\text{pf}}$  mem propagation is more stable because the memory term explicitly takes deviations of the Pederson criterion into account. This explanation of the occurrence of the propagation instability is supported by the observation that choosing a less stringent Pederson criterion threshold leads to earlier and more pronounced instability onset in both cases.

The finding that even the “analytically ground-state tailored” approximations show energy deviations after long enough propagation indicates the delicate nature of the  $\text{Na}_5$  test and sets an upper limit for what can be expected from the TD GKLI with numerical energy minimization. GKLI shows first energy deviations on the order of Fig. 12 at around 150 fs. Deviations on the order of  $1 \times 10^{-6}$  % can be detected after about 75 fs. The calculation with FOBO localization at every time step behaves similar to TD GKLI, but energy deviations at later times are higher than in the GKLI case.

The second test is how the different approaches perform after an initial momentum boost. As there are no further external perturbations after the boost the energy should remain constant. Figure 12(b) shows the energy as a function of time after a  $1 \times 10^{-5}$  eV boost excitation. For standard KLI SIC, the energy starts to drift after 22 fs. In the energy-minimizing TD GKLI calculations, the unitary optimization algorithm needs to perform a couple of iterations per time step to find the TD transformation. Therefore, also in GKLI the numerical procedure is now more involved and one expects a greater impact of associated numerical inaccuracies. Notable energy deviations can be observed from about 150 fs on and the GKLI energy exhibits first deviations from the GS energy on the order of  $5 \times 10^{-6}$  % at about 50 fs. The phase factor approximations are now no longer exact, but nevertheless somewhat more stable. Similar to the earlier discussed systems with

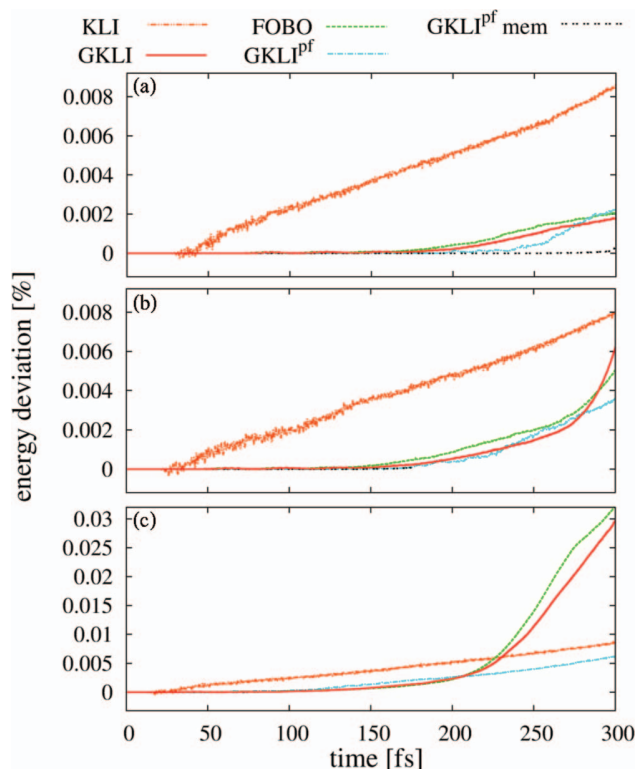


FIG. 12. Energy deviation  $\Delta E = |E^{\text{app}}(t) - E^{\text{app}}(0)|/|E^{\text{app}}(0)|$  of several xc functional approximations during propagation of (a) the  $\text{Na}_5$  GS, the  $\text{Na}_5$  GS after an initial boost excitation of (b)  $1 \times 10^{-5}$  eV, and of (c)  $1 \times 10^{-2}$  eV. The boost was oriented in x-, y-, and z-direction with equal distribution.

local excitations, they also for  $\text{Na}_5$  provide a quite reliable description of the excitations, where the two lowest pronounced excitation peaks are at 2.0 eV and 2.2 eV.

Figure 12(c) shows the situation after a  $1 \times 10^{-2}$  eV boost, i.e., a much stronger excitation. In this case, the drifts are on a larger scale and also appear earlier than before. As a boost of this magnitude results in sizable dynamical changes of the electronic structure, deviations from the true potential are more likely to occur and lead to more involved stability problems. We note, in particular, that the energy-minimizing GKLI total energy after some point in time drifts away with a steeper slope. This indicates that if the propagation has lost the path of stable energy evolution up to a certain extend, effects due to the zero-force theorem violation take over and explicit energy minimization at each time step is no longer able to support stability for the  $\text{Na}_5$  system. Similar findings hold for the TD scheme with FOBO localization.

In summary, our stability analysis has shown that the  $\text{Na}_5$  cluster is a difficult case for all propagation schemes. Even schemes in which the unitary transformation is chosen analytically in such a way that it should lead to an exact propagation show energy drifts after long propagation times. The accuracy with which the Pederson criterion is numerically fulfilled has a notable influence on the propagation stability. These findings indicate that for systems that are as delicate as  $\text{Na}_5$  already the accuracy with which the GS can be achieved plays a role and the problem is thus to some extent independent of the propagation scheme. However, it is a reassuring finding

that the TDGKLI schemes show much better stability than the standard TDKLI scheme. As a general rule, we recommend that whenever propagation schemes are used in combination with orbital functionals and the TDKLI or TDGKLI approximations, one should test for stability of the scheme and one should be aware of that instabilities may result in spurious spectral features. A recent suggestion for evaluating real-time signals<sup>126</sup> may allow to reduce the necessary length of the time evolution below the 40 fs that we aimed at so far.

- <sup>1</sup>J. P. Perdew and A. Zunger, *Phys. Rev. B* **23**, 5048 (1981).
- <sup>2</sup>Y. Zhang and W. Yang, *J. Chem. Phys.* **109**, 2604 (1998).
- <sup>3</sup>S. J. A. van Gisbergen, P. R. T. Schipper, O. V. Gritsenko, E. J. Baerends, J. G. Snijders, B. Champagne, and B. Kirtman, *Phys. Rev. Lett.* **83**, 694 (1999).
- <sup>4</sup>G. Onida, L. Reining, and A. Rubio, *Rev. Mod. Phys.* **74**, 601 (2002).
- <sup>5</sup>S. Ögüt, J. R. Chelikowsky, and S. G. Louie, *Phys. Rev. Lett.* **79**, 1770 (1997).
- <sup>6</sup>M. Rohlfing and S. G. Louie, *Phys. Rev. Lett.* **80**, 3320 (1998).
- <sup>7</sup>M. Rohlfing and S. G. Louie, *Phys. Rev. B* **62**, 4927 (2000).
- <sup>8</sup>I. Vasiliev, S. Ögüt, and J. R. Chelikowsky, *Phys. Rev. B* **65**, 115416 (2002).
- <sup>9</sup>M. L. Tiago and J. R. Chelikowsky, *Phys. Rev. B* **73**, 205334 (2006).
- <sup>10</sup>M. A. L. Marques, A. Castro, and A. Rubio, *J. Chem. Phys.* **115**, 3006 (2001).
- <sup>11</sup>C. Toher, A. Filippetti, S. Sanvito, and K. Burke, *Phys. Rev. Lett.* **95**, 146402 (2005).
- <sup>12</sup>A. Dreuw, J. Weisman, and M. Head-Gordon, *J. Chem. Phys.* **119**, 2943 (2003).
- <sup>13</sup>D. J. Tozer, *J. Chem. Phys.* **119**, 12697 (2003).
- <sup>14</sup>S. Kümmel, L. Kronik, and J. P. Perdew, *Phys. Rev. Lett.* **93**, 213002 (2004).
- <sup>15</sup>T. Yanai, D. P. Tew, and N. C. Handy, *Chem. Phys. Lett.* **393**, 51 (2004).
- <sup>16</sup>J.-D. Chai and M. Head-Gordon, *J. Chem. Phys.* **128**, 084106 (2008).
- <sup>17</sup>E. Livshits and R. Baer, *Phys. Chem. Chem. Phys.* **9**, 2932 (2007).
- <sup>18</sup>T. Stein, L. Kronik, and R. Baer, *J. Am. Chem. Soc.* **131**, 2818 (2009).
- <sup>19</sup>A. Karolewski, T. Stein, R. Baer, and S. Kümmel, *J. Chem. Phys.* **134**, 151101 (2011).
- <sup>20</sup>T. Körzdörfer, J. S. Sears, C. Sutton, and J.-L. Brédas, *J. Chem. Phys.* **135**, 204107 (2011).
- <sup>21</sup>A. Karolewski, L. Kronik, and S. Kümmel, "A perspective on tuned range-separated hybrid functionals" (unpublished).
- <sup>22</sup>C. D. Pemmaraju, S. Sanvito, and K. Burke, *Phys. Rev. B* **77**, 121204(R) (2008).
- <sup>23</sup>A. Ruzsinszky, J. P. Perdew, G. I. Csonka, G. E. Scuseria, and O. A. Vydrov, *Phys. Rev. A* **77**, 060502(R) (2008).
- <sup>24</sup>T. Körzdörfer, M. Mundt, and S. Kümmel, *Phys. Rev. Lett.* **100**, 133004 (2008).
- <sup>25</sup>T. Grabo, T. Kreibich, and E. K. U Gross, in *Strong Coulomb Correlation in Electronic Structure: Beyond the Local Density Approximation*, edited by V. Anisimov (Gordon and Breach, Tokyo, 2000).
- <sup>26</sup>J. P. Perdew, R. G. Parr, M. Levy, and J. L. Balduz, *Phys. Rev. Lett.* **49**, 1691 (1982).
- <sup>27</sup>J. P. Perdew, *Adv. Quantum Chem.* **21**, 113 (1990).
- <sup>28</sup>T. Körzdörfer and S. Kümmel, in *Theoretical and Computational Developments in Modern Density Functional Theory*, edited by A. K. Roy (Nova Science, New York, 2012).
- <sup>29</sup>N. T. Maitra, K. Burke, and C. Woodward, *Phys. Rev. Lett.* **89**, 023002 (2002).
- <sup>30</sup>E. K. U. Gross, J. F. Dobson, and M. Petersilka, in *Density Functional Theory*, edited by R. F. Nalewajski, Topics in Current Chemistry Vol. 181 (Springer, Berlin, 1996), p. 81.
- <sup>31</sup>S. Kümmel, in *Fundamentals of Time-Dependent Density Functional Theory*, edited by M. A. L. Marques, N. T. Maitra, F. M. S. Nogueira, E. K. U. Gross, and A. Rubio (Springer-Verlag, Berlin, 2012), Chap. 6, pp. 125–138.
- <sup>32</sup>N. T. Maitra and D. G. Tempel, *J. Chem. Phys.* **125**, 184111 (2006).
- <sup>33</sup>N. T. Maitra, *J. Chem. Phys.* **122**, 234104 (2005).
- <sup>34</sup>M. Hellgren and E. K. U. Gross, *Phys. Rev. A* **85**, 022514 (2011).
- <sup>35</sup>T. Körzdörfer, S. Kümmel, and M. Mundt, *J. Chem. Phys.* **129**, 014110 (2008).

- <sup>36</sup>M. R. Pederson, R. A. Heaton, and C. C. Lin, *J. Chem. Phys.* **80**, 1972 (1984).
- <sup>37</sup>M. R. Pederson, R. A. Heaton, and C. C. Lin, *J. Chem. Phys.* **82**, 2688 (1985).
- <sup>38</sup>M. R. Pederson and C. C. Lin, *J. Chem. Phys.* **88**, 1807 (1988).
- <sup>39</sup>J. Garza, J. A. Nichols, and D. A. Dixon, *J. Chem. Phys.* **112**, 7880 (2000).
- <sup>40</sup>S. Patchkovskii, J. Autschbach, and T. Zieger, *J. Chem. Phys.* **115**, 26 (2001).
- <sup>41</sup>J. Messud, P. M. Dinh, P.-G. Reinhard, and E. Suraud, *Phys. Rev. Lett.* **101**, 096404 (2008).
- <sup>42</sup>J. Messud, P. M. Dinh, P.-G. Reinhard, and E. Suraud, *Ann. Phys.* **324**, 955 (2009).
- <sup>43</sup>S. Kümmel and J. P. Perdew, *Mol. Phys.* **101**, 1363 (2003).
- <sup>44</sup>M. Dauth, T. Körzdörfer, S. Kümmel, J. Ziross, M. Wiessner, A. Schöll, F. Reinert, M. Arita, and K. Shimada, *Phys. Rev. Lett.* **107**, 193002 (2011).
- <sup>45</sup>S. Klüpfel, P. Klüpfel, and H. Jónsson, *Phys. Rev. A* **84**, 050501(R) (2011).
- <sup>46</sup>D. Hofmann, S. Klüpfel, P. Klüpfel, and S. Kümmel, *Phys. Rev. A* **85**, 062514 (2012).
- <sup>47</sup>O. Gunnarsson and B. I. Lundqvist, *Phys. Rev. B* **13**, 4274 (1976).
- <sup>48</sup>O. A. Vydrov, G. E. Scuseria, J. P. Perdew, A. Ruzsinszky, and G. I. Csonka, *J. Chem. Phys.* **124**, 094108 (2006).
- <sup>49</sup>J. F. Janak, *Phys. Rev. B* **18**, 7165 (1978).
- <sup>50</sup>D. P. Chong, O. V. Gritsenko, and E. J. Baerends, *J. Chem. Phys.* **116**, 1760 (2002).
- <sup>51</sup>S. Kümmel and L. Kronik, *Rev. Mod. Phys.* **80**, 3 (2008).
- <sup>52</sup>C. A. Ullrich, U. J. Grossmann, and E. K. U. Gross, *Phys. Rev. Lett.* **74**, 872 (1995).
- <sup>53</sup>M. Mundt and S. Kümmel, *Phys. Rev. A* **74**, 022511 (2006).
- <sup>54</sup>H. O. Wijewardane and C. A. Ullrich, *Phys. Rev. Lett.* **100**, 056404 (2008).
- <sup>55</sup>S. Kümmel and J. P. Perdew, *Phys. Rev. B* **68**, 035103 (2003).
- <sup>56</sup>J. B. Krieger, Y. Li, and G. J. Iafrate, *Phys. Rev. A* **46**, 5453 (1992).
- <sup>57</sup>M. Mundt, S. Kümmel, R. van Leeuwen, and P.-G. Reinhard, *Phys. Rev. A* **75**, 050501(R) (2007).
- <sup>58</sup>X.-M. Tong and S.-I. Chu, *Phys. Rev. A* **57**, 452 (1998).
- <sup>59</sup>X.-M. Tong and S.-I. Chu, *Int. J. Quantum Chem.* **69**, 293 (1998).
- <sup>60</sup>J. Messud, P. M. Dinh, P.-G. Reinhard, and E. Suraud, *Phys. Rev. A* **80**, 044503 (2009).
- <sup>61</sup>P. M. Dinh, J. Messud, P.-G. Reinhard, and E. Suraud, *J. Phys.: Conf. Ser.* **248**, 012024 (2010).
- <sup>62</sup>J. Messud, P. M. Dinh, P.-G. Reinhard, and E. Suraud, *Ann. Phys.* **523**, 270 (2011).
- <sup>63</sup>T. Körzdörfer, S. Kümmel, N. Marom, and L. Kronik, *Phys. Rev. B* **79**, 201205(R) (2009).
- <sup>64</sup>C. A. Ullrich, P.-G. Reinhard, and E. Suraud, *J. Phys. B* **31**, 1871 (1998).
- <sup>65</sup>S.-I. Chu, *J. Chem. Phys.* **123**, 062207 (2005).
- <sup>66</sup>S. I. Chu and D. A. Telnov, *Intense Ultrashort Laser Fields in Computational Studies of New Materials II: From Ultrafast Processes and Nanostructures to Optoelectronics, Energy Storage and Nanomedicine*, edited by T. F. George, D. Jelski, R. R. Letfullin, and G. Zhang (World Scientific, 2011), pp. 75–101.
- <sup>67</sup>J. C. Slater, *Phys. Rev.* **81**, 385 (1951).
- <sup>68</sup>C. A. Ullrich, P.-G. Reinhard, and E. Suraud, *Phys. Rev. A* **62**, 053202 (2000).
- <sup>69</sup>D. Hofmann, T. Körzdörfer, and S. Kümmel, *Phys. Rev. Lett.* **108**, 146401 (2012).
- <sup>70</sup>C.-H. Park, A. Ferretti, I. Dabo, N. Poilvert, and N. Marzari, e-print [arXiv:1108.5726v1](http://arxiv.org/abs/1108.5726v1).
- <sup>71</sup>S. F. Boys, *Rev. Mod. Phys.* **32**, 296 (1960).
- <sup>72</sup>J. M. Foster and S. F. Boys, *Rev. Mod. Phys.* **32**, 300 (1960).
- <sup>73</sup>J. Pipek and P. G. Mezey, *J. Chem. Phys.* **90**, 4916 (1989).
- <sup>74</sup>K. Yabana and G. F. Bertsch, *Phys. Rev. B* **54**, 4484 (1996).
- <sup>75</sup>K. Yabana and G. F. Bertsch, *Int. J. Quantum Chem.* **75**, 55 (1999).
- <sup>76</sup>M. Mundt and S. Kümmel, *Phys. Rev. B* **76**, 035413 (2007).
- <sup>77</sup>M. Mundt, *J. Theor. Comput. Chem.* **8**, 561 (2009).
- <sup>78</sup>L. Kronik, A. Makmal, M. L. Tiago, M. M. G. Alemany, M. Jain, X. Huang, Y. Saad, and J. R. Chelikowsky, *Phys. Status Solidi B* **243**, 1063 (2006).
- <sup>79</sup>A. Castro, M. A. L. Marques, and A. Rubio, *J. Chem. Phys.* **121**, 3425 (2004).
- <sup>80</sup>E. S. Fois, J. I. Penman, and P. A. Madden, *J. Chem. Phys.* **98**, 6352 (1993).
- <sup>81</sup>T. Abrudan, J. Eriksson, and V. Koivunen, *Signal Process.* **89**, 1704 (2009).
- <sup>82</sup>M. E. Casida, *Recent Advances in Density Functional Methods, Part I*, edited by D. P. Chong (World Scientific, Singapore, 1995), Vol. 1, Chap. 5, pp. 155–192.
- <sup>83</sup>S. Kümmel, K. Andrae, and P.-G. Reinhard, *Appl. Phys. B* **73**, 293 (2001).
- <sup>84</sup>R. A. Broglia, G. Colò, G. Onida, and H. E. Roman, *Solid State Physics of Finite Systems* (Springer, Berlin, 2004), pp. 68–70.
- <sup>85</sup>M. Thiele and S. Kümmel, *Phys. Chem. Chem. Phys.* **11**, 4631 (2009).
- <sup>86</sup>C. B. Bulliard, M. Allen, G. Wirtz, E. Haselbach, K. A. Zachariasse, N. Detzer, and S. Grimme, *J. Phys. Chem. A* **103**, 7766 (1999).
- <sup>87</sup>C. Jamorski, J. B. Foresman, C. Thilgen, and H.-P. Lüthi, *J. Chem. Phys.* **116**, 8761 (2002).
- <sup>88</sup>M. J. G. Peach, P. Benfield, T. Helgaker, and D. J. Tozer, *J. Chem. Phys.* **128**, 044118 (2008).
- <sup>89</sup>In PARSEC, core electrons are treated by norm conserving pseudopotentials of Troullier-Martins type.<sup>90,91</sup> We used the following grid spacings: 0.3 bohr for the H chains, 0.35 bohr for C<sub>4</sub>H<sub>6</sub>, C<sub>6</sub>H<sub>8</sub>, DMABN, and the dipeptide model, 0.37 bohr for C<sub>8</sub>H<sub>10</sub> and C<sub>10</sub>H<sub>12</sub>, 0.5 bohr for the hydrogenated silicon clusters, and 0.7 bohr for the Na clusters.
- <sup>90</sup>N. Troullier and J. L. Martins, *Phys. Rev. B* **43**, 1993 (1991).
- <sup>91</sup>We used LDA pseudopotentials with the following core cut-off radii  $r_c$ :  $r_c(\text{C}) = 1.29$  bohrs,  $r_c(\text{H}) = 1.39$  bohrs,  $r_c(\text{N}) = 1.50$  bohrs,  $r_c(\text{Na}) = 3.09$  bohrs,  $r_c(\text{O}) = 1.45$  bohrs, and  $r_c(\text{Si}) = 1.79$  bohrs for all channels in all cases, except PA where we used  $r_c(\text{C}) = 1.60$  bohrs.
- <sup>92</sup>B. Champagne, D. H. Mosley, M. Vračko, and J.-M. André, *Phys. Rev. A* **52**, 178 (1995).
- <sup>93</sup>P. Mori-Sánchez, Q. Wu, and W. Yang, *J. Chem. Phys.* **119**, 11001 (2003).
- <sup>94</sup>S. Kümmel and L. Kronik, *Comput. Mater. Sci.* **35**, 321 (2006).
- <sup>95</sup>R. Armiento, S. Kümmel, and T. Körzdörfer, *Phys. Rev. B* **77**, 165106 (2008).
- <sup>96</sup>B. Champagne and B. Kirtman, *Int. J. Quantum Chem.* **109**, 3103 (2009).
- <sup>97</sup>O. V. Gritsenko, S. J. A. van Gisbergen, P. R. T. Schipper, and E. J. Baerends, *Phys. Rev. A* **62**, 012507 (2000).
- <sup>98</sup>O. Christiansen, H. Koch, and P. Jørgensen, *Chem. Phys. Lett.* **243**, 409 (1995).
- <sup>99</sup>D. Varsano, A. Marini, and A. Rubio, *Phys. Rev. Lett.* **101**, 133002 (2008).
- <sup>100</sup>TURBOMOLE V6.0 2009, a development of University of Karlsruhe and Forschungszentrum Karlsruhe GmbH, 1989–2007, TURBOMOLE GmbH, 2007, see <http://www.turbomole.com>.
- <sup>101</sup>Ch. Haettig and F. Weigend, *J. Chem. Phys.* **113**, 5154 (2000).
- <sup>102</sup>F. Weigend, F. Furche, and R. Ahlrichs, *J. Chem. Phys.* **119**, 12753 (2003).
- <sup>103</sup>M. Schreiber, M. R. Silva-Junior, S. P. A. Sauer, and W. Thiel, *J. Chem. Phys.* **128**, 134110 (2008).
- <sup>104</sup>M. van Faassen, P. L. de Boeij, R. van Leeuwen, J. A. Berger, and J. G. Snijders, *Phys. Rev. Lett.* **88**, 186401 (2002).
- <sup>105</sup>D. Rocca, D. Lu, and G. Galli, *J. Chem. Phys.* **133**, 164109 (2010).
- <sup>106</sup>U. Itoh, Y. Toyoshima, and H. Onuki, *J. Chem. Phys.* **85**, 4867 (1986).
- <sup>107</sup>D. R. J. Boyd, *J. Chem. Phys.* **23**, 922 (1955).
- <sup>108</sup>G. W. Bethke and M. K. Wilson, *J. Chem. Phys.* **26**, 1107 (1957).
- <sup>109</sup>H. Shirakawa, E. J. Louis, A. G. MacDiarmid, C. K. Chiang, and A. J. Heeger, *J. Chem. Soc., Chem. Commun.* **1977**, 578.
- <sup>110</sup>C. K. Chiang, C. R. Fincher, Y. W. Park, A. J. Heeger, H. Shirakawa, E. J. Louis, S. C. Gau, and A. G. MacDiarmid, *Phys. Rev. Lett.* **39**, 1098 (1977).
- <sup>111</sup>B. Champagne, E. A. Perpète, S. J. A. van Gisbergen, E. J. Baerends, J. G. Snijders, C. Soubra-Ghaoui, K. A. Robins, and B. Kirtman, *J. Chem. Phys.* **109**, 10489 (1998).
- <sup>112</sup>M. J. G. Peach, E. I. Tellgren, P. Salek, T. Helgaker, and D. J. Tozer, *J. Phys. Chem.* **111**, 11930 (2007).
- <sup>113</sup>A. Karolewski, R. Armiento, and S. Kümmel, *J. Chem. Theory Comput.* **5**, 712 (2009).
- <sup>114</sup>Reliable excitation energies are difficult to state as many different numbers are available in the literature and a clear experimental investigation seems to be difficult. Yet, as an orientation we found experimental excitation energies for C<sub>4</sub>H<sub>6</sub> at 5.71 eV,<sup>115</sup> for C<sub>6</sub>H<sub>8</sub> at 4.93 eV,<sup>116</sup> for C<sub>8</sub>H<sub>10</sub> at 4.38 eV,<sup>117</sup> and for C<sub>10</sub>H<sub>12</sub> at 3.98 eV.<sup>117</sup>
- <sup>115</sup>W. C. Price and A. D. Walsh, *Proc. R. Soc. A* **174**, 220 (1940).
- <sup>116</sup>R. M. Gavin, Jr., S. Risemberg, and S. A. Rice, *J. Chem. Phys.* **58**, 3160 (1973); W. C. Price and A. D. Walsh, *Proc. R. Soc. A* **185**, 182 (1946).
- <sup>117</sup>K. L. D'Amico, C. Manos, and R. L. Christensen, *J. Am. Chem. Soc.* **102**, 1777 (1980).
- <sup>118</sup>J. P. Perdew, K. Burke, and M. Ernzerhof, *Phys. Rev. Lett.* **77**, 3865 (1996).
- <sup>119</sup>L. Serrano-Andrés and M. P. Fülcher, *J. Am. Chem. Soc.* **120**, 10912 (1998).

- <sup>120</sup>D. J. Tozer, R. D. Amos, N. C. Handy, B. O. Roos, and L. Serrano-Andrés, *Mol. Phys.* **97**, 859 (1999).
- <sup>121</sup>We optimized the geometry with the TURBOMOLE (Ref. 100) program package using the B3LYP and Fully Optimized Contracted Gaussian Basis Sets of Triple Zeta Valance Quality (def2-TZVP).<sup>123</sup>
- <sup>122</sup>As an aside we note that the dipeptide provides more examples of the serious failures of TD LDA as there is another CT excitation which TD LDA seriously underestimates.<sup>88</sup> However, in contrast to the TD LDA excitation at 5.15 eV the latter carries practically no oscillator strength and is therefore less interesting and less suited for RT investigation.
- <sup>123</sup>A. Schäfer, C. Huber, and R. Ahlrichs, *J. Chem. Phys.* **100**, 5829 (1994).
- <sup>124</sup>D. A. Telnov, J. T. Heslar, and S. Chu, *Chem. Phys.* **391**, 88 (2011).
- <sup>125</sup>D. A. Telnov and S. Chu, *Phys. Rev. A* **80**, 043412 (2009).
- <sup>126</sup>X. Andrade, J. N. Sanders, and A. Aspuru-Guzik, e-print [arXiv:1205.6485v1](https://arxiv.org/abs/1205.6485v1).



# Manuscript 1

## Integer particle preference during charge transfer in Kohn-Sham theory

D. Hofmann and S. Kümmel

*Theoretical Physics IV, University of Bayreuth, D-95440 Bayreuth, Germany*

Physical Review Letters, submitted (2012)

©2012 The American Physical Society

### ABSTRACT

We investigate the static and dynamic charge transfer that is triggered by external electric fields in model molecular wires. A self-interaction correction in Kohn-Sham density functional theory leads to the desired integer electron transfers that do not occur with standard functionals which miss Coulomb blockade effects. Analysis of the multiplicative exchange-correlation potential in stationary cases and during real-time propagation shows how the local exchange-correlation potential builds up step and reverse-step structures that enforce the integer particle preference. The role of spin-symmetry breaking is discussed.



# Integer particle preference during charge transfer in Kohn-Sham theory

D. Hofmann and S. Kümmel

*Theoretical Physics IV, University of Bayreuth, D-95440 Bayreuth, Germany*

(Dated: August 6, 2012)

We investigate the static and dynamic charge transfer that is triggered by external electric fields in model molecular wires. A self-interaction correction in Kohn-Sham density functional theory leads to the desired integer electron transfers that do not occur with standard functionals which miss Coulomb blockade effects. Analysis of the multiplicative exchange-correlation potential in stationary cases and during real-time propagation shows how the local exchange-correlation potential builds up step and reverse-step structures that enforce the integer particle preference. The role of spin-symmetry breaking is discussed.

PACS numbers: 31.15.E, 71.15.Mb, 31.15.ee, 73.23.HK

The large error that “standard density functionals” such as the local density approximation, generalized gradient approximations, and regular hybrids show for long-range charge-transfer (CT) problems has been one of the most serious and most limiting deficiencies of (time-dependent) density functional theory ((TD)DFT). The fact that standard functionals seriously overestimate CT has long been known [1–5], and the CT problem shows up in many guises. Yet, the various manifestations of TDDFT’s CT problem typically fall into one of two important areas. The first one is the calculation of CT excitations that are part of linear response absorption spectra. Great progress has been made in this field in recent years [6]. The second is the area of quantum transport and molecular electronics. In the latter field the performance of (TD)DFT in practice is still debated. DFT has frequently been combined with non-equilibrium Green’s function theory for calculating transport characteristics. However, it has been argued that this approach can be severely in error [3–5, 7, 8] due to the limited interpretability of DFT eigenvalues. The latter is due to the self-interaction error [3, 4, 7] and the lack of a derivative discontinuity [9, 10] in standard density functionals [3, 5, 7, 8].

Therefore, alternative schemes have been proposed that aim at exploiting the power of real-time propagation methods [11, 12]. These works have shown the conceptual strengths of approaching the conductance CT problem in real space and real time by devising ways of how leads can be modeled. With the open system quantum problem set up in such a way that real-time propagation in the central molecular region has a solid theoretical basis [11], the molecular conductance problem of TDDFT has been reduced to finding exchange-correlation (xc) functional approximations that incorporate the physics that is decisive for this type of CT.

This is still a very considerable challenge, as there is a huge and even qualitative gap between the transport characteristics that standard functionals deliver, and the characteristics that are found in reality. With the present work we take a step towards closing this gap. We demon-

strate that a Kohn-Sham (KS) self-interaction correction (SIC) not only remedies the large overestimation of the response that is obtained with (semi)local functionals, but can also enforce the principle of integer preference in CT. Integer preference can be seen in relation to Coulomb blockade [13] and has long been considered a correlation phenomenon that would be beyond the abilities of readily applicable functionals. By analyzing the local KS potential, we can pinpoint step and reverse-step structures in the xc potential that are crucial for enforcing the integer preference. The results not only encourage the use of KS SIC. They stress the important role of spin-symmetry breaking and provide guiding insights for the further development of functionals that should yield reliable transport characteristics.

Due to the decisive role that self-interaction and the derivative discontinuity play in the conductance problem, it is a close lying idea to employ the SIC of Ref. [1] for studying the CT question. By its very definition,  $E_{xc}^{SIC}[n_{\uparrow}, n_{\downarrow}] = E_{xc}^{app}[n_{\uparrow}, n_{\downarrow}] - \sum_{\sigma=\uparrow, \downarrow} \sum_{j=1}^{N_{\sigma}} [E_H[n_{j\sigma}] + E_{xc}^{app}[n_{j\sigma}, 0]]$ , i.e., by subtracting Hartree energy  $E_H$  and xc energy  $E_{xc}^{app}$  contributions for all occupied orbital densities  $n_{j\sigma}(\mathbf{r}) = |\varphi_{j\sigma}(\mathbf{r})|^2$  from a given xc approximation, the SIC energy is one-electron self-interaction free and incorporates a derivative discontinuity. Using recently developed ground-state [14] and TD KS SIC schemes [15] we can employ the SIC as a KS functional with one multiplicative potential. Thus, we can study the potential structure that develops during electron transfers in real space and real time, allowing to gain insight into the functioning of KS theory.

We use real-valued ground-state KS orbitals, but for the reasons explained in [15, 16] the energy minimizing orbitals, TD KS orbitals, and orbital transformations are complex and we use SIC only in combination with the local spin density approximation (LSDA). All calculations were done with the Bayreuth version [17] of the PARSEC real-space program package [18], with parameters chosen in analogy to Ref. [15]. Our SIC studies use the Generalized Optimized Effective Potential (GOEP) and the Generalized Krieger-Lee-Iafrate (GKLI) approxima-

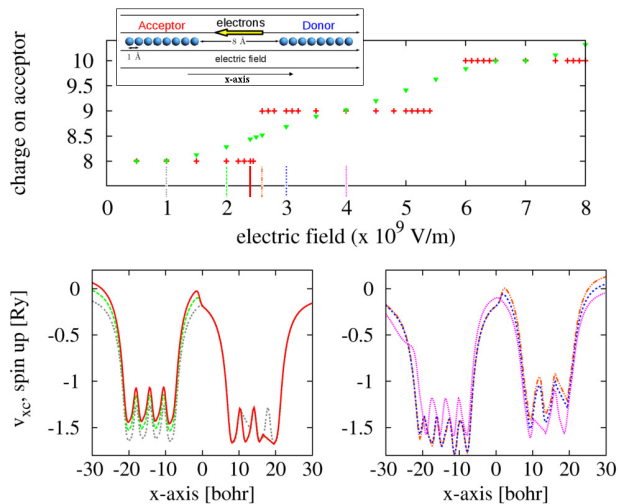


FIG. 1. (Color online) Upper panel: Charge on the left (acceptor, A) hydrogen chain as a function of an external electric field that is applied to the model CT system of H atoms depicted in the inset. Triangles represent LSDA, crosses GKLI-SIC results. In each case, the charge on A is obtained by integration of the density in the left half space of our real-space grid. The two lower panels show the up-spin  $v_{xc}$  of GKLI-SIC along the x-axis for three field strengths before (left) and after (right) the first electron jump. The six field strengths are indicated by vertical lines in the upper panel. Observe how  $v_{xc}$  first builds a pronounced step that works against the electron transfer to A, and then a reverse step that ensures that the electron stays on A.

tion (GKLI-SIC) [14, 15] to the GOEP.

Hydrogen chains have frequently served as model systems that provide tough challenges in terms of a correct description of the CT physics while being technically transparent. We here use the setup [4] that is depicted in the upper part of Fig. 1. Two hydrogen chains, both containing eight H atoms separated by 1 Å, are aligned along the  $x$ -axis with a separation of 8 Å. We apply an electric field along the  $x$ -axis and monitor how charge is transferred from the right H chain (donor, D) to the left H chain (acceptor, A) depending on the field strength. As the distance between the H chains is large, the inter-chain coupling is small and physical electron transfer occurs by integer electron jumps [4]. Thus, up to a certain field strength no charge flow should take place. As soon as the field exceeds a specific strength, one electron, i.e., one (integer) unit of  $e$  should jump from D to A and remain there unless the field strength is reduced. Increasing the field strength further, further integer electron jumps should occur.

However, the CT that one obtains from standard functionals as exemplified by LSDA (triangles in the upper panel of Fig. 1) is completely different and qualitatively wrong [4]. In LSDA, fractional CT occurs from a field strength of  $1.5 \times 10^9$  V/m on. With increasing field

strength there is a gradual transfer of charge to A until one unit of  $e$  has been transferred at a field strength of  $4.0 \times 10^9$  V/m. Further increasing the field strength leads to further gradual CT until the electron number on A reaches a short plateau at a field strength of about  $6.5 \times 10^9$  V/m which indicates the second transferred unit of  $e$ . Using a hybrid functional, the plateaus are broader, but overall one obtains a similarly wrong CT picture [4].

The picture changes completely as one goes from LSDA to SIC. Straightforward SIC of the LSDA functional within the KS framework is sufficient to recover the decisive physical principle of integer preference in CT. In the GKLI-SIC data (crosses in the upper panel of Fig. 1) one observes only integer numbers of electrons on the H chains with electron jumps occurring at field strengths of about  $2.5 \times 10^9$  V/m and  $5.7 \times 10^9$  V/m. We also performed full GOEP calculations up to  $3.5 \times 10^9$  V/m. They yield the same results as GKLI, i.e., the GKLI approximation is well justified. The electron jumps in GKLI-SIC occur at about the same field strengths at which half of an electron is transferred from D to A in LSDA.

Further insight into how the different xc approximations realize the CT can be gained by analyzing the calculations in detail. Restricting the occupation numbers of the KS scheme to integers leads to non-convergent calculations for LSDA. The self-consistent LSDA iterations converged only when fractional occupation numbers were allowed, and the converged calculations then showed fractional charges on each of the H<sub>8</sub> subunits. In the generalized SIC scheme, however, integer occupation numbers are natural as the unitary transformation that connects KS orbitals and energy minimizing orbitals is intrinsically defined only for integer occupations [19], and the integer occupation calculations converge.

Looking at the situation in which the electrons are initially equally distributed over D and A and in which spin is treated explicitly, there are in principle four possibilities for realizing a single integer electron jump: (i) one D spin-up ( $\uparrow$ ) electron jumps to A  $\uparrow$ , (ii) one D spin-down ( $\downarrow$ ) electron jumps to A  $\downarrow$ , (iii) one D  $\uparrow$  electron transfers to the  $\downarrow$  channel of A, and (iv) one D  $\downarrow$  electron transfers to the  $\uparrow$  channel of A. Out of these four possible realizations, (i) and (ii) are analogous with respect to  $v_{xc}$  features and so are (iii) and (iv). Therefore, it suffices to discuss explicitly only one of each class. One may argue that cases (iii) and (iv) are unphysical as the transferring electric field can hardly induce a spin-flip. Yet, we deliberately discuss this situation because it contributes to revealing how the SIC describes CT.

Our calculations show that all four realizations in GKLI-SIC give the same total energy, and the electron jumps occur at the same field strengths. Also, the two different CT scenarios both lead to a weak aufbau principle violation [22]: Although the aufbau principle is guaranteed within both spin channels separately, one electron should be transferred between the spin channels to fulfill

the aufbau principle in the entire system. In other words, there is an unoccupied KS eigenstate in one of the spin channels that is lower in energy than the highest occupied orbital of the other spin channel. In this way, one type of realization “points back” to the other one, and vice versa. This reflects that physically the transfer of one  $\uparrow$  electron is as likely as the one of one  $\downarrow$  electron. The situation is thus reminiscent of the “static correlation” situations that are notoriously difficult for DFT. Yet, GKLI-SIC successfully realizes a one-electron CT by breaking the spin symmetry. The important observation is that the spin-symmetry breaking here occurs in a system with a considerable number of electrons (not just two) and that it is systematic: When we average over (i) and (ii), or (iii) and (iv), or all four possible realizations – which are energetically degenerate – then there remains no spin-polarization. Thus, KS SIC yields the physically correct picture. We therefore argue that spin-symmetry breaking [20, 21] can be seen as a powerful feature of KS theory, not a bug.

How exactly KS theory with its multiplicative, local potential realizes the integer CT is an important question. The two lower panels of Fig. 1 depict the GKLI-SIC xc potential of the spin-up channel in which the electron jump occurs (i.e., realization (i)) for three external fields of increasing strength before (left) and after (right) the electron jump. As the field increases, a step structure of increasing height builds up in between the two H chains, together with a relative shift of the potential between D and A sides (lower left panel). With these features the SIC xc potential works against a spurious fractional CT. After the field has become so strong that an electron transfers from D to A, another important feature manifests: a *reverse* step and potential shift appear, keeping the newly arrived electron on A (lower right panel). With a further increase of the external field these features become less pronounced, “making room” for the next electron transfer.

Figure 2 extends the picture by showing and comparing both spin channels for a larger range of external fields and for the different realizations that were discussed above. Part (a) shows the realization in which both spin channels contain eight electrons throughout, i.e., this is the type of situation that we just looked at in the lower half of Fig. 1. As just discussed, with increasing external field the potential on the A side is shifted upwards with respect to the potential on the D side and a step appears in  $v_{xc}$ . As long as no electron transfer has occurred both spin channels are the same. But as the external field goes beyond  $2.5 \times 10^9$  V/m, spin symmetry breaks as one electron transfers in one of the spin channels. For the sake of this discussion and consistent with Fig. 1 we assume that the transferred electron has up-spin. Then, the up-spin xc potential (left part of Fig. 2 (a)) builds up the reverse step that we already discussed in the lower right panel of Fig. 1, and the right part of Fig. 2 (a)

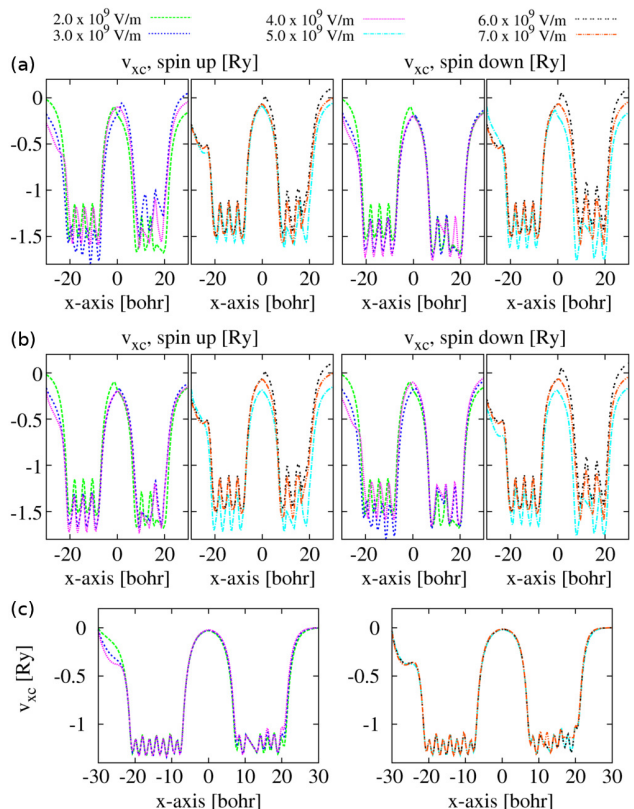


FIG. 2. (Color online) Panel (a) depicts the GKLI-SIC xc potential along the  $x$ -axis for external fields of strengths from  $2.0 \times 10^9$  V/m to  $7.0 \times 10^9$  V/m. The up-spin  $v_{xc}$  is shown in the left two figures and the down-spin one in the right two figures. Both spin channels contain eight electrons. Step structures develop in  $v_{xc}$  of different spin channels and at different field strengths (see discussion in the main text). Part (b) depicts xc potentials similar to (a), but for the situation that after the first electron jump nine electrons are in the spin-down and seven in the spin-up channel. Panel (c) shows  $v_{xc}$  of LSDA, which is identical for both spin channels and shows no step structures.

shows that the step simply vanishes in the down-spin potential. As the external field is further increased the step in the up-spin  $v_{xc}$  decreases as discussed in Fig. 1, but a new step rises in the spin-down channel. This new step counteracts the second electron transfer, until finally a spin-down electron is transferred to A. After this second transfer, we observe a step in both spin channels that supports both electrons to stay on A.

Fig. 2 (b) depicts the GKLI-SIC xc potential for the situation that after the first electron jump nine electrons are in the spin-down and seven in the spin-up channel, i.e., number (iii) of the four realizations that were discussed above. In this case, the electron changes spin assignment when it hops from D to A and one more electron of each spin channel is on A than on D after the first electron jump. Therefore, the reverse step discussed in

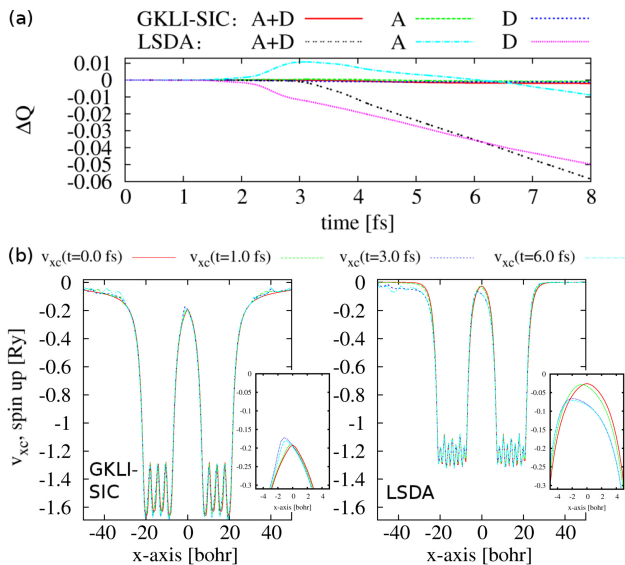


FIG. 3. (a) Change of charge  $\Delta Q$  of the acceptor (A), the donor (D), and the sum of A and D during time propagation using the GKLI-SIC and LSDA potentials and an external field of  $8.0 \times 10^9$  V/m (see text). (b) Snapshots of the TD  $v_{xc}$  taken at different times. Left: GKLI-SIC. Right: LSDA. The small insets in each case enlarge the xc potential in between the two chains. See main text.

the previous situation builds up in both spin channels to counteract back-transfer of the electron, but is less pronounced. These steps decrease as the field strength increases further, and new steps counteracting the second electron jump gradually emerge in  $v_{xc}$  of spin up and down. With the second electron jump, the symmetric distribution of eight electrons per spin channel is recovered and steps in both spin channels keep the electrons on A.

Fig. 2 (c) demonstrates that the step structures are missing completely in  $v_{xc}$  of the LSDA functional. This explains why the LSDA leads to a gradual transfer of charge instead of realistic integer electron jumps.

Finally, we investigate the CT behavior of our model system time-dependently. To this end, we apply an external field in dipole approximation along the  $x$ -axis and increase the field strength linearly within the first two fs of the propagation from zero to  $8.0 \times 10^9$  V/m and then keep it constant. As part of the density may be accelerated to the boundary of our grid, we use an absorbing boundary to prevent this density from being spuriously reflected back to the system. Figure 3 (a) reveals notable differences between LSDA and GKLI-SIC already at the early stages of the time evolution: In LSDA, almost from the start a notable fraction of charge transfers from D to A. In addition we observe ionization of the system at later times as fractions of the density arrive at the left boundary. GKLI-SIC shows a different behavior, as the integrated charges differ only slightly from their initial

values [23]. This behavior may again be understood in terms of  $v_{xc}$  structures. Figure 3 (b) shows snapshots of the TD xc potential. In analogy to the previously discussed figures, for GKLI-SIC a TD step that counteracts spurious CT emerges between the chains, here now as a function of time. Similar steps occur at the outer system boundaries and prevent the system from being ionized. The LSDA  $v_{xc}$  misses such structures. Instead, the potential barrier decreases when charge moves so that CT is too easy and spurious ionization occurs. Observing transfer of an integer charge is not possible with the present setup in either case, as the absorbing boundary changes the norm of the density and we thus observe not only effects of the transfer, but also effects of the boundary. Schemes such as the one of Ref. [11] can overcome this hurdle. Yet, our setup here already shows that also in a truly TD simulation the KS SIC approach cures deficiencies that standard functionals have with respect to the type of CT that is relevant for transport scenarios.

In conclusion, we investigated static and dynamic CT and found that KS SIC enforces the important principle of integer preference in CT. We discussed the role of spin-symmetry breaking and analyzed the local xc potential. The interplay of step structures and reverse-step structures appearing in turn in the different spin channels is decisive for enforcing integer CT. These insights not only let KS SIC appear as a readily applicable, parameter-free functional that cures decisive transport deficiencies, but they may also serve as guiding lines in the further development of functionals. TDDFT using real-time techniques is thus a promising route for an accurate first-principles description of transport phenomena.

We acknowledge financial support by the DFG Graduiertenkolleg 1640 and the German-Israeli Foundation.

- 
- [1] J. P. Perdew and A. Zunger, Phys. Rev. B **23**, 5048 (1981).
  - [2] D. J. Tozer, J. Chem. Phys. **119**, 12697 (2003); A. Dreuw, J. L. Weisman, and M. Head-Gordon, J. Chem. Phys. **119**, 2943 (2003); N. T. Maitra, J. Chem. Phys. **122**, 234104 (2005).
  - [3] C. Toher, A. Filippetti, S. Sanvito, and K. Burke, Phys. Rev. Lett. **95**, 146402 (2005).
  - [4] S.-H. Ke, H. U. Baranger, and W. Yang, J. Chem. Phys. **126**, 201102 (2007).
  - [5] Z.-F. Liu, J. P. Bergfield, K. Burke, and C. A. Stafford, Phys. Rev. B **85**, 155117 (2012).
  - [6] T. Yanai, D. P. Tew, and N. C. Handy, Chem. Phys. Lett. **393**, 51 (2004); J.-D. Chai and M. Head-Gordon, J. Chem. Phys. **128**, 084106, (2008); T. Stein, L. Kronik, and R. Baer, J. Am. Chem. Soc. **131**, 2818 (2009).
  - [7] C. Toher and S. Sanvito, Phys. Rev. Lett. **99**, 056801 (2007); Phys. Rev. B **77**, 155402 (2008).
  - [8] M. Koentopp, K. Burke, and F. Evers, Phys. Rev. B **73**, 121403(R) (2006).
  - [9] J. P. Perdew, R. G. Parr, M. Levy, and J. L. Balduz,

- Phys. Rev. Lett. **49**, 1691 (1982).
- [10] M. Mundt and S. Kümmel, Phys. Rev. Lett. **95**, 203004 (2005).
- [11] S. Kurth, G. Stefanucci, C.-O. Almbladh, A. Rubio, and E. K. U. Gross, Phys. Rev. B **72**, 035308 (2005).
- [12] C.-L. Cheng, J. S. Evans, and T. Van Voorhis, Phys. Rev. B **74**, 155112 (2006).
- [13] S. Kurth, G. Stefanucci, E. Khosravi, C. Verdozzi, and E. K. U. Gross, Phys. Rev. Lett. **104**, 236801 (2010).
- [14] T. Körzdörfer, S. Kümmel, and M. Mundt, J. Chem. Phys. **129**, 014110 (2008).
- [15] D. Hofmann, T. Körzdörfer, and S. Kümmel, Phys. Rev. Lett. **108**, 146401 (2012); D. Hofmann and S. Kümmel, J. Chem. Phys., accepted.
- [16] D. Hofmann, S. Klüpfel, P. Klüpfel, and S. Kümmel, Phys. Rev. A **85** 062514 (2012).
- [17] M. Mundt and S. Kümmel, Phys. Rev. B **76**, 035413 (2007).
- [18] L. Kronik, A. Makmal, M. L. Tiago, M. M. G. Alemany, M. Jain, X. Huang, Y. Saad, and J. R. Chelikowsky, Phys. status solidi B **243**, 1063 (2006).
- [19] T. Körzdörfer, PhD-Thesis, University of Bayreuth (2009).
- [20] J. I. Fuks, A. Rubio, and N. T. Maitra, Phys. Rev. A **83**, 042501 (2011).
- [21] I. Dreissigacker and M. Lein, Chem. Phys. **391**, 143 (2011).
- [22] Such violations have also been observed for other systems, see A. Makmal, S. Kümmel, and L. Kronik, Phys. Rev. A **83**, 062512 (2011).
- [23] Small changes of these observables may result from outer parts of the orbitals that may extend over the boundary of the integration half spaces during propagation due to polarization in the external field.